USE OF ALTERNATING CURRENT FIELD MEASUREMENT (ACFM) TECHNIQUE FOR SIZING INTERNAL SURFACE DEFECTS ON THIN-WALLED AUSTENITIC STAINLESS STEEL PIPES

WING HENDROPRASETYO AKBAR PUTRA

USE OF ALTERNATING CURRENT FIELD MEASUREMENT (ACFM) TECHNIQUE FOR SIZING INTERNAL SURFACE DEFECTS ON THIN-WALLED AUSTENITIC STAINLESS STEEL PIPES

By

©Wing Hendroprasetyo Akbar Putra, S.T.

A thesis submitted to the School of Graduate Studies
in partial fulfillment of the requirements for
the degree of Master of Engineering

Faculty of Engineering and Applied Science
Memorial University of Newfoundland
October 1999

St. John's Newfoundland Canada

To:

Istimarmi Djoko Suroso & Helen Saporo Saadiah

for their patience and continuing encouragement

ABSTRACT

The demand for more reliable materials to face corrosion problems in process plant equipment has led to the use of advanced materials such as stainless steel for many piping systems. As severe localised corrosion sometimes attacks these steels, a reliable inspection technique is needed to detect and characterise such damage, prior to failure of the system. This thesis explores the potential of Alternating Current Field Measurement (ACFM) as a suitable technique for addressing this problem. ACFM is a relatively new electromagnetic based non-destructive testing (NDT) technique that can be used for inspecting electrically conductive materials. The technique offers the potential to detect and size surface, subsurface, or remote surface defects in components made from either carbon or stainless steels.

On the Hibernia platform, stainless steel piping systems that are used to transport freshwater or seawater are sometimes attacked by localised corrosion processes near welds.

Experiments were carried out to develop models to predict the actual depth and length of defects on the inside surface of 6-Mo austenitic stainless steel pipes using the ACFM technique. Two different pipe wall thicknesses were considered in the experiments. Artificial defects of variable depth and length were made using a slitting wheel. Some of the defects were located in the parent metal and others were located at

the weld toe. The experimental results indicate that it is possible to reliably detect and characterise backwall corrosion damage in 6-Mo piping systems using ACFM. Larger defects were noted to produce clearer indications, as would be expected for this NDT technique. It was also apparent that there was no significant difference between results obtained from defects located in the parent metal and results obtained from similar defects located at the weld toe, suggesting that changes in material properties near the weld (e.g. variations in magnetic permeability) have an insignificant influence on the ACFM signals.

ACKNOWLEDGEMENTS

The following people deserve recognition for their contributions:

- The government of the Republic of Indonesia who provided funding for the program.
- Dr. M.R. Haddara as primary supervisor and Associate Dean of Engineering Graduate Studies and Research for his advice.
- Dr. Craig C. Monahan as co-supervisor for his help and guidance throughout the study.
- The staff of Technical Service of Memorial University of Newfoundland for their assistance in manufacturing the test specimens.
- All friends and relatives for their support and help.

TABLE OF CONTENTS

LIST OF FIGURES

LIST OF TABLES

LIST OF NOTATIONS

α	beam angle
B_x	magnetic field component parallel to the crack length
B_z	magnetic field component perpendicular to the crack length
δ_s	skin depth
d	diameter of the disc
D	distance between two contact points
f	frequency of the alternating current
H	crack depth
κ	electric conductivity of the material
λ	wavelength
l	length of the near zone
μ_o	magnetic permeability of the free space
μ	relative magnetic permeability of the material
P	length of the crack face
ρ	resistivity of the material
S	standard penetration depth

t	depth of the defect
t/T	defect depth to wall thickness ratio
V	potential difference

Ch. 1

INTRODUCTION

1.1. General

A growing demand for better-engineered equipment and structures has led to the research and development of advanced materials to replace ordinary carbon steels. Stainless steels are a preferable material for many industrial applications as they have excellent corrosion resistance, high strength, oxidation resistance at high temperature, and resistance to creep. As their corrosion resistance relies on passivity, the use of stainless steels must be followed by careful control. If the passivity is available, the corrosion resistance approaches that of noble metals. Otherwise, the corrosion resistance is reduced to that of iron and the stainless steels become susceptible to corrosion attack.

On offshore structures, including the Hibernia platform, 6-Mo austenitic stainless steel pipes are used for transporting aerated seawater around the plant. Type 6-Mo stainless steel is used due to its excellent resistance to seawater corrosion. Although the parent pipe material generally exhibits excellent corrosion resistance, localized attack can occur at welded joints in the inner surface, where incorrect welding procedures can reduce the corrosion resistance of the material.

Improper control of heat input during welding can create a heterogeneous heat-affected zone (HAZ) that is susceptible to corrosion. It is often found that corrosion preferably attacks HAZ, rather than base metal, due to the change in material properties in that region. Corrosion tends to be highly localized in nature and can cause sudden leakage if not detected immediately. Therefore, periodic inspection is needed to ensure that the system remains fit for purpose.

Non-destructive testing (NDT) techniques are commonly used for inspecting plant equipment because they are non-intrusive (i.e. the components or systems examined remain fit for service after testing and it may not be necessary to shut down the process during inspection). In contrast, destructive testing (DT) techniques cannot be used for this purpose since they may cause significant physical or chemical changes to the components. Normally, such techniques can only be used on a statistical sampling basis and would be inappropriate for expensive, large items such as piping systems. When NDT techniques are used, care must be taken and the process should be controlled so that not only qualitative, but also quantitative information is received and the information is both accurate and useful [Hull, 1988]. If an NDT technique is

misapplied, it can lead to serious errors in judgement of the component or system quality. Therefore, depending on the application, more than one NDT technique may be used to carry out an inspection. Although there is some overlap between the various test methods, they tend to be complementary to one another.

In summary, the use of NDT techniques can bring benefits in many ways. One obvious benefit of using NDT techniques is the identification of defects which, if left undetected, could result in catastrophic failures which would be very costly in money and possibly in lives. The introduction of any inspection system incurs cost, but the effective use of suitable inspection techniques will give rise to very considerable financial savings. Therefore, rapid and accurate NDT techniques are required to detect and characterise defects under specific field conditions. The reliability of an NDT technique depends upon factors such as the nature of the structure under examination and the type of defect being sought [Silk, 1987]. The reliability of any NDT technique is a measure of the efficiency of the technique in detecting discontinuities of a specific type, shape and size. However, the imposition of super sensitive inspection system which is too sensitive can be very wasteful in terms of both time and money, as excessive inspection may not necessarily result in an increase in system or product performance [Hull, 1988].

There are several NDT techniques that can be employed to detect defects in 6-Mo austenitic stainless steel pipes. However, not all of these techniques are likely to give good performance, either in terms of time and cost, or in terms of reliability and sensitivity. Alternating Current Field Measurement (ACFM) has been selected for this

study because it is an NDT technique which is available commercially and can be used more widely, particularly in the offshore industry where it offers some advantages over other conventional NDT techniques. The technique can be applied relatively easily by trained personnel, without causing significant disruption to normal operations. As well, on the basis of its physical principle of operation, the ACFM technique appears to be capable of detecting and characterising remote surface defects in 6-Mo austenitic stainless steel piping systems.

1.2. Research Objectives

ACFM is typically used to detect and characterise defects breaking the external surfaces of components made from carbon steels. The technique can also be used to detect and characterise internal and/or remote face damage in duplex and austenitic stainless steels. However, caution must be exercised when inspecting materials other than carbon steels, as the inspection procedure may be different and interpretation of the results may require special consideration of the material's electromagnetic properties. The major difference between carbon steel and 6-Mo austenitic stainless steel is that the former is a magnetic material, while the latter is a non-magnetic material. Since defect sizing is based on a theoretical analysis of the measured signals, sizing models developed for characterising external surface-breaking defects cannot be used to characterise internal surface-breaking defects.

The major objectives of this research are as follows:

1. To verify the capability of ACFM technique in detecting remote surface breaking (i.e. backwall) defects in 6-Mo stainless steel piping.
2. To determine a threshold depth for the detection of backwall defects in 6-Mo stainless steel piping, mainly for 3.4 mm and 3.8 mm pipe wall thicknesses.
3. To develop a model for predicting the actual depth and length of backwall defects based on ACFM signals obtained by scanning the external surface of the pipe wall.
4. To evaluate the influence of the heat-affected zone on the above model predictions. A comparison of results obtained from the defects located in the base metal and weld HAZ will be used to judge whether changes in material properties caused by welding affect the model predictions.

1.3. Format

This thesis consists of six chapters. Chapter 1 includes an introduction to the topic of interest and presents the main objectives of the research. Chapter 2 is a literature review of stainless steels and the various NDT techniques. Chapter 3 details the experimental procedures followed in the course of performing this work. Chapter 4 covers data collection and analysis and includes an evaluation of the various models, which are developed to correlate the ACFM signals with actual defect dimensions. Chapter 5 discusses a summary of the results obtained from the experiments. And

finally, important conclusions and recommendation for future work are presented in Chapter 6.

Ch. 2

REVIEW OF LITERATURE

2.1. Characteristics of Stainless Steels

2.1.1 Introduction

It was mentioned in the previous chapter that the material used in this study was 6-Mo austenitic stainless steel. This section explains briefly, the classification and properties of stainless steels in order to give the reader an understanding of why stainless steels have become materials of choice for many industrial applications.

The history and development of stainless steels began in the early 20th century in England and Germany. Since that time, their use has become an integral part of material world and has played an important role in the development of many industries, such as power generation, chemical and petrochemical plants.

Stainless steels are iron-based alloys containing up to 1.0% carbon and at least 11% chromium [Davis, 1994]. The chromium provides stainless steels with the capability to form an invisible adherent passive film on the surface that protects the material from further reaction with the environment. The surface film is normally a *chromium-rich oxide* that is automatically formed and self-heals if ruptured in the presence of oxygen. The formation of the layer occurs within seconds after an active stainless steel surface is exposed to an oxidizing environment such as air, aerated water, or oxidizing acids [Baboian, 1995]. As long as the layer is present on the surface, the corrosion resistance of stainless steels approaches that of noble metals. However, in certain environments, the layer can be destroyed, either globally or locally and the stainless steels can corrode as if they were carbon steels. The protective film which forms on stainless steel surfaces is sometimes referred to as *thin film*, while the film which forms on the surfaces of mild/carbon steels is referred to as *thick film*.

2.1.2. Classification of Stainless Steels

Molten steel poured into a mold at the steel mill becomes, on cooling, either an ingot or a casting. An ingot is destined for shaping into desirable materials by mechanical working such as rolling or forging. Steels processed in this manner are called *wrought steels*. Meanwhile, those formed into usable shapes by casting are called *cast steels*. Stainless steel alloys may be either wrought or cast. Both wrought and cast stainless steels can be classified into five major groups: 1) austenitic, 2) ferritic, 3) martensitic, 4) duplex (austenitic-ferritic), and 5) precipitation-hardening. The first four

groups are classified based on the microstructure of the alloys, while the fifth group is classified based on the type of heat-treatment used.

2.1.2.1. Austenitic Stainless Steels

Austenitic stainless steels have a face-centered cubic (FCC) microstructure. They are basically iron-chromium-nickel alloys containing 16% to 25% chromium and 7% to 35% nickel, while the carbon content is normally ranges from less than 0.03% to a maximum of 0.08% [Bringas, 1995]. In some austenitic alloys (e.g. manganese-substitute austenitic stainless steel), nickel is replaced by manganese. Manganese, together with carbon and nitrogen, contributes to the stability of the austenite phase. Carbon and nitrogen are readily soluble in the FCC structure. The addition of nitrogen to the alloy increases its strength. Austenitic stainless steels are non-magnetic and cannot be hardened by heat-treatment [Chawla, 1993]. In general, these alloys have very high corrosion resistance and excellent ductility, weldability, formability, and toughness, even at cryogenic temperatures. Although the alloys cannot be hardened by heat-treatment, they can be hardened by cold working with the degree of work hardening depending on the alloy content. Increasing the alloy content decreases the work hardening rate [Davis, 1994].

In addition to the traditional austenitic stainless steels, there is a relatively new group of austenitic alloys called the superaustenitic stainless steels. Superaustenitic stainless steels have a chemical composition between that of the austenitic and nickel-

base alloys. Examples of these alloys are alloy 20 (UNS N08020, 20%Cr-35%Ni-2.5%Mo-3.5%Cu), alloy 904L (UNS N08904, 20%Cr-25%Ni-4.5%Mo-1.5%Cu), AISI type 304 (UNS S30400), and 6-Mo alloys [Bringas, 1995].

6-Mo alloys include UNS S31254, N08367 and N08925, which have a composition 20%Cr, 6%Mo, 0.2%N and 18-25%Ni. These alloys have been widely used in marine-related applications such as seawater handling equipment, since they exhibit almost total immunity to pitting corrosion in ambient temperature seawater (0°C to 30°C) and high-chloride environments. In addition, they show greater resistance to stress corrosion cracking than do the traditional austenitic stainless steels [Bringas, 1995].

2.1.2.2. Ferritic Stainless Steels

Ferritic stainless steels are basically iron-chromium alloys containing 11% to 30% chromium with only small amounts of austenite-forming elements, such as carbon, nitrogen, and nickel [Davis, 1994]. These alloys have a body-centered cubic (BCC) microstructure. They are ferromagnetic and cannot be hardened by heat treatment [Chawla, 1993]. Since their crystal structure does not change in heating, they must be hardened by cold work. These alloys also possess good ductility and formability. At high temperature, they have relatively poor tensile strength, while at low temperature their toughness can be poor [Bringas, 1995]. These alloys have the lowest strength properties of the stainless steels [Chawla, 1993]. Ferritic alloys are particularly noted

for their resistance to general liquid corrosion, high temperature oxidation, and pitting and chloride-stress corrosion cracking. Their cost is relatively low.

Ferritic stainless steels are commonly used in general construction applications where special resistance to heat or corrosion is required. Although the cost is considerably cheaper than that of nickel-bearing austenitic stainless steels, both alloys have comparable corrosion resistance. In general, the ductility and toughness of ferritic alloys are somewhat lower than that of nickel-bearing austenitic stainless steels [Bringas, 1995]. Examples of these alloys are AISI type 405 (UNS S40500), type 409 (UNS S40900), type 442 (UNS S44200).

Ferritic stainless steels called superferritics, containing high-chromium with low interstitial elements, have recently been developed. These alloys contain 19% to 30% chromium and 1.5% to 4.5% nickel and molybdenum. Alloys in this category have better resistance to pitting, crevice corrosion, and chloride-stress corrosion cracking than conventional ferritic stainless steels. The addition of molybdenum and the very low carbon and nitrogen content have improved their ductility and fabricability. Generally, these alloys are used for water-cooling systems in chemical industry and power plants when cooling water contains chlorides [Davis, 1994].

2.1.2.3. Martensitic Stainless Steels

Martensitic stainless steels are basically similar to iron-carbon alloys that are austenised, hardened by quenching, then tempered to increase ductility and toughness

[Davis, 1994]. These alloys contain about 11% to 20% chromium [Bringas, 1995], 0.1 to 1.0% carbon [Chawla, 1993], and have limited corrosion resistance. Small amounts of other elements such as aluminum, nickel, niobium, sulphur, and selenium are added for specific attributes [Chawla, 1993].

All martensitic stainless steels are ferromagnetic and their heat-treated structure is body-centered tetragonal (BCT). They are used more for their high strength and hardenability, than for their corrosion resistance [Baboian, 1995]. Their strength is highly correlated with their carbon content. A higher carbon content results in higher strength but lower toughness. These alloys are normally used for applications that require corrosion and abrasion resistance, such as pump impellers and knives [Chawla, 1993]. Examples of these alloys are AISI type 410 (UNS S41000), type 416 (UNS S41600).

2.1.2.4. Duplex Stainless Steels

Duplex stainless steels are chromium-nickel-molybdenum alloys in which the alloying elements are added in such proportion as to retain both austenite and ferrite in the microstructure at room temperature. The chromium content of these alloys is about 18% to 26% while the nickel content varies from 3% to 6.5% [Bringas, 1995]. Their composition is controlled to provide a balance between austenite-stabilizing elements (Ni, Mn, N, Cu, and C) and ferrite-stabilizing elements (Cr, Mo, and Si) to produce a desired proportion of duplex structure for optimum properties [Chawla, 1993].

Some duplex stainless steels have ferrite grains in an austenitic matrix (ferrite-rich), some have austenite grains in ferrite matrix (austenite-rich), and others have a composition more or less equally balanced between the two. Experience shows that a ferrite/austenite balance close to 50:50 is the most desirable composition [Chawla, 1993].

The purpose of developing duplex stainless steels is to combine the properties of both austenitic and ferritic stainless steels. The duplex alloys have corrosion resistance similar to austenitic stainless steels, but strength and stress-corrosion cracking resistance greater than that of austenitic stainless steels. Their toughness and ductility are normally between the austenitics and ferritics. Unlike the austenitics, these alloys are magnetic [Chawla, 1993].

The original alloy in this family was predominantly ferritic S32900 [Davis, 1994]. Addition of nitrogen to duplex alloys such as S32950 and S31803 increases the amount of austenite to nearly 50%. In addition, nitrogen improves as-welded corrosion properties, chloride corrosion resistance, and toughness. the improvement in toughness is probably related to the higher amount of austenite present [Davis, 1994].

2.1.2.5. Precipitation-Hardening Stainless Steels

Of the stainless steels, the precipitation-hardening group has the greatest useful strength and heat resistance. These alloys are chromium-nickel grades that can be hardened by an aging treatment [Davis, 1994] and can be classified as austenitic (such

as S66286), semi-austenitic (such as S17700), or martensitic (such as S17400). The classification is determined by their solution-annealed microstructure. Austenitic types are solution treated around 1200°C, quenched, then aged at 700°C – 800°C [Bringas, 1995]. The alloys contain precipitation-hardening elements such as copper, aluminum, titanium, or niobium that are used to achieve age hardening [Davis, 1994].

Semi-austenitic alloys are subsequently heat-treated, resulting in transformation of austenite to martensite. Cold working is sometimes used to facilitate the aging reaction [Davis, 1994]. Chemical compositions of semi-austenitic alloys are arranged carefully to provide a balance between austenite-stabilizing elements and ferrite-stabilizing elements. The result is an alloy which has austenite, or an austenite-ferrite mixture in the annealed condition, and is able to transform to martensitic as a result of thermal treatment [Bringas, 1995].

The martensitic types are more widely used than the austenitic or semi-austenitic types. The balance between ferrite and austenite-stabilizing elements is such that after solution treatment and cooling to room temperature, the alloys are in a martensitic condition. Solution treatment is then followed by an aging treatment for precipitation-hardening [Bringas, 1995]. The martensitic types have better combination of strength and corrosion resistance due to the higher chromium, nickel, and molybdenum contents, as well as their restricted carbon (0.040 max) levels [Davis, 1994]. The low carbon content of the martensitic precipitation-hardening stainless steels is especially critical for toughness and good ductility. However, this low carbon content reduces the wear resistance of these alloys.

Precipitation-hardening alloys can have high tensile yield strength, up to 1700 MPa [Davis, 1994]. These alloys generally have good ductility and toughness with moderate to good corrosion resistance. A better combination of strength and corrosion resistance is achieved with the martensitic type.

2.1.3. Magnetic Permeability of Stainless Steels

The magnetic behavior of stainless steels varies from nonmagnetic to ferromagnetic. Ferromagnetic materials may have soft or hard magnetic characteristics [Davis, 1994]. A soft magnetic characteristic means that the alloy can be magnetized by relatively low-strength magnetic fields. When the applied magnetic field is removed, the steel will have a relatively low residual magnetism. Conversely, alloys that have a hard magnetic characteristic are difficult to magnetize, but retain a large amount of residual magnetism after exposure to a strong magnetic field. The ease with which a material can be magnetized is expressed by a dimensionless parameter called *magnetic permeability* [Davis, 1994].

Magnetic permeability indicates the ease by which magnetic lines flow through the material. When a high magnetic permeability material is magnetized, a large number of magnetic lines flow through the material and there is a tendency for the lines to concentrate in it. If a high magnetic permeability material is exposed to an electric field (e.g. as with ACFM or eddy current testing), most of the magnetic lines induced by the

electric field will be concentrated in the material close to the surface. This phenomenon is referred as a *thin skin* effect.

On the other hand, if a low magnetic permeability material is being magnetised, only a small number of magnetic lines flow through the material and these tend to be distributed relatively evenly through the component thickness. This phenomenon is called a *thick skin* effect. In general, *thick skin* materials are more difficult to magnetize than *thin skin* materials.

All austenitic stainless steels are nonmagnetic (i.e. *thick skin* materials). Their D.C. magnetic permeability is about 1.003 to 1.005 [Davis, 1994]. Certain austenitic stainless steels, such as the 302 and 304 types, exhibit a weak ferromagnetic characteristic. The difference in magnetic performance among grades reflects their composition. For example, the higher-nickel grades exhibit lower magnetic permeability than the lower-nickel grades [Davis, 1994].

Ferritic stainless steels are ferromagnetic with a soft magnetic characteristic and possess high magnetic permeability. Their D.C. magnetic permeability is about 1.0×10^3 to 2.6×10^3 [Davis, 1994]. All martensitic and most precipitation-hardening stainless steels are also ferromagnetic. Due to stress induced by hardening, these alloys exhibit permanent magnetic properties in the hardened condition [Davis, 1994]. In general, ferromagnetic stainless steels have lower magnetic permeability than carbon steels.

2.2. Techniques of Nondestructive Testing

2.2.1. Introduction

It is of great concern that both individual components and complete engineering assemblies or structures are free from damaging defects and other possible causes of premature failure. A series of inspection instruments and techniques has been evolved over the years and new methods are still being developed to assist in the process of assessing the integrity and reliability of parts and assemblies. Nondestructive testing and evaluation methods are widely used in industry for checking the quality of production and also as part of routine inspection and maintenance in service [Hull, 1988].

The term nondestructive testing (NDT) was adopted during the Second World War to describe the technology of defect detection in engineering materials and components [Silk, 1987]. The testing was said to be nondestructive since any specimen examined remained fit for service after the test.

NDT techniques can be grouped into four basic categories [Silk, 1987]. Firstly, there are techniques that are based on direct visual methods, either with or without aids. Secondly, there are techniques that involve the propagation of elastic vibration/waves within specimens. Thirdly, there are techniques that use radiation to inspect for flaws. Fourthly, there are techniques that employ electromagnetic fields to interrogate materials [Silk, 1987].

The purpose of this chapter is to briefly describe each group of NDT techniques, together with their applications, advantages and limitations.

2.2.2. Visual Inspection

Visual inspection is the most basic type of NDT technique. The method covers a wide range of field, from simply picking up a specimen in the hand to sophisticated TV monitoring systems. A visual inspection conducted on the surface of a specimen can both locate defects and give warning of changes in general condition. However, its reliability is highly affected by the human factor since even an experienced worker can be fooled, by the presence of scratches or machining marks, into seeing defects which are not present [Silk, 1987]. Due to that reason, there are some aids to visual inspection which help to reveal defects more readily and consistently.

2.2.2.1. Liquid Penetrant Inspection

Liquid penetrant inspection is used for detecting surface-breaking defects such as cracks, laminations, surface porosity, laps, and folds. The principle of the technique is that a liquid is drawn by capillary attraction into the defects, and after subsequent development, any surface-breaking defects may be rendered visible to the human eye [Hull, 1988].

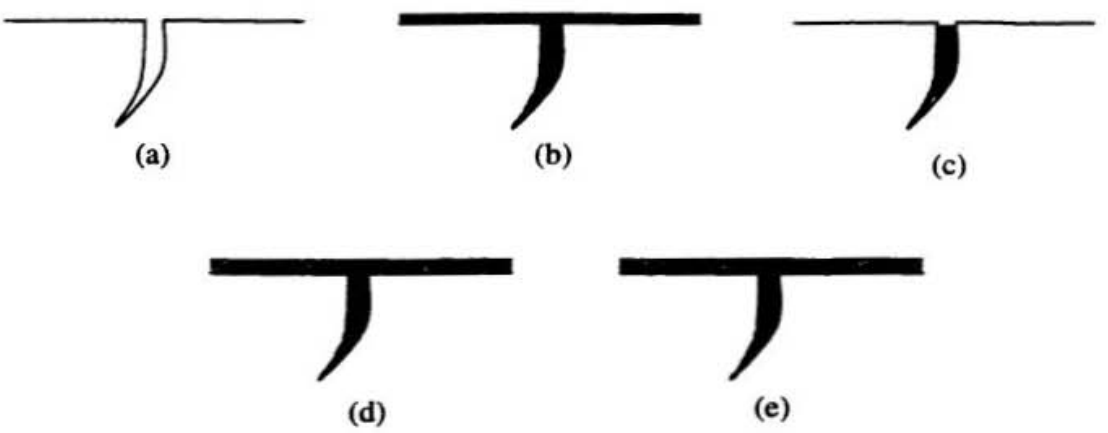

Figure 2.1. Steps in liquid penetrant inspection: (a) material surface clean and grease-free; (b) application of penetrant on the surface and penetrant absorbed into a defect; (c) removal of excess penetrant; (d) application of developer on the surface; (e) penetrant absorbed into developer giving indication of defect.

Liquid penetrant inspection has the advantage of being comparatively simple, and the equipment is cheaper than that required for other NDT techniques. The technique can be used on any non-absorbent or non-porous surface materials such as wrought and cast products in both ferrous and non-ferrous metals and alloys, ceramics, glasswares, and some polymer components. The technique is suitable for components of any size and shape, and is used for both the quality control inspection of semi-finished and finished products and for routine in-service inspection of components [Hull, 1988].

A major limitation of liquid penetrant inspection is that the technique can detect surface-breaking defects, only. The technique also relies on the properties of the penetrant liquid to enter the defect and this will be affected by the defect condition. Thus, defects already filled with liquid or corrosion product, or defects which are very

tight may not allow the penetration of the penetrant and may not show up. On the other hand, shallow surface features such as scratches may allow some penetration and these will show up on the record as clearly as more important defects [Silk, 1987]. Table 2.1 gives a summary of the liquid penetrant inspection technique.

Table 2.1. Summary of the liquid penetrant inspection technique.

Method:	Material surface is covered with penetrating liquid that enters surface-connected defects. After removing excess penetrant and applying developer powder, liquid penetrant will reveal the defect on the surface.
Discontinuities:	Cracks, pinholes, laps, seams, and leaks.
Materials:	All non-porous, non-absorbing.
Features to which applied:	Surfaces, entire objects, complex shapes.
Advantages:	• Simple process and less costly. • Can be used for routine in-line inspection.
Limitations:	• Discontinuities must be surface-connected and open. • Access required for surface cleaning and decontamination. • False indication can arise from shallow scratches. • Surface porosity can mask important indications. • Depth of defect is not indicated.

2.2.2.2. Magnetic Particle Inspection

Magnetic particle inspection is a sensitive method of locating surface and shallow sub-surface defects in ferromagnetic components. The technique is conducted by introducing a magnetic field into the component, and magnetic particles (either wet or dry) are then applied to the surface of the component. Magnetisation may be induced by using permanent magnets, electromagnets, or by passing high currents through or around the component. If the specimen surface is cracked, a portion of magnetic field is forced to leave the specimen locally, forming a stray field on the surface of the component, and the magnetic particles will be attracted by the stray field, revealing a defect. Figure 2.2 illustrates the important effect of defect orientation/location on detectability. Cracks which are aligned parallel to the magnetic field direction may not show up.

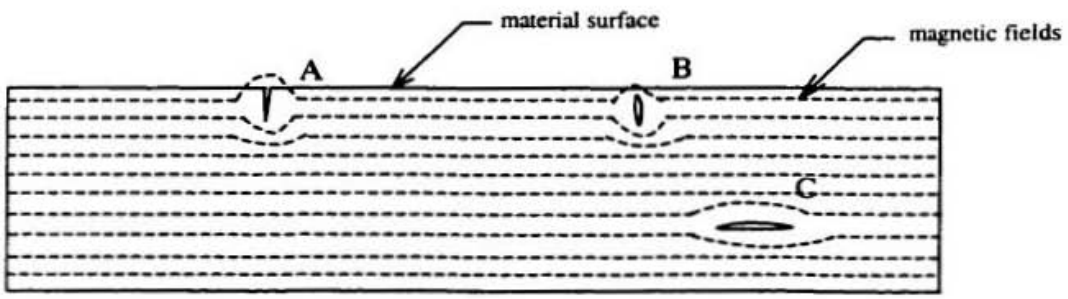

Figure 2.2. Magnetic particle inspection. Defects A and B are detectable, while defect C is likely to remain undetected.

A major advantage of the magnetic particle inspection is that the technique is quite sensitive to very fine surface flaws. It is also possible to obtain indications from some discontinuities that do not break the surface [Hull, 1988]. When using this technique, it

is often unnecessary to have intensive pre-cleaning of the surface. It is often possible to obtain good indications, even if discontinuities contain contaminating materials.

A major limitation is that the technique is only suitable for ferromagnetic materials. Furthermore, to obtain the best results, the induced magnetic fields should be normal to any defects. This means that two or more magnetising sequences will be needed. In addition, the sensitivity of magnetic particle inspection is reduced if the surface of the component is covered by a film of paint or other non-magnetic layer. It is often necessary to demagnetise the component after magnetic particle inspection. Removal of magnetic particles may also be required. A summary of the technique is given in Table 2.2.

Table 2.2. Summary of the magnetic particle inspection technique.

Method:	Test object is magnetised, then magnetic particles applied to surface accumulate over the area where the magnetic field leaks as a result of surface or sub-surface defects.
Discontinuities:	Cracks, seams, pores, and inclusions.
Materials:	Ferromagnetic
Features to which applied:	Surfaces and substrates, regular and uniform shapes.

Table 2.2. Summary of the magnetic particle inspection technique (continued).

Advantages:	• Sensitive to fine surface flaws. • Possibility of detecting subsurface defects. • Often unnecessary to pre-clean the surface intensively.
Limitations:	• Clean and smooth surface is sometimes required. • Magnetic field orientation and strength are critical. • Demagnetisation may be a problem. • Removal of magnetic particles and vehicle may be required.

2.2.3. Acoustic Methods

2.2.3.1. Ultrasonic Testing

Ultrasonic testing is a technique for detecting internal defects by using sound waves that are propagated through the material. Sound waves are elastic waves, which can be propagated through both fluid and solid media. Ultrasonic is a term used for elastic waves that have frequencies higher than the audible range of frequency. The range of audible frequency is from 20 Hz to 20 kHz. The waves used for nondestructive inspection of materials are usually within the range of 0.5 MHz to 20 MHz [Hull, 1988]. In fluids, sound travels in longitudinal waves in which the particles move in the direction of wave propagation. In solids, sound travels in transverse or shear waves in which particle movement is normal to the direction of wave propagation.

With any ultrasonic technique, there are four main things to consider [Silk, 1987]. Firstly, there is the way in which the specimen is stimulated; the most common approach is to use a piezoelectric transducer. Secondly, one must consider the various interactions of the elastic waves in the specimen that determine the response to the probe. Thirdly, there must be a detector to monitor the response, which incorporates any special post-processing to extract information from the received signals. Finally, there should be a strategy (i.e. how one selects and arranges probe and detector to do the job most effectively) [Silk, 1987].

The most commonly used ultrasonic system is shown in Figure 2.3. The left-hand side blip which appears on the Cathode Ray Tube (CRT) screen corresponds to the initial pulse and further blips appear on the time base, corresponding to signal echoes received. The height of the echo is generally proportional to the size of the reflecting surface, but it is also affected by the distance traveled by the signal and attenuation effects within the material [Hull, 1988].

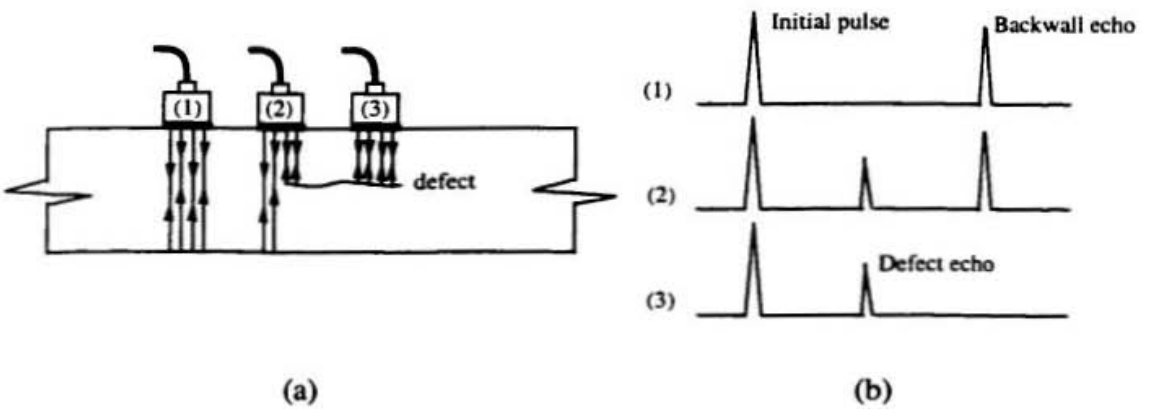

Figure 2.3. Scan display: (a) reflections obtained from defect and backwall; (b) CRT screen display.

The ultrasonic waves generated by a disc-shaped crystal will emerged initially as a parallel-sided beam which later diverges [Hull, 1988], as shown in Figure 2.4. The spread of the beam, α, is related to the frequency and the disc dimension by the relationship:

$$\sin\frac{\alpha}{2} = \frac{1.12\lambda}{d} \qquad (2.1)$$

where: λ = the wavelength (mm)

d = the diameter of the disc (mm).

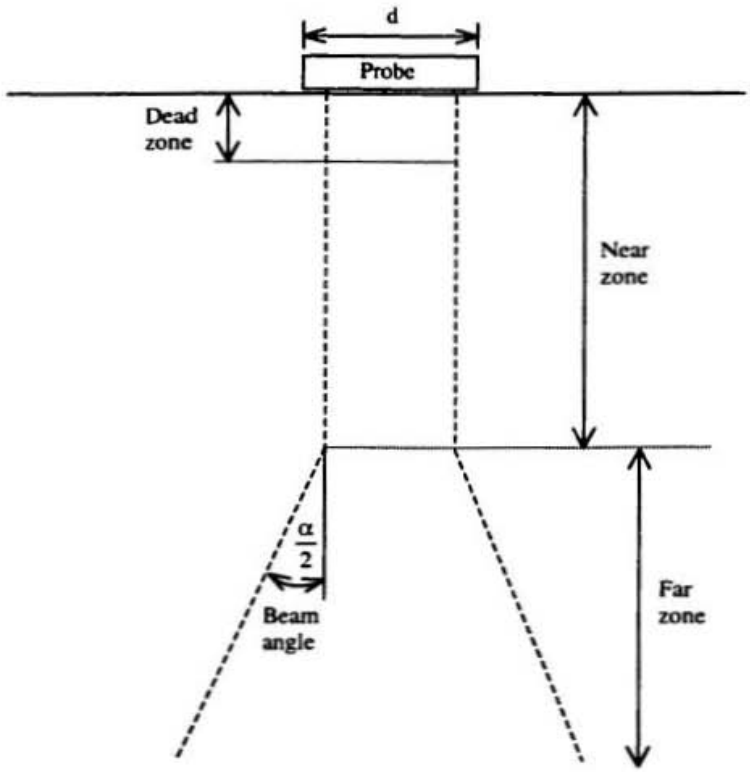

Figure 2.4. Zones in an ultrasonic beam.

An ultrasonic beam can be divided into three zones: the dead zone, the near zone and the far zone. The dead zone is the distance below the surface of the component in which a defect cannot be detected. This can be explained as follows: When an alternating current is applied across a disc of piezo-electric crystal, the disc will contract and expand, generating a short duration pulse of ultrasonic waves in the surrounding medium. Although the disc is heavily damped, it does not stop vibrating immediately after the current is stopped, but will continue vibrating for a short time. During this time, it is not possible for the disc to detect defects in the component. The near zone is the region in which propagation of the ultrasonic beam in the component is almost parallel sided (see Figure 2.4). The length l of the near zone is given by the relationship [Hull, 1988]:

$$l = \frac{d^2}{4\lambda} \tag{2.2}$$

where: d = the diameter of the disc (mm).

λ = the wavelength (mm)

The far zone is the region beyond the near zone where beam spread occurs (see Figure 2.4).

There are several advantages of ultrasonic inspection. The technique is suitable for the detection, identification, and size assessment of a wide variety of both surface and sub-surface defects in metallic materials. With particular attention, it can be used to inspect non-metallic materials. Also, the technique has no significant radiation hazard requiring operational precautions. Modern ultrasonic equipment is compact and light,

and can be operated either from a standard mains supply or internal battery. These features make the equipment become extremely portable, relatively inexpensive, and extremely versatile.

A limitation of ultrasonic inspection is that there are a number of materials that rapidly attenuate the elastic waves [Silk, 1987]. Because of this problem, care should be taken in selecting the frequency of inspection. Other problem is that spurious signals can arise as a result of scatter effects, geometric complexity, angled defects and multiple reflections (elliptical defects) [Hull, 1988]. Also, the technique is not useful in the inspection of plastics, some heavy metals, and certain composite materials [Silk, 1987]. Furthermore, due to the dead zone, ultrasonic testing cannot be used to inspect thin materials (i.e. materials less than 5 mm in thickness). When it is used to inspect thin materials, inaccuracy will arise and may lead to misinterpretation. The problem can be overcome by using special probes or by adding a "shoe", i.e. a layer of appropriate thickness to the probe to ensure that the dead zone is within the probe. It means that additional equipment is still needed. A summary of the technique is given in Table 2.3.

Table 2.3. Summary of the ultrasonic testing technique.

Method:	Ultrasonic waves are transmitted through test material. Ultrasonic echoes and reflections indicate discontinuities in the material.
Discontinuities:	Cracks, voids, laminations, and inclusions.
Materials:	Metals, non-metals, composites.

Table 2.3. Summary of the ultrasonic testing technique (continued).

Features to which applied:	Flat parts, tube parts, welded joints, uniform and regular shapes.
Advantages:	• No significant radiation hazard. • Equipment can be portable, compact and light.
Limitations:	• Coupling is required. • Spurious signals may arise as a result of scatter effects, geometric complexity, angled defects, and multiple reflections (elliptical defects). • Cannot be used to inspect thin materials.

2.2.3.2. Acoustic Emission

When a structure or component is subjected to stress at a particular level, high frequency sound waves within the range 50 kHz to 10 MHz [Hull, 1988] are generated in the component and are emitted in discrete pulses. These emissions then propagate through the component and are detected by a sensor or series of sensors placed on the component surface which, in turn, convert the wave energy into electrical signals. These signals are then amplified, stored, processed and displayed [Hull, 1988]. Figure 2.5 shows a schematic diagram for acoustic emission technique.

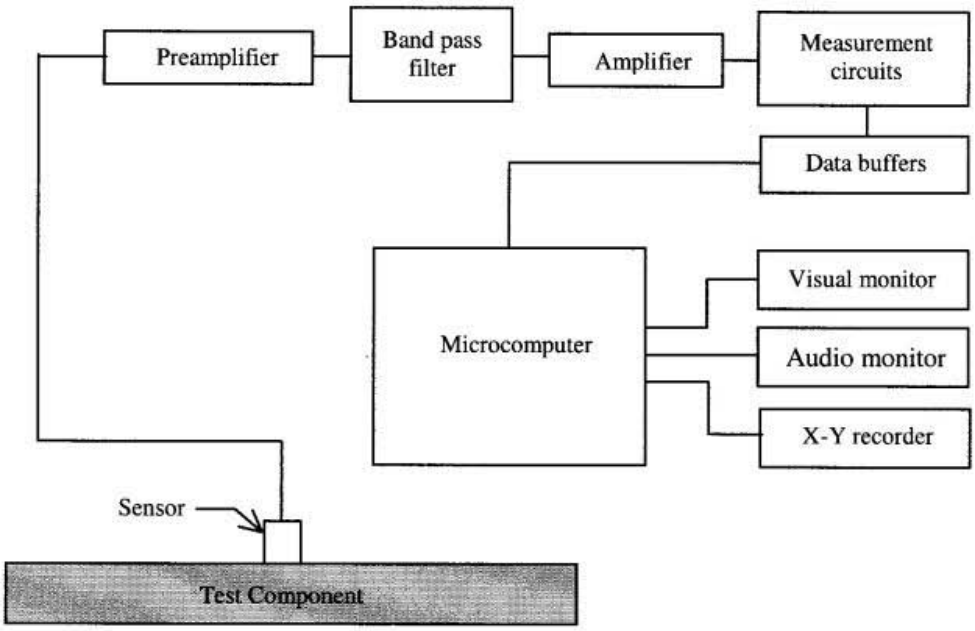

Figure 2.5. Schematic diagram for an acoustic emission technique.

Basically, there are two types of acoustic emission released from materials: a continuous type, and an intermittent or burst type [Hull, 1988]. Continuous emissions are normally of low amplitude and are associated with plastic deformation and the movement of dislocations within a material. Burst emissions are high-amplitude-short-duration pulses resulting from the development and growth of cracks.

There are three basic approaches of using acoustic emission as an NDT technique [Halmshaw, 1991]:

1. Several detectors (sensors) and timing circuits can be used to locate the source of the acoustic emission (i.e. to locate the region where stresses are causing something

to happen, such as crack propagation). The defect can then be pinpointed and characterized using another NDT technique.

2. The rate of emission during stressing can be monitored to discover any sudden changes in emission rate which might be indicative of the formation of new defects.

3. The rate of emission can be monitored and an attempt can be made to relate this to the growth of a defect to determine the remaining safe life of a structure.

Acoustic emission can be used to monitor a wide variety of materials including metals, ceramics, polymers, composites, and woods. The method is non-localized, meaning that is not necessary to examine a specific region of a structure. Large areas can be continuously monitored for stress corrosion cracking and/or corrosion fatigue. The sensitivity of this technique is quite good, as it is possible to detect a growing crack of about 2×10^{-4} mm in length, which is much smaller than that which could be detected by conventional techniques [Hull, 1988].

Acoustic emission has the following limitations: not all discontinuities emit detectable signals; signals can be hidden from the sensors by geometry, noise or absorption, and are affected by material properties; the technique does not determine the size of the discontinuity; there is no standardized method of data interpretation, so the creation of a signature catalog for signal interpretation is required [Hayward, 1978]. The technique is summarised in Table 2.4.

Table 2.4.Summary of the acoustic emission technique.

Method:	High frequency sound waves are emitted from plastic deformation or fracture. Ultrasonic emission rate and intensity indicates crack initiation/propagation and/or deformation induced by stressing.
Discontinuities:	Cracks, corrosion, , plastic deformation.
Materials:	Metals, non-metals, composites.
Features to which applied:	Entire structures, particular area, welds, dynamic monitoring.
Advantages:	• Can monitor large area. • Can perform continuous monitoring. • Sensitive technique.
Limitations:	• Sensors and test component should be in contact. • Acoustic coupling and stressing sources are required. • Signal interpretation could be difficult.

2.2.4. Radiography

The basic principle behind radiography is that very-short-wavelength electromagnetic radiation in the range of 10^{-13} to 10^{-9} m [Hayward, 1978], namely x-

rays or γ-rays will penetrate through solid media, but will be partially absorbed by the medium. The radiation, which passes through the material, can then be detected and recorded on either film or sensitized paper, viewed on a fluorescent screen, or detected and monitored by electronic sensing equipment [Hull, 1988].

The amount of absorption depends on the density and thickness of the material and on the intensity of the radiation. The amount of absorption will also be affected by the presence of certain defects such as voids or porosity within the material. Defects will significantly reduce the thickness of the material in that area so that more radiation is transmitted to the film, producing a darker (higher density) image. A lower density images means extra thickness or high absorption. Figure 2.6 illustrates how radiography can be used to detect a subsurface defect in a plate.

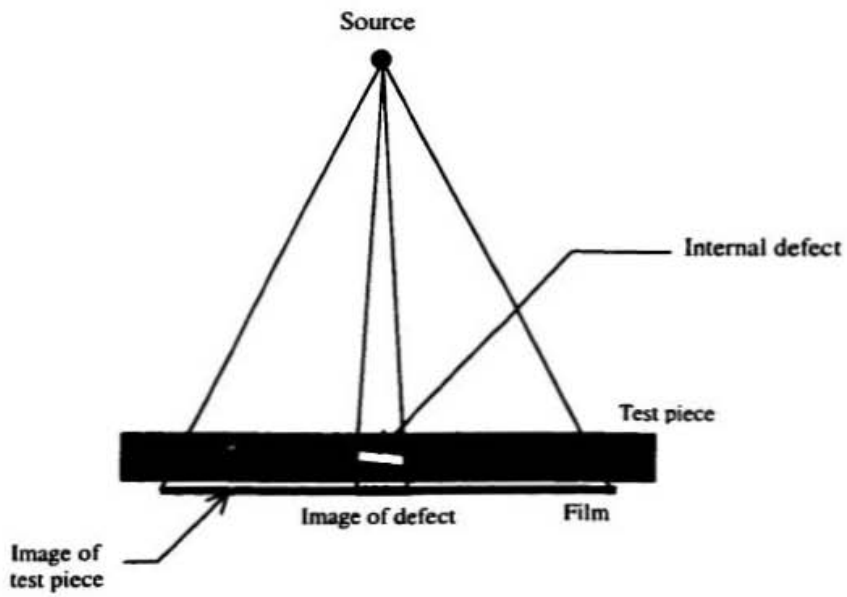

Figure 2.6. Radiographic principle.

X-rays are produced by bombarding a metal target (anode) with a beam of high-velocity electrons. The major components of an x-ray tube are a cathode (used to emit electrons) and an anode target. Both are contained within a high vacuum envelope. A schematic view of an x-ray tube is shown in Figure 2.7.

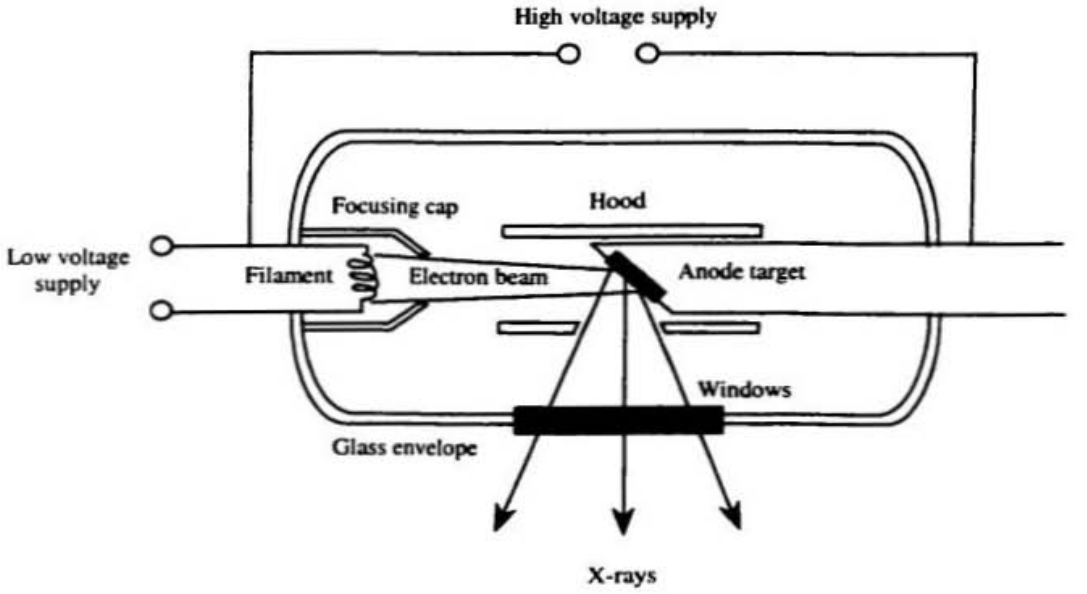

Figure 2.7. Schematic view of an x-ray tube.

γ radiation is generated during the decay of radioactive nuclei. The specific isotopes generally used as γ-ray sources for radiography are Caesium-137, Cobalt-60, Iridium-192, and Thulium-170. Since x-rays are produced by an instrument, they can be switched on and off relatively easily. Conversely, since γ radiation comes from radioactive materials and are continuously emitted, they must be stored and transported in a shielded container. Exposure of the source to the specimen is conducted by

removing part of this shield for a suitable length of time. Figure 2.8 illustrates a γ-ray source container with a flexible cable.

An advantage of radiography is its capability to detect any features in a component or structure provided there are sufficient differences in thickness or density within the material. Radiographic techniques are frequently used for checking welds and castings, and in many instances, the technique is specified for the inspection of mechanical components. Radiography can be used to inspect most types of non-metallic and metallic materials, both ferrous and non-ferrous, having a wide range of material thickness. However, problems can arise when the technique is used to inspect very high- or very low-density materials [Hull, 1988].

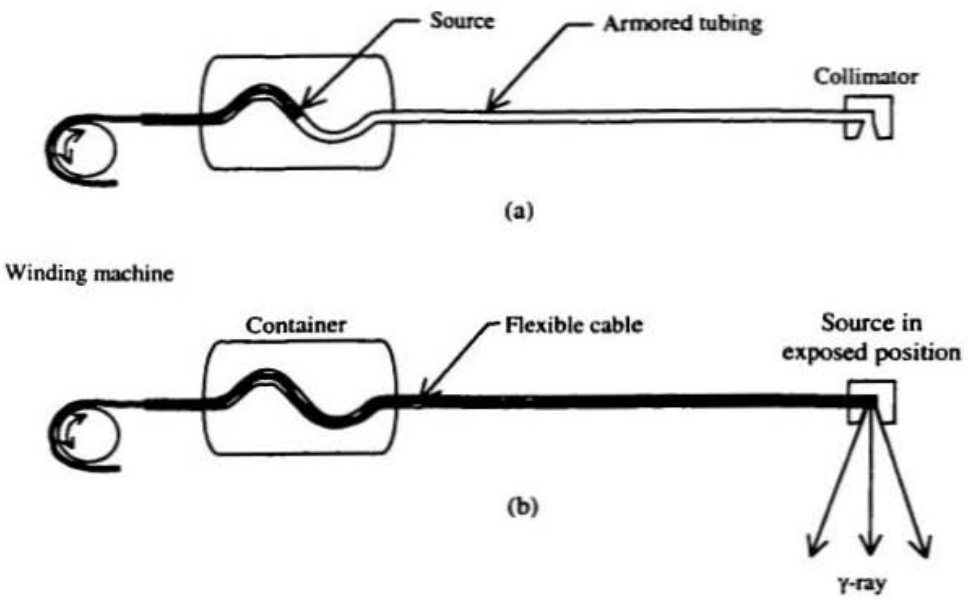

Figure 2.8. γ-ray source container with flexible cable: (a) closed position; (b) opened position.

Although radiography is a very useful NDT technique, it has some relatively unattractive features. The equipment tends to be expensive, compared to other NDT instruments. The operating costs for radiography are also high, and the set-up time is often lengthy. Another aspect that adds to radiography cost is the need to protect personnel from the effect of radiation. Strict safety precautions have to be employed when using radiography [Hull, 1988]. One other limitation of radiography is that the ability to locate a defect will depend upon its orientation relative to the beam. Planar-type defects such as cracks are not always detectable. Table 2.5 shows summary of radiographic inspection technique.

Table 2.5. Summary of the radiography technique.

Method:	Penetrating radiation emitted by x-ray generator or isotope source is imposed on a test component. Radiation transmitted or attenuated by the component is used to detect internal flaws within the component.
Discontinuities:	Cracks, porosity, voids, inclusions, internal malstructure, and density variation.
Materials:	Ferrous or non-ferrous metals, non-metals, composites.
Features to which applied:	Entire components, wide range of shape and size.

Table 2.5. Summary of the radiography technique.

Limitations:	• Set-up time for instrument is lengthy and operation cost is high. • Access to opposite side of the component is normally required. • Voltage, exposure time, and focal spot size are critical. • Radiation hazard.

2.2.5. Electromagnetic Techniques

2.2.5.1. Eddy Current Testing

The basic principle underlying the eddy current testing is that if an alternating current flows in a coil in close proximity to an electrically conductive surface, the magnetic field of the coil will induce circulating (eddy) currents in the surface. The eddy currents in the surface will produce a magnetic field that will be in opposition to the primary magnetic field surrounding the coil. Interaction between these two magnetic fields causes a back electromotive force (EMF) in the coil and affect the loading on the coil thus changing its impedance value.

If the material is uniform in composition and dimension, the impedance value of a search coil placed close to the surface should be the same at all points on the surface. If the material contains a discontinuity, the distribution of eddy currents and their

magnitude will be altered in its vicinity. There will be an interruption of the eddy current flow and a consequent reduction in the magnetic field associated with the eddy currents; thus the coil impedance value will be altered. The impedance of a coil can be determined by measuring the voltage across it. In eddy current testing equipment, changes in coil impedance can be indicated on a meter or chart recorder, or displayed on a CRT screen [Hull, 1988].

There are two common search coils used: flat or pancake type coils, and solenoid type coils (Figure 2.9). The pancake coil is suitable for the examination of flat surfaces while the solenoid type is usually used in examining solid or tubular cylindrical parts. For many test and inspection purposes, one or more coils are mounted in a holder to form an inspection probe.

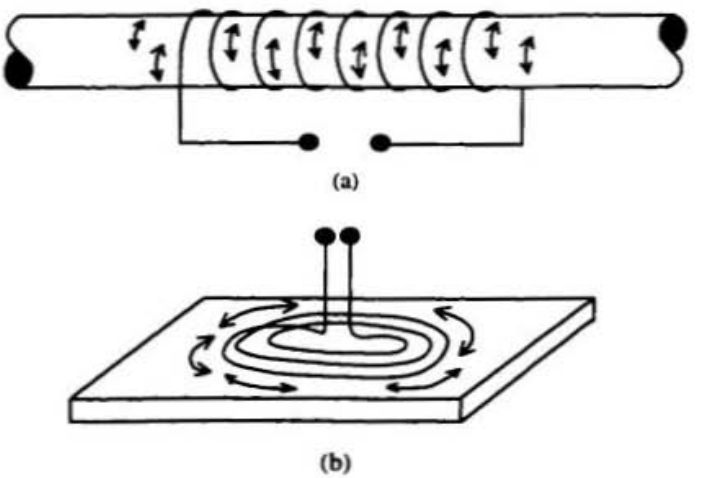

Figure 2.9. (a) Solenoid type coil. (b) Pancake type coil [Hull, 1988].

Eddy current testing equipment consists of four basic parts: the input circuit, the oscillator, the signal processor, and the display. Figure 2.10 shows the basic eddy current testing equipment.

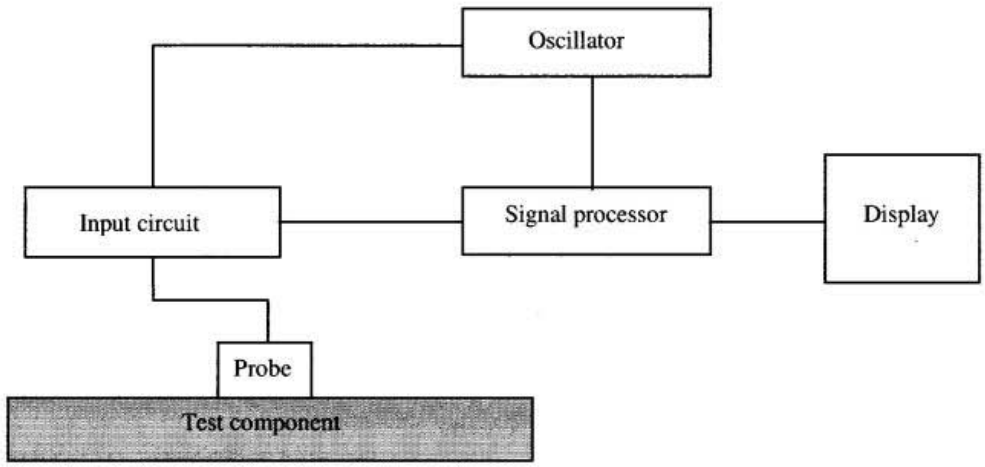

Figure 2.10. Basic eddy current equipment.

A major advantage of the eddy current technique is that it can be used for crack detection and location. An immediate assessment of crack depth and length can also be given. Furthermore, the technique can be used to detect surface and sub-surface defects within components, to determine the thickness of either conducting or non-conducting surface coatings on ferrous or non-ferrous materials, and to measure physical properties such as electrical conductivity, magnetic permeability and hardness [Hull, 1988]. Since it is not necessary for the inspection probe to be in direct electrical contact with the part being tested, the method can be adapted for many applications such as high-speed automatic inspection.

However, care should be taken since eddy current techniques are based on an indirect measurement system. It is necessary to establish clearly the relationship between the structural and geometrical characteristics of a test piece and the instrument response, since indications are affected by more than one physical property of the component. Otherwise, interpretation of the signals may be difficult.

Before employing this technique to inspect a component, the equipment must be calibrated, using a block of material that has same properties as the test component, to obtain reference magnetic currents. For example, if it is desired to size the depth of a crack located close to weld metal, the equipment must be calibrated using a test block made from the same material and containing a crack located close to the weld metal with known depth. Also, since the technique induces electric current fields within the component, the material under test must be electrically conductive. Thus, the technique is largely restricted to metals.

Eddy currents are not distributed uniformly throughout a part under inspection. Their density is higher at the component surface immediately beneath the coil and becomes negligible at some distance below the surface of large components. This phenomenon is commonly referred to as the *skin effect*. The skin effect limits inspection to the outer layers of the component and reduces its sensitivity to deep defects. The depth below the surface at which the magnitude of the eddy current field is reduced to 37% of the value of surface current is called the *standard penetration depth*. The standard penetration depth can be estimated using the relationship [Hull, 1988]:

$$S = 15900\sqrt{\left(\frac{\rho}{\mu f}\right)} \qquad (2.3)$$

where: S = standard penetration depth (mm)

ρ = resistivity of the material (Ω.mm)

μ = relative magnetic permeability of the material

(μ = 1 for non-ferromagnetic materials)

f = frequency of the alternating current (Hz).

Frequencies in the range of 1 kHz – 5 MHz are normally used for the inspection of non-magnetic materials, while frequencies lower than 1 kHz are often employed to inspect magnetic materials [Hull 1988]. For non-magnetic materials, the choice of frequency becomes relatively simple if the technique is used to detect surface flaws, only. In such cases, relatively high frequencies are normally used. Conversely, detection of subsurface defects at considerable depth requires the use of low frequencies, which sacrifices sensitivity. For ferromagnetic materials inspection, due to the relatively low penetration depth, very low frequencies are required to inspect for subsurface flaws. Higher frequencies can be used to inspect for surface defects only.

Figure 2.11 illustrates the important effect of defects orientation/location on detectability. The defects must interrupt the surface eddy current flow to be detected. Defects lying parallel to the current path will not cause any significant interruption and may not be detected.

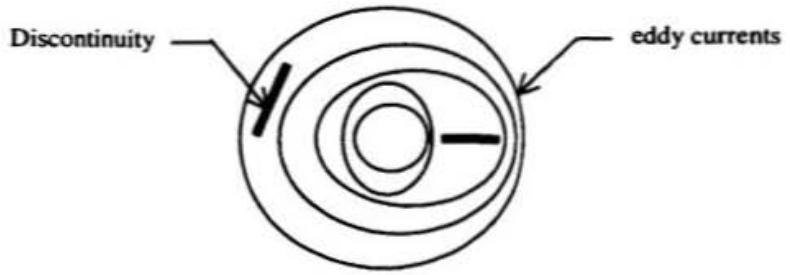

Figure 2.11. Effect of defect orientation on detectability of eddy current technique.

Table 2.6. Summary of the eddy current technique.

Method:	Localised alternating currents induced in test component. Change of impedance value from magnetic field surrounding secondary/eddy current indicates flaws.
Discontinuities:	Cracks, seams, pits, and inclusions.
Materials:	Ferrous or non-ferrous metals, alloys, electrically conducting materials.
Features to which applied:	Surface, sub-surface, regular and uniform shapes.
Advantages:	• Immediate assessment of crack depth and length. • Can be used to measure coating thickness. • Can be used to determine physical properties of materials. • Can be used for high-speed automatic inspection.

Table 2.6. Summary of the eddy current technique (continued)

Limitations	• Non-contacting, but close proximity of probe to surface is required. • False indications as a result of local variations in permeability or physical metallurgy, edge effects, and lift-off effects. • Calibration is required prior to inspection. • Low penetration, limited to near-surface flaws.

2.2.5.2. Potential Drop Crack Measuring Technique

This technique is based on the introduction of a uniform current into the specimen in a direction at right angles to a crack and the measurement of surface voltages around the crack using a contacting probe [Lugg, 1996]. If two closely spaced electrical contact points are applied to the surface of a specimen and a uniform high frequency potential current is injected through the contacts into the specimen, there will be a potential difference between the contacts.

The technique can be carried out with either direct and alternating current. As there is no skin effect with the direct current system, the technique tends to be more suitable for measurement of deep cracks (i.e. cracks more than 5 mm deep). If an alternating current system is used, the current is carried in a thin layer at the metal surface due to the skin effect [Halmshaw, 1991]. The depth of penetration of the alternating current

into the surface of the material is termed the skin depth. There are several factors affecting the skin depth and the relationship between these factors and the skin depth is as follows [Raine and Monahan, 1996]:

$$\delta_s = \frac{1}{\sqrt{\mu \mu_0 \kappa \pi f}} \tag{2.4}$$

where: δ_s = skin depth

μ = relative magnetic permeability of the material

μ_0 = magnetic permeability of free space

κ = electrical conductivity of the material

f = frequency of the alternating current.

When sizing a deep crack using the direct current system, a significantly higher potential is required to inject the field into the component than that for the alternating current system. Consequently, high direct current potential can possibly heat the component and change its electrical resistivity, thus affecting the direct current potential drop (DCPD) signals. Therefore, alternating current potential drop (ACPD) is more commonly used than DCPD. With ACPD, the instrument mainly consists of an alternating current supply, a voltmeter display, and a suitable probe with two contact points.

To illustrate the potential drop technique, consider two contact points placed at a considerable distance D apart on a flat surface. To obtain a uniform potential field in the component, the distance between the two contacts should be arranged not too close. If a probe is placed on any current line in the region that contains no crack (see Figure

2.12), it will record the same potential difference V_1 over the path length between the contact points. The measurement of V_1 is required as a reference potential. If there is a crack on the surface (see Figure 2.13), the path length between the contact points becomes D + 2h, where h is the depth of the crack, and a second potential difference is measured as V_2 [Halmshaw, 1991]. Then:

$$\frac{V_1}{D} = \frac{V_2}{D + 2h} \tag{2.5}$$

$$h = \left(\frac{V_2}{V_1} - 1 \right) \frac{D}{2} \tag{2.6}$$

If the two potential differences V_1 and V_2 are measured, no prior calibration of the equipment is needed, thus eliminating many causes of error. Potential difference techniques are based on an assumption that the crack to be measured is infinitely long. When the crack is short, current flows around the crack ends and this leads to underestimate of the depth.

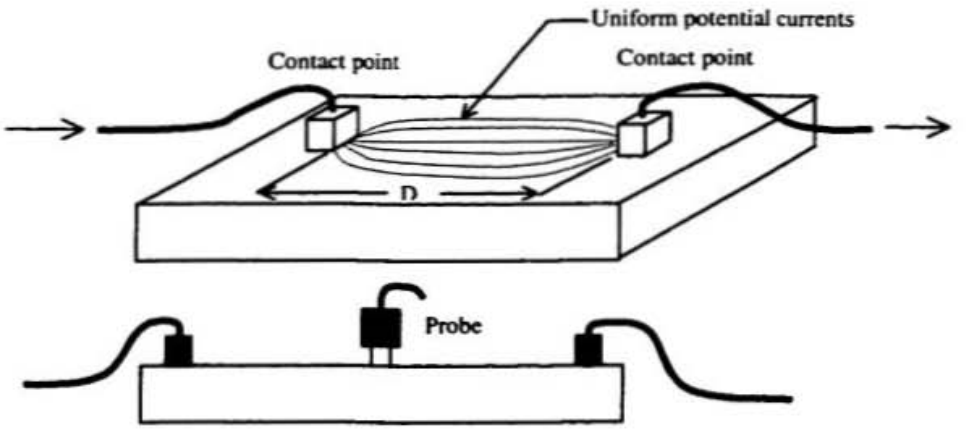

Figure 2.12. Potential drop technique: no crack between the two contact points.

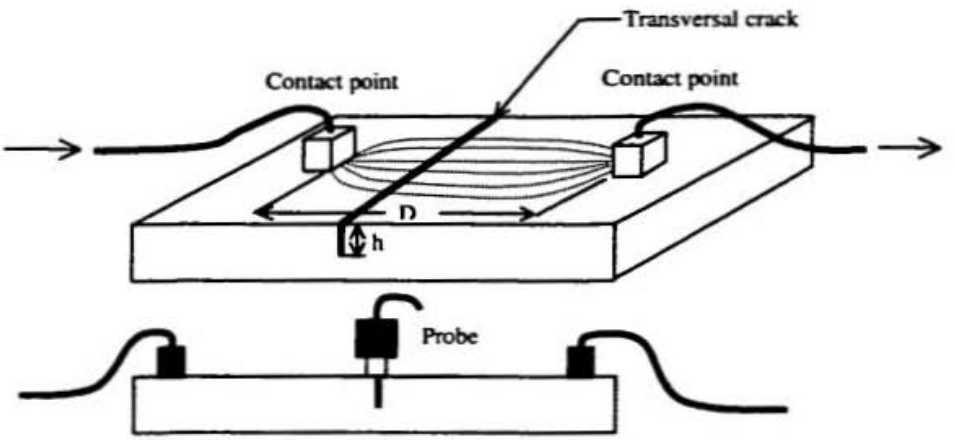

Figure 2.13. Potential drop technique: a crack between the two contact points.

On an inclined crack, a potential drop instrument measures the length of the crack face, P, not the penetrated depth, h (Figure 2.14) [Halmshaw, 1991].

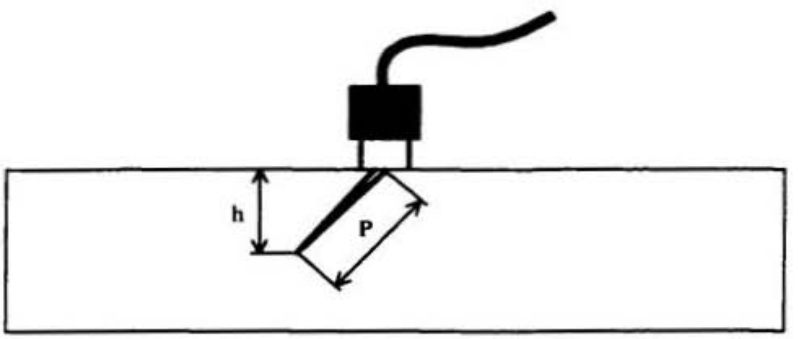

Figure 2.14. Potential drop crack height measurement on an inclined crack [Halmshaw, 1991].

The potential difference crack measuring technique can be used on any electrically conductive material. The main applications of the technique are [Halmshaw, 1991]:

1. To measure the depth of a crack found on the specimen surface by other inspection methods.

2. To monitor the depth of a crack during the service life of a component.

On flat surfaces, where a uniform electrical field can be achieved, the results of crack depth measurement by this method can be very good.

A limitation of this technique is that on irregular-shaped specimens, it may be very difficult to ensure a uniform field across the cracked area. However, this lack of uniformity can be measured and corrected by taking a series of reading over an area adjacent to, but not across the crack. Since the technique injects potential current into the component surface, a direct contact between probes and the component surface is required. Consequently, surface cleaning is required before inspecting. Also, as the technique is not intended for crack detection, other techniques are still needed to find the defects. Table 2.7 gives a summary of the potential drop technique.

Table 2.7. Summary of the potential drop crack measuring technique.

Method:	A uniform electric current is injected between two contact points on the surface of a component. The potential difference between the two points is used to size the crack for depth.
Discontinuities:	Depth of cracks, pits, voids.
Materials:	Metals, some alloys, electrically conductive materials.

Table 2.7. Summary of the potential drop crack measuring technique (continued).

Feature to which applied:	Surface, subsurface, remote surface, regular and uniform shapes.
Advantages:	• Assessment of crack depth and length. • Can be used to monitor crack depth during service life of a component. • Accurate measurement is achieved on flat surfaces.
Limitations:	• Contacting technique requiring surface cleaning before testing. • False indications as a result of complex geometry, local variation in permeability or physical metallurgy, edge effects, and lift-off effects. • Flaws should be oriented perpendicular to the current lines.

2.2.5.3. Alternating Current Field Measurement Technique

Alternating Current Field Measurement (ACFM) is based on the flow of a uniform high frequency alternating current within the material and the measurement of associated electromagnetic fields close to the surface. When an alternating current is passed through a coil, magnetic fields are generated by the coil in the direction perpendicular to the current flow. If the coil is placed in close proximity to an electrically conductive material, the current will be introduced into the surface of the

material. The introduction of the alternating current into the material is accomplished by an ACFM probe.

The standard probe used in the ACFM technique consists of a large induction coil to introduce the uniform high frequency alternating current into the material and two small pick-up coils, designated as B_x and B_z to measure the magnetic field components on the surface [Raine and Monahan, 1996]. Figure 2.15 shows an ACFM pencil probe and Figure 2.16 shows the orientation of the magnetic field components on the surface of the material. Note that the x direction is parallel to the crack orientation and the z direction is perpendicular to the plate surface.

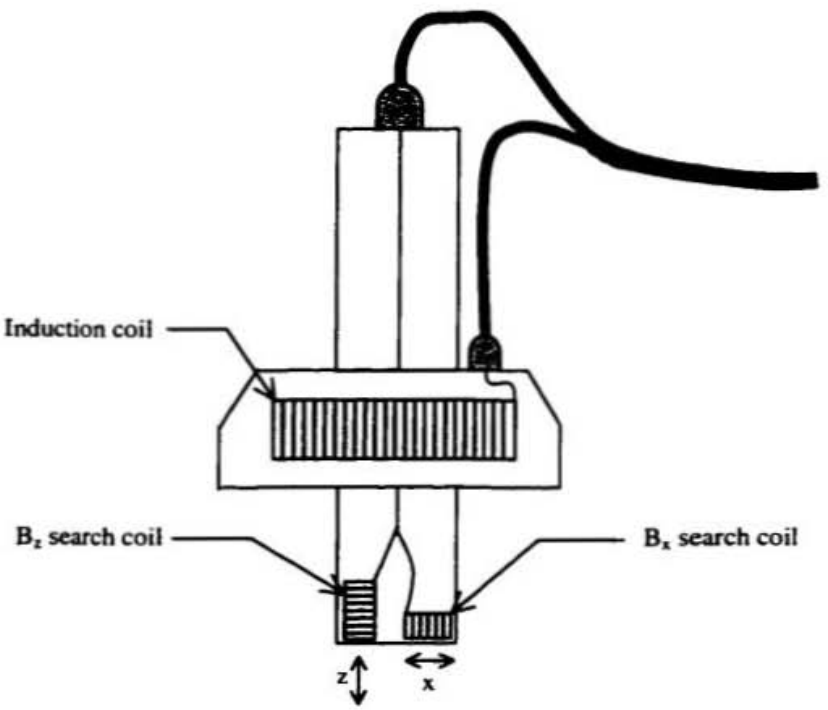

Figure 2.15. Pencil probe used in ACFM technique [Raine and Monahan,. 1996].

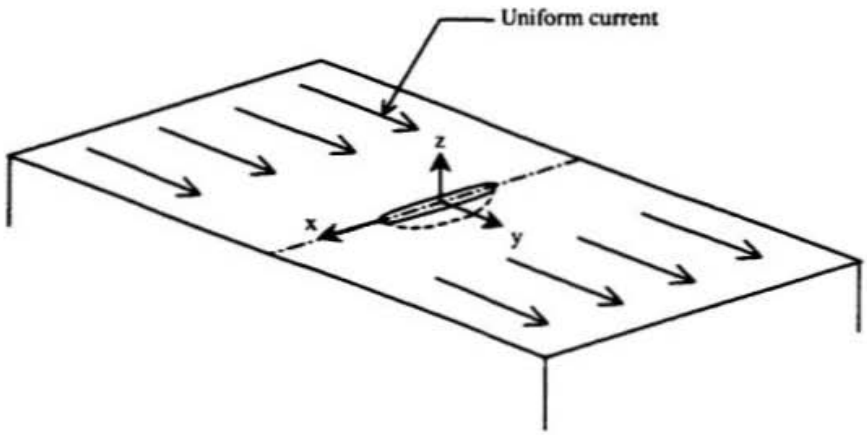

Figure 2.16. Orientation of the magnetic fields on the surface of a component.

When the uniform high frequency alternating current field is induced into the material, the presence of a surface discontinuity such as a crack will disturb the uniform field distribution. The field will take the path of least resistance; thus there is a tendancy for some of the current to be diverted around the ends of the crack. Deviation of the uniform current around the ends of the crack resulting in a rise in the B_x signal just before the crack ends and a sudden drop in the signal due to less current flowing toward the crack centre [Carroll, 1998]. Concentration of the current near the ends of the crack causes positive and negative peaks to appear in the B_z signals. Figure 2.17 illustrates the basic principles of the ACFM technique.

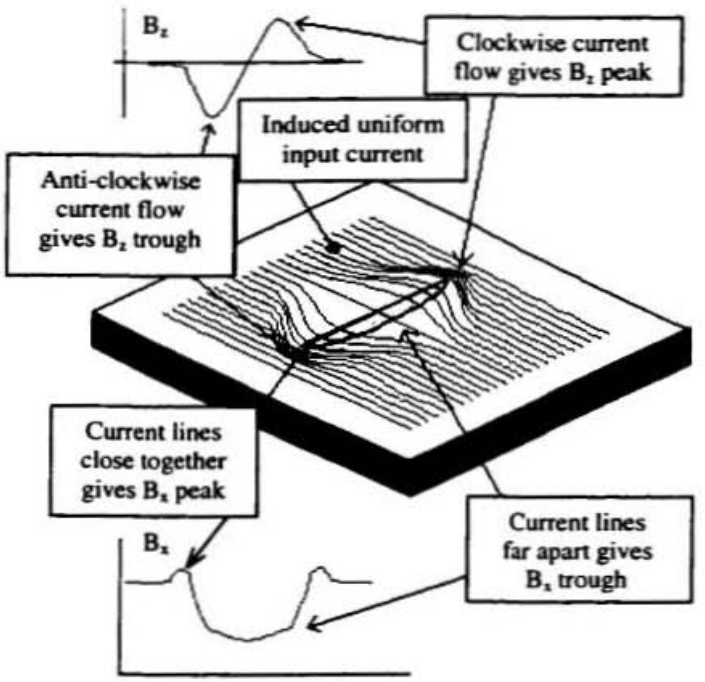

Figure 2.17. Qualitative explanation of the nature of the B_x and B_z signals around a crack [TSC Ltd. Home Page, 1999].

The peaks in the B_z signal are used to provide information on defect location and length. Using a mathematical model based on a theoretical interpretation of the field perturbations caused by a defect, the technique calculates the depth and length of the defect, thus allowing for an immediate evaluation of component integrity. Since the significance of a defect, in terms of structural integrity, generally depends on the depth of the defect, the ACFM technique gives valuable information. Estimating crack depth and length requires knowledge of the background B_x level, minimum B_x level, and B_z estimates of crack length [Lewis, 1991].

Within the ACFM graphics display, the B_x and B_z signals are plotted as a function of time as the probe is traversed parallel to the defect. Removing the time base from the measurement of B_x and B_z, and graphing one against the other results in *a butterfly plot* [Raine and Monahan, 1996]. The relationship between B_x and B_z in the butterfly plot is shown in Figure 2.18.

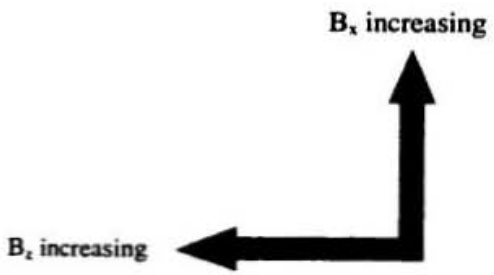

Figure 2.18. B_x and B_z in the butterfly plot.

The advantage of the butterfly plot becomes apparent when the technique is used for crack detection. When there is considerable noise in the B_x and B_z signals, the butterfly plot enables the operator to clearly differentiate between spurious indications and true crack signals [Raine and Monahan, 1996]. Figure 2.19 shows the ACFM signals obtained from scanning a remote surface crack in a 6-Mo austenitic stainless steel pipe.

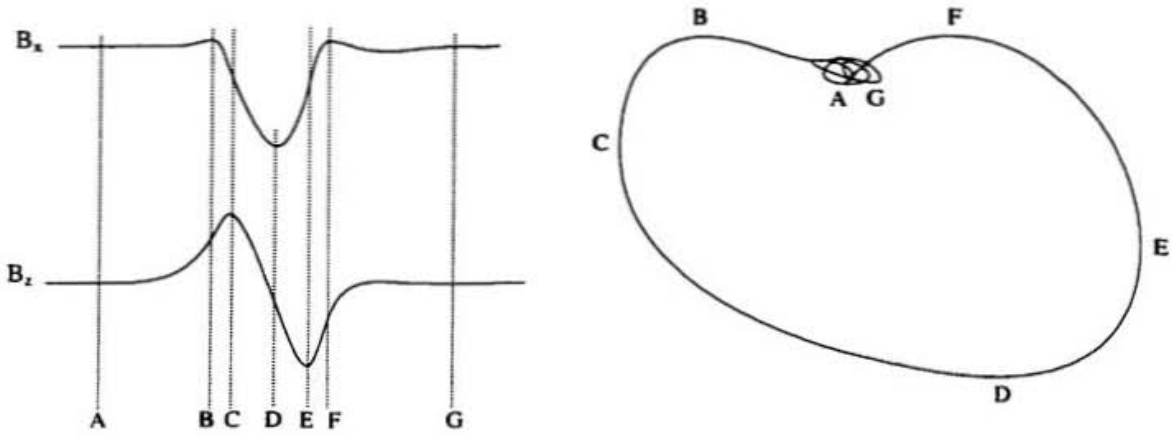

Figure 2.19. ACFM signals of a remote-surface-breaking defect in a 6-Mo austenitic SS pipe.

As with the ACPD technique, the depth of penetration of the alternating current is affected by factors such as frequency, relative magnetic permeability, and electrical conductivity. The skin thickness can then be calculated using equation (2.4):

$$\delta_s = \frac{1}{\sqrt{\mu \mu_0 \kappa \pi f}}$$

It is apparent from equation (2.4) that materials with high permeability or conductivity will have relatively small skin depths. At a frequency of about 5 kHz, ferromagnetic steel has a skin depth of 0.1 mm, high conductivity materials such as aluminum, tungsten and zinc have skin a depth of 1-2 mm, and low conductivity materials such as titanium, stainless steel and Inconel have a skin depth of 5 to 8 mm [Lugg, 1992]. At a frequency of 200 Hz, the skin depth in austenitic stainless steels can approach 30 mm [Carroll, 1998].

A major advantage of the ACFM technique is its ability to detect defects and estimate their depth accurately, as compared to other NDT techniques that only give detection, or at best, length information. The technique can be used for defect detection and characterisation in a wide range of electrically conductive materials such as carbon steels, stainless steels, aluminum, and even titanium [Raine and Monahan, 1996]. The technique is non-contacting [Lugg, et. al, 1988], insensitive to lift-off and unaffected by the presence of non-metallic coatings and oxide layers on the surface of material [Raine and Monahan, 1996]. The technique can be used to inspect over rough surfaces and through coatings up to 5 mm thick [Raine and Monahan, 1996].

Since it is unnecessary to remove protective coatings or clean the component surface extensively, the inspection time can be greatly reduced and significant cost savings realized. Defect detection and sizing is based on mathematical modelling of the magnetic field perturbations caused by a defect, which means that no calibration is required, thus reducing the possibility of operator error. By using mathematical modelling in defects sizing, problems of differences between behaviour of currents at slots and cracks, and differences at material properties can be avoided [TSC Ltd. Home Page, 1999]. However, the sizing algorithms developed for magnetic steels cannot be used for non-magnetic materials and additional work is needed to develop new algorithms for this purpose [Raine and Monahan, 1996]. Since the technique provides data storage, off-line reanalysis of the defects can be carried out to improve auditability [TSC Ltd. Home Page, 1999].

A limitation of the ACFM technique is that it is only applicable for inspecting electrically conductive materials and it cannot be used to detect defects in non-conducting materials. Due to the high magnetic permeability of carbon steels, the technique cannot be used to detect subsurface defects in these materials. However, in low magnetic permeability materials such as duplex and austenitic stainless steels, the technique can be used to detect subsurface and back-wall defects in materials up to 30 mm thick [Carroll, 1998]. The reason for this is the thicker skin depth which is produced in less magnetic materials, enabling the technique to penetrate deeper into the material [Raine and Monahan, 1996].

Since the technique relies on the interpretation of induced magnetic field components, it must be ensured that the surface being inspected is in an unmagnetised state. Therefore, if the component has been previously inspected using other magnetic techniques (e.g. magnetic particle inspection), demagnetisation must be carried out on the material before using ACFM. When inspecting weld regions, care must be taken since these regions can contain weld spatter or grinding marks which can cause spurious signals which may be confused with real defect signals. A summary of the ACFM technique is provided in Table 2.8.

Table 2.8. Summary of the ACFM technique.

Method:	A uniform high frequency alternating current electric field is introduced into the surface of a component. The presence of a defect disturbs the associated electromagnetic field and the perturbations are displayed graphically.
Discontinuities:	The depth and length of cracks, pits seams, voids.
Materials:	Metals, some alloys, electrically conductive materials.
Feature to which applied:	Surface, regular and uniform shapes.
Advantages:	• Accurately measures depth and length of defect. • Can detect surface, subsurface or remote-surface defects. • Non contacting technique. • Can inspect over rough surfaces and through coatings. • Rapid and cost effective inspection can be achieved. • No need to calibrate the instrument prior to each use.
Limitations:	• Only applicable for inspecting electrically conductive materials. • Gives better results for flat or smooth surfaces. • Flaws should be oriented perpendicular to the electric field direction. • Materials to be inspected should be demagnetised.

2.2.6. Advantages of ACFM over the other NDT Techniques

It was the purpose of this research to detect and measure the actual depth and length of remote-surface-breaking defects in 6-Mo austenitic stainless steel pipes. The pipes used in the research were 3.4 mm and 3.8 mm thick and were considered to be thin-walled pipes. Artificial defects were fabricated using a slitting wheel and were located in the base metal and near the weld toe. The defect geometry was chosen to be representative of the type of localized corrosion damage sometimes found near weld seams in 6-Mo pipework used on the Hibernia oil platform. A more detailed explanation of the specimen preparation procedure is given in the next chapter. This section is intended to explain the advantages of ACFM over other NDT techniques for characterising the type of defects considered in this research.

The first technique discussed was visual inspection. Visual inspection, either with or without aids, is not applicable to this case. Remote-surface-breaking defects will not be detectable when visual inspection is conducted from the outer surface. Similarly, liquid penetrant testing, as an aid to the visual technique, is also unsuitable for this inspection task. Furthermore, since 6-Mo austenitic SS is a non-magnetic material, the magnetic particle inspection technique cannot be used.

Ultrasonic testing is a competitive technique with ACFM. Ultrasonic testing can be used to inspect for internal defects and weld defects in any metals, non-metals, and composites. However, due to the presence of a dead zone (explained earlier), this

technique is not suitable for inspecting thin materials. Since the pipes used in the research are considered to be thin-walled, ultrasonic testing will not work properly.

Acoustic emission can be used to monitor crack initiation and propagation within pipelines. However, if the technique is used to monitor the whole structure, several sensors or probes must be installed at numerous locations. The number of sensors required in this case renders the technique cumbersome and costly. Although the technique can provide continuous monitoring of the structure over a period of time, it does not indicate the size of the defect detected. Hence, other NDT techniques are still required to determine the size of the defect.

Radiography is capable of detecting remote-surface defects in 6-Mo austenitic stainless steel, but interpretation of the image may be difficult since the thickness of the pipe is quite small. Also, if the depth of the defect is small, for example 1 mm or less, the density difference between a defective region and an adjacent area which is undamaged will be very small. As a result, the defect will be undetectable. Further, radiography is only capable of indicating the length of the defect, and not its depth. Furthermore, radiography can be expensive to apply when it is required to inspect a large quantity of pipework. The set-up time required before inspection and the radiation hazard associated with radiography are additional factors which render the technique less attractive than ACFM.

Other NDT techniques that can be used to inspect for surface-breaking defects are eddy current testing and ACPD. Eddy current testing is the main rival to ACFM when it comes to detecting and sizing surface and subsurface defects. Although eddy current

testing may be able to detect and characterize the type of remote-surface-defects considered in this research, the technique does not work well if scanning is carried out in the vicinity of weld metal. When defects are located near a weld, the distribution of the circular/non-uniform eddy currents will be altered by the presence of weld metal. Hence, there will be a change in the magnetic field associated with the eddy currents, thus leading to a change in the coil impedance value. This phenomenon will affect signal interpretation. The non-uniform nature of the eddy current also limits its sensitivity to deep defects because the current does not flow to the bottom. In addition, eddy current testing equipment must be calibrated before being used. The calibration procedure will vary from one application to another, depending on the material and defect geometry. When scanning weld defects, for example, the equipment must be calibrated on a material in the same condition as the test component. If the technique is intended to measure the depth of a crack, calibration must be conducted on a cracked material with known depth. With ACFM, the electric currents flow uniformly over the surface of the component and are not affected by the presence of weld metal. Besides being able to indicate defects at welds, the ACFM technique is also capable of determining the length and depth of such defects.

Alternating Current Potential Drop (ACPD) can be used to size cracks for length and depth and the technique is able to work in the vicinity of weld metal. However, the technique is contacting and, thus, the area to be inspected must be free from surface coatings and/or oxide layers. If the inspection is to be conducted over large areas, the cleaning requirement will be costly and time consuming. Further, protective coatings must be repaired after the inspection task is accomplished. The ACPD technique also

requires that a reference voltage reading be taken from a crack-free surface during the inspection. Error in taking the reference potential measurement will lead to inaccuracy in estimating the depth and length of the defect. In comparison, the ACFM technique is non-contacting, which means that surface cleaning requirement is unnecessary, and inspection time and cost can therefore be reduced. Also, the ACFM technique requires no calibration, which makes the inspection process easier and reduces the risk of error. All of these advantages help to reduce inspection time and cost. Finally, since ACFM has the potential to detect surface, subsurface and remote surface defects, either in the base metal or near the weld metal, the technique is considered, by the author, to be the best choice for addressing the inspection problem considered in this research.

Ch. 3

EXPERIMENTAL PROCEDURES

3.1. Introduction

Experiments were carried out to obtain data to be used to develop models for predicting the length and depth of remote surface defects stainless steel piping. Details of test specimen preparation and equipment set-up are given in the following sections and the experimental results are presented in the next chapter.

The material used in this study was 6-Mo austenitic stainless steel pipe. Due to low magnetic permeability of this material, electric field induced by ACFM probe can penetrate the material relatively deeply. Deep penetration of the electric fields enables defects on the remote surface to be detected and their depth and length to be calculated.

3.2. Specimen Preparation

Two different sizes of 6-Mo austenitic stainless steel pipes were used in the experiments. Each pipe had a circumferential weld seam near the middle of its length. Artificial defects were machined into the inner surface of the base metal and weld toe using a 1 mm thick by 102 mm diameter slitting saw. All defects were flat-bottomed with curved sides. The defects were designed to simulate the type of localised corrosion damage in piping system installed on the Hibernia platform. The reason for machining defects at the weld toe as well as the base metal is that the metallurgical structure of the weld metal may change due to welding. A change in the metallurgical structure can affect the magnetic permeability of the metal which, in turn, can affect the ACFM signals. It was considered important to investigate this effect and, if necessary, account for it during model development.

To avoid *edge effects*, defects machined in the base metal were located a minimum of 40 mm from the free ends of the pipe. The edge effect is a perturbation in the ACFM signals due to a concentration of the induced current at the plate end. Detailed dimensions of test specimens are given in Figure 3.1 and Table 3.1.

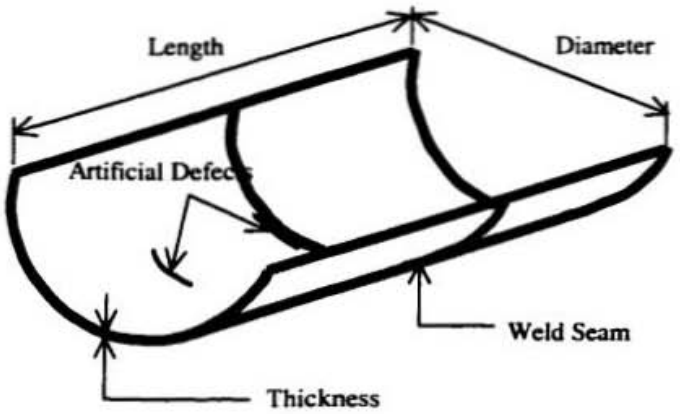

Figure 3.1. Test specimen.

Table 3.1. Dimension of the pipes used in the experiment.

	Pipe 1	**Pipe 2**
Thickness (mm)	3.4	3.8
Diameter (mm)	155	215
Length (mm)	300	300

To investigate the effect of defect size on the ACFM signals and develop models for predicting the depth and length of the backwall defects, two sets of experiments were conducted, each involving comparisons. In experiment set no. 1, the comparison was between similar defects locations in pipes of two different thicknesses. For this purpose, the location of the artificial defects were as follows:

1. In the base metal of the 3.4 mm pipe wall thickness.
2. In the base metal of the 3.8 mm pipe wall thickness.

In the experiment set no. 1, the defects were used to obtain a relationship between signal ratio against actual defect depth, and between B_z defect length against actual defect length. The details of the calculation are presented in the next chapter.

As in Table 3.2, six different series of actual depths were machined in the base metal of the 3.4 mm wall thickness, i.e. 1.0 mm, 1.5 mm, 2.0 mm, 2.5 mm, 2.8 mm, and 3.0 mm. The lengths of the defects were made to vary for each depth, i.e. from 35 mm to 51 mm. Six different series of actual depths were also machined in the base metal of the 3.8 mm pipe wall thickness, ranging from 1.0 mm to 3.5 mm, with a 0.5 mm depth increment.

In experiment set no. 2, the comparison was between defects in pipe of the same thickness, but at different locations where the metallurgy of the metal also differed. Locations of the artificial defects in the experiment set no. 2 are as follows:

1. In the base metal of the 3.8 mm pipe wall thickness.
2. At the weld toe (heat-affected zone) of the 3.8 mm pipe wall thickness.

The defects located in the base metal and weld toe of the 3.8 mm pipe wall thickness were used to obtain a relationship between signal ratio against actual depth, and between B_z defect length against actual defect length. The details of the calculation are presented in Chapter 4.

As in Table 3.3, six different series of actual depth were machined at the weld toe and base metal of the 3.8 mm pipe, ranging from 1.0 mm to 3.5 mm, with a 0.5 mm depth increment. To evaluate the influence of the heat-affected zone on the ACFM signals, the length of the defects for the same depths in both locations were machined equal.

Table 3.2. Dimensions of the artificial defects in the 3.4 mm and the 3.8 mm pipe wall thickness (experiment set no. 1).

Wall thickness	Actual Defects Depth (mm)	Actual Defects Length (mm)
3.4 mm	1.0	35
	1.5	42
	2.0	46
	2.5	47
	2.8	48
	3.0	51
3.8 mm	1.0	36
	1.5	38
	2.0	41
	2.5	43
	3.0	45
	3.5	48

Table 3.3. Dimensions of the artificial defects at the weld toe and the base metal of the 3.8 mm pipe wall thickness (experiment set no. 2).

Defects Location	Actual Defects Depth (mm)	Actual Defects Length (mm)
Weld Toe (HAZ)	1.0	44
	1.5	45
	2.0	46
	2.5	47
	3.0	49
	3.5	50
Base Metal	1.0	44
	1.5	45
	2.0	46
	2.5	48
	3.0	49
	3.5	50

3.3. Apparatus

A model U9b ACFM crack microgauge manufactured by Technical Software Consultants (TSC) Ltd. was used in conjunction with a micro-pencil probe type 163. The ACFM crack microgauge model U9b represents a significant advance in inspection technology and provides the capability of both ACPD and ACFM techniques. The U9b model is portable and designed primarily for on-site use. The micro-pencil probe is manufactured with high sensitivity coils. Using this probe, the butterfly plot is distorted since the search coils, i.e. the B_x and B_z coils, are not coincident. Figure 3.2 illustrates the dimension of the micro-pencil probe.

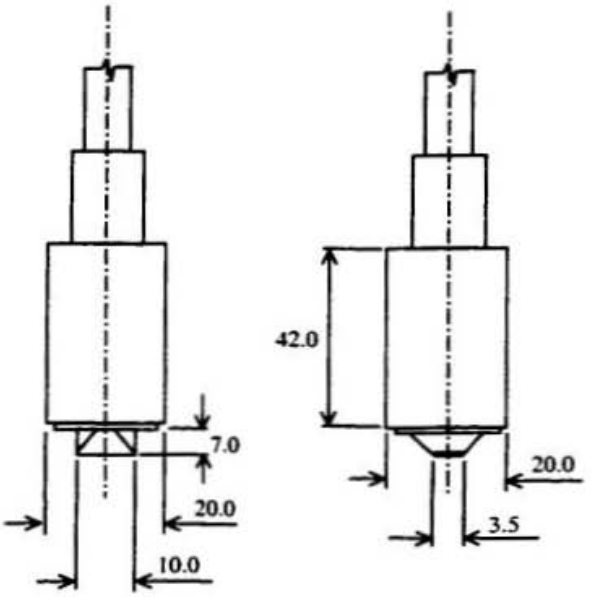

Figure 3.2. Top side micro-pencil probe type 163.

A Pentium 150, 32 MB RAM external computer was used to control the instrument during the experiments. TSC's QFM version 2 software was installed on the computer for monitoring and graphing data obtained from the ACFM probe. The computer allows the data to be stored thus improving auditability and allowing off-line reanalysis or year-n-year comparison of defect size. Figure 3.3 shows the U9b ACFM crack microgauge connected to the external computer.

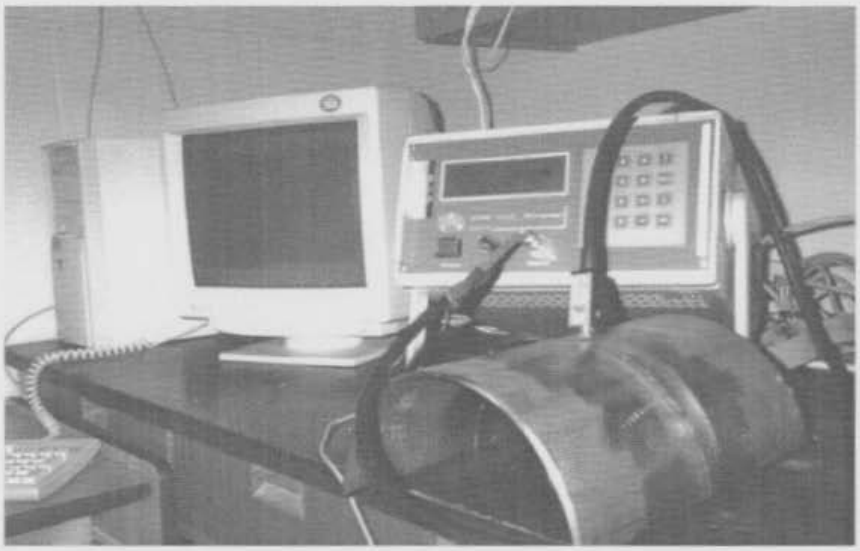

Figure 3.3. The U9b ACFM crack microgauge connected to the external computer.

3.4. Defect Identification

It is necessary to understand the behavior of the ACFM signals to identify the appearance of a defect. During scanning, it is important to look at the B_x and B_z traces all the time and to take notice of any loops on the butterfly plot. If the B_x signal shows a dip, a defect may exist in that area. If the butterfly plot makes any significant loops, additional scans should be carried out over a broad area either side of the signal. This is particularly important if the butterfly is moving up or down the screen. A butterfly moving up or down the screen with any sort of looping is likely to be a long crack [Smith, 1997]. Figure 3.4 illustrates a decision tree for crack identification.

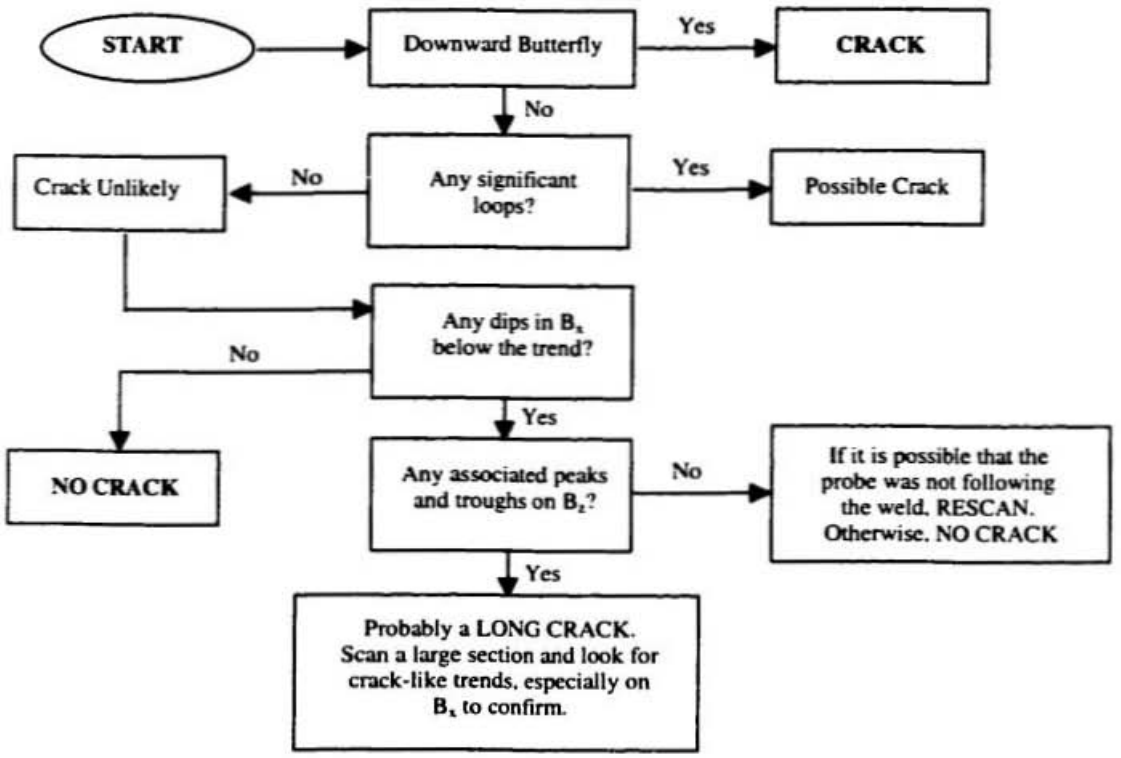

Figure 3.4. Decision tree for crack identification [Smith, 1997].

3.5. Scanning of Defects

Before starting the experiments, some parameters related to instrument settings had to be chosen to optimise the appearance of the signals. Improper selection of the instrument settings can cause *noise* in the signals. Noise is a condition where the B_x, B_z, and butterfly plot are not shown clearly on the screen due to random perturbations in the signals (e.g. variations in magnetic permeability of the base material and/or stray electromagnetic fields). Figure 3.5 shows noise in the ACFM signal and Figure 3.6 displays the instrument settings used in conjunction with the micro-pencil probe.

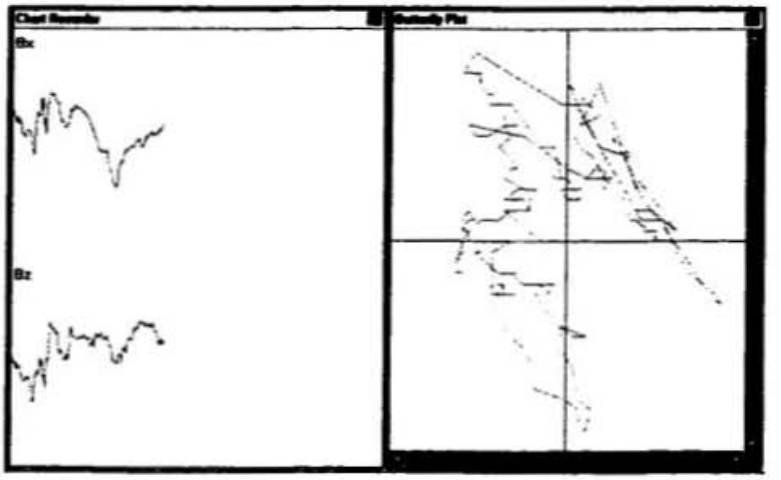

Figure 3.5. "Noise" in the ACFM signal.

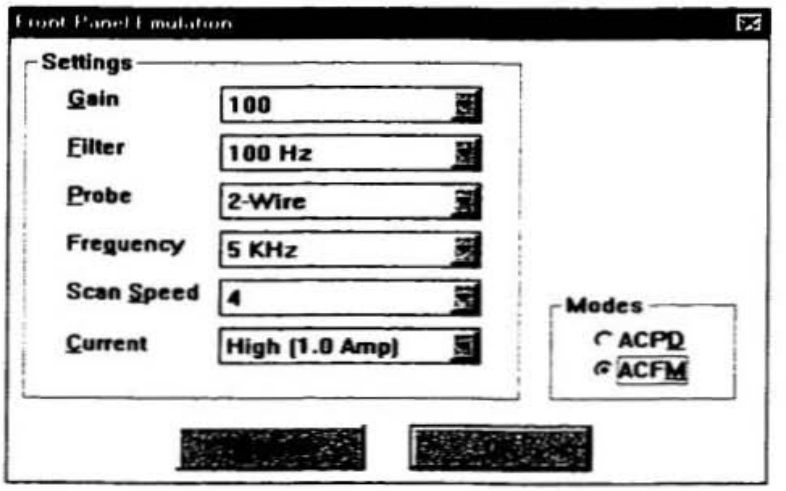

Figure 3.6. Instrument settings used in the experiments.

Gain is an amplification factor applied to the raw input voltage after an initial amplification of $\times 10^5$. Filter is used to cut-off frequency after rectification, thus reducing noise in the display. There are two choices of filter in the U9b instrument: 1

Hz for stable, high precision readings such as in ACPD crack growth monitoring and 100 Hz for rapid response time such as in manual ACFM crack detection.

Probe types used in the U9b instrument are classified by the number of wires used in the connection. Standard ACFM probes use the 2-wire setting and ACPD probes use the 3-wire setting. The frequency of the output current used in the standard ACFM technique is 5 kHz. Amperage reveals the output current amplitude. The U9b instrument has two choices of current: high (1.0 Amps) and low (0.5 Amps).

For each different defects depth, scanning was carried out five times. During scanning, the probe was traversed on the external surface of the pipe, parallel to the artificial defect located in the internal surface of the pipe. The travel speed of the probe was maintained at approximately 15 mm/second to obtain good sensitivity. Figure 3.7 illustrates the scanning process on the external surface of a 3.4 mm pipe wall thickness.

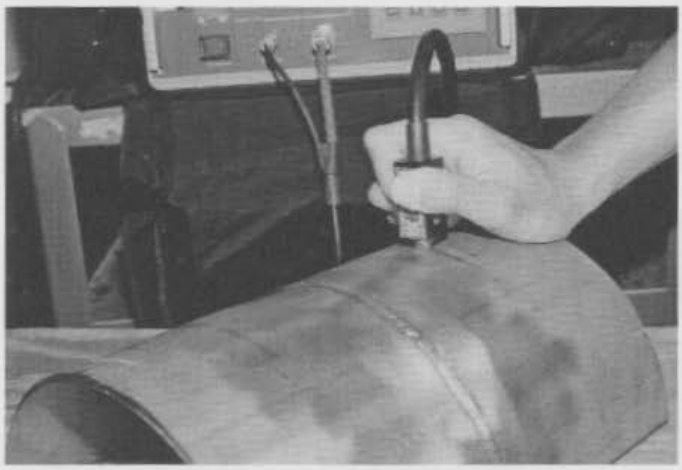

Figure 3.7. Scanning process on the external surface.

The results of the scanning are showed in Appendix A, B, C, and D. Appendix A shows the ACFM signals obtained from scanning of the defects located in the inner surface of the base metal of the 3.4 mm pipe wall thickness, i.e. defects location no. 1. Appendix B shows the ACFM signals obtained from scanning of the defects located in the inner surface of the base metal of the 3.8 mm pipe wall thickness, i.e. defects location no. 2. Appendix C shows the signals obtained from scanning of the defects located in the inner surface of the heat-affected zone (weld toe) of the 3.8 mm pipe wall thickness (defect location no. 3). Appendix D shows the signals obtained from scanning of the defects located in the inner surface of the base metal of the 3.8 mm pipe wall thickness (defects location no.4).

During each scan, when the B_z signal reached the peak and trough, i.e. the defect ends, the specimen surface was marked along the centreline of the probe. To accurately locate the peak and trough, the probe should be moved back and forth near the defect ends while watching the B_z signal on the computer screen. The physical length between the marks, i.e. peak and trough, is called B_z length.

The B_x signal is used to calculate a non-dimensional parameter called the *signal ratio*. The measurements used to calculate the signal ratio are the minimum and background B_x values. If the background level is relatively constant, as depicted in Figure 3.8 (a), the background B_x value can be taken from either side of the trough. On the other hand, if the B_x signal is as illustrated in Figure 3.8 (b), the background B_x value is determined from both sides of the trough by taking an average value.

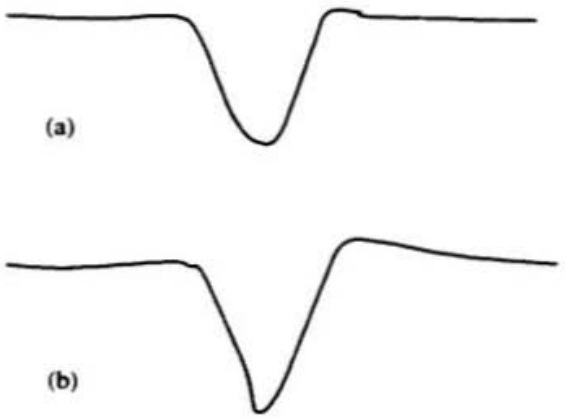

Figure 3.8. Determination of background B_x level.

Ch. 4

DATA COLLECTION AND ANALYSIS

4.1. Introduction

Data obtained from the experiments is presented in Tables 4.1 and 4.2. An analysis of the data was carried out using a regression technique called *ordinary least squares* (OLS). OLS is a widely used approach. It yields coefficient estimates of the line that minimises the sum of the squared residual error. Residual error is the difference between the observed and fitted values, determined by the regression equation. Statistical software package Minitab (release 12) was used for the regression analysis.

Fitting a straight-line model is often preferable to fitting a polynomial model to curved data, since the lines might give some idea of a relationship between the two measured variables. Using a polynomial model might be equally good for estimation over the range of the data, but it might not work well outside the range of the data [Ryan, 1994].

Whenever fitting a model to a set of data, plotting of the data and residuals is suggested. Scatterplots of the data and residual help in diagnosing potential problems and spotting outliers. Outliers are observations that are far from the majority of the data. A scatterplot is a basic tool for understanding the relationship between two measured variables. Sometimes, transformation should be used since some problems such as curvilinearity, heterocedasticity, and nonnormality can occur in the raw data. Models that originally appear inappropriate may become reasonable after transformation [Hamilton, 1992].

To develop model equations, a *dummy variable* (0, 1 dichotomies) is used. A dummy variable is useful to analyze a model with a categorical predictor (x). Intercept dummy variables and slope dummy variables are used to test for differences in intercepts and slopes.

The *signal ratio* term which appears in Table 4.1 and Table 4.2. is a non-dimensional parameter calculated using the relationship:

$$\text{Signal ratio} = \frac{\text{Bx background} - \text{Bx minimum}}{\text{Bx background}} \qquad (4.1)$$

The signal ratio is used to represent the defect depth because its magnitude is not affected by variations in the magnetic permeability of the material undergoing interrogation or by changes to the gain setting in the ACFM instrument.

Table 4.1. Scanning results obtained from the defects located in the base metal of 3.4 mm and 3.8 mm pipe wall thickness.

Pipe Wall Thickness (T)	Actual Defect Depth (t)	Defect Depth-to-Wall-Thickness Ratio (t/T)	Signal Ratio	Actual Defect Length	Bz Defect Length
3.8	1.0	0.26	0.007210388	36	16.2
3.4	1.0	0.29	0.008849618	35	14.8
3.8	1.5	0.39	0.007382795	38	16.8
3.4	1.5	0.44	0.012734065	42	19.8
3.8	2.0	0.53	0.012764877	41	17.6
3.4	2.0	0.59	0.022037603	46	23.8
3.8	2.5	0.66	0.022665491	43	18.2
3.4	2.5	0.74	0.030293492	47	22.0
3.8	3.0	0.79	0.032576014	45	20.4
3.4	2.8	0.82	0.041028229	48	22.2
3.4	3.0	0.88	0.048625404	51	21.6
3.8	3.5	0.92	0.082020397	48	21.2

NOTE: All thickness, length and depth are in mm.

Table 4.2. Scanning results obtained from the defects located in the base metal and the weld toe of 3.8 mm pipe wall thickness.

Pipe Wall Thickness (T)	Actual Defect Depth (t)	Defect Depth-to-Wall-Thickness Ratio (t/T)	Signal Ratio (Base Metal)	Signal Ratio (Weld Toe)	Actual Defect Length (Base Metal)	Actual Defect Length (Weld Toe)	Bz Defect Length (Base Metal)	Bz Defect Length (Weld Toe)
3.8	1.0	0.26	0.011247227	-	44	-	19.6	-
3.8	1.5	0.39	0.009672751	0.008701657	45	45	20.4	20.4
3.8	2.0	0.53	0.015625250	0.016789413	46	46	20.6	20.6
3.8	2.5	0.66	0.024301461	0.021383546	48	47	21.4	20.8
3.8	3.0	0.79	0.041679162	0.035686905	49	49	21.8	21.2
3.8	3.5	0.92	0.078462027	0.077875324	50	50	21.4	21.8

NOTE: All thickness, length and depth are in mm.

4.2. Regression Analysis of Signal Ratio against Actual Defects Depth

To be able to predict defect depth from the signal ratio, a relationship between the two variables was developed. This relationship is in the form of equations obtained from linear regressions of the data compiled in Table 4.1.

Since there are two different wall thickness, i.e. 3.4 mm and 3.8 mm, a dummy variable is used to differentiate between the two thickness. Hence, the three variables used in the regression analysis are as follows:

y — estimated defect depth;

x_1 — thickness type: dummy variable coded 0 for 3.4 mm and 1 for the 3.8 mm;

x_2 — natural logarithm of signal ratio ($\log_e$ signal ratio).

In raw form, a plot of the actual defect depth against the signal ratio showed negatively skewed distributions. It was therefore decided to use a natural logarithm of the signal ratio. The analysis was carried out by regressing the natural logarithm of the signal ratio and the dummy variable to the actual defect depth. Figure 4.1 and Figure 4.2 show scatterplots of the signal ratio against the actual defect depth.

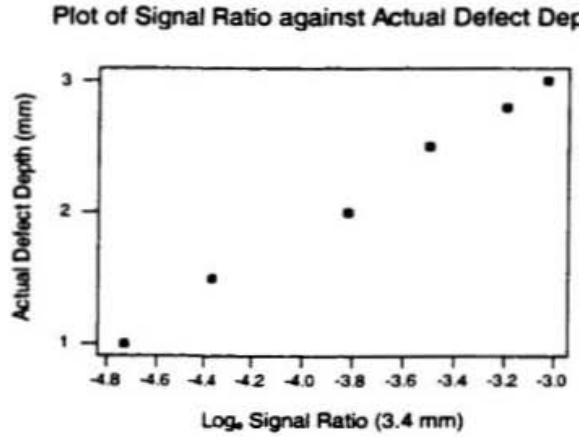

Figure 4.1. Plot of signal ratio against actual defect depth for pipe having 3.4 mm wall thickness.

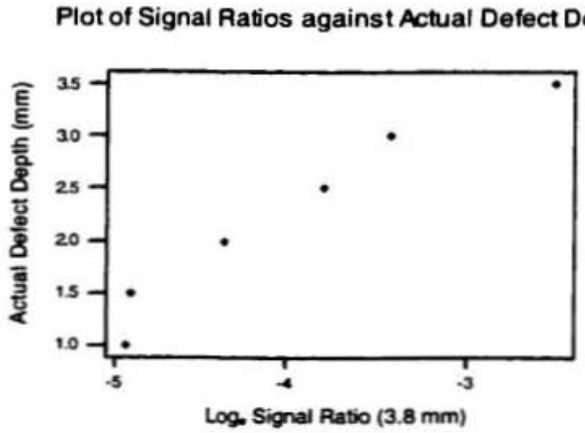

Figure 4.2. Plot of signal ratio against actual defect depth for pipe having 3.8 mm wall thickness.

The regression analysis yielded:

$$y = 6.02 + 0.339\ x_1 + 1.03\ x_2 \qquad (4.2)$$

Equation (4.2) has a significance level (p-value) for the dummy variable equal to 0.011. The significance level is the smallest value of the confidence interval (α) for which the test results are statistically significant [Mendenhall, 1983]. Since the assumed significance level for the experiments is 0.05 and the p-value obtained from analysis was 0.011, the dummy variable in this case is not significant and can be neglected.

Analysis is then performed by regressing the actual defect depth against the natural logarithm of signal ratio for each thickness. For the 3.4 mm wall thickness, regression analysis yielded:

$$y = 6.52 + 1.16\, x_2 \tag{4.3}$$

A plot of the regression equation is depicted in Figure 4.3.

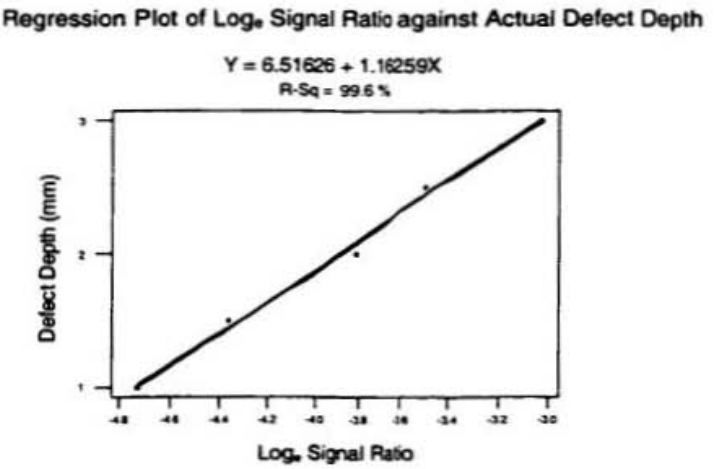

Figure 4.3. Regression plot of $\log_e$ signal ratio against actual defect depth for pipe having 3.4 mm wall thickness.

To check whether the derived model can be used with confidence, regression diagnostic procedures are performed on the equation. The procedure is to plot residuals against fitted values of the estimated defect depth. The residual plots of equation (4.3) are as follows:

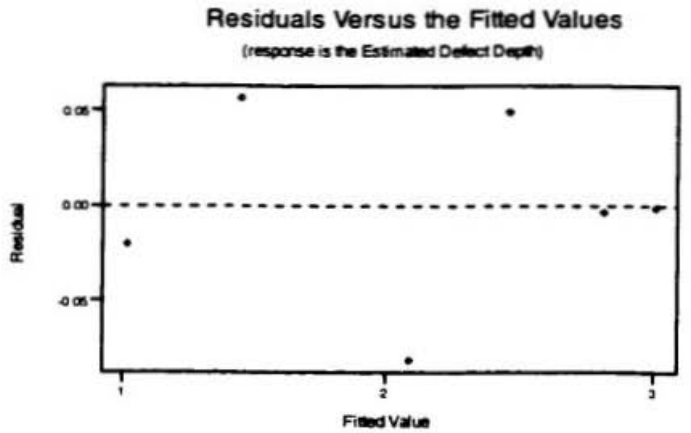

Figure 4.4. Plot of residual against fitted value of the equation (4.3).

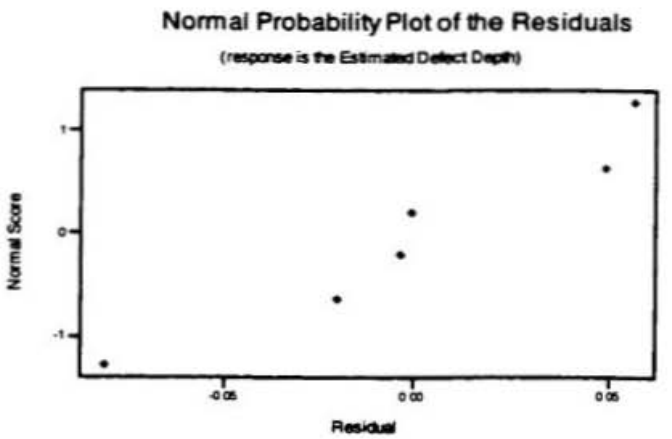

Figure 4.5. Plot of residual against normal score of the equation (4.3).

For the 3.8 mm wall thickness, the regression analysis yielded:

$$y = 6.1 + 0.966\, x_2 \qquad (4.4)$$

The regression plot of equation (4.4) is depicted in Figure 4.6.

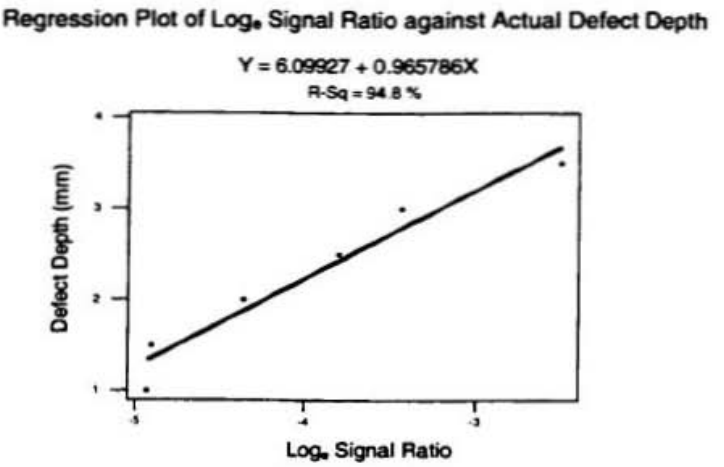

Figure 4.6. Regression plot of $\log_e$ signal ratio against actual defect depth for pipe having 3.8 mm wall thickness.

The residual plots of equation (4.4) are depicted in Figure 4.7 and Figure 4.8.

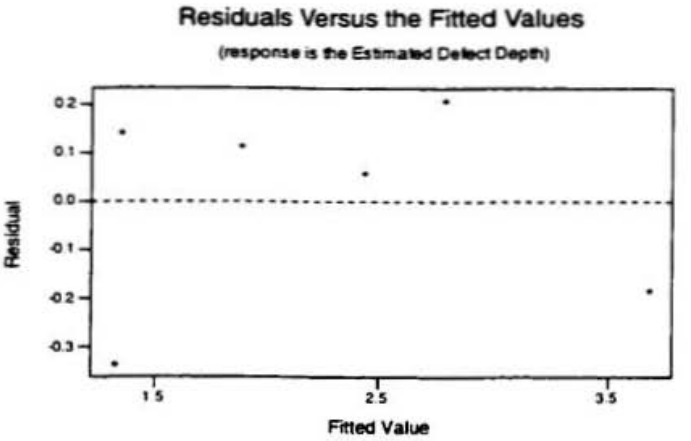

Figure 4.7. Plot of residual against fitted value of the equation (4.4).

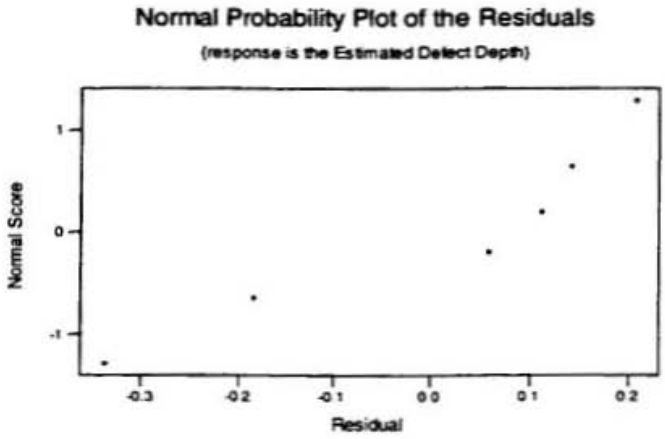

Figure 4.8. Plot of residual against normal score of the equation (4.4).

The plots of residual against normal score of both models (Figure 4.5 and Figure 4.8) show a linearity pattern, and the plots of residual against fitted value (Figure 4.4 and Figure 4.7) result in a random scatter plot. This indicates that population errors are normal and identically distributed. Therefore, the equations (equation (4.3) and equation (4.4)) can be used for model predictions.

4.3. Regression Analysis of B_z Defect Length against Actual Defect Length

In this section, the same method is used to analyse the data from Table 4.1. In doing so, the three variables to be used in the regression analysis are as follows:

y — estimated defect length;

x_1 — thickness type: dummy variable coded 0 for 3.4 mm and 1 for 3.8 mm;

x_2 — B_z defect length.

Scatterplots of the B_z against the actual defect length are depicted in Figure 4.9 and 4.10.

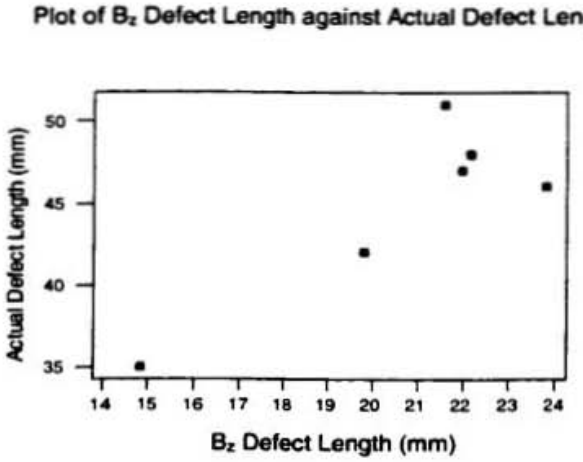

Figure 4.9. Plot of B_z against actual defect length for pipe having 3.4 mm wall thickness.

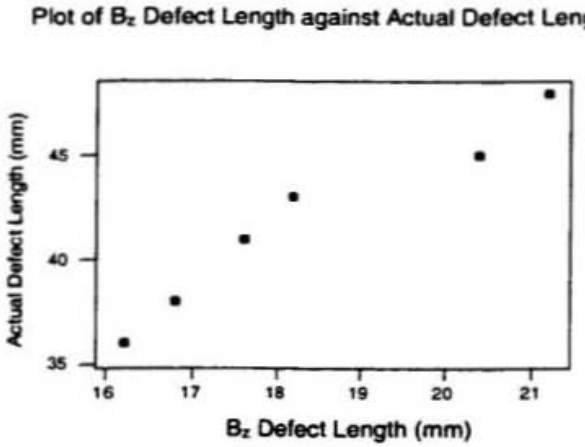

Figure 4.10. Plot of B_z against actual defect length for pipe having 3.8 mm wall thickness.

The regression analysis yielded:

$$y = 9.21 + 0.96\, x_1 + 1.72\, x_2 \qquad (4.5)$$

The dummy variable of equation (4.5) has a significance level equal to 0.543. Since the significance level is higher than that of the assumption, equation (4.5) can be used for model predictions.

As thickness type (x_1) in equation (4.5) is an intercept dummy variable, for the 3.4 mm wall thickness:

$$y = 9.21 + 0.96\,(0) + 1.72\, x_2$$

$$= 9.21 + 1.72\, x_2 \qquad (4.6)$$

For the 3.8 mm wall thickness, equation (4.5) yielded:

$$y = 9.21 + 0.96\,(1) + 1.72\, x_2$$

$$= 10.17 + 1.72\, x_2 \qquad (4.7)$$

Plots of equation (4.6) and (4.7) are shown in Figure 4.11. The two lines in Figure 4.11 only differ in the value of the intercept. The lines suggest that estimated defect length increases by the increase in the B_z defect length. For any given B_z defect length, defects in the 3.8 mm thick pipe wall tend to have a longer estimated defect length than those in the 3.4 mm thick pipe wall. The defect depth to thickness ratio (t/T), however, affects the strength of the ACFM signals. At the same actual length and depth, defects in the 3.4 mm pipe wall thickness generate stronger signals due to a higher t/T, which appears to result in a longer B_z length.

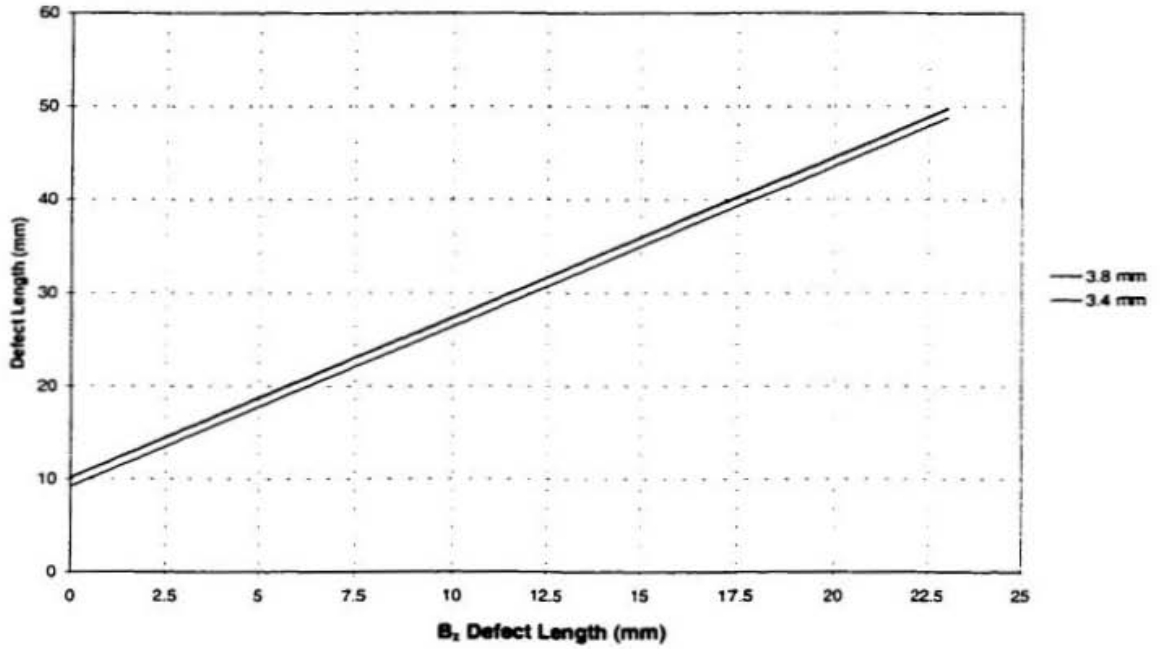

Figure 4.11. Regression plot of B_z defect length against actual defect length and the intercept dummy variable.

Therefore, an analysis was conducted to regress the dummy variable, the B_z defect length, and the t/T. The variables used in the regression analysis were as follows:

y — estimated defect length;

x_1 — thickness type: dummy variable coded 0 for 3.4 mm and 1 for 3.8 mm thickness;

x_2 — B_z defect length;

x_3 — defect depth-to-wall-thickness ratio (t/T).

Regression analysis yielded:

$$y = 22.3 - 1.01\,x_1 + 0.638\,x_2 + 14.8\,x_3 \qquad (4.8)$$

Equation (4.8) suggests that for the same value of signal ratio and t/T, the estimated defect length of a defect located in the 3.4 mm thick pipe wall tends to be longer than that in the 3.8 mm thick pipe wall.

4.4. Regression Analysis of Signal Ratio against Actual Defect Depth for Defects Located in Base Metal and Weld Toe

Sections 4.5 and 4.6 explain the relationship between the signal ratio and the estimated defect depth, and between the B_z length and estimated length of defects machined in the base metal and weld toe of the 3.8 mm pipe wall thickness. The purpose of the regression analysis is to judge whether changes in material properties caused by welding affect the model predictions.

Data used in the analysis are obtained from Table 4.2. The same procedure, i.e. using a dummy variable due to account for the two different defect locations, has been used. The three variables to be used in the regression analysis are as follows:

y — estimated defect depth;

x_1 — defect location: dummy variable coded 0 for defects located at the weld toe and 1 for defects in the base metal;

x_2 — natural logarithm of signal ratio.

Since the plots of actual defect depth versus signal ratio in raw form have negatively skewed distributions, logarithms of the signal ratio are used. Figure 4.12 and Figure 4.13 depict scatterplots of the signal ratio versus the actual defect depth.

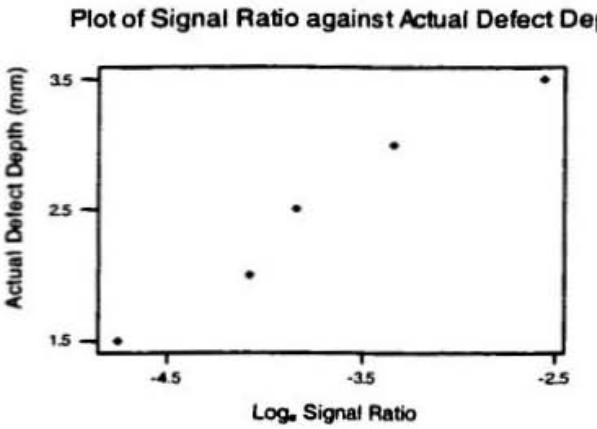

Figure 4.12. Plot of signal ratio against actual defect depth for defects at the weld toe of the 3.8 mm pipe wall thickness.

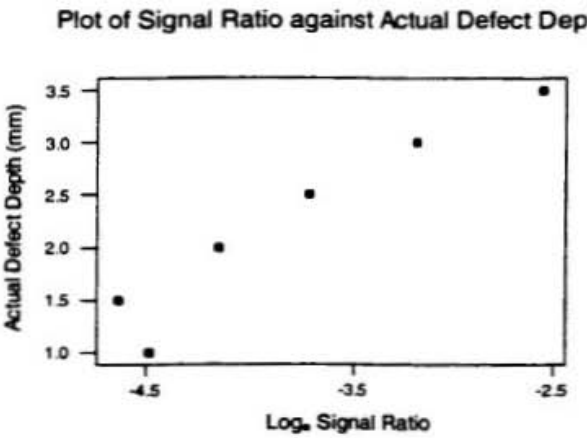

Figure 4.13. Plot of signal ratio against actual defect depth for defects in the base metal of the 3.8 mm pipe wall thickness.

Regression analysis yielded:

$$y = 6.35 - 0.172\, x_1 + 1.04\, x_2 \tag{4.9}$$

Since the regression equation has a significance level equal to 0.263, the model can be used with confidence to represent the relationship between the signal ratio and the estimated defect depth. As x_1 in equation (4.9) is an intercept dummy variable, for defects located at the weld toe:

$$y = 6.35 - 0.172\,(0) + 1.04\, x_2$$

$$= 6.35 + 1.04\, x_2 \tag{4.10}$$

For defects located in the base metal:

$$y = 6.35 - 0.172\,(1) + 1.04\, x_2$$

$$= 6.178 + 1.04\, x \tag{4.11}$$

To test for a difference in slopes, an interaction term called a *slope dummy variable* is used. The slope dummy variable is produced by multiplying together a dummy and measurement variable [Hamilton, 1992]. If x_1 is a dummy variable and x_2 is a measurement variable, then $x_1 \cdot x_2$ is the slope dummy variable. Regressing the actual defect depth (Table 4.2, column 2) against the signal ratio (x_2) and the slope dummy variable (signal ratio times defects location) yielded:

$$y = 6.25 + 1.01\, x_2 + 0.0503\, x_1\, x_2 \tag{4.12}$$

For defects located at the weld toe ($x_1 = 0$), equation (4.12) becomes:

$$y = 6.25 + 1.01\, x_2 + 0.0503\,(0)\, x_2$$

$$y = 6.25 + 1.01\, x_2 \tag{4.13}$$

For defects located in the base metal ($x_1 = 1$), equation (4.12) yielded:

$$y = 6.25 + 1.01\, x_2 + 0.0503\, (1)\, x_2$$

$$= 6.25 + 1.0603\, x_2 \qquad (4.14)$$

Analysis of equations (4.13) and (4.14) is presented in Chapter 5.

4.5. Regression Analysis of B_z Defect Length against Actual Defect Length for Defects Located in Base Metal and Weld Toe

Three variables are also used in this regression analysis. The three variables are as follows:

y — estimated length of defects located at the weld toe and base metal;

x_1 — defect location: dummy variable coded 0 for a defect at the weld toe and 1 for a defect in the base metal;

x_2 — B_z defect length.

Figure 4.14 and Figure 4.15 show scatterplots of the actual and B_z defect length.

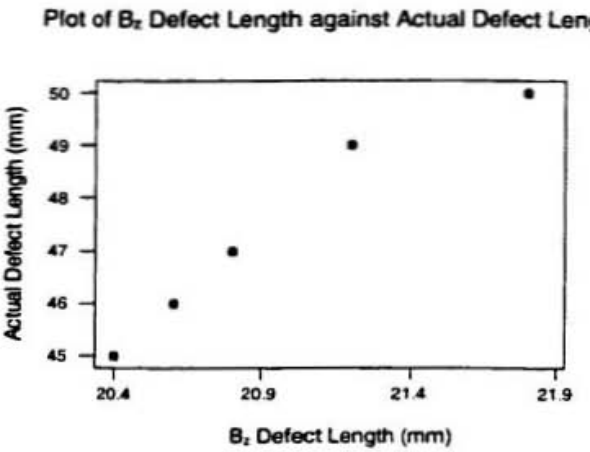

Figure 4.14. Plot of B_z against actual defect length for defects at the weld toe of the 3.8 mm pipe wall thickness.

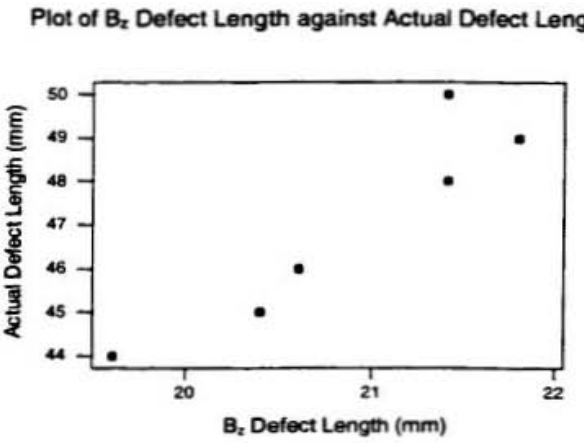

Figure 4.15. Plot of B_z against actual defect length for defects in the base metal of the 3.8 mm pipe wall thickness.

Regression analysis yielded:

$$y = -14.5 - 0.124\ x_1 + 2.95\ x_2 \qquad (4.15)$$

Since the dummy variable of equation (4.15) has a significance level equal to 0.809, the model can be used to predict the defect length from the B_z length.

In equation (4.15), location type (x_1) becomes an intercept dummy variable. For defects located at the weld toe:

$$y = -14.5 - 0.124\ (0) + 2.95\ x_2$$

$$= -14.5 + 2.95\ x_2 \qquad (4.16)$$

For defects in the base metal:

$$y = -14.5 - 0.124\ (1) + 2.95\ x_2$$

$$= -14.624 + 2.95\ x_2 \qquad (4.17)$$

Plots of equation (4.16) and (4.17) are depicted in Figure 4.16. The two lines in Figure 4.16 have the same slope but differ in intercept. The lines show that the estimated length always increases with increases in the B_z length. The plots also suggest that for any given B_z length, the estimated length of a defect located at the weld toe is slightly longer, i.e. 0.124 mm longer, than that of a defect located in the base metal. Since the crack length sizing accuracy of the ACFM technique is about ± 0.5 mm, the difference of 0.124 mm between the estimated length of a defect located at the weld toe and a defect located in the base metal is not significant and may be ignored.

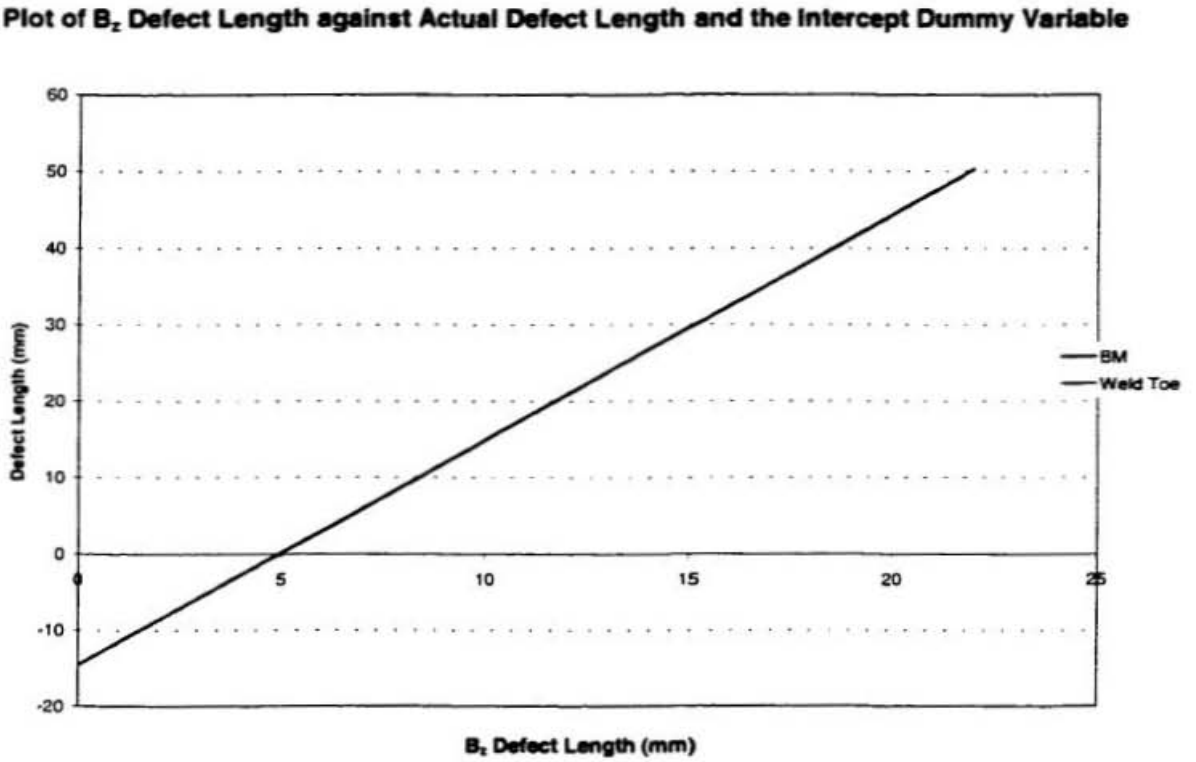

Figure 4.16 Regression plot of B_z defect length against actual defect length and the intercept dummy variable for defects location.

However, since the magnitude of the B_z length is affected by t/T, this variable should be considered in the regression. A regression analysis was therefore carried out to regress the dummy variable, the B_z length, and the t/T ratio. Variables used in the regression are as follows:

y — estimated defect length of defects located at the weld toe and base metal;

x_1 — defect location: dummy variable coded 0 for defects at the weld toe and 1 for defects in the base metal;

x_2 — B_z length;

x_3 — defect depth to pipe thickness ratio (t/T).

Regression analysis yielded:

$$y = 33.5 + 0.2\, x_1 + 0.396\, x_2 + 8.49\, x_3 \qquad (4.18)$$

Equation (4.18) suggests that for the same value of signal ratio and t/T, the estimated length of a defect located at the weld toe tends to be longer than that of one located in the base metal.

Ch. 5

DISCUSSION OF RESULTS

It would appear that the ACFM technique can be used to detect backwall-breaking defects in 6-Mo austenitic stainless steel pipes. Since the austenitic stainless steels are nonmagnetic with a low-magnetic permeability characteristic, when an electric field is induced into these materials, magnetic lines generated by the field are not concentrated near the surface. The lines are distributed relatively uniformly thoroughout the material. Therefore, capability of ACFM to detect backwall defects is remarkably good. On the other hand, the sensitivity of the ACFM technique to external surface-breaking defects in the austenitic stainless steels is less than its sensitivity to external surface-breaking defects in ferromagnetic materials such as carbon steels, which have a high magnetic permeability characteristic.

One of the major objectives of this research was to determine the threshold depth of ACFM for the detection of backwall surface-breaking defects in 6-Mo stainless steel piping. The threshold depth is defined as the minimum depth of defect that can be detected using the ACFM technique. The experiment was started by machining a 1 mm deep defect into the base metal of a piece of 3.8 mm wall thickness pipe. Although the defect had a small depth-to-wall-thickness ratio (t/T), the ACFM signals obtained from scanning the defect (i.e. the B_x, B_z, and butterfly plots) could be used to detect the defect. However, care had to be exercised, due to the presence of noise in the signals which could mask the defect. In this 1 mm deep defect, scanning should be conducted carefully to obtain indication of the defect, since there were lots of noise in the signals. Therefore, it was decided that if the depth of the defect were made less than 1 mm, e.g. 0.5 mm, the ACFM technique would not be able to detect the defect due to too much noise in the ACFM signals.

When a defect having the same depth, i.e. 1 mm, was machined at the weld toe, the ACFM probe was not able to detect the defect. The signals could not reveal the defect due to noise in the B_x and B_z traces. After increasing the defect depth to 1.5 mm, it was observed that the ACFM probe could detect the defect. Therefore, based on these experimental results, it is concluded that the minimum depth of defect located in base metal that can be characterised by the ACFM technique is 1 mm, or $t/T = 0.26$. Using $t/T = 0.26$, the minimum depth of defect in the base metal of a 3.4 mm wall thickness pipe that can be estimated is as follows:

$$\frac{t}{T} = 0.26$$

$$t = 0.26 \times 3.4$$

$$= 0.88 \text{ mm}$$

where: t = defect depth (mm)

T = pipe thickness (mm).

For the 3.8 mm wall thickness pipe, the minimum depth of defect that could be detected in the weld toe using the ACFM technique, was found to be 1.5 mm, which resulted in a minimum t/T value of 0.39. Using this minimum t/T value, the threshold depth of a defect located in the weld toe of a 3.4 mm wall thickness pipe can be estimated as follow:

$$\frac{t}{T} = 0.39$$

$$t = 0.39 \times 3.4$$

$$= 1.33 \text{ mm}$$

where: t = defect depth (mm)

T = pipe thickness (mm)

With regard to the regression analysis of signal ratio against the actual defect depth for defects located in the base metal, Figure 5.1 shows the regression lines of equation (4.3) and (4.4):

$y = 6.52 + 1.16\ x_2$; for defects in 3.4 mm wall thickness pipe;

$y = 6.1 + 0.966\ x_2$; for defects in 3.8 mm wall thickness pipe.

where: y = estimated defect depth [mm]

x_2 = $\log_e$ signal ratio.

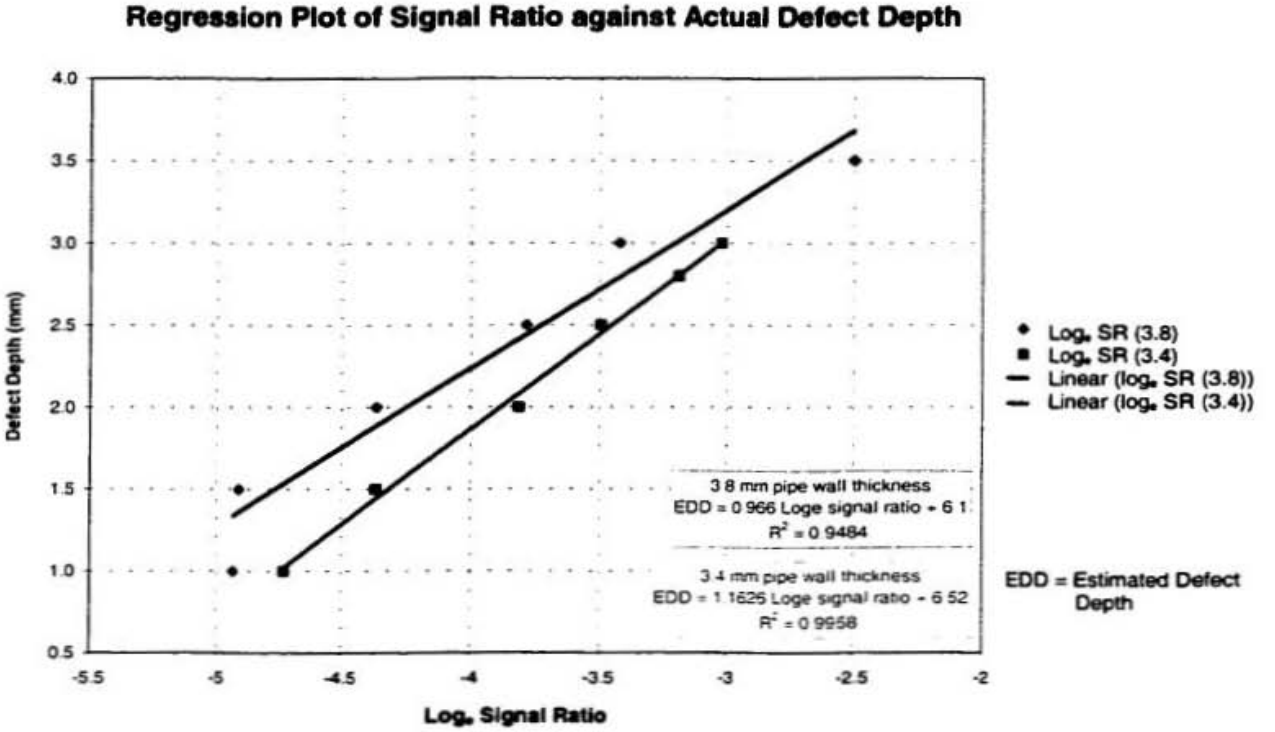

Figure 5.1. Regression plot of signal ratio against actual defect depth

Figure 5.1 shows that for the same value of signal ratio, the estimated depth of defects located in the 3.8 mm wall thickness pipe is greater than that of defects located in the 3.4 mm wall thickness pipe. In other words, for the same value of estimated depth, the signal ratio obtained from the 3.4 mm wall thickness pipe is stronger than that obtained from the 3.8 mm wall thickness pipe.

The t/T factor, however, affects the strength of the signals. For the same defect depth (t), the ratio of t/T for the 3.4 mm wall thickness pipe will always be greater than that for the 3.8 mm wall thickness pipe, resulting in stronger signals received by the ACFM instrument. Using equations (4.3) and (4.4), the estimated depth of the defects can then be calculated. Table 5.1 shows a comparison between the actual and estimated depth of the defects located in 3.4 mm and 3.8 mm thick pipe walls.

Table 5.1. Actual and estimated depths of the defects located in 3.4 mm and 3.8 mm wall thickness pipes.

Wall Thickness	Actual Depth (mm)	Estimated Depth (mm)	Difference (%)
3.4 mm	1.0	1.02	2.39
	1.5	1.45	3.53
	2.0	2.09	4.23
	2.5	2.46	1.82
	2.8	2.81	0.26
	3.0	3.01	0.16
	Average		2.07
3.8 mm	1.0	1.34	33.55
	1.5	1.36	9.45
	2.0	1.89	5.64
	2.5	2.44	2.33
	3.0	2.79	6.93
	3.5	3.68	5.26
	Average		10.52

Regression analysis of the B_z length against the actual length yielded equation (4.8):

$$y = 22.3 - 1.01\,x_1 + 0.638\,x_2 + 14.8\,x_3$$

where: y = estimated length [mm]

x_1 = dummy variable; 0 for 3.4 mm, and 1 for 3.8 mm thickness

x_2 = B_z length [mm]

x_3 = t/T.

Equation (4.8) suggests that for the same value of the signal ratio and t/T, the estimated length of a defect located in the base metal of the 3.4 mm wall thickness pipe tends to be longer than that in the 3.8 mm wall thickness pipe. Table 5.2 gives a comparison between the actual, B_z, and estimated lengths of defects located in the base metal of 3.4 mm and 3.8 mm wall thickness pipes.

Table 5.2. Actual, B_z, and estimated length of the defects located in 3.4 mm and 3.8 mm wall thickness pipes.

Wall Thickness	Actual Length	B_z Length	Estimated Length	Difference (%) (Est. to Actual)	Difference (%) (B_z to Actual)
3.4 mm	35	14.8	36.03	2.96	57.71
	42	19.8	41.44	1.33	52.86
	46	23.8	46.22	0.48	48.26
	47	22	47.29	0.61	53.19
	48	22.2	48.60	1.25	53.75
	51	21.6	49.10	3.72	57.65
	Average			1.72	53.90

Table 5.2. Actual, B_z, and estimated length of the defects located in 3.4 mm and 3.8 mm wall thickness pipes (continued).

Wall Thickness	Actual Length	B_z Length	Estimated Length	Difference (%) (Est. to Actual)	Difference (%) (B_z to Actual)
3.8 mm	36	16.2	35.47	1.46	55.00
	38	16.8	37.78	0.58	55.79
	41	17.6	40.36	1.55	57.08
	43	18.2	42.67	0.77	57.68
	45	20.4	46.00	2.22	54.67
	48	21.2	48.43	0.90	55.83
	Average			1.25	56.01

Regression analysis of the actual depth against signal ratio for defects located at the weld toe and the base metal of the 3.8 mm wall thickness pipe yielded equations (4.10) and (4.11):

$y = 6.35 + 1.04\ x_2$; for defects located at the weld toe;

$y = 6.178 + 1.04\ x_2$; for defects located in the base metal,

where: y = estimated defect depth [mm]

x_2 = $\log_e$ signal ratio.

Plots of equations (4.10) and (4.11) are shown in Figure 5.2. The two lines in Figure 5.2 show that the estimated depth in both cases increases with increasing signal ratio. From Figure 5.2, the difference in intercept of the equation (4.10) and (4.11), i.e. 0.172 showing that for the same value of signal ratio, defects located at the weld toe will

always be deeper by 0.172 mm than defects in the base metal. In other words, for the same estimated depth, the ACFM signals obtained from the defects located in the base metal are stronger than those associated with defects in the weld toe, resulting in a greater signal ratio.

Plot of Signal Ratio against Actual Defect Depth and the Intercept Dummy Variable

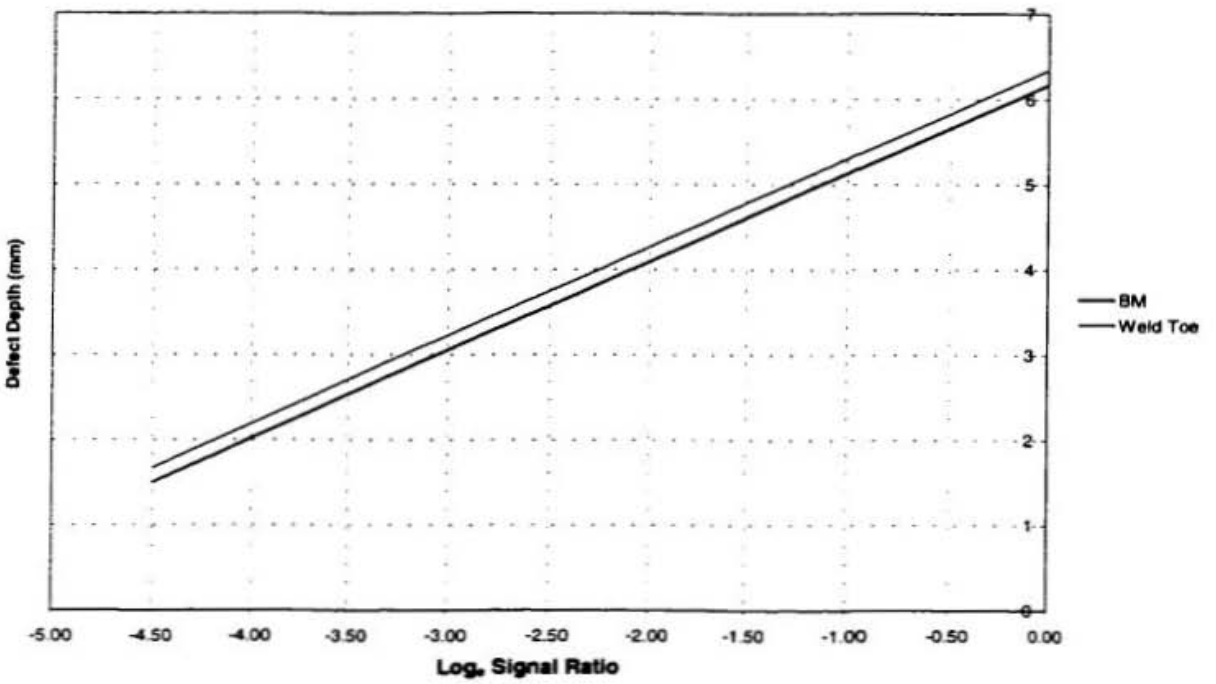

Figure 5.2. Regression plot of signal ratio against actual depth and the intercept dummy variable.

Table 5.3 shows the actual and estimated depth of defects located at the weld toe and the base metal of the 3.8 mm wall thickness pipe.

Table 5.3. Actual and estimated depth of the defects at the weld toe and the base metal of 3.8 mm wall thickness.

Defects Location	Actual Depth (mm)	Estimated Depth (mm)	Difference (%)
Weld Toe	1.0	N/A	N/A
	1.5	1.42	5.60
	2.0	2.1	4.98
	2.5	2.35	5.96
	3.0	2.88	3.88
	3.5	3.70	5.58
	Average		5.20
Base Metal	1.0	1.51	51.09
	1.5	1.35	9.73
	2.0	1.85	7.36
	2.5	2.31	7.52
	3.0	2.87	4.48
	3.5	3.53	0.89
	Average		13.51

Regression analysis of the interaction between signal ratio and the actual depth of defects located in both locations (i.e. base metal and weld toe) yielded equations (4.13) and (4.14). These equations are depicted in Figure 5.3. In Figure 5.3, the slope of the base metal line is slightly higher by an amount equal to the coefficient of the slope

dummy variable, i.e. 0.0503. The difference in slopes reveals that decreases in estimated defect depth due to decreases in the signal ratio for defects located in the base metal are more significant than for defects located at the weld toe.

Plot of Signal Ratio against Actual Defect Depth and the Slope Dummy Variable

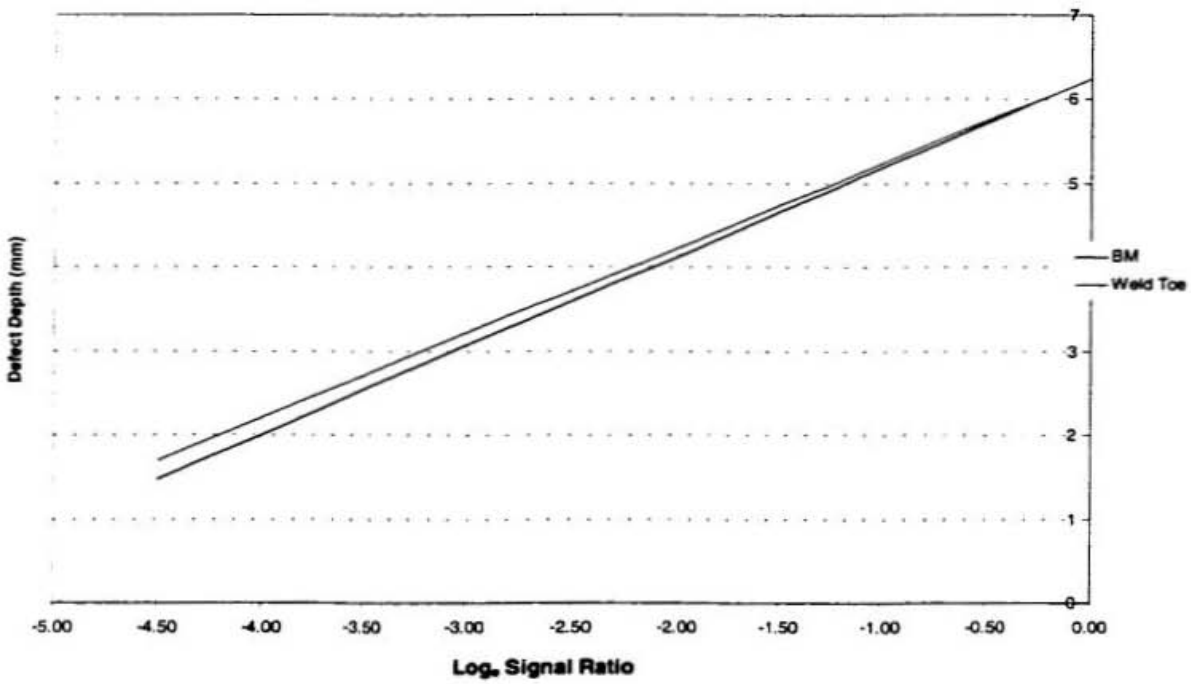

Figure 5.3. Regression plot of signal ratio against actual defect depth and the slope dummy variable.

Regression analysis of the B_z defect length against the actual defect length for defects located at the weld toe and the base metal of the 3.8 mm wall thickness pipe yielded equation (4.18):

$$y = 33.5 + 0.2\,x_1 + 0.396\,x_2 + 8.49\,x_3$$

where: y = estimated length [mm]

x_1 = dummy variable; 0 for weld toe, and 1 for base metal

x_2 = B_z length [mm]

x_3 = t/T.

Based on the equation 4.18, the estimated length of defects located at the weld toe, for the same values of signal ratio and t/T, tends to be longer than for defects located in the base metal. Table 5.4 gives a comparison between the actual, estimated and B_z lengths of defects located in the weld toe and base metal of 3.8 mm wall thickness pipe.

Table 5.4. Actual, B_z, and estimated lengths of the defects at the weld toe and the base metal of 3.8 mm wall thickness pipe.

Defects Location	Actual Length	B_z Length	Estimated Length	Difference (%) (Est. to Actual)	Difference (%) (B_z to Actual)
Weld Toe	44	N/A	N/A	N/A	N/A
	45	20.4	44.89	0.25	54.67
	46	20.6	46.16	0.34	55.22
	47	20.8	47.34	0.72	55.74
	49	21.2	48.60	0.81	56.73
	50	21.8	49.94	0.11	56.40
	Average			0.45	55.75

Table 5.4. Actual, B_z, and estimated lengths of the defects at the weld toe and the base metal of 3.8 mm wall thickness pipe (continued).

Defects Location	Actual Length	B_z Length	Estimated Length	Difference (%) (Est. to Actual)	Difference (%) (B_z to Actual)
Base Metal	44	19.6	43.67	0.75	55.45
	45	20.4	45.09	0.20	54.67
	46	20.6	46.36	0.78	55.22
	48	21.4	47.78	0.46	55.42
	49	21.8	49.04	0.08	55.51
	50	21.4	49.99	0.03	57.20
	Average			0.38	55.58

In Table 5.2 and 5.4, B_z lengths appear to be considerably shorter than actual length. The difference between the two lengths is more than 50%, which is quite significant. This can be explained as follows:

When a uniform alternating current field approaches a defect on the surface of the material, the field will take the path of least resistance; thus some (but not all) of the current will be diverted around the ends of the defect, resulting in a concentration of current that causes positive and negative peaks to appear in the B_z signal. In the case of backwall defect, as investigated in this study, when the uniform alternating current field is introduced into the material, less of the current is diverted around the ends of the defect. As the concentrations of current are not located around the defect's ends but somewhere nearer the defect's centre, the B_z defect length tends to be substantially

shorter than the actual defect length. The depth of penetration of the field (skin depth) and the geometry of the defect thereby influence the location of the B_z peaks.

Ch. 6

CONCLUSIONS AND RECCOMMENDATIONS

The ACFM technique, which is readily available in the offshore industry, is capable of detecting backwall defects in 6-Mo austenitic stainless steel piping systems. A micro-pencil probe was used to conduct this study because it is manufactured with small pick-up coils to provide better sensitivity to shallow defects. Since the pick-up coils in the micro-pencil probe are not coincident, the butterfly plot becomes slightly distorted. However, this does not affect the interpretation of the signals or defect sizing accuracy.

The ability of ACFM to detect and characterise back wall defects in austenitic stainless steel piping systems is an attractive feature which can eliminate the use of costly combination techniques such as radiography to locate the exact defect location and ultrasonic testing to predict defect depth. Furthermore, for pipes having small wall thickness (e.g. 3 – 4 mm), conventional ultrasonic testing that has no additional shoe in its probe will not work and ACFM is the only technique can be used to detect and size the defects accurately.

The test setup used in this study provided a series of data that was used to develop models for predicting defect depth and length based on actual depth and length. The test setup, however, provided insufficient data to develop models for accurate defect sizing. Accordingly, more data should be provided in future work to improve the reliability of sizing predictions.

The defect depth- to-wall thickness ratio (t/T) is a significant factor which should be considered in future experiments, since its value affects the strength of the ACFM signals. The t/T value is quite significant in predicting defect length based on the B_z length, since greater t/T values result in stronger signals and smaller t/T values result in weaker signals.

The threshold depth of detection for defects located in the base metal of 3.8 mm thick 6-Mo pipe is 1 mm, while the threshold depth of defects located at the weld toe of the same pipe is 1.5 mm. Using the t/T values obtained from the threshold depths for the base metal and the weld toe of the 3.8 mm thick pipe, threshold depths for defects located in the base metal and the weld toe of the 3.4 mm thick pipe could be estimated.

The calculations resulted in a threshold depth of t equal to 0.88 mm for defects located in the base metal and t equal to 1.33 mm for defects located at the weld toe of 3.4 mm thick pipe.

Regression analysis of the signal ratio against the actual defect depth produced the following results:

Estimated Depth = 6.25 + 1.16 Log_e Signal Ratio, for 3.4 mm pipe wall thickness;

Estimated Depth = 6.1 + 0.966 Log_e Signal Ratio, for 3.8 mm pipe wall thickness.

Regression analysis of the B_z length against the actual defect length gave the following results:

Estimated Length = 22.3 – 1.01 dummy + 0.638 B_z Crack Length + 14.8 (t/T);

Dummy variable is coded 0 for 3.4 mm pipe thickness and 1 for 3.8 mm pipe thickness.

Regression analysis of the actual defect depth against the signal ratio for defects located at the weld toe and the base metal of 3.8 mm pipe thick pipes resulted in:

Estimated defect depth = 6.35 + 1.04 Log_e Signal Ratio, for defects at the weld toe;

Estimated defect depth = 6.178 + 1.04 Log_e Signal Ratio, for defects in the base metal.

Regression analysis of the B_z length against the actual length for defects located at the weld toe and in the base metal of 3.8 mm pipe thickness resulted in:

Estimated Length = 33.5 + 0.2 dummy + 0.396 B_z Length + 8.49 (t/T);

Dummy variable is coded 0 for defect at weld toe and 1 for defect in base metal.

Variations in material properties (e.g. magnetic permeability) caused by welding do not appear to affect the model predictions significantly. Although the influence of

the heat-affected zone on the ACFM model predictions is remarkably low, care must be exercised when welding austenitic stainless steels. Incorrect welding procedures can reduce the corrosion resistance of 6-Mo material and lead to localised corrosion attack at welded joints.

As these experiments were conducted using only two different pipe thicknesses, the results are valid only for the two thicknesses. Also, if the proposed models are used in practice, the actual length of defects investigated should be close to the range of defects examined in the experiments. Accordingly, it is recommended that additional experiments be carried out using more variation in the range of defect length. Also, it is recommended that additional experiments be conducted using pipe thickness other than 3.4 mm and 3.8 mm, to obtain more versatile models for defect characterisation. However, inaccuracy in using the equations derived from this study may arise in practice due to some factors such as personnel who carry out the inspection and defect geometry.

REFERENCES

Baboian, R., "Corrosion Test and Standards: Application and Interpretation", ASTM, Philadelphia, 1995.

Bradford, Samuel A., "Corrosion Control", Van Nostrand Reinhold, NY, 1993.

Bringas, John E., "The Metals Black Book: Ferrous Metals", Casti Publishing Inc., Alberta, 1995.

Carroll, Blair L., "Investigation into the Detection and Classification of Defect Colonies Using ACFM Technology", M. Eng. Thesis, Memorial University of Newfoundland, 1998.

Chawla, Sohan L., and Rajeswar K. Gupta, "Materials Selection for Corrosion Control", ASM International, Material Park, Ohio, 1993.

Davis, J.R., "Stainless Steels", ASM Specialty Handbook, ASM International, Material Park, Ohio, 1994.

Dover, W. D., Collins, R., and Michael, D. H., "Review of Development in ACPD and ACFM", The British Journal of Non-Destructive Testing, Vol. 33, No. 3, pp. 121-127, 1991.

Fontana, Mars G., "Corrosion Engineering", Mc Graw-Hill, Singapore, 3rd edition, 1987.

Halmshaw, R., "Non-destructive Testing", Edward Arnold, London, 2nd edition, 1991.

Hamilton, Lawrence C., "Regression with Graphics, A Second Course in Applied Statistics", Brooks/Cole Publishing Company, Pacific Grove, California, 1992.

Hayward, Gordon P., "Introduction to Non-destructive Testing", American Society for Quality Control, Wisconsin, 1978.

Hull, Barry, and Vernon John, "Non-destructive Testing", Springer-Verlag, New York, 1988.

Lewis A. M., "The Modelling of Electromagnetic Methods for Nondestructive Testing of Fatigue Cracks", Ph. D. Thesis, Department of Mechanical Engineering, University of London, U.K., 1991.

Lugg, Martin C., "ACFM Crack Microgauge Model U9b, User Manual", Technical Software Consultant Ltd., Milton Keynes, U.K., 1996.

Lugg, Martin C., "An Introduction to ACFM", Technical Software Consultant Ltd., U.K., 1992.

Lugg, M. C., Lewis, A. M., Michael, D. H., and Dover, W. D., "The Non-Contacting ACFM Technique", Electromagnetic Inspection, IOP Meeting No. 12, Institute of Physics, pp. 41-81, 1988.

Mendenhall, William, "Introduction to Probability and Statistics", Duxbury Press, Boston, 6th edition, 1983.

Raine, Alan G., and Craig C. Monahan, "Alternating Current Field Measurement (ACFM): A New Technique for the NDT of Process Plant and Piping Components", NDE Engineering Codes and Standards and Materials Characterization, ASME PVP-vol. 322, NDE-vol. 15, pp. 87-93, 1996.

Raine, Alan G., Dover, W. D., and J. R. Rudlin, "Trials on Coated Nodes", IOCE 92 Conference Proceedings, Aberdeen, U.K., October, 1992.

Ryan, Barbara F., and Bryan L. Joiner, "Minitab Handbook", Duxbury Press, Belmont, California, 3rd edition, 1994.

Silk, M. G., A. M. Stoneham, and J. A. G. Temple, "The Reliability of Non-destructive Inspection", Adam Hilger, Bristol, 1987.

Smith, Michael C., "ACFM Inspection Procedure for U9b ACFM Instrument and QFM v2.x", Technical Software Consultant Ltd., Milton Keynes, U.K., 1997.

Smith, Michael C., "QFM Vn. 2.x User Manual, Level 1", Technical Software Consultant Ltd., Milton Keynes, U.K., 1996.

Smith, Michael C., "QFM Vn. 2.x User Manual, Level 2", Technical Software Consultant Ltd., Milton Keynes, U.K., 1997.

Technical Software Consultants Ltd. Homepage: http://www.tscuk.demon.co.uk, Milton Keynes, U.K., 1999.

Appendix A

ACFM Scans for the Defects Located in the Inner Surface of the Base Metal of 3.4 mm Pipe Wall Thickness

Table A.1. Scanning data from file **D10T34.wdf**

Data from Scanning I			
Pipe wall thickness	: 3.4 mm	Minimum B_x reading	: 1654
Defect depth	: 1.0 mm	Actual length	: 35 mm
Background B_x reading	: 1672	B_z length	: 14 mm
Data from Scanning II			
Pipe wall thickness	: 3.4 mm	Minimum B_x reading	: 1678
Defect depth	: 1.0 mm	Actual length	: 35 mm
Background B_x reading	: 1696	B_z length	: 15 mm
Data from Scanning III			
Pipe wall thickness	: 3.4 mm	Minimum B_x reading	: 1707
Defect depth	: 1.0 mm	Actual length	: 35 mm
Background B_x reading	: 1718	B_z length	: 15 mm
Data from Scanning IV			
Pipe wall thickness	: 3.4 mm	Minimum B_x reading	: 1700
Defect depth	: 1.0 mm	Actual length	: 35 mm
Background B_x reading	: 1713	B_z length	: 15 mm
Data from Scanning V			
Pipe wall thickness	: 3.4 mm	Minimum B_x reading	: 1674
Defect depth	: 1.0 mm	Actual length	: 35 mm
Background B_x reading	: 1691	B_z ength	: 15 mm

D10T34.wdf – Scanning I

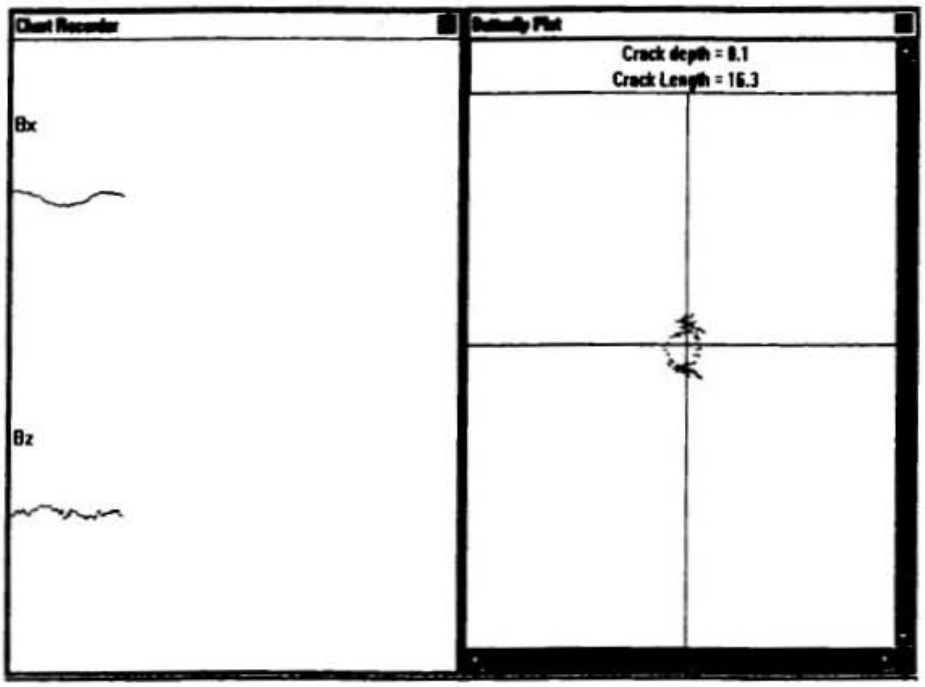

D10T34.wdf – Scanning II

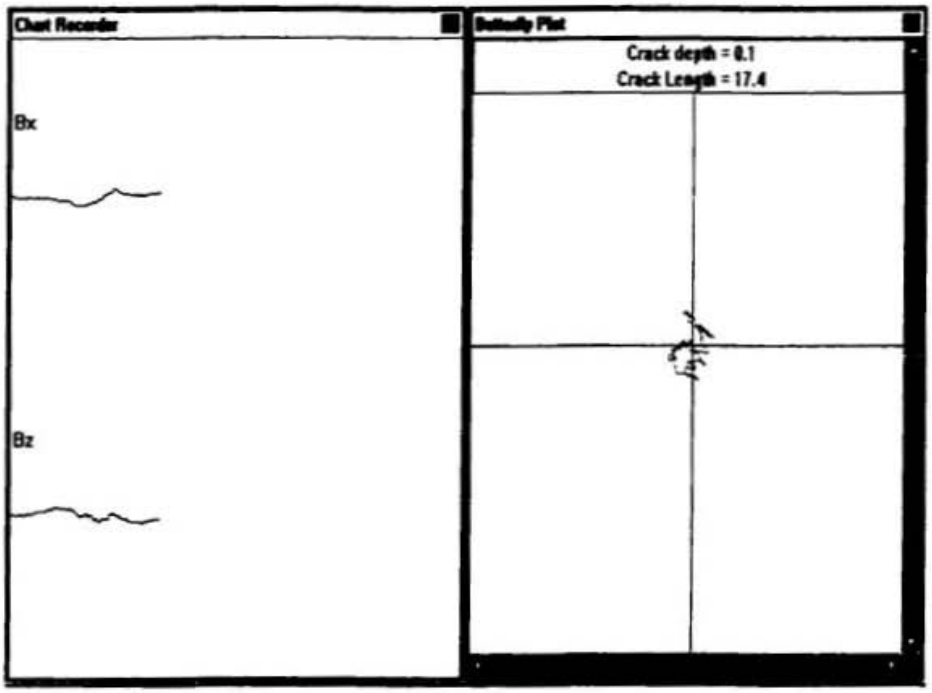

D10T34.wdf – Scanning III

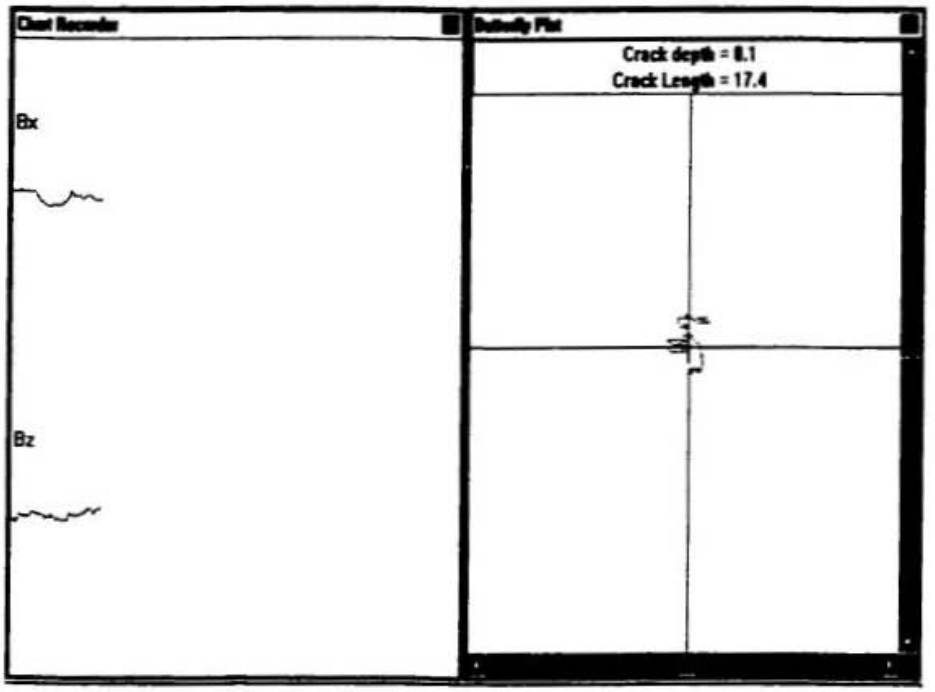

D10T34.wdf – Scanning IV

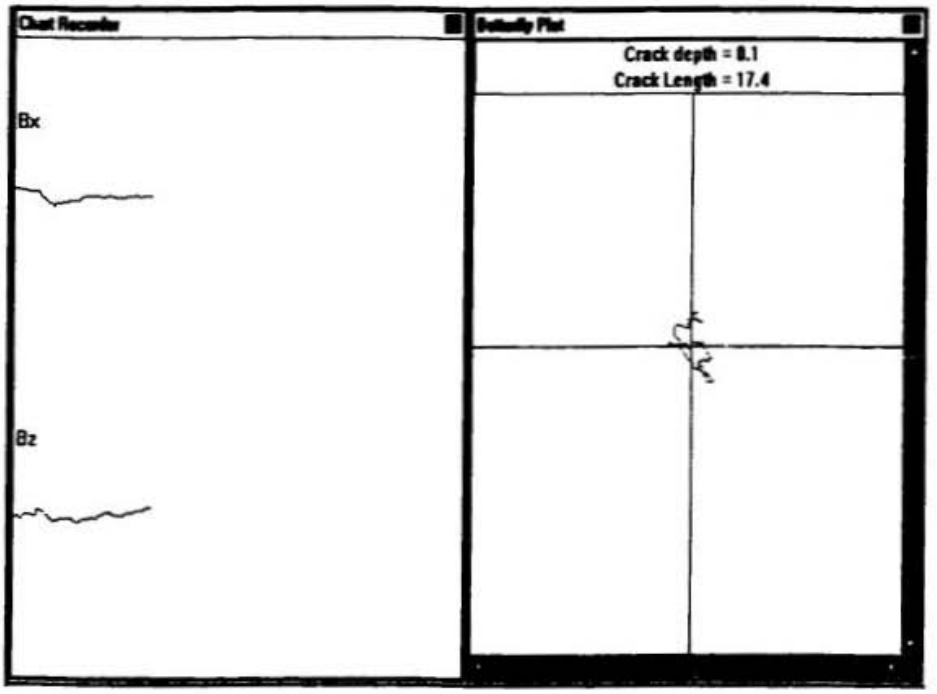

D10T34.wdf – Scanning V

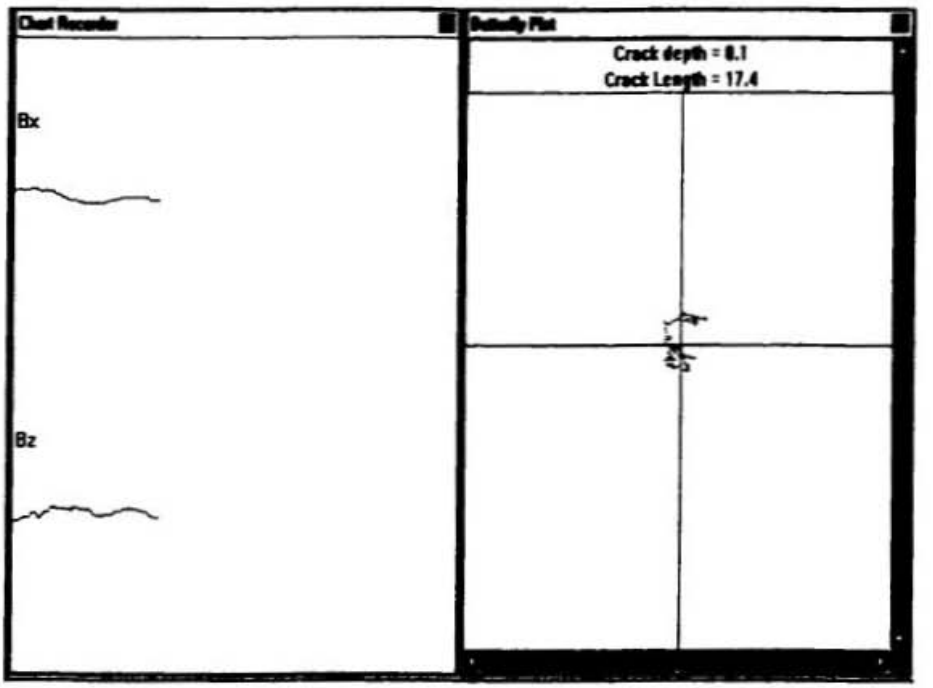

Table A.2. Scanning data from file **D15T34.wdf**

Data from Scanning I			
Pipe wall thickness	: 3.4 mm	Minimum B_x reading	: 1673
Defect depth	: 1.5 mm	Actual length	: 42 mm
Background B_x reading	: 1695	B_z length	: 18 mm
Data from Scanning II			
Pipe wall thickness	: 3.4 mm	Minimum B_x reading	: 1672
Defect depth	: 1.5 mm	Actual length	: 42 mm
Background B_x reading	: 1694	B_z length	: 21 mm
Data from Scanning III			
Pipe wall thickness	: 3.4 mm	Minimum B_x reading	: 1674
Defect depth	: 1.5 mm	Actual length	: 42 mm
Background B_x reading	: 1694	B_z length	: 22 mm
Data from Scanning IV			
Pipe wall thickness	: 3.4 mm	Minimum B_x reading	: 1675
Defect depth	: 1.5 mm	Actual length	: 42 mm
Background B_x reading	: 1699	B_z length	: 19 mm
Data from Scanning V			
Pipe wall thickness	: 3.4 mm	Minimum B_x reading	: 1679
Defect depth	: 1.5 mm	Actual length	: 42 mm
Background B_x reading	: 1699	B_z Crack Length	: 19 mm

D15T34.wdf – Scanning I

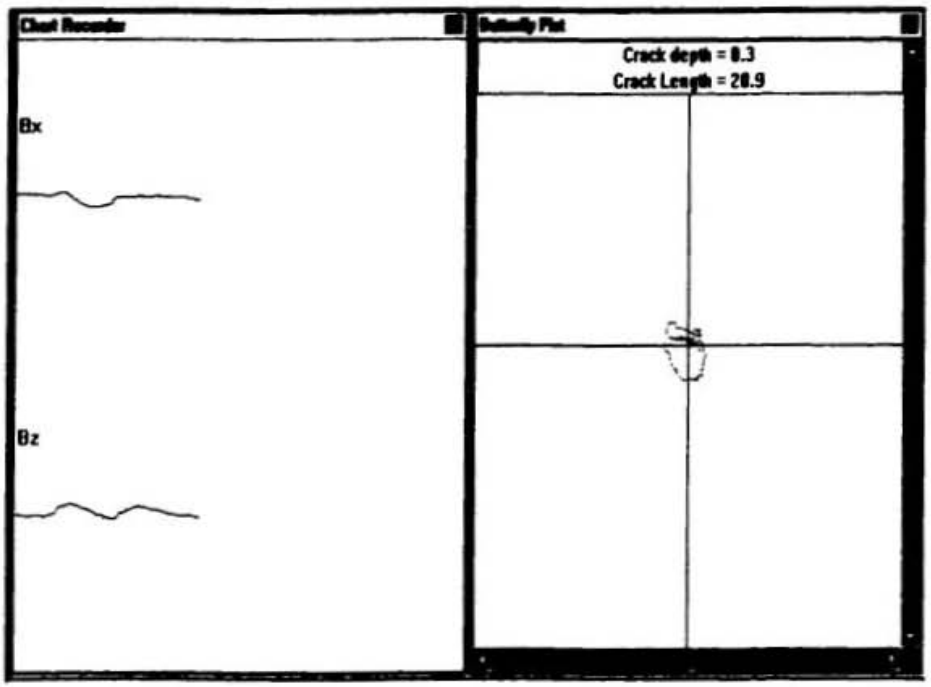

D15T34.wdf – Scanning II

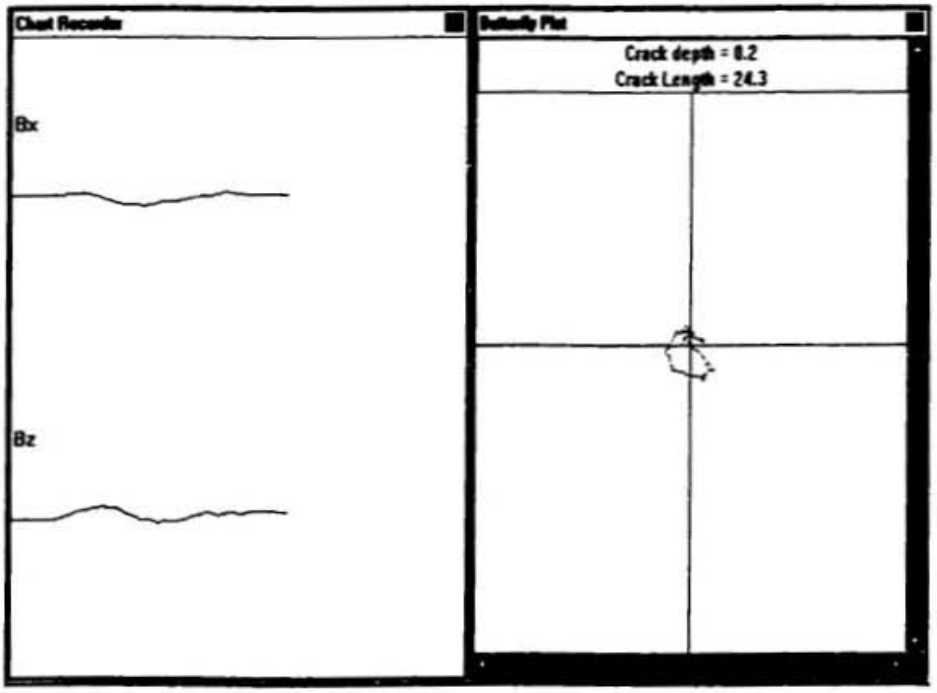

D15T34.wdf – Scanning III

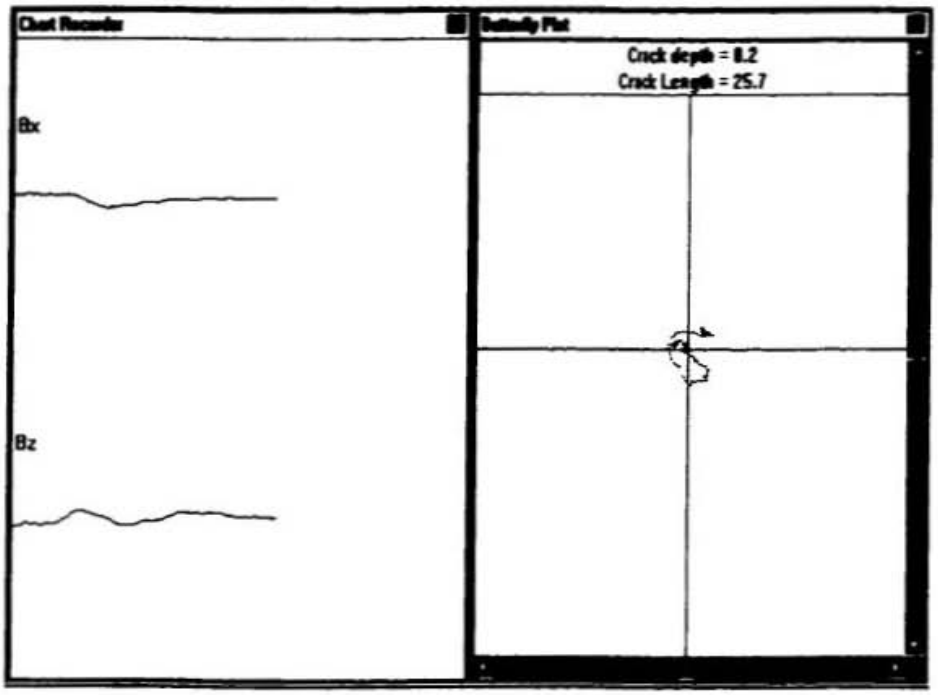

D15T34.wdf – Scanning IV

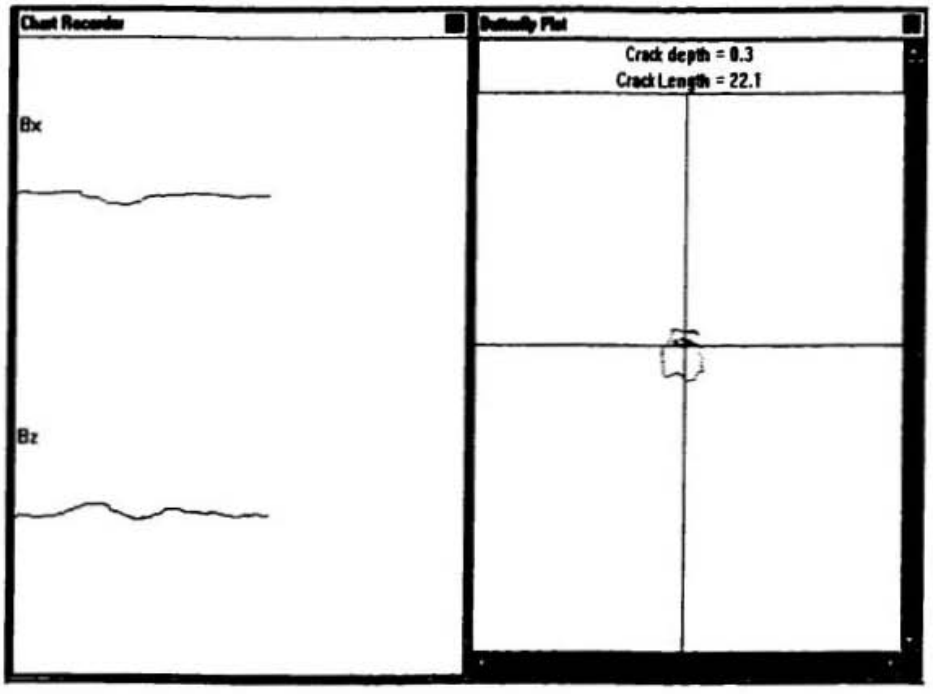

D15T34.wdf – Scanning V

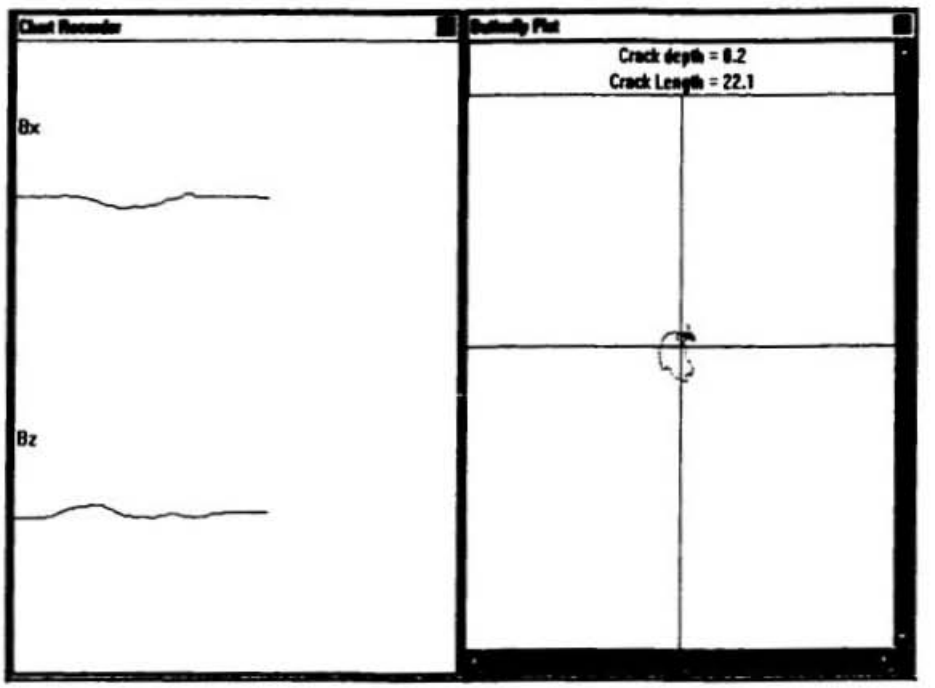

Table A.3. Scanning data from file **D20T34.wdf**

Data from Scanning I			
Pipe wall thickness	: 3.4 mm	Minimum B_x reading	: 1652
Defect depth	: 2.0 mm	Actual length	: 46 mm
Background B_x reading	: 1692	B_z length	: 24 mm
Data from Scanning II			
Pipe wall thickness	: 3.4 mm	Minimum B_x reading	: 1657
Defect depth	: 2.0 mm	Actual length	: 46 mm
Background B_x reading	: 1693	B_z length	: 24 mm
Data from Scanning III			
Pipe wall thickness	: 3.4 mm	Minimum B_x reading	: 1645
Defect depth	: 2.0 mm	Actual length	: 46 mm
Background B_x reading	: 1684	B_z length	: 23 mm
Data from Scanning IV			
Pipe wall thickness	: 3.4 mm	Minimum B_x reading	: 1651
Defect depth	: 2.0 mm	Actual length	: 46 mm
Background B_x reading	: 1686	B_z Crack Length	: 24 mm
Data from Scanning V			
Pipe wall thickness	: 3.4 mm	Minimum B_x reading	: 1649
Defect depth	: 2.0 mm	Actual length	: 46 mm
Background B_x reading	: 1685	B_z length	: 24 mm

D20T34.wdf – Scanning I

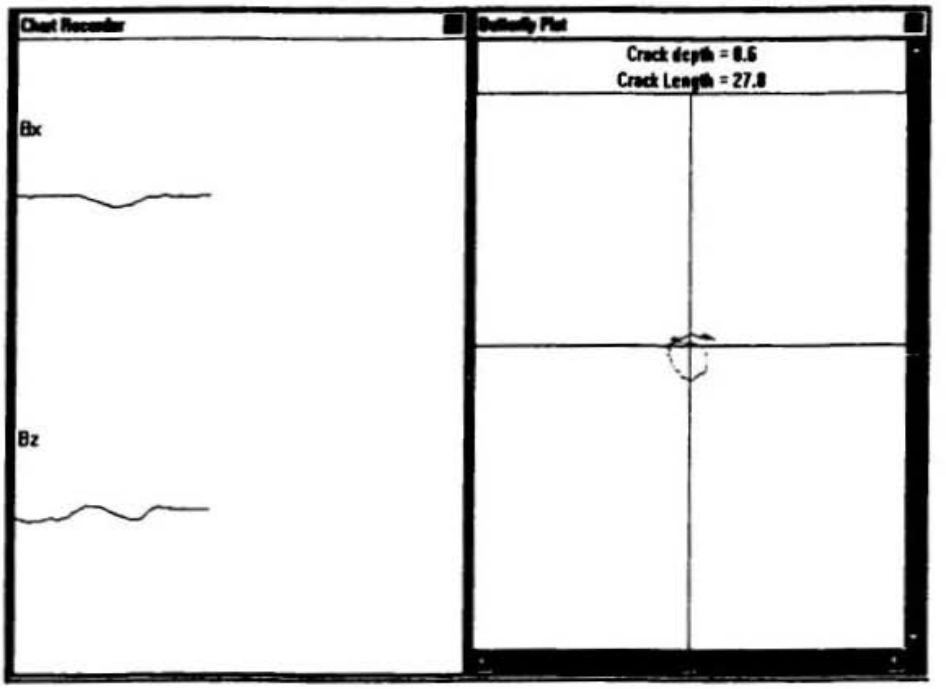

D20T34.wdf – Scanning II

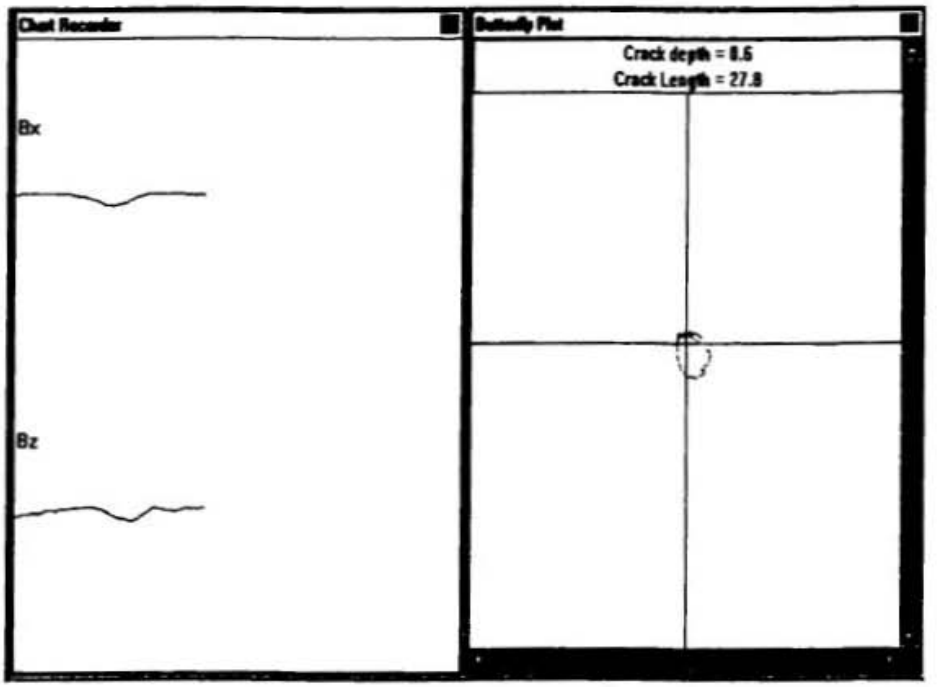

D20T34.wdf – Scanning III

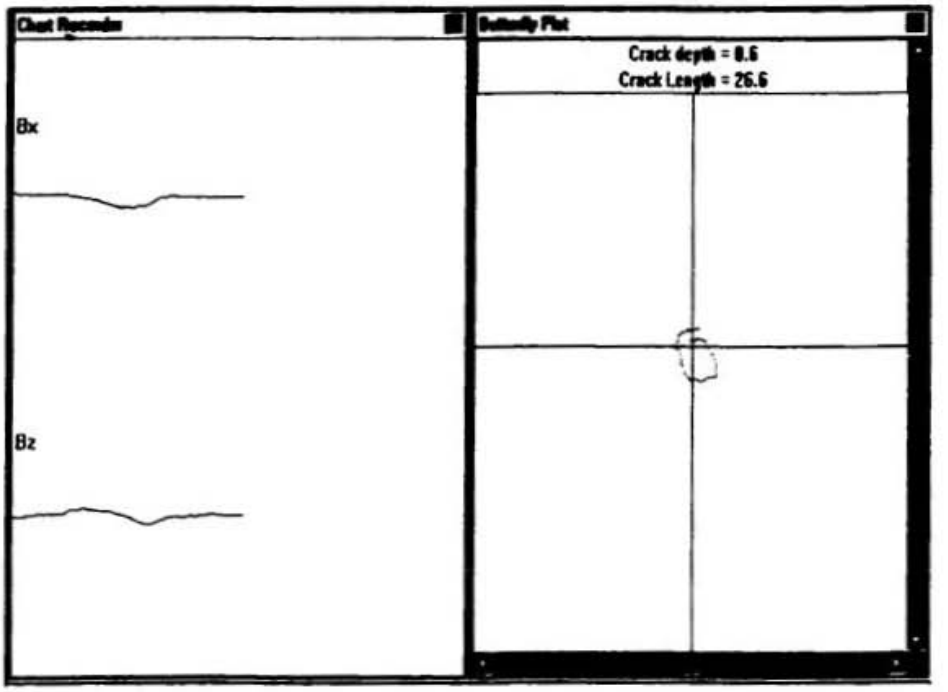

D20T34.wdf – Scanning IV

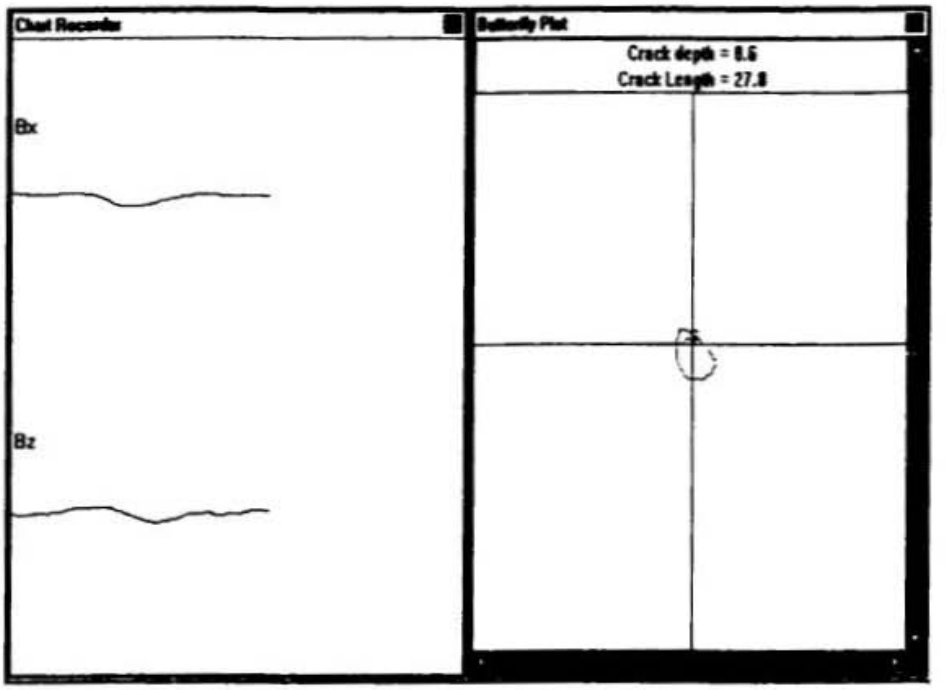

D20T34.wdf – Scanning V

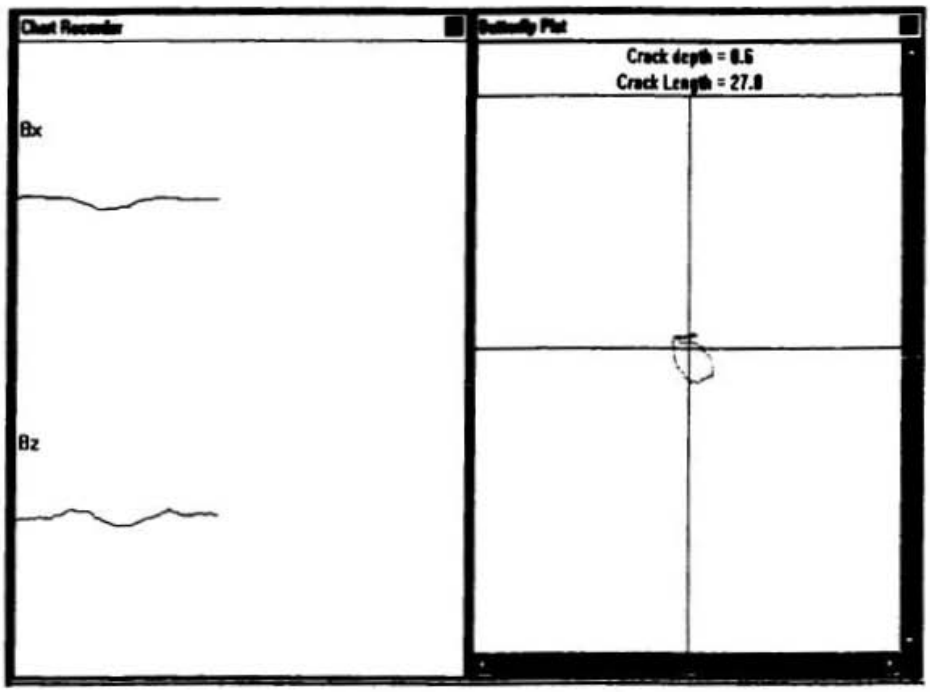

Table A.4. Scanning data from file **D25T34.wdf**

Data from Scanning I			
Pipe wall thickness	: 3.4 mm	Minimum B_x reading	: 1606
Defect depth	: 2.5 mm	Actual length	: 47 mm
Background B_x reading	: 1658	B_z length	: 22 mm
Data from Scanning II			
Pipe wall thickness	: 3.4 mm	Minimum B_x reading	: 1618
Defect depth	: 2.5 mm	Actual length	: 47 mm
Background B_x reading	: 1670	B_z length	: 20 mm
Data from Scanning III			
Pipe wall thickness	: 3.4 mm	Minimum B_x reading	: 1635
Defect depth	: 2.5 mm	Actual length	: 47 mm
Background B_x reading	: 1684	B_z length	: 23 mm
Data from Scanning IV			
Pipe wall thickness	: 3.4 mm	Minimum B_x reading	: 1636
Defect depth	: 2.5 mm	Actual length	: 47 mm
Background B_x reading	: 1686	B_z length	: 23 mm
Data from Scanning V			
Pipe wall thickness	: 3.4 mm	Minimum B_x reading	: 1637
Defect depth	: 2.5 mm	Actual length	: 47 mm
Background B_x reading	: 1688	B_z length	: 22 mm

D25T34.wdf – Scanning I

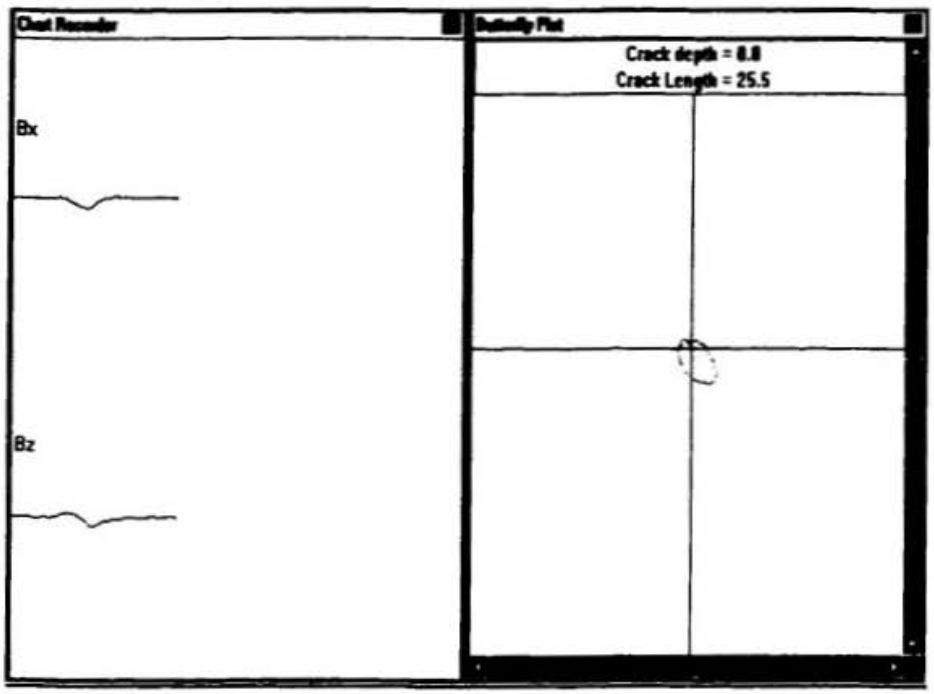

D25T34.wdf – Scanning II

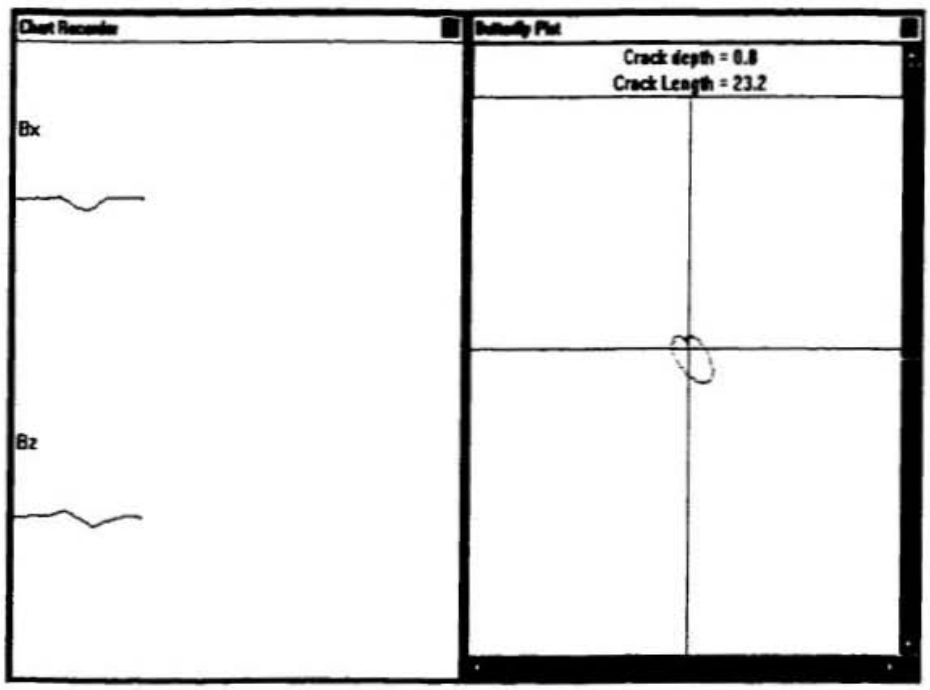

D25T34.wdf – Scanning III

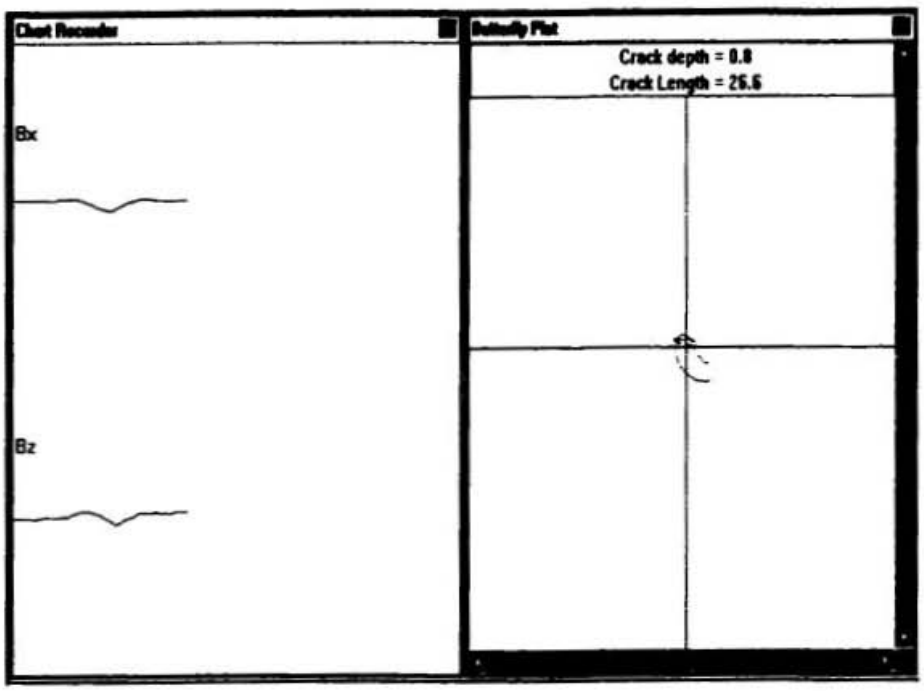

D25T34.wdf – Scanning IV

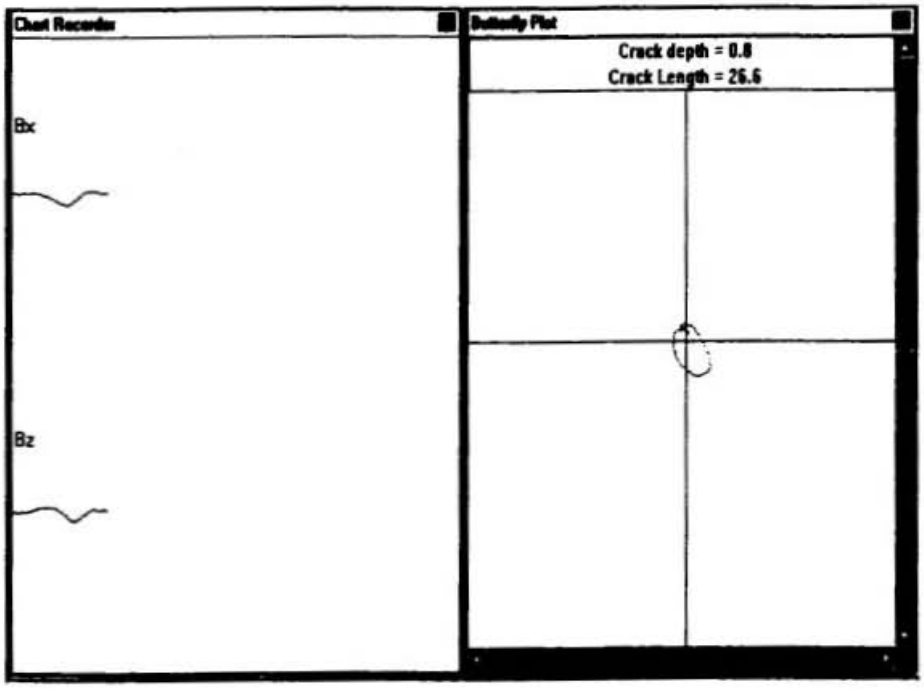

D25T34.wdf – Scanning V

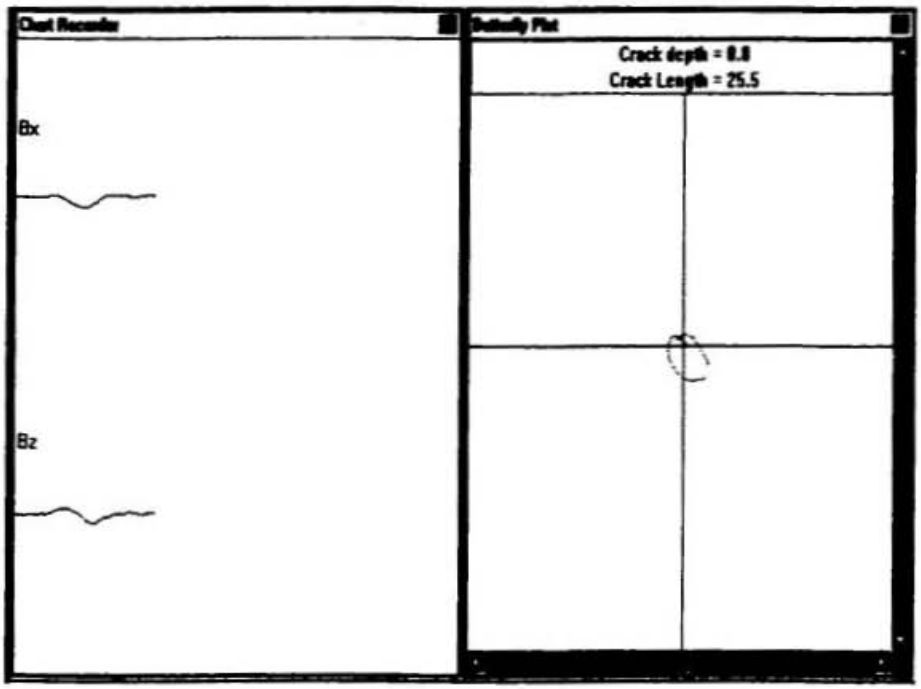

Table A.5. Scanning data from file **D28T34.wdf**

Data from Scanning I			
Pipe wall thickness	: 3.4 mm	Minimum B_x reading	: 1603
Defect depth	: 2.8 mm	Actual length	: 48 mm
Background B_x reading	: 1673	B_z length	: 22 mm
Data from Scanning II			
Pipe wall thickness	: 3.4 mm	Minimum B_x reading	: 1601
Defect depth	: 2.8 mm	Actual length	: 48 mm
Background B_x reading	: 1669	B_z length	: 22 mm
Data from Scanning III			
Pipe wall thickness	: 3.4 mm	Minimum B_x reading	: 1602
Defect depth	: 2.8 mm	Actual length	: 48 mm
Background B_x reading	: 1669	B_z length	: 22 mm
Data from Scanning IV			
Pipe wall thickness	: 3.4 mm	Minimum B_x reading	: 1608
Defect depth	: 2.8 mm	Actual length	: 48 mm
Background B_x reading	: 1675	B_z length	: 23 mm
Data from Scanning V			
Pipe wall thickness	: 3.4 mm	Minimum B_x reading	: 1603
Defect depth	: 2.8 mm	Actual length	: 48 mm
Background B_x reading	: 1674	B_z length	: 22 mm

D28T34.wdf – Scanning I

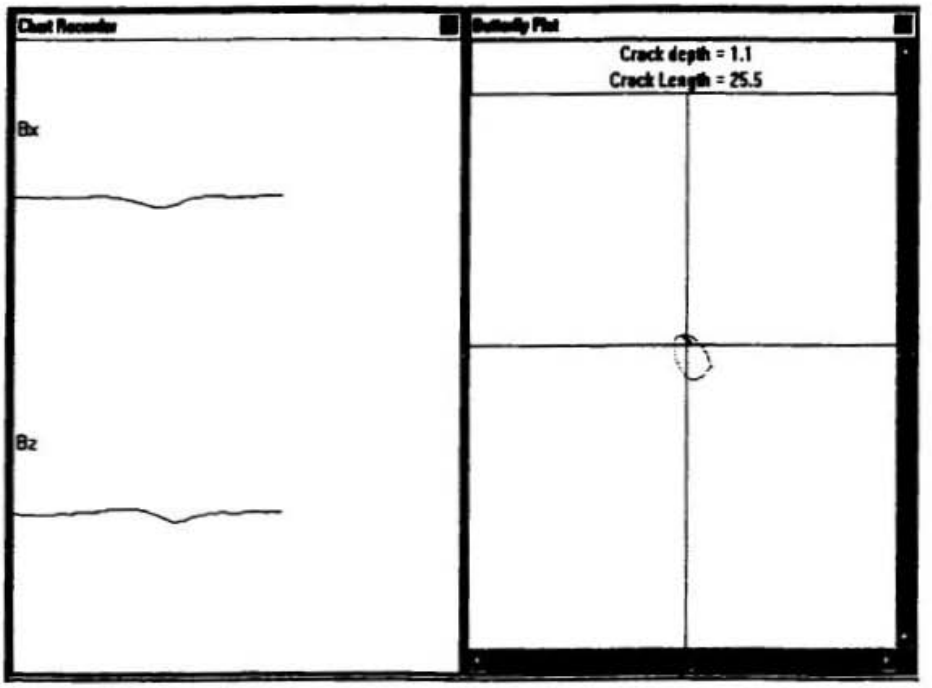

D28T34.wdf – Scanning II

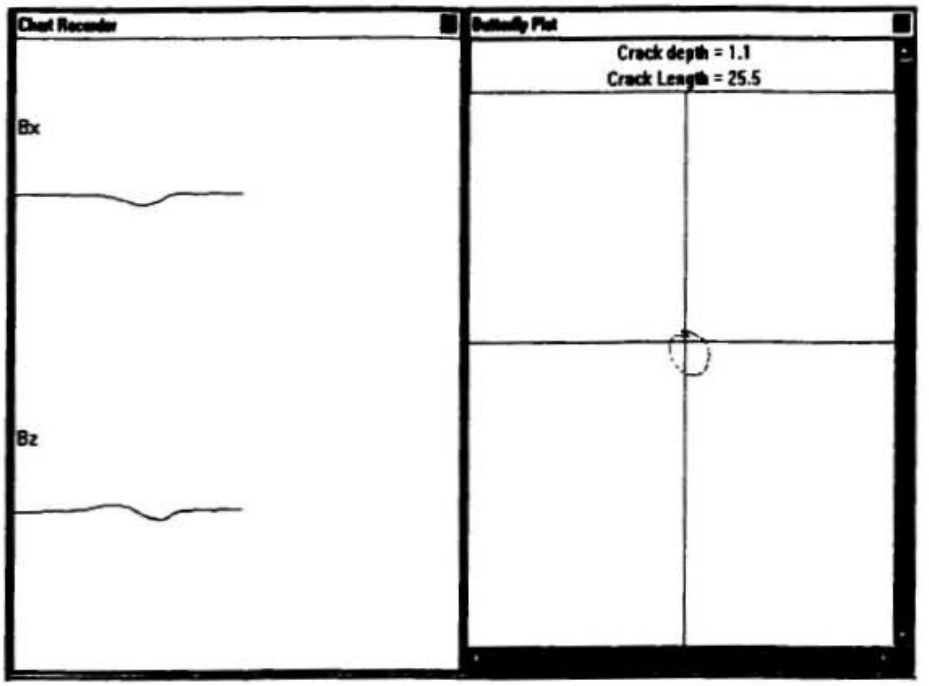

D28T34.wdf – Scanning III

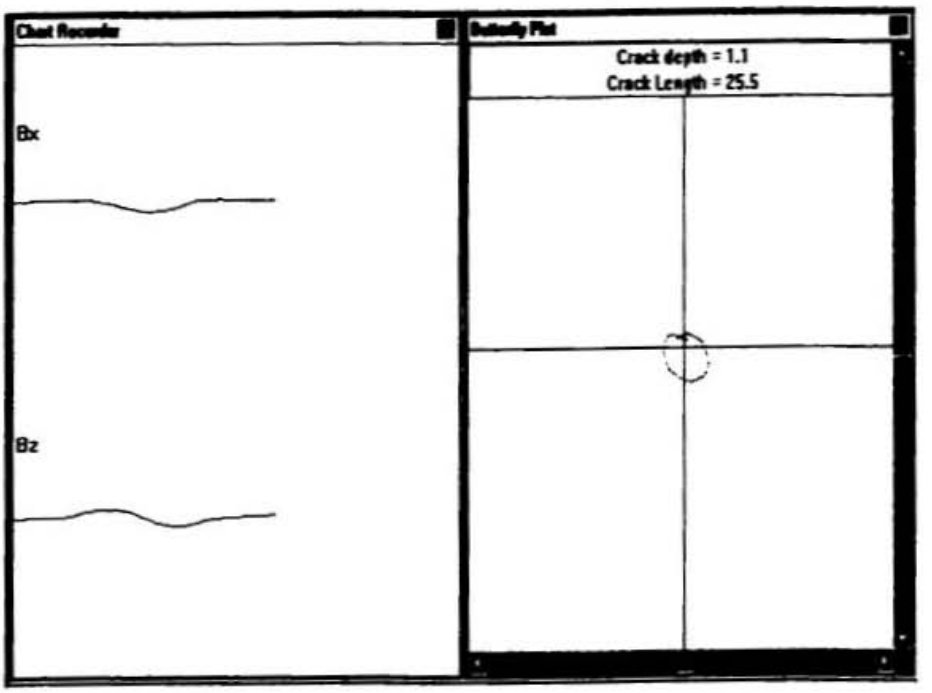

D28T34.wdf – Scanning IV

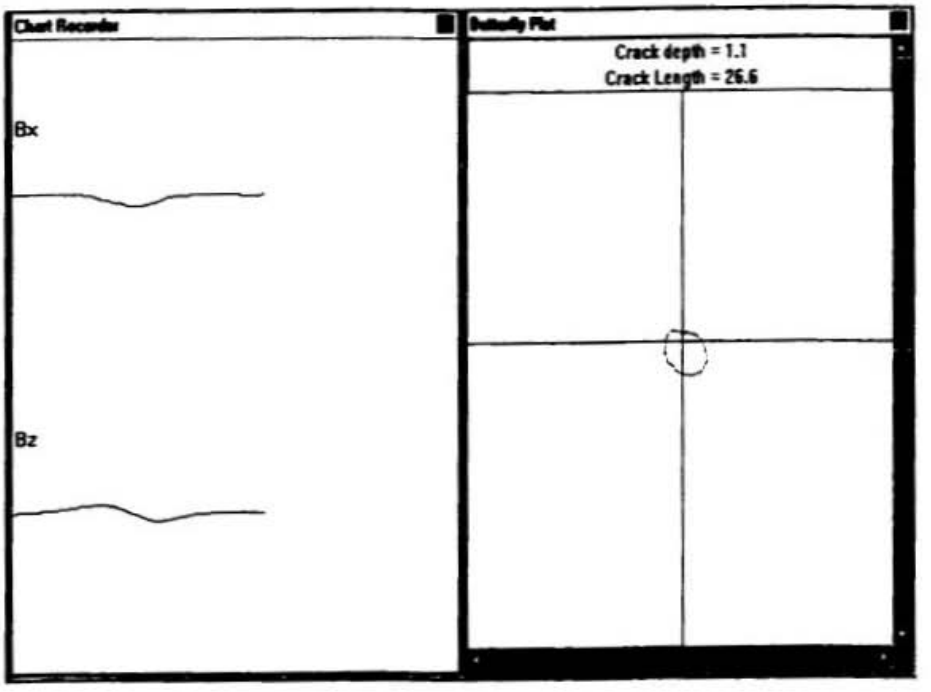

D28T34.wdf – Scanning V

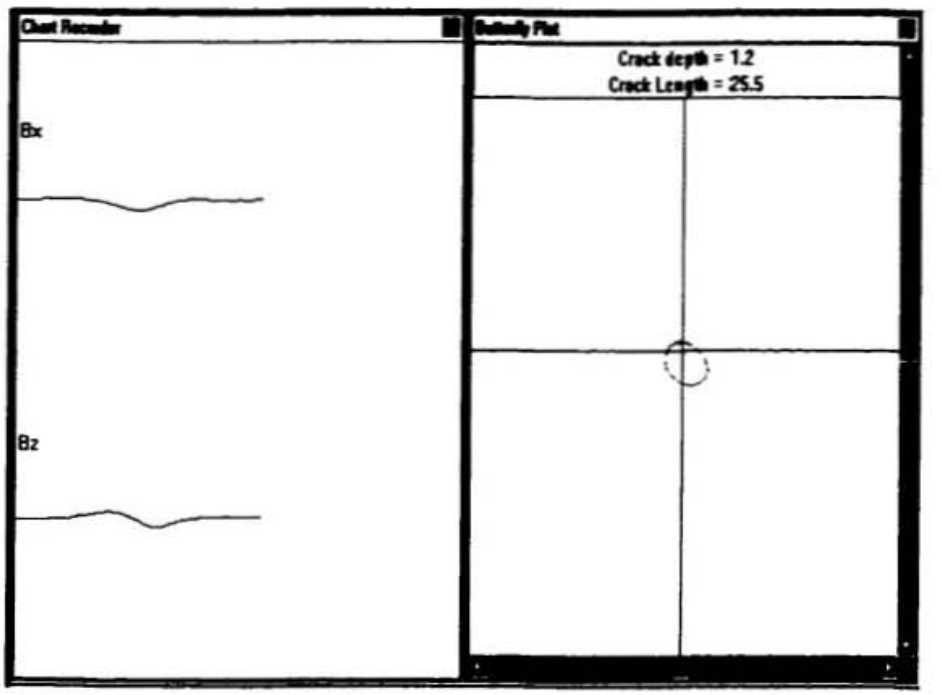

Table A.6. Scanning data from file **D30T34.wdf**

Data from Scanning I			
Pipe wall thickness	: 3.4 mm	Minimum B_x reading	: 1615
Defect depth	: 3.0 mm	Actual length	: 51 mm
Background B_x reading	: 1700	B_z Crack Length	: 24 mm
Data from Scanning II			
Pipe wall thickness	: 3.4 mm	Minimum B_x reading	: 1616
Defect depth	: 3.0 mm	Actual length	: 51 mm
Background B_x reading	: 1695	B_z Crack Length	: 20 mm
Data from Scanning III			
Pipe wall thickness	: 3.4 mm	Minimum B_x reading	: 1604
Defect depth	: 3.0 mm	Actual length	: 51 mm
Background B_x reading	: 1690	B_z Crack Length	: 22 mm
Data from Scanning IV			
Pipe wall thickness	: 3.4 mm	Minimum B_x reading	: 1615
Defect depth	: 3.0 mm	Actual length	: 51 mm
Background B_x reading	: 1696	B_z length	: 21 mm
Data from Scanning V			
Pipe wall thickness	: 3.4 mm	Minimum B_x reading	: 1611
Defect depth	: 3.0 mm	Actual length	: 51 mm
Background B_x reading	: 1692	B_z length	: 21 mm

D30T34.wdf – Scanning I

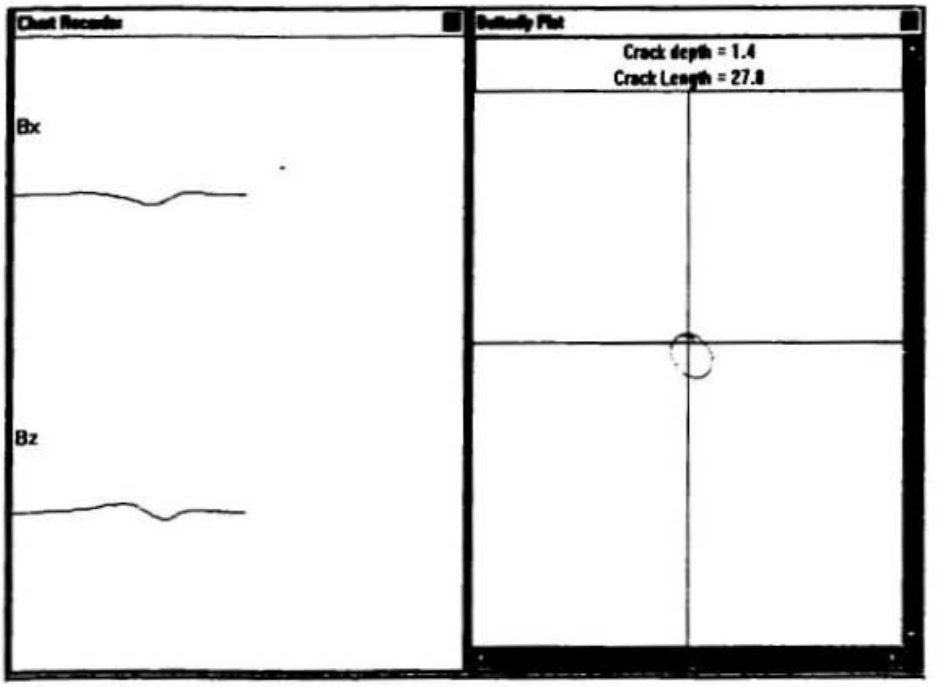

D30T34.wdf – Scanning II

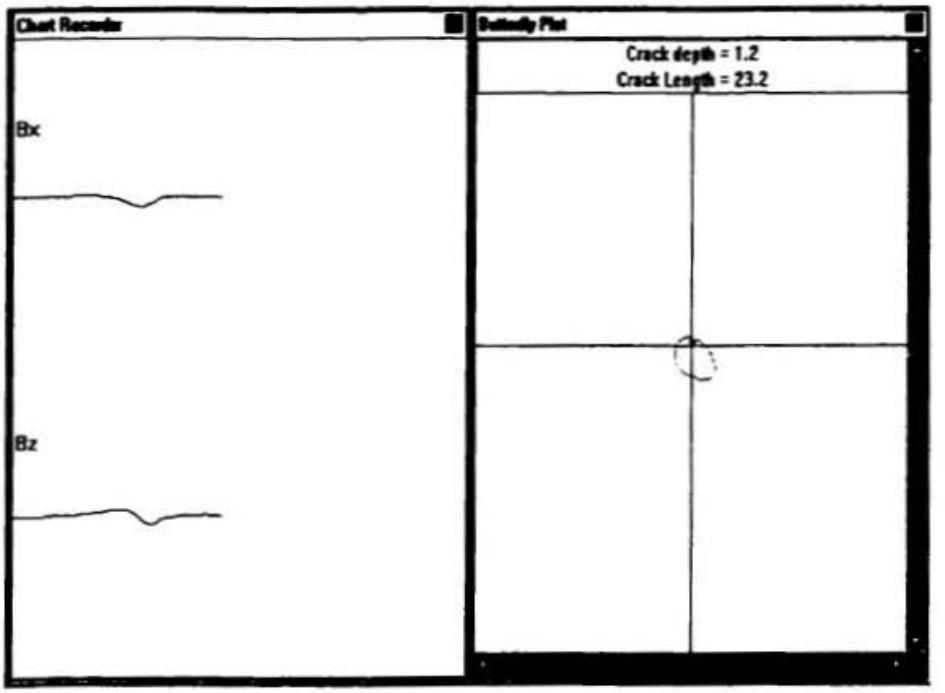

D30T34.wdf – Scanning III

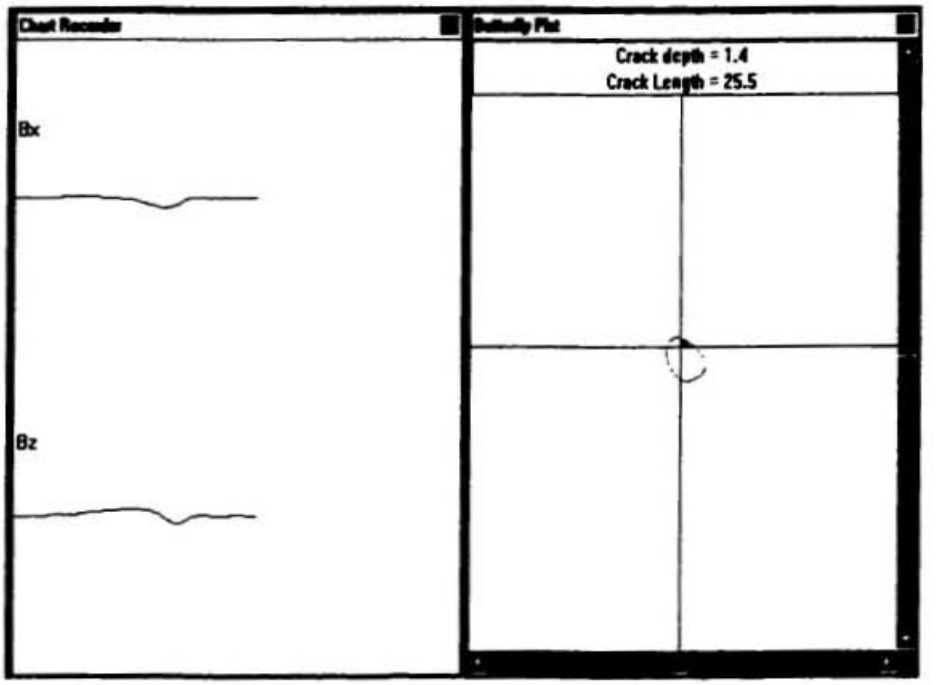

D30T34.wdf – Scanning IV

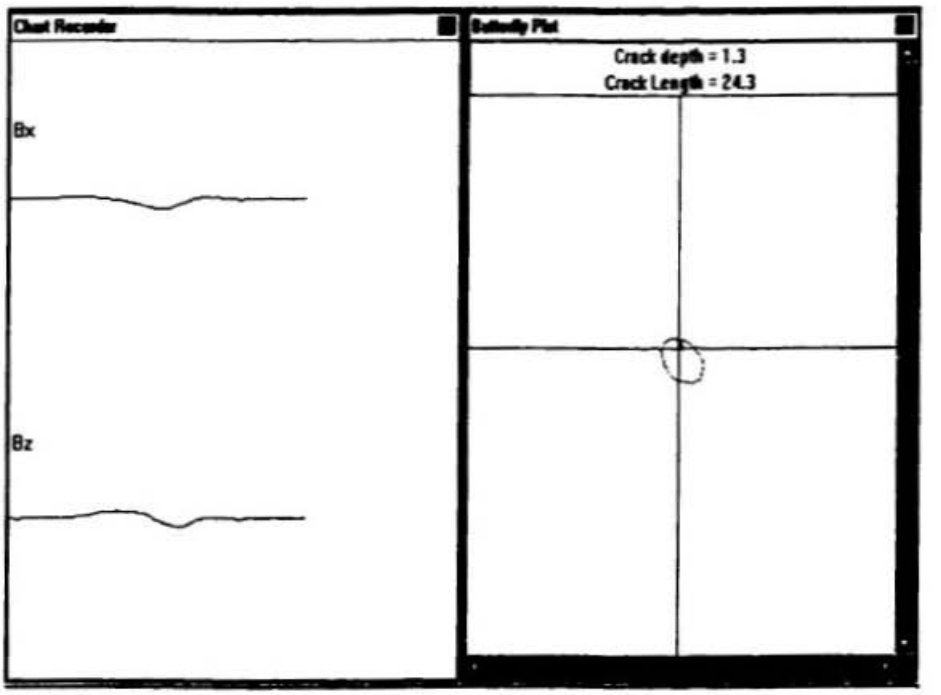

D30T34.wdf – Scanning V

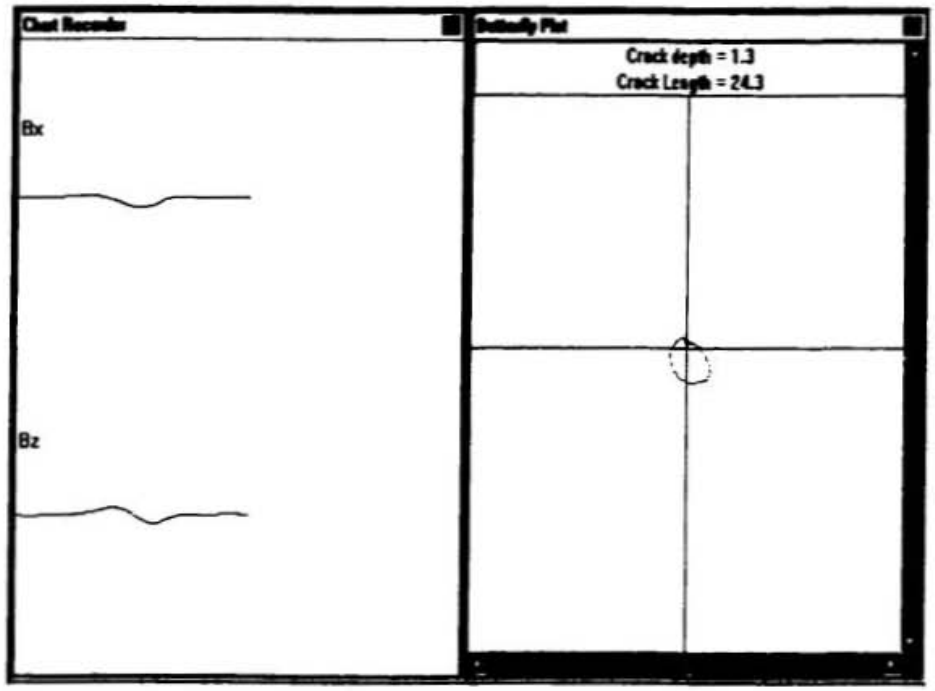

Table A.7. Summary table of scanning data from file **D10T34.wdf**

D10T34.wdf			
Actual Depth	**Signal Ratio**	**Actual Length**	**B_z Length**
1.0	0.01076555	35	14
1.0	0.010613208	35	15
1.0	0.006402794	35	15
1.0	0.00990099	35	15
1.0	0.010638298	35	15
Average	**0.009664168**	**35**	**14.8**

Table A.8. Summary table of scanning data from file **D15T34.wdf**

D15T34.wdf			
Actual Depth	**Signal Ratio**	**Actual Length**	**B_z Length**
1.5	0.014723204	42	18
1.5	0.012987013	42	21
1.5	0.011806375	42	22
1.5	0.015285126	42	19
1.5	0.01177163	42	19
Average	**0.01331467**	**42**	**19.8**

Table A.9. Summary table of scanning data from file **D20T34.wdf**

D20T34.wdf			
Actual Depth	**Signal Ratio**	**Actual Length**	**B_z Length**
2.0	0.023640662	46	24
2.0	0.021841795	46	24
2.0	0.023159145	46	23
2.0	0.021339656	46	24
2.0	0.021945433	46	24
Average	0.022385338	46	23.8

Table A.10. Summary table of scanning data from file **D25T34.wdf**

D25T34.wdf			
Actual Depth	**Signal Ratio**	**Actual Length**	**B_z Length**
2.5	0.031363088	47	22
2.5	0.031137725	47	20
2.5	0.029097387	47	23
2.5	0.029655991	47	23
2.5	0.03021327	47	22
Average	0.030293492	47	22

Table A.11. Summary table of scanning data from file **D28T34.wdf**

D28T34.wdf			
Actual Depth	**Signal Ratio**	**Actual Length**	**B_z Length**
2.8	0.041841004	48	22
2.8	0.04074296	48	22
2.8	0.040143799	48	22
2.8	0.04	48	23
2.8	0.042413381	48	22
Average	**0.041028229**	**48**	**22.2**

Table A.12. Summary table of scanning data from file **D30T34.wdf**

D30T34.wdf			
Actual Depth	**Signal Ratio**	**Actual Length**	**B_z Length**
3.0	0.05	51	24
3.0	0.046044864	51	20
3.0	0.049199763	51	22
3.0	0.045508274	51	21
3.0	0.046745562	51	21
Average	**0.047499693**	**51**	**21.6**

Appendix B

ACFM Scans for the Defects Located in the Inner Surface of the Base Metal of 3.8 mm Pipe Wall Thickness

Table B.1. Scanning data from file **D10T38.wdf**

Data from Scanning I			
Pipe wall thickness	: 3.8 mm	Minimum B_x reading	: 1707
Defect depth	: 1.0 mm	Actual length	: 36 mm
Background B_x reading	: 1717	B_z length	: 17 mm
Data from Scanning II			
Pipe wall thickness	: 3.8 mm	Minimum B_x reading	: 1699
Defect depth	: 1.0 mm	Actual length	: 36 mm
Background B_x reading	: 1714	B_z length	: 14 mm
Data from Scanning III			
Pipe wall thickness	: 3.8 mm	Minimum B_x reading	: 1715
Defect depth	: 1.0 mm	Actual length	: 36 mm
Background B_x reading	: 1729	B_z length	: 17 mm
Data from Scanning IV			
Pipe wall thickness	: 3.8 mm	Minimum B_x reading	: 1704
Defect depth	: 1.0 mm	Actual length	: 36 mm
Background B_x reading	: 1719	B_z length	: 17 mm
Data from Scanning V			
Pipe wall thickness	: 3.8 mm	Minimum B_x reading	: 1711
Defect depth	: 1.0 mm	Actual length	: 36 mm
Background B_x reading	: 1721	B_z length	: 16 mm

D10T38.wdf – Scanning I

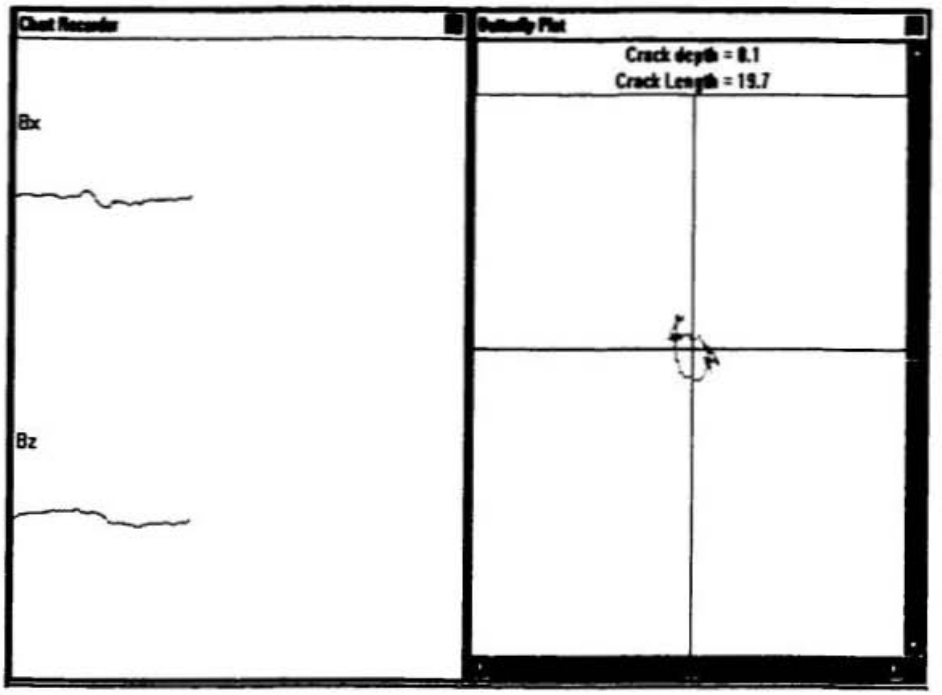

D10T38.wdf – Scanning II

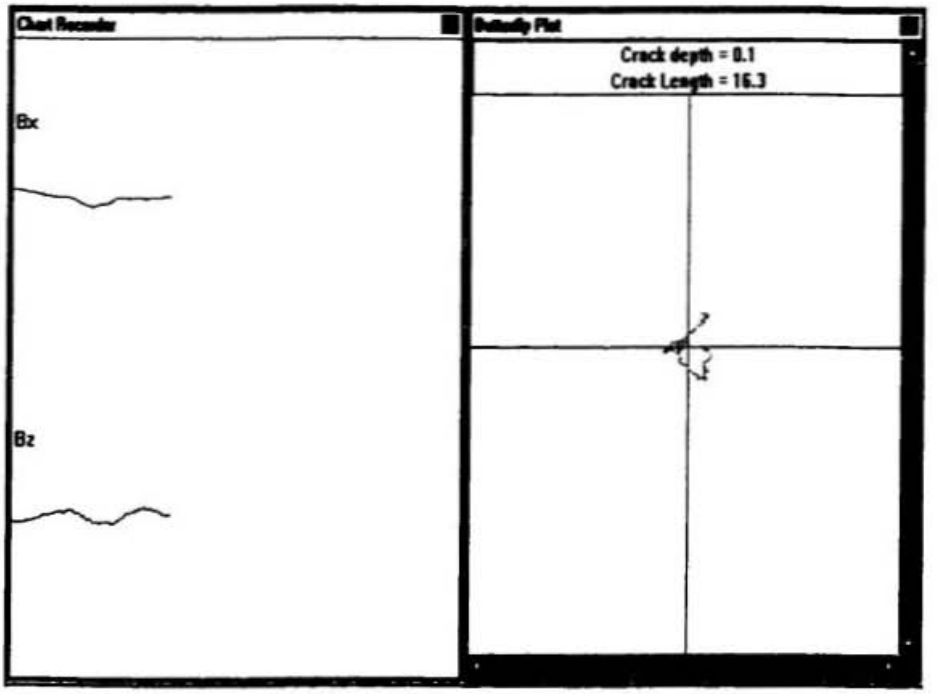

D10T38.wdf – Scanning III

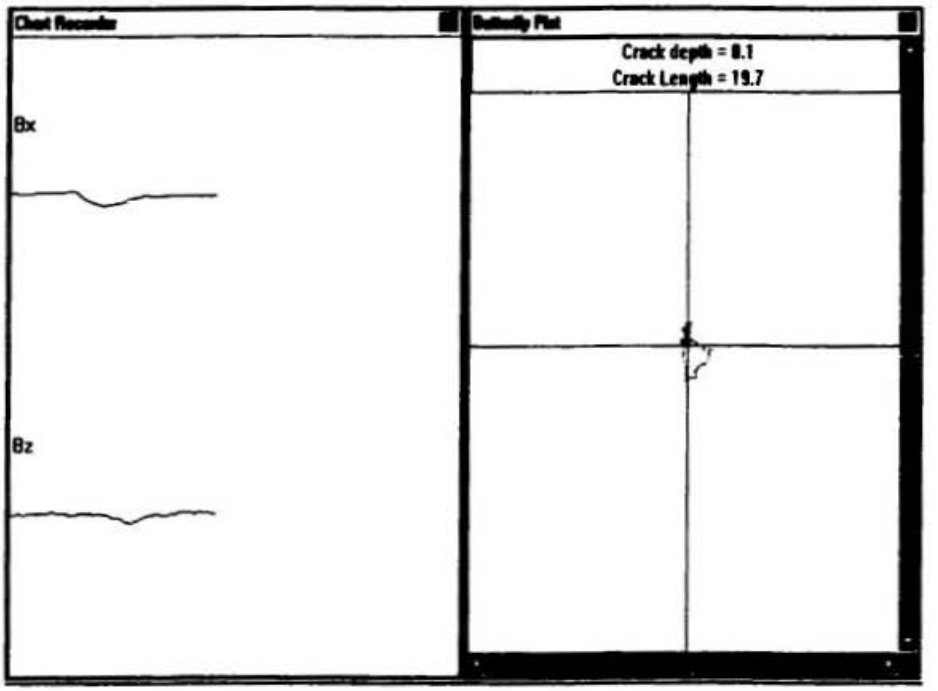

D10T38.wdf – Scanning IV

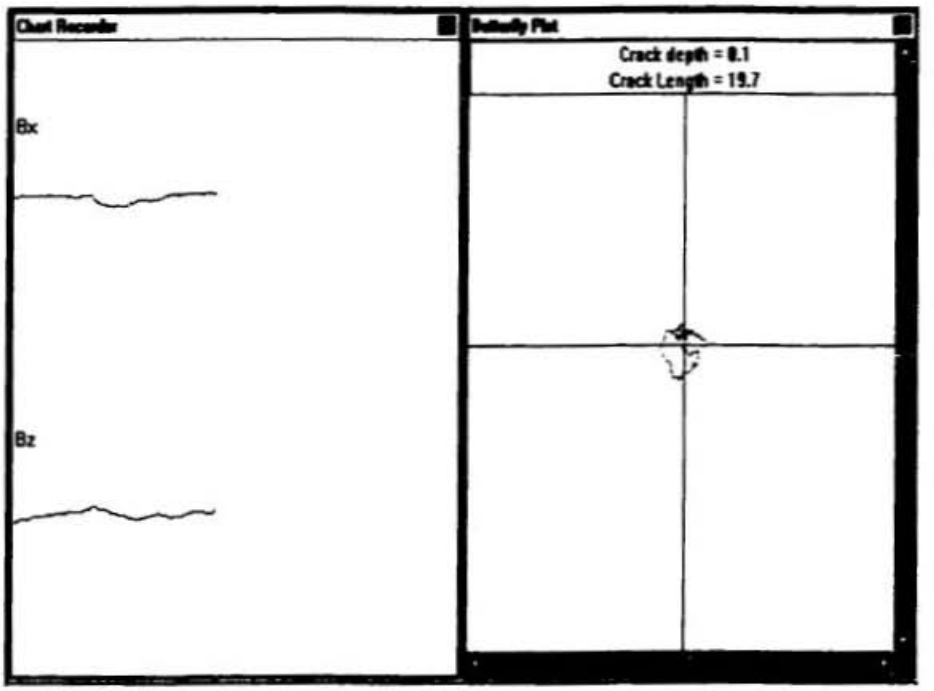

D10T38.wdf – Scanning V

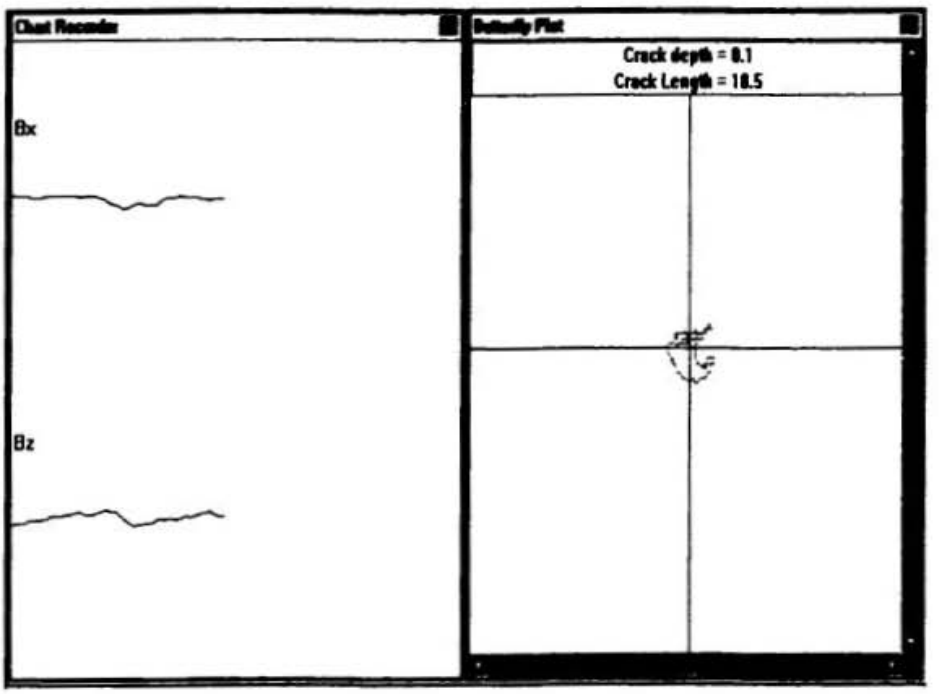

Table B.2. Scanning data from file **2D15T38.wdf**

Data from Scanning I			
Pipe wall thickness	: 3.8 mm	Minimum B_x reading	: 1699
Defect depth	: 1.5 mm	Actual length	: 38 mm
Background B_x reading	: 1712	B_z length	: 17 mm
Data from Scanning II			
Pipe wall thickness	: 3.8 mm	Minimum B_x reading	: 1676
Defect depth	: 1.5 mm	Actual length	: 38 mm
Background B_x reading	: 1689	B_z length	: 16 mm
Data from Scanning III			
Pipe wall thickness	: 3.8 mm	Minimum B_x reading	: 1720
Defect depth	: 1.5 mm	Actual length	: 38 mm
Background B_x reading	: 1733	B_z length	: 16 mm
Data from Scanning IV			
Pipe wall thickness	: 3.8 mm	Minimum B_x reading	: 1675
Defect depth	: 1.5 mm	Actual length	: 38 mm
Background B_x reading	: 1686	B_z length	: 17 mm
Data from Scanning V			
Pipe wall thickness	: 3.8 mm	Minimum B_x reading	: 1698
Defect depth	: 1.5 mm	Actual length	: 38 mm
Background B_x reading	: 1711	B_z length	: 18 mm

2D15T38.wdf – Scanning I

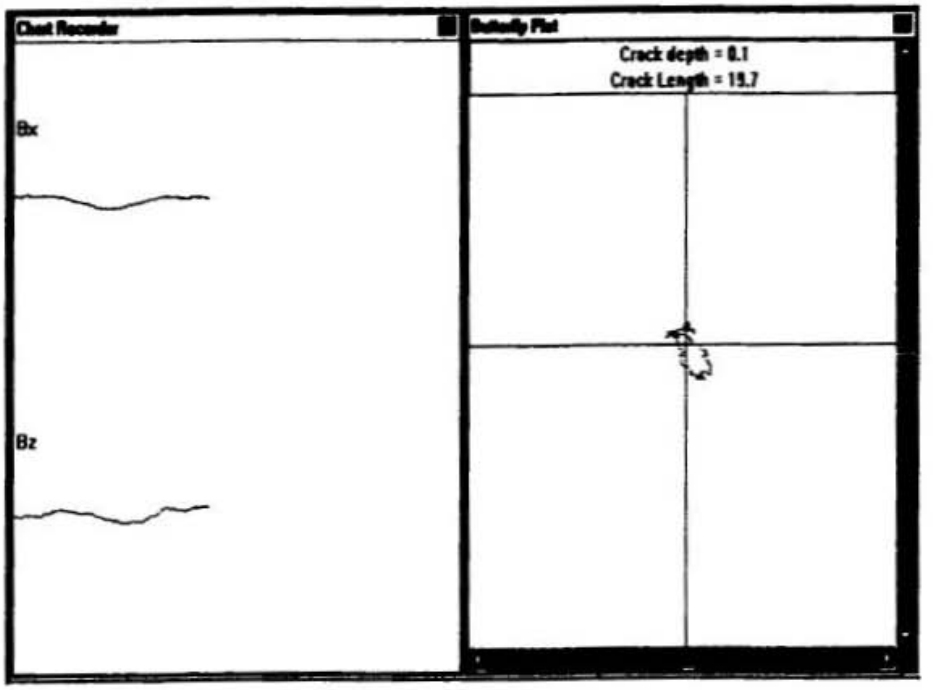

2D15T38.wdf – Scanning II

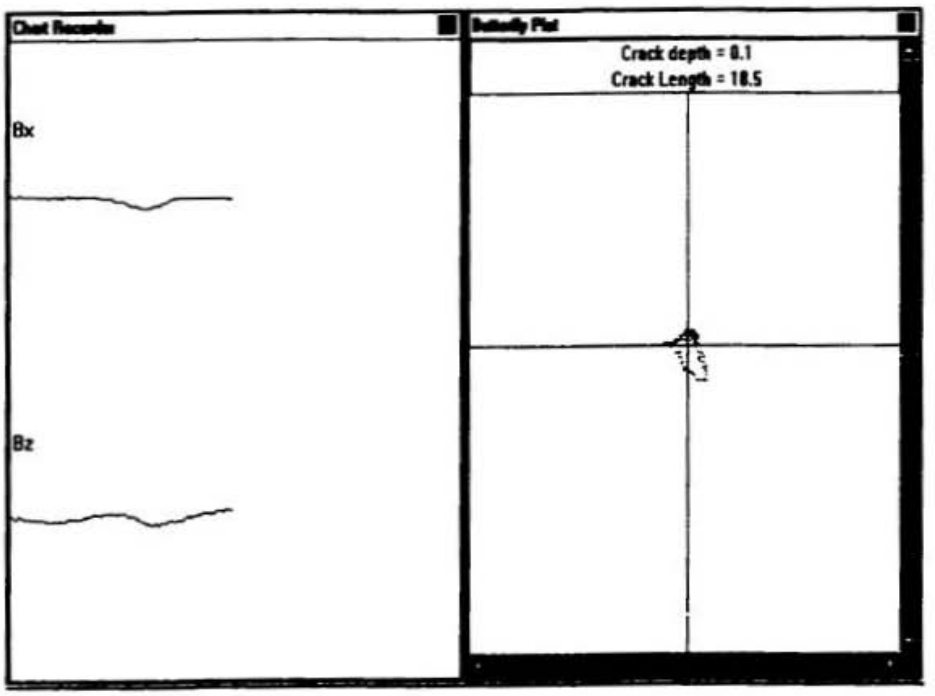

2D15T38.wdf – Scanning III

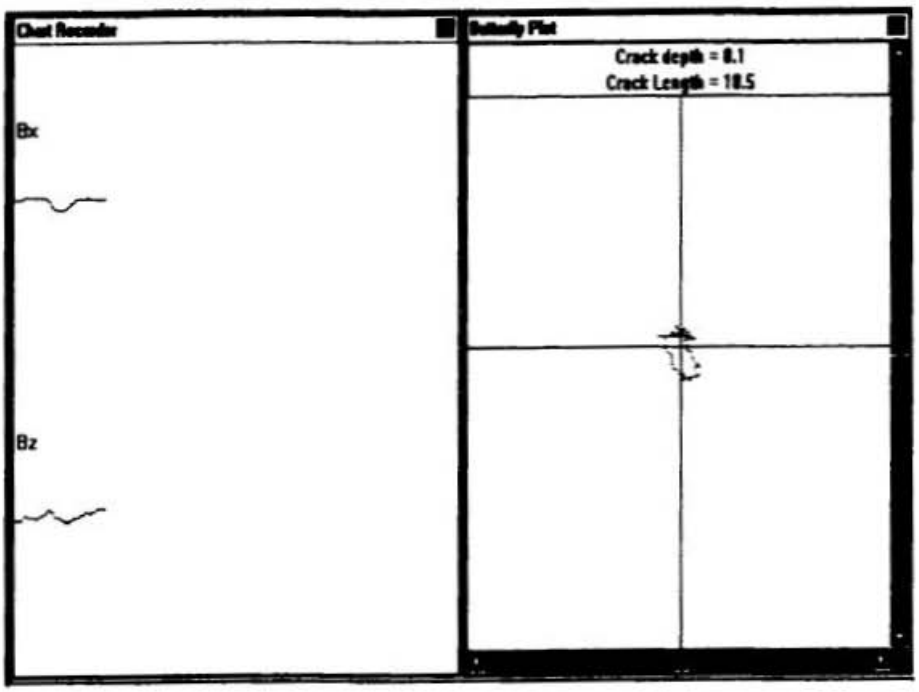

2D15T38.wdf – Scanning IV

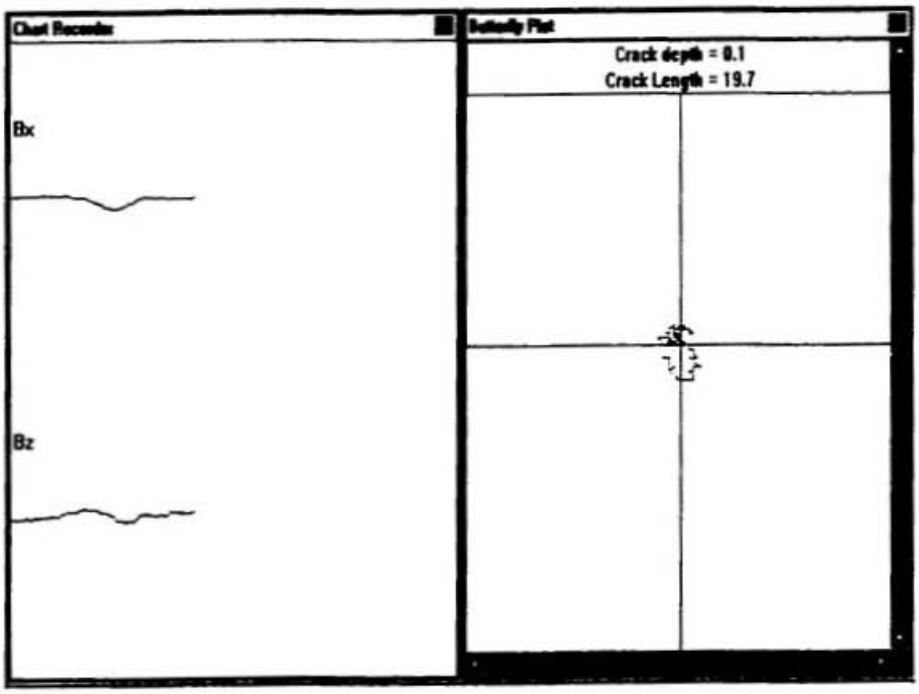

2D15T38.wdf – Scanning V

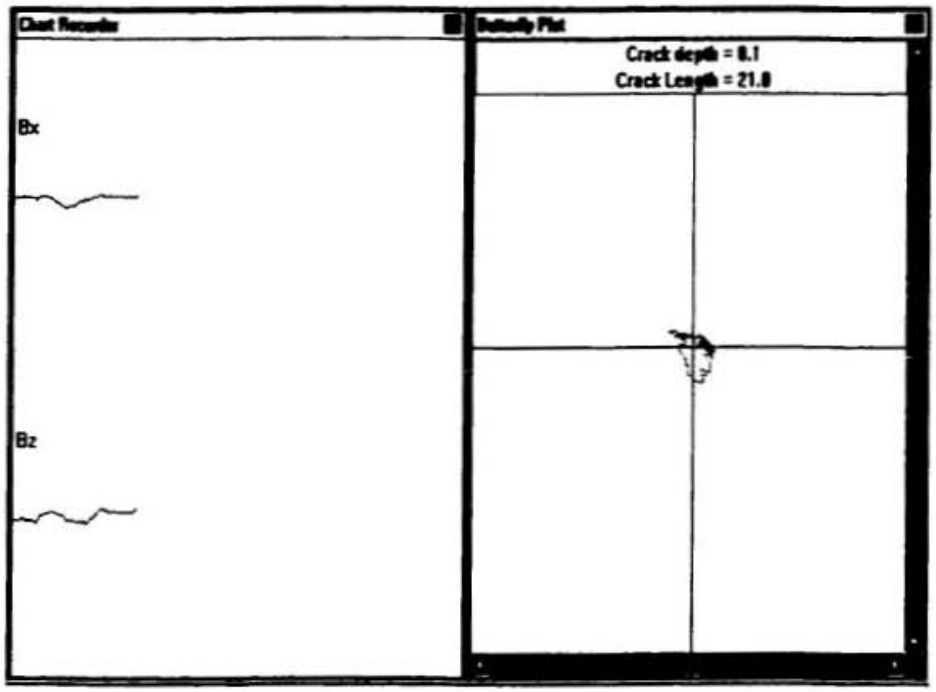

Table B.3. Scanning data from file **D20T38.wdf**

Data from Scanning I			
Pipe wall thickness	: 3.8 mm	Minimum B_x reading	: 1700
Defect depth	: 2.0 mm	Actual length	: 41 mm
Background B_x reading	: 1721	B_z length	: 17 mm
Data from Scanning II			
Pipe wall thickness	: 3.8 mm	Minimum B_x reading	: 1649
Defect depth	: 2.0 mm	Actual length	: 41 mm
Background B_x reading	: 1671	B_z length	: 18 mm
Data from Scanning III			
Pipe wall thickness	: 3.8 mm	Minimum B_x reading	: 1691
Defect depth	: 2.0 mm	Actual length	: 41 mm
Background B_x reading	: 1712	B_z length	: 16 mm
Data from Scanning IV			
Pipe wall thickness	: 3.8 mm	Minimum B_x reading	: 1679
Defect depth	: 2.0 mm	Actual length	: 41 mm
Background B_x reading	: 1701	B_z length	: 19 mm
Data from Scanning V			
Pipe wall thickness	: 3.8 mm	Minimum B_x reading	: 1712
Defect depth	: 2.0 mm	Actual length	: 41 mm
Background B_x reading	: 1735	B_z length	: 18 mm

D20T38.wdf – Scanning I

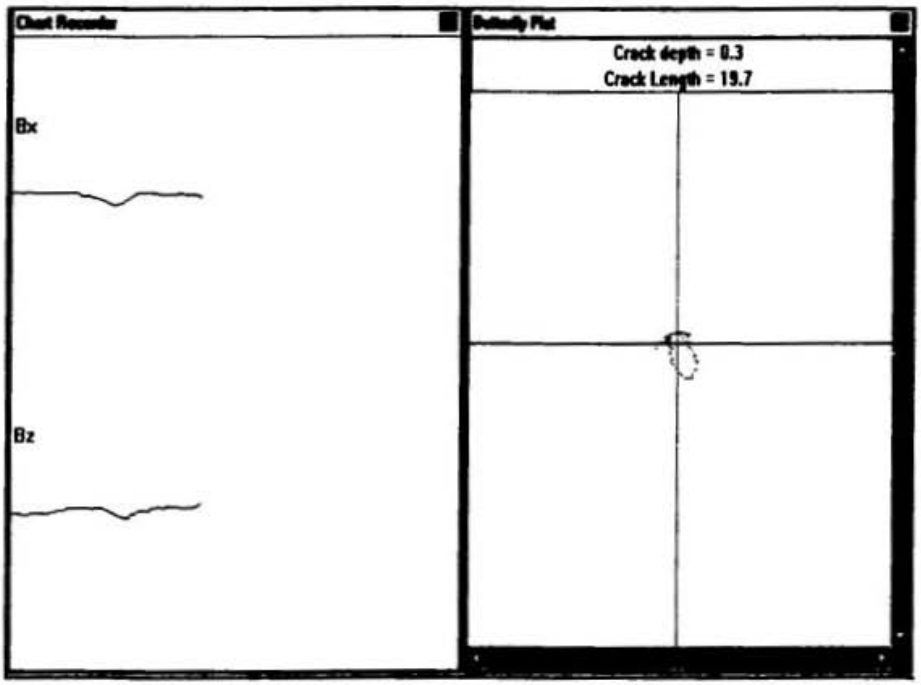

D20T38.wdf – Scanning II

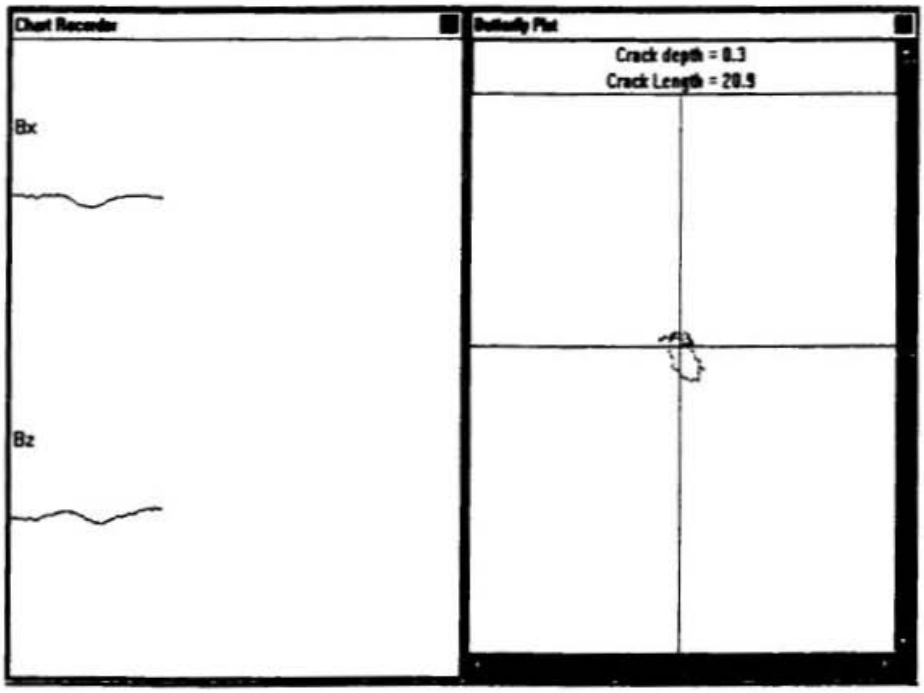

D20T38.wdf – Scanning III

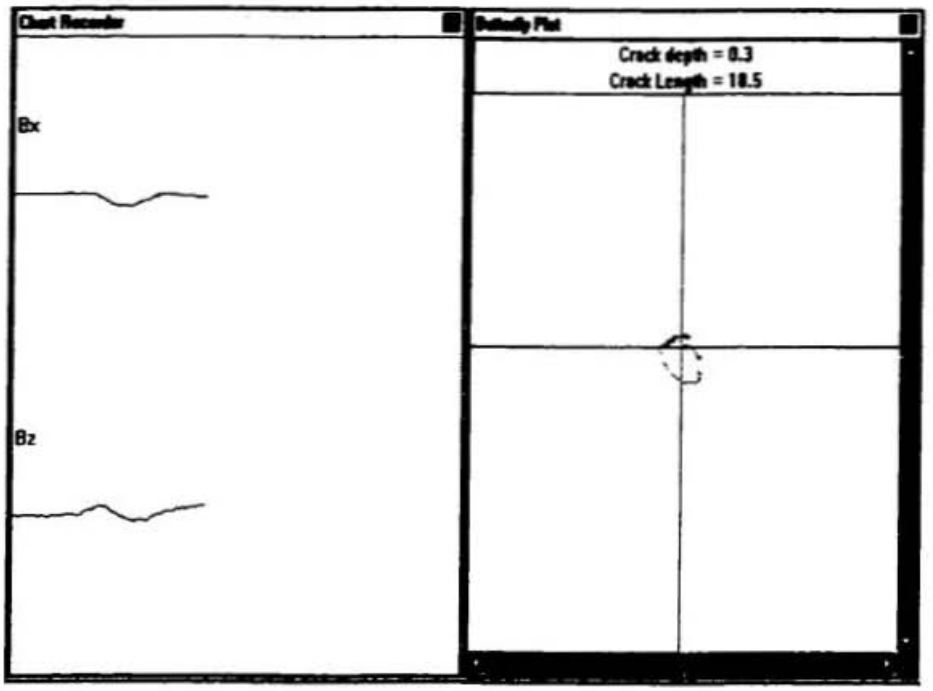

D20T38.wdf – Scanning IV

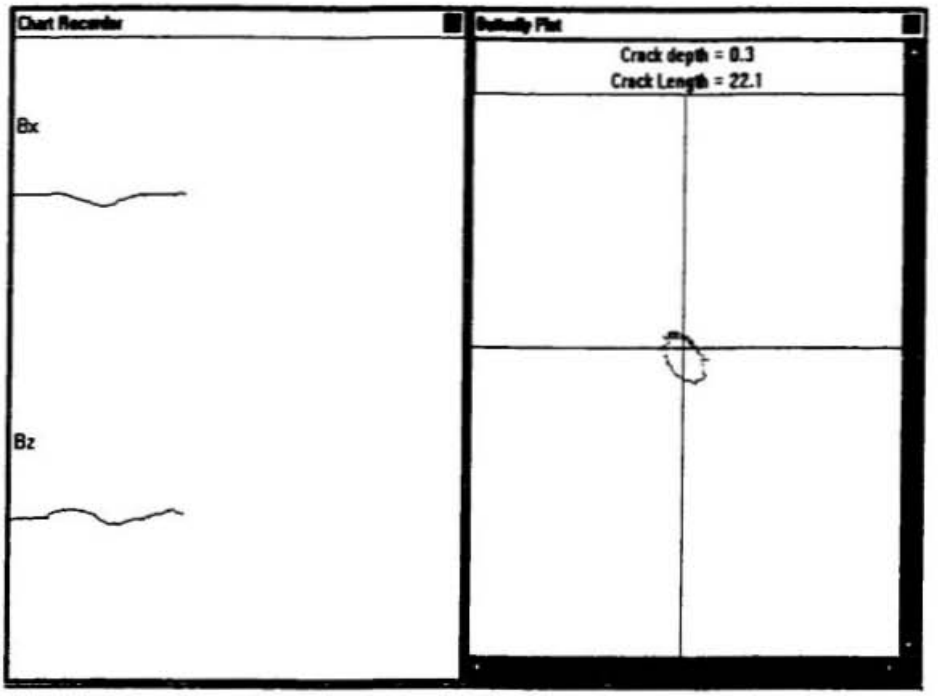

D20T38.wdf – Scanning V

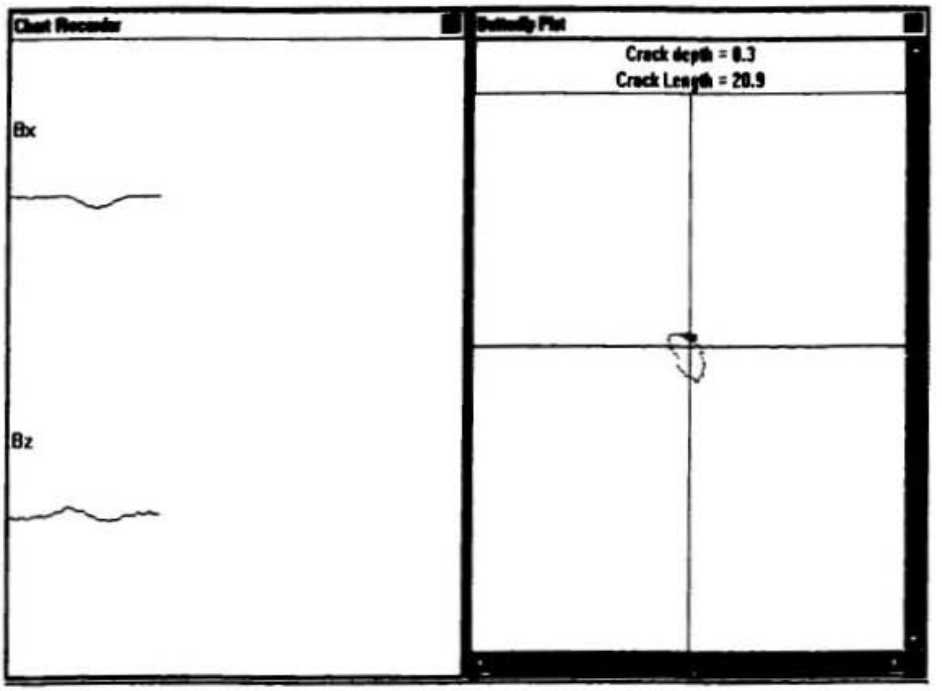

Table B.4. Scanning data from file **2D25T38.wdf**

Data from Scanning I			
Pipe wall thickness	: 3.8 mm	Minimum B_x reading	: 1680
Defect depth	: 2.5 mm	Actual length	: 43 mm
Background B_x reading	: 1717	B_z length	: 17 mm
Data from Scanning II			
Pipe wall thickness	: 3.8 mm	Minimum B_x reading	: 1663
Defect depth	: 2.5 mm	Actual length	: 43 mm
Background B_x reading	: 1706	B_z length	: 18 mm
Data from Scanning III			
Pipe wall thickness	: 3.8 mm	Minimum B_x reading	: 1667
Defect depth	: 2.5 mm	Actual length	: 43 mm
Background B_x reading	: 1709	B_z length	: 17 mm
Data from Scanning IV			
Pipe wall thickness	: 3.8 mm	Minimum B_x Reading	: 1674
Defect depth	: 2.5 mm	Actual length	: 43 mm
Background B_x Reading	: 1711	B_z length	: 20 mm
Data from Scanning V			
Pipe wall thickness	: 3.8 mm	Minimum B_x reading	: 1683
Defect depth	: 2.5 mm	Actual length	: 43 mm
Background B_x reading	: 1718	B_z length	: 19 mm

2D25T38.wdf – Scanning I

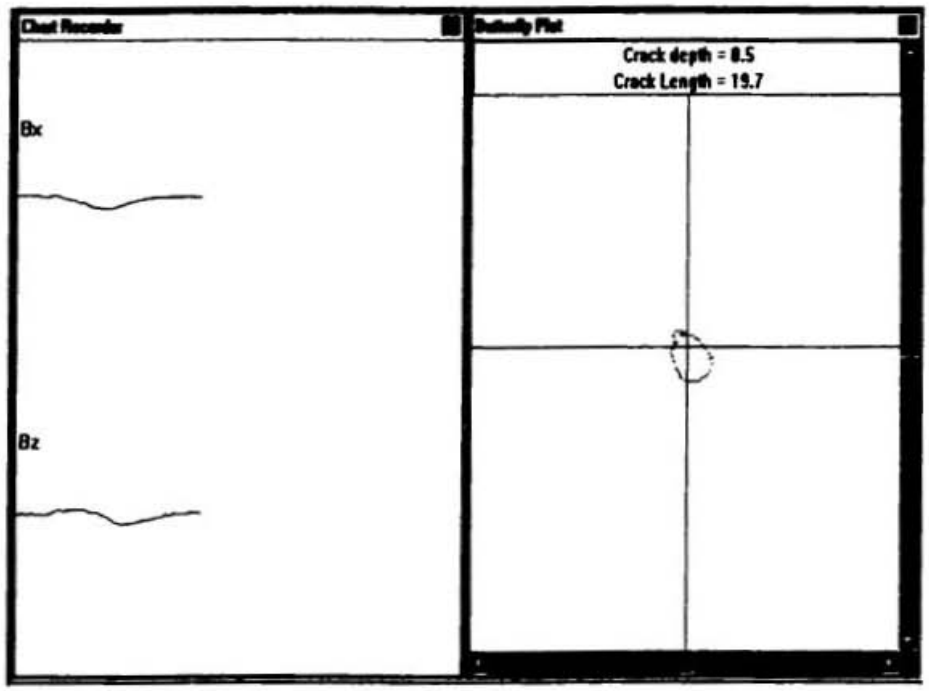

2D25T38.wdf – Scanning II

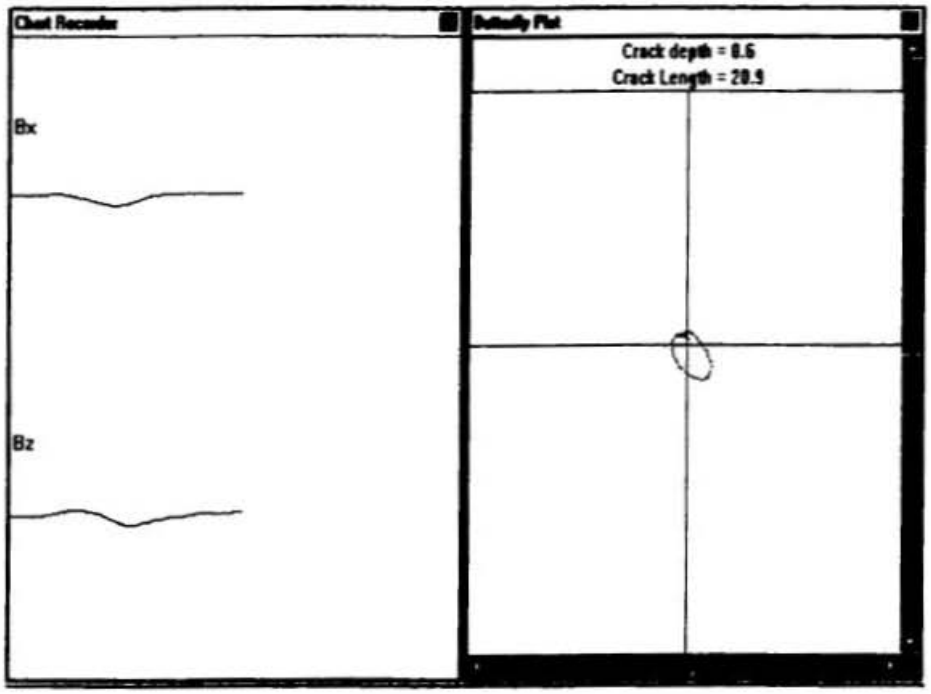

2D25T38.wdf – Scanning III

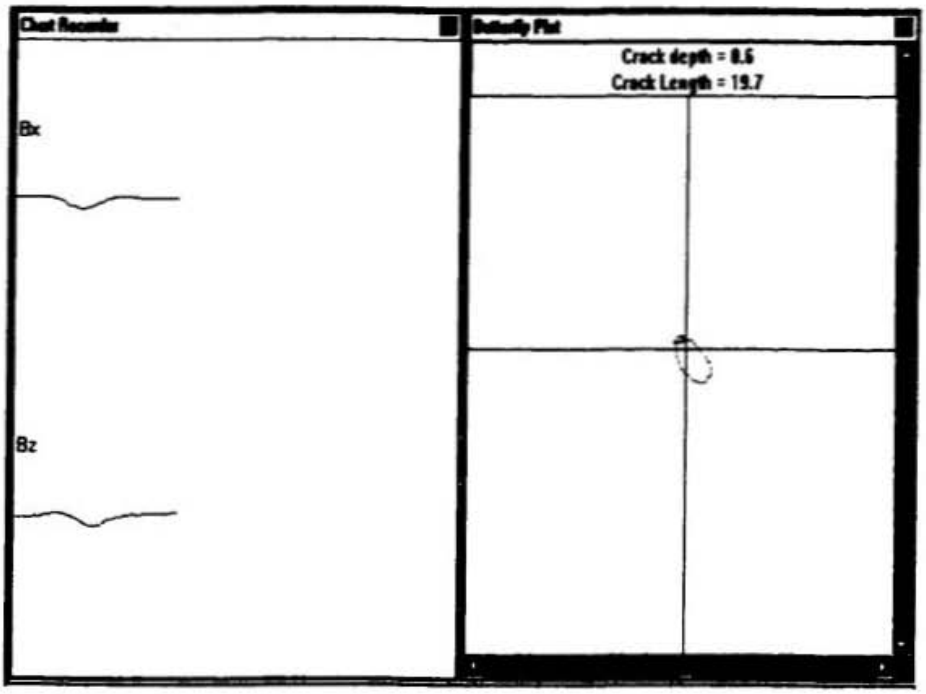

2D25T38.wdf – Scanning IV

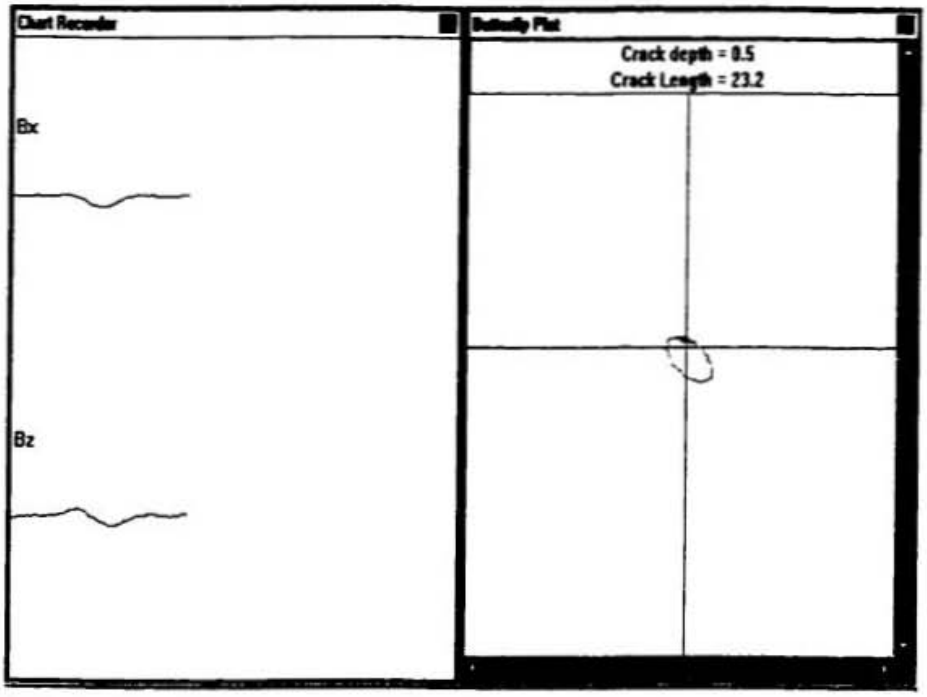

2D25T38.wdf – Scanning V

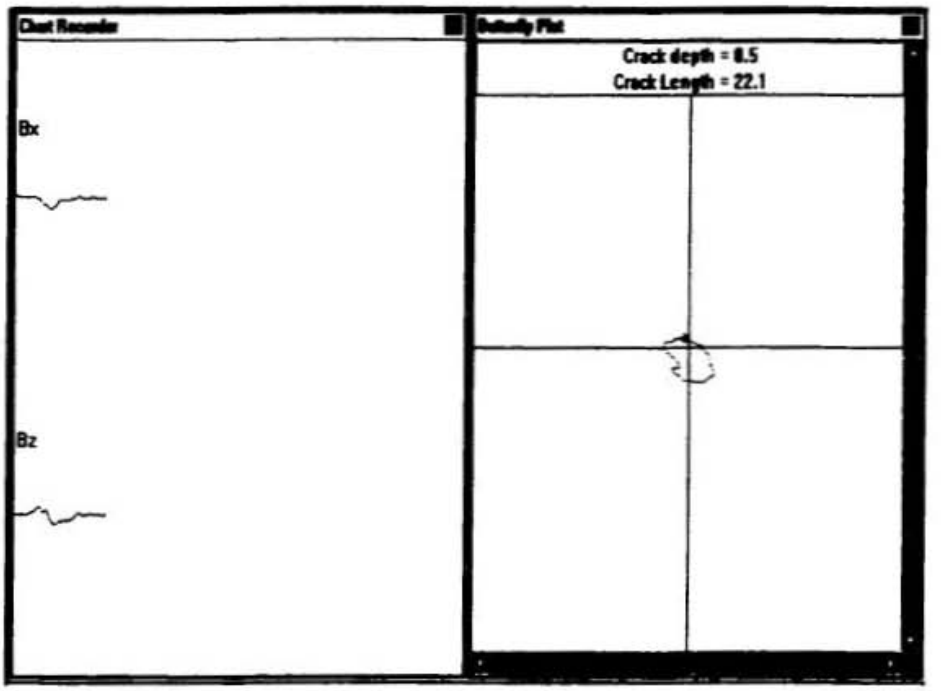

Table B.5. Scanning data from file name **D30T38.wdf**

Data from Scanning I			
Pipe wall thickness	: 3.8 mm	Minimum B_x reading	: 1674
Defect depth	: 3.0 mm	Actual length	: 45 mm
Background B_x reading	: 1731	B_z length	: 22 mm
Data from Scanning II			
Pipe wall thickness	: 3.8 mm	Minimum B_x reading	: 1665
Defect depth	: 3.0 mm	Actual length	: 45 mm
Background B_x reading	: 1719	B_z length	: 18 mm
Data from Scanning III			
Pipe wall thickness	: 3.8 mm	Minimum B_x reading	: 1700
Defect depth	: 3.0 mm	Actual length	: 45 mm
Background B_x reading	: 1761	B_z length	: 21 mm
Data from Scanning IV			
Pipe wall thickness	: 3.8 mm	Minimum B_x reading	: 1665
Defect depth	: 3.0 mm	Actual length	: 45 mm
Background B_x reading	: 1721	B_z length	: 20 mm
Data from Scanning V			
Pipe wall thickness	: 3.8 mm	Minimum B_x reading	: 1668
Defect depth	: 3.0 mm	Actual length	: 45 mm
Background B_x reading	: 1722	B_z length	: 21 mm

D30T38.wdf – Scanning I

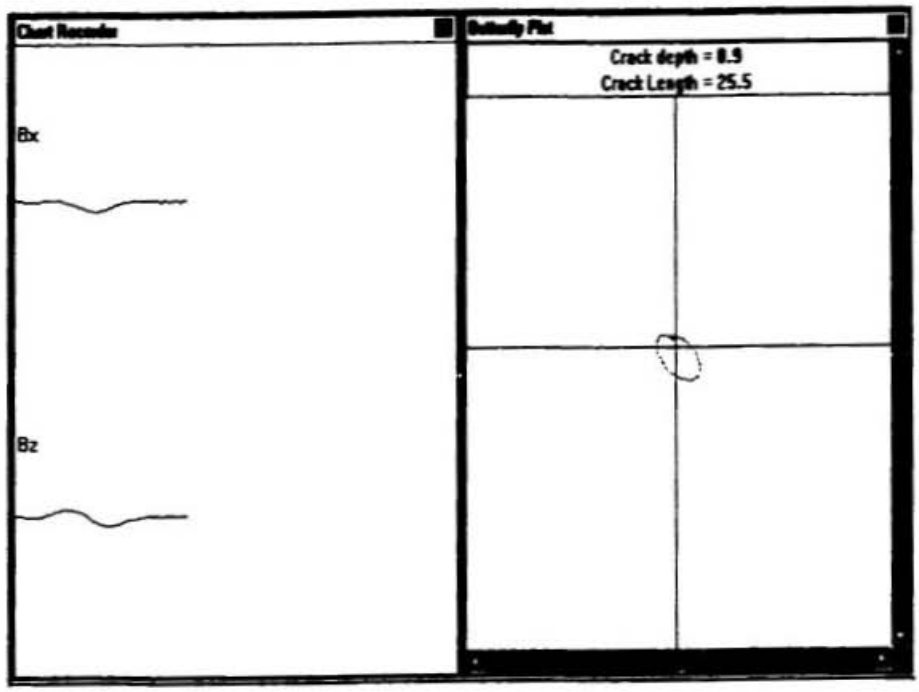

D30T38.wdf – Scanning II

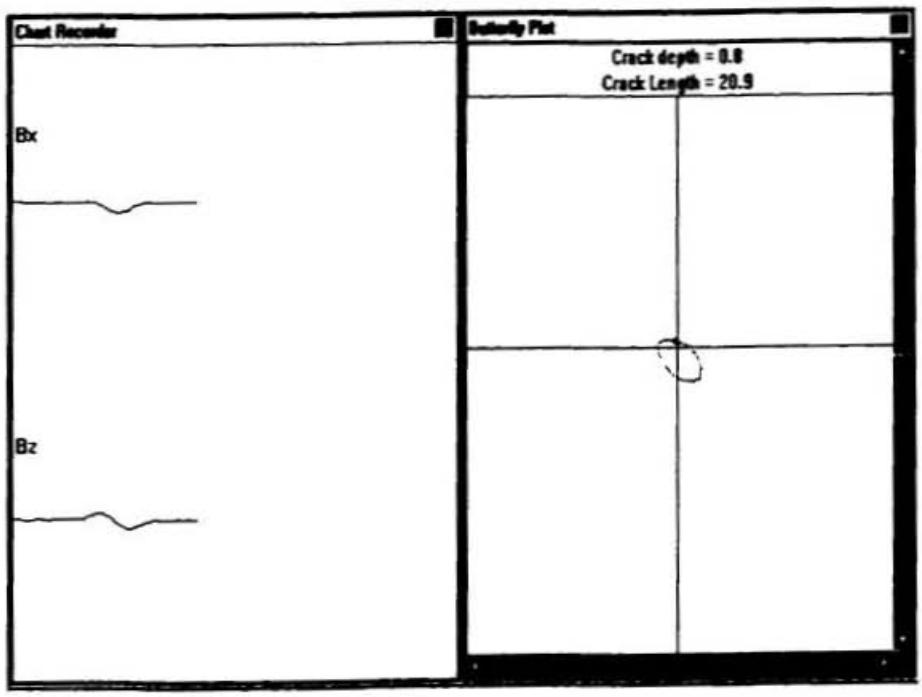

D30T38.wdf – Scanning III

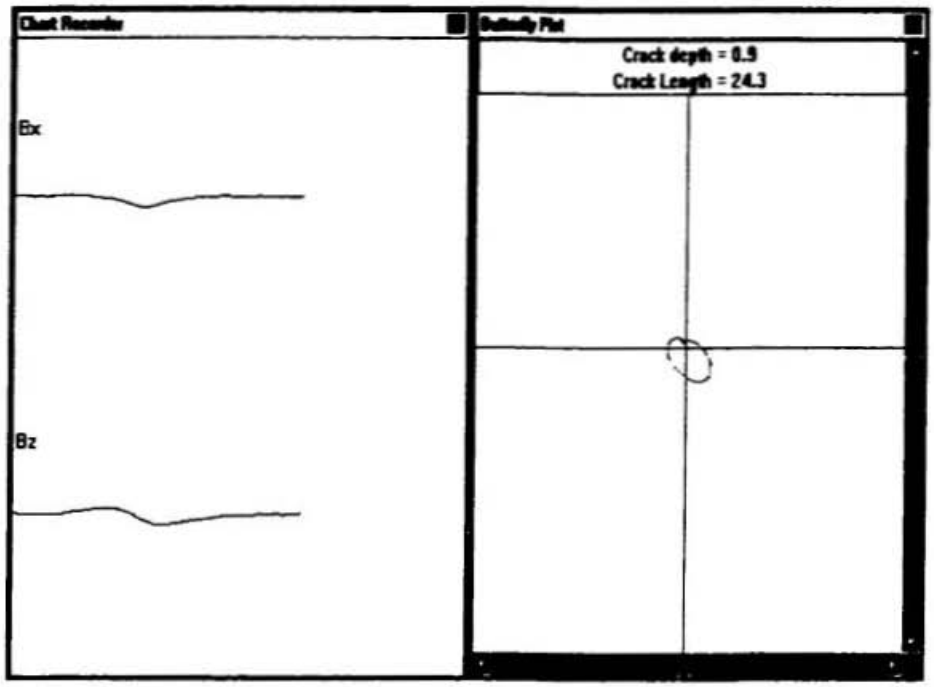

D30T38.wdf – Scanning IV

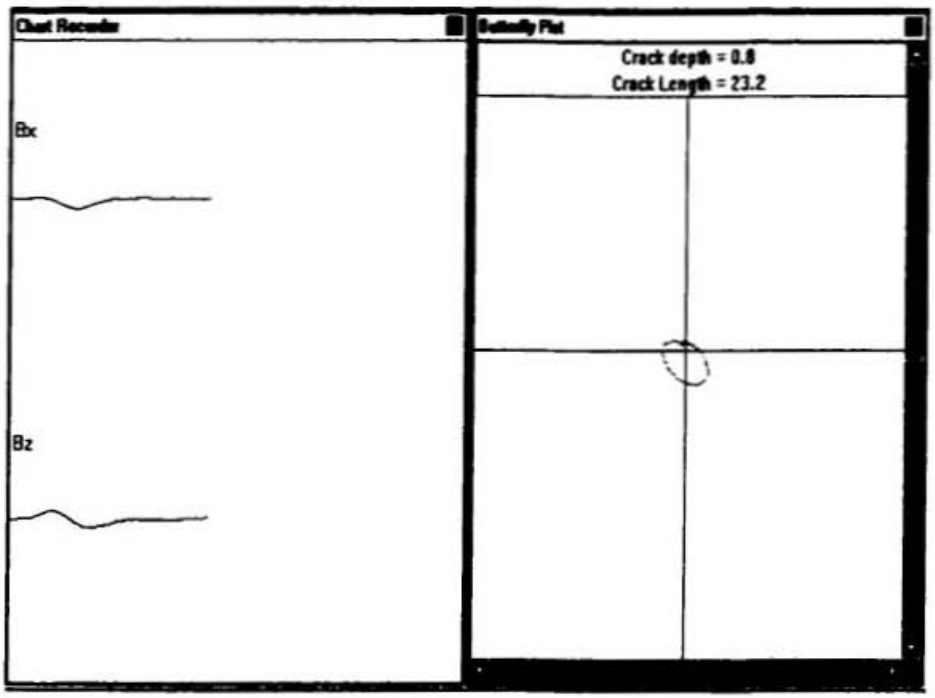

D30T38.wdf – Scanning V

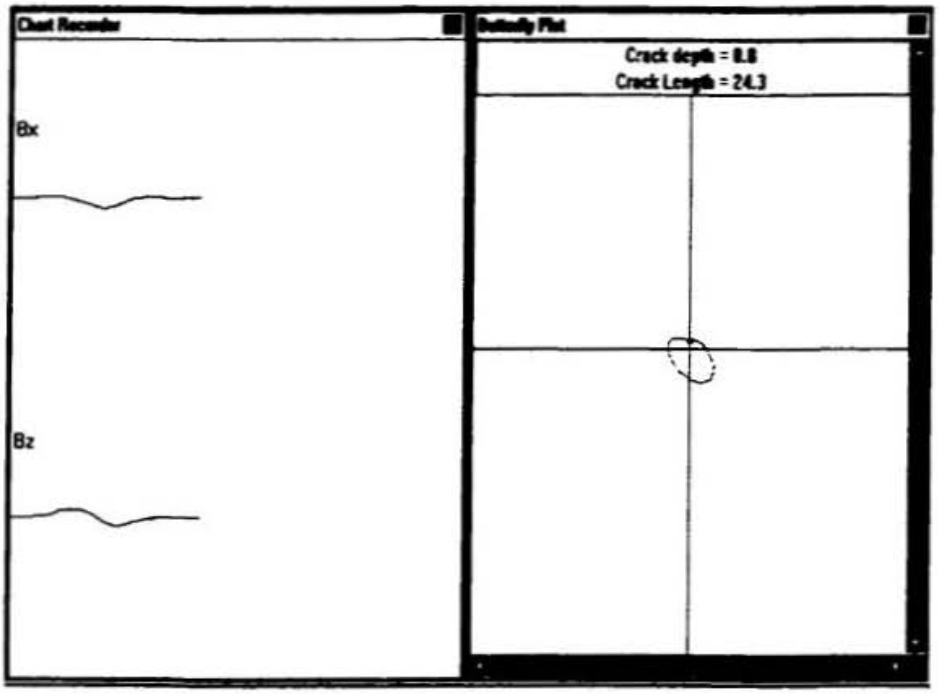

Table B.6. Scanning data from file **D35T38.wdf**

Data from Scanning I			
Pipe wall thickness	: 3.8 mm	Minimum B_x reading	: 1592
Defect depth	: 3.5 mm	Actual length	: 48 mm
Background B_x reading	: 1727	B_z length	: 22 mm
Data from Scanning II			
Pipe wall thickness	: 3.8 mm	Minimum B_x reading	: 1578
Defect depth	: 3.5 mm	Actual length	: 48 mm
Background B_x reading	: 1720	B_z length	: 22 mm
Data from Scanning III			
Pipe wall thickness	: 3.8 mm	Minimum B_x reading	: 1585
Defect depth	: 3.5 mm	Actual length	: 48 mm
Background B_x reading	: 1725	B_z length	: 20 mm
Data from Scanning IV			
Pipe wall thickness	: 3.8 mm	Minimum B_x reading	: 1581
Defect depth	: 3.5 mm	Actual length	: 48 mm
Background B_x reading	: 1725	B_z length	: 20 mm
Data from Scanning V			
Pipe wall thickness	: 3.8 mm	Minimum B_x reading	: 1577
Defect depth	: 3.5 mm	Actual length	: 48 mm
Background B_x reading	: 1723	B_z length	: 22 mm

D35T38.wdf – Scanning I

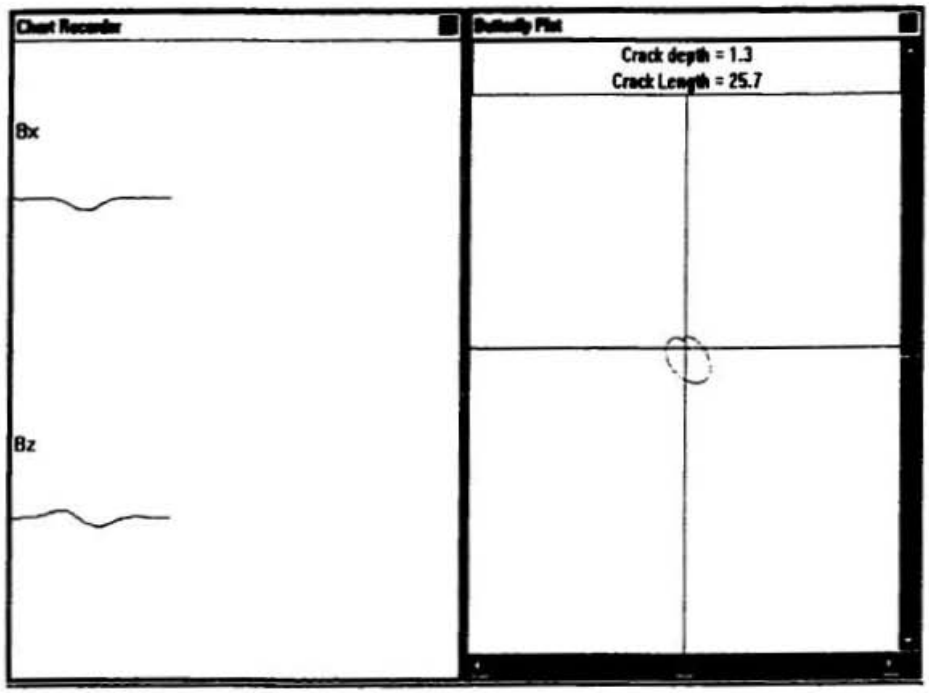

D35T38.wdf – Scanning II

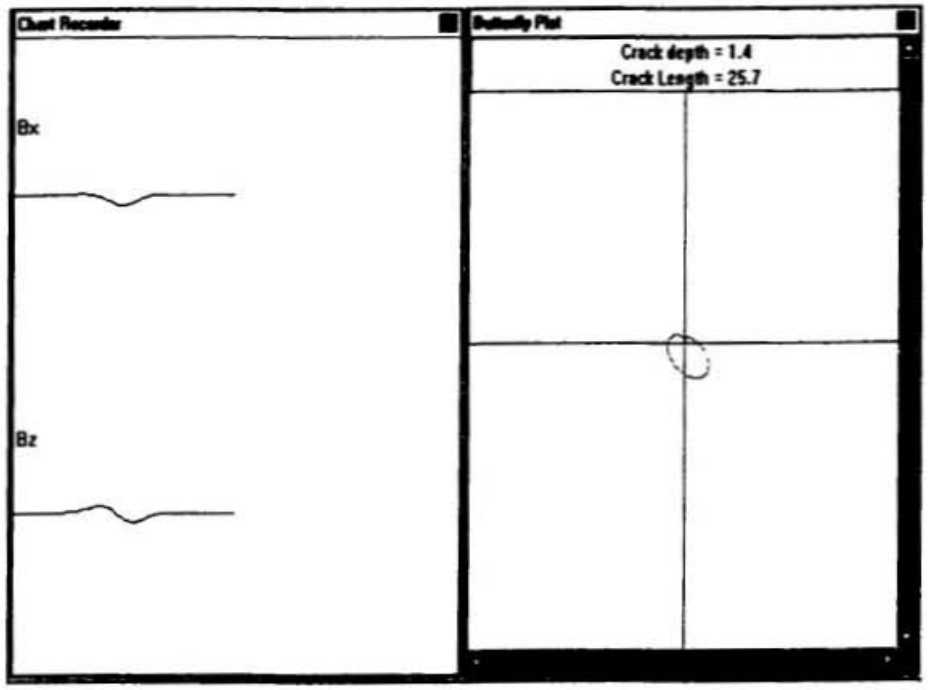

D35T38.wdf – Scanning III

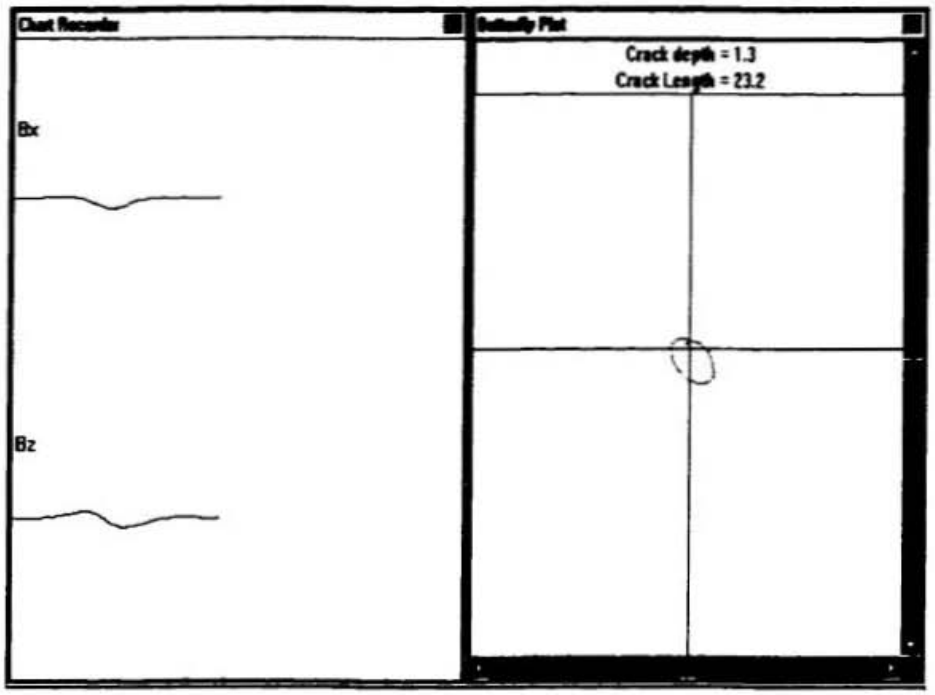

D35T38.wdf – Scanning IV

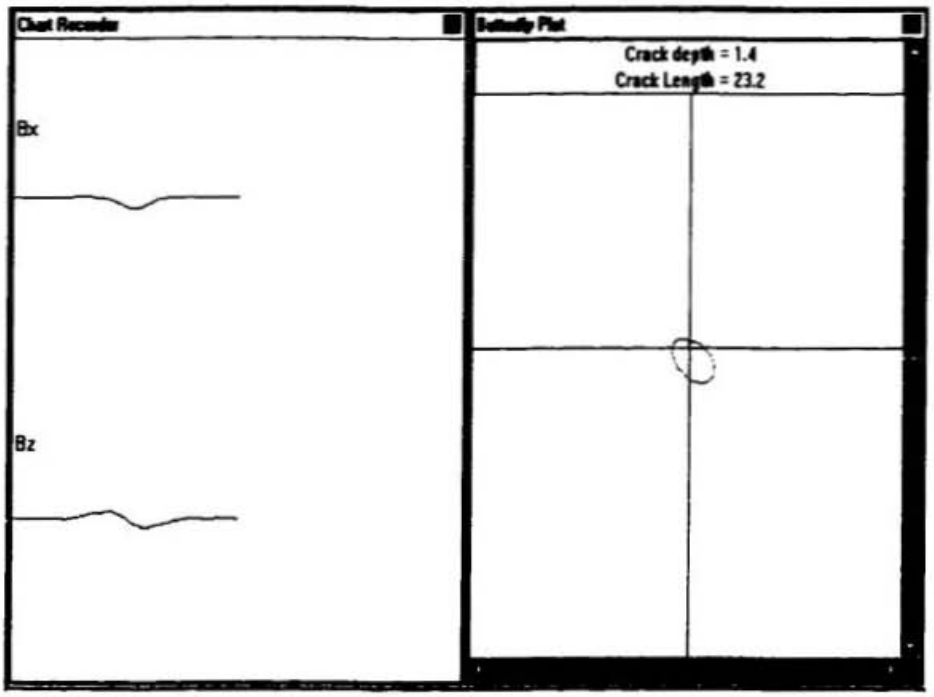

D35T38.wdf – Scanning V

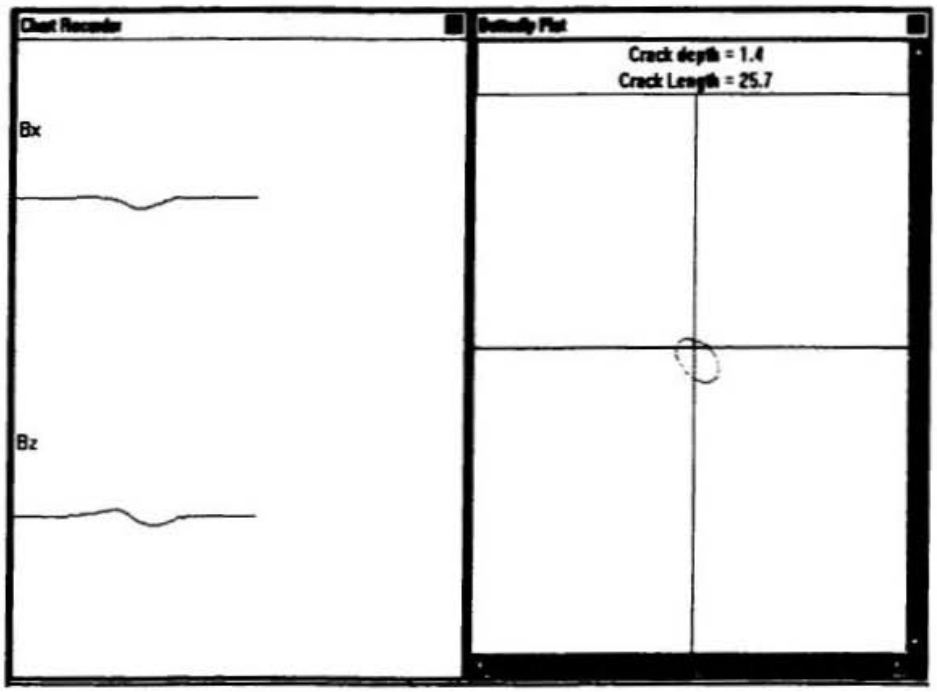

Table B.7. Summary table of scanning data from file **D10T38.wdf**

D10T38.wdf			
Actual Depth	**Signal Ratio**	**Actual Length**	**B_z Length**
1.0	0.005824112	36	17
1.0	0.008751459	36	14
1.0	0.008097166	36	17
1.0	0.008726003	36	17
1.0	0.005810575	36	16
Average	**0.007441863**	**36**	**16.2**

Table B.8. Summary table of scanning data from file **2D15T38.wdf**

2D15T38.wdf			
Actual Depth	**Signal Ratio**	**Actual Length**	**B_z Length**
1.5	0.007593458	38	17
1.5	0.007696862	38	16
1.5	0.007501443	38	16
1.5	0.006524318	38	17
1.5	0.007597896	38	18
Average	**0.007382795**	**38**	**16.8**

Table B.9. Summary table of scanning data from file **D20T38.wdf**

D20T38.wdf			
Actual Depth	**Signal Ratio**	**Actual Length**	**B_z Length**
2.0	0.012202208	41	17
2.0	0.013165769	41	18
2.0	0.012266355	41	16
2.0	0.012933568	41	19
2.0	0.013256484	41	18
Average	**0.012764877**	**41**	**17.6**

Table B.10. Summary table of scanning data from file **2D25T38.wdf**

2D25T38.wdf			
Actual Depth	**Signal Ratio**	**Actual Length**	**B_z Length**
2.5	0.021549214	43	17
2.5	0.025205158	43	18
2.5	0.024575775	43	17
2.5	0.021624781	43	20
2.5	0.020372526	43	19
Average	**0.022665491**	**43**	**17.6**

Table B.11. Summary table of scanning data from file **D30T38.wdf**

D30T38.wdf			
Actual Depth	**Signal Ratio**	**Actual Length**	**B_z Length**
3.0	0.032928943	45	22
3.0	0.031413613	45	18
3.0	0.034639409	45	21
3.0	0.032539221	45	20
3.0	0.031358885	45	21
Average	**0.032576014**	**45**	**20.4**

Table B.12. Summary table of scanning data from file **D35T38.wdf**

D35T38.wdf			
Actual Depth	**Signal Ratio**	**Actual Length**	**B_z Length**
3.5	0.078170237	48	22
3.5	0.08255814	48	22
3.5	0.08115942	48	20
3.5	0.083478261	48	20
3.5	0.084735926	48	22
Average	**0.082020397**	**48**	**21.2**

Appendix C

ACFM Scans for the Defects Located in the Inner Surface of the Heat -affected zone of 3.8 mm Pipe Wall Thickness

Table C.1. Scanning data from file **W10T38.wdf**

Data from Scanning I			
Pipe wall thickness	: 3.8 mm	Minimum B_x Reading	: -
Defect depth	: 1.0 mm	Actual length	: 44 mm
Background B_x reading	: -	B_z length	: -
Data from Scanning II			
Pipe wall thickness	: 3.8 mm	Minimum B_x Reading	: -
Defect depth	: 1.0 mm	Actual length	: 44 mm
Background B_x reading	: -	B_z length	: -
Data from Scanning III			
Pipe wall thickness	: 3.8 mm	Minimum B_x Reading	: -
Defect depth	: 1.0 mm	Actual length	: 44 mm
Background B_x reading	: -	B_z length	: -
Data from Scanning IV			
Pipe wall thickness	: 3.8 mm	Minimum B_x Reading	: -
Defect depth	: 1.0 mm	Actual length	: 44 mm
Background B_x reading	: -	B_z length	: -
Data from Scanning V			
Pipe wall thickness	: 3.8 mm	Minimum B_x Reading	: -
Defect depth	: 1.0 mm	Actual length	: 44 mm
Background B_x reading	: -	B_z length	: -

W10T38.wdf – Scanning I

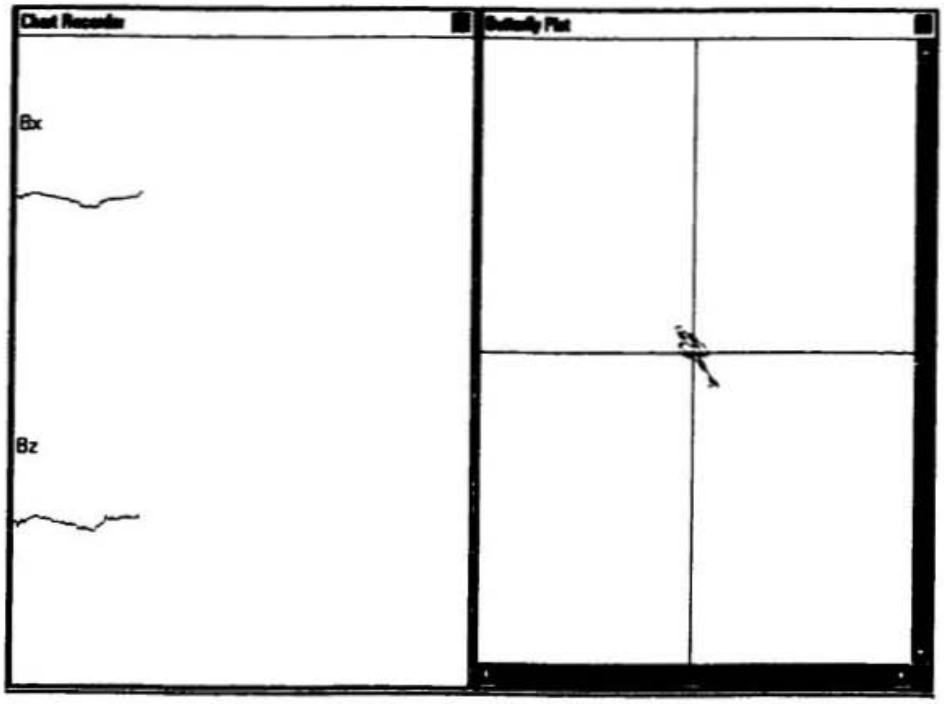

W10T38.wdf – Scanning II

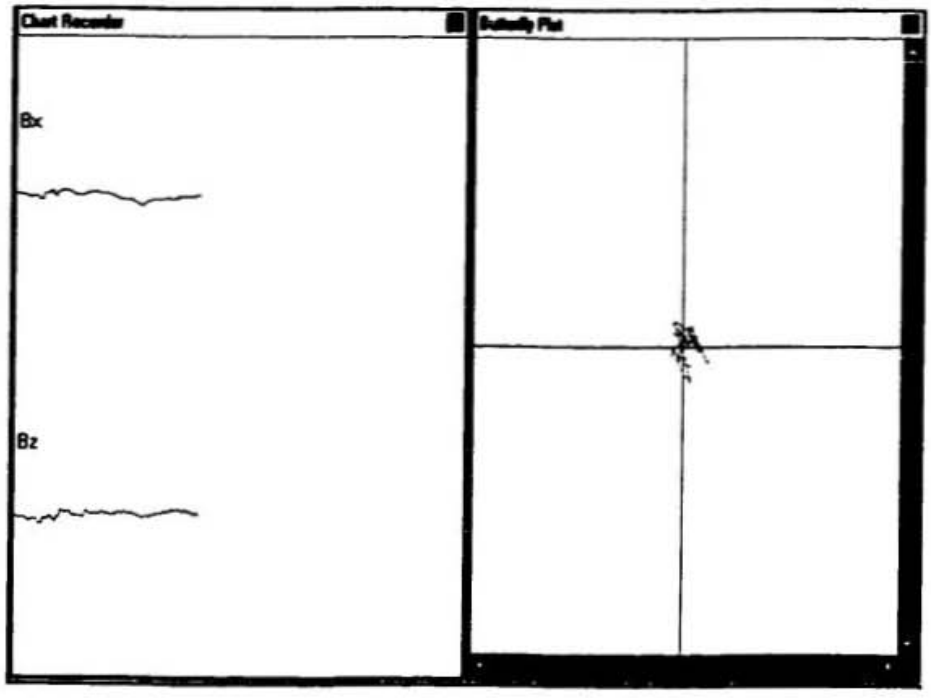

W10T38.wdf – Scanning III

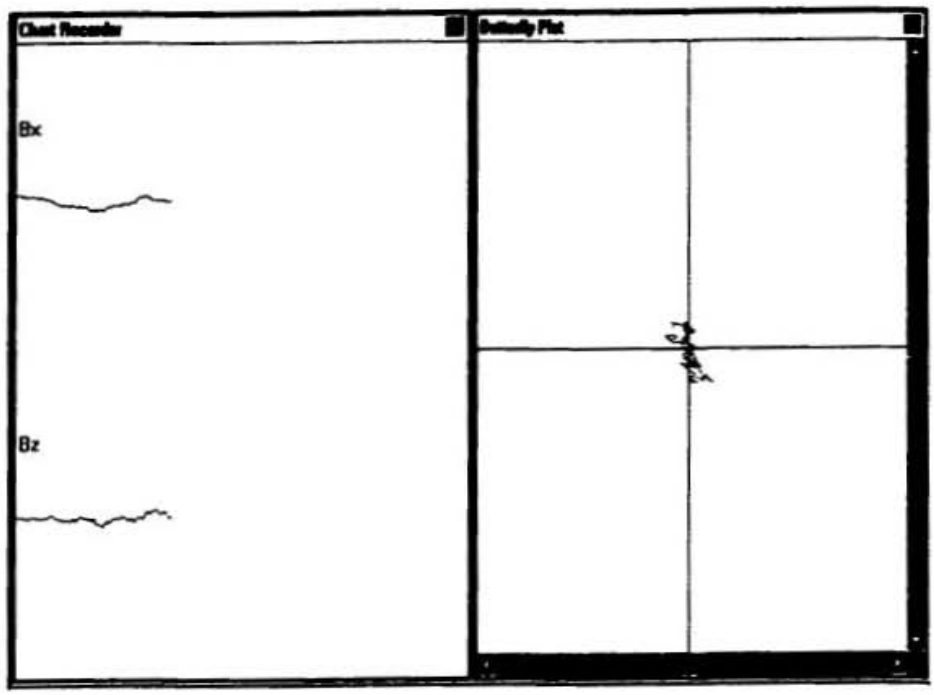

W10T38.wdf – Scanning IV

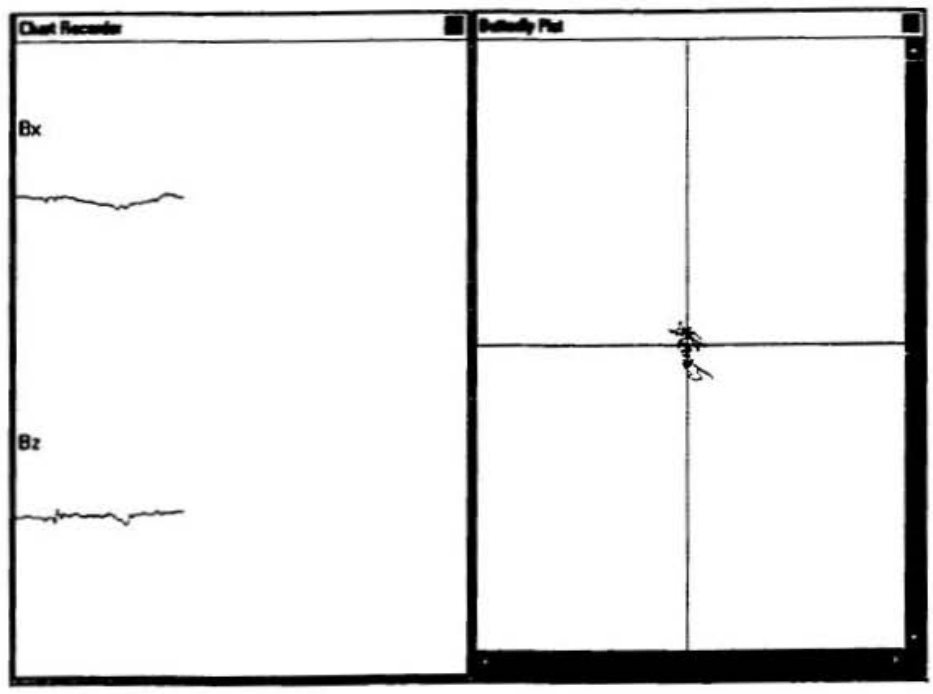

W10T38.wdf – Scanning V

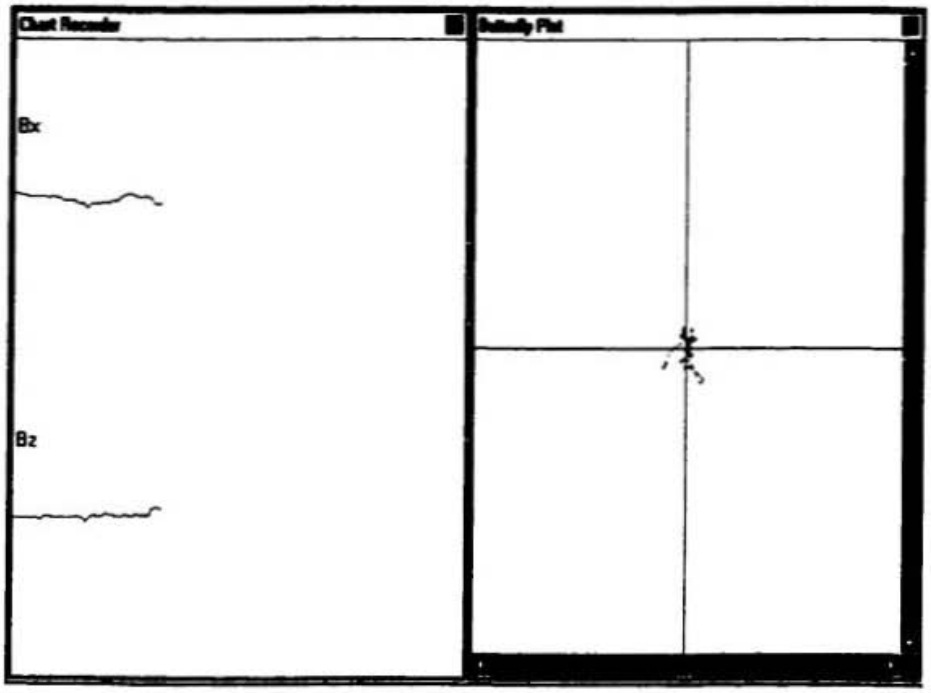

Table C.2. Scanning data from file **W15T38.wdf**

Data from Scanning I			
Pipe wall thickness	: 3.8 mm	Minimum B_x reading	: 1725
Defect depth	: 1.5 mm	Actual length	: 45 mm
Background B_x reading	: 1742	B_z length	: 20 mm
Data from Scanning II			
Pipe wall thickness	: 3.8 mm	Minimum B_x reading	: 1732
Defect depth	: 1.5 mm	Actual length	: 45 mm
Background B_x reading	: 1745	B_z length	: 20 mm
Data from Scanning III			
Pipe wall thickness	: 3.8 mm	Minimum B_x reading	: 1734
Defect depth	: 1.5 mm	Actual length	: 45 mm
Background B_x reading	: 1752	B_z length	: 20 mm
Data from Scanning IV			
Pipe wall thickness	: 3.8 mm	Minimum B_x reading	: 1731
Defect depth	: 1.5 mm	Actual length	: 45 mm
Background B_x reading	: 1744	B_z length	: 21 mm
Data from Scanning V			
Pipe wall thickness	: 3.8 mm	Minimum B_x reading	: 1735
Defect depth	: 1.5 mm	Actual length	: 45 mm
Background B_x reading	: 1750	B_z length	: 21 mm

W15T38.wdf – Scanning I

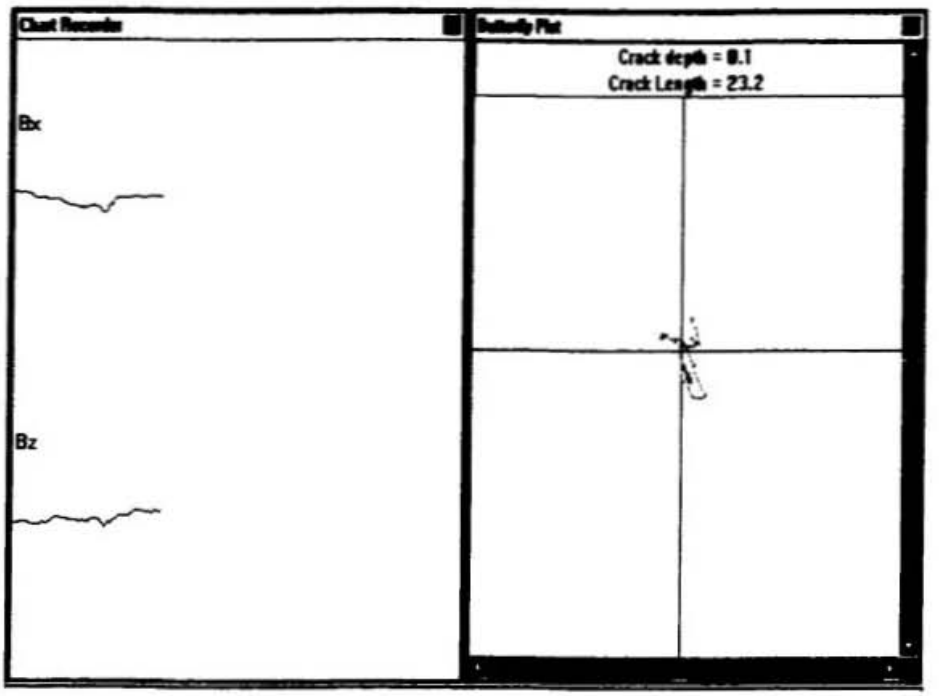

W15T38.wdf – Scanning II

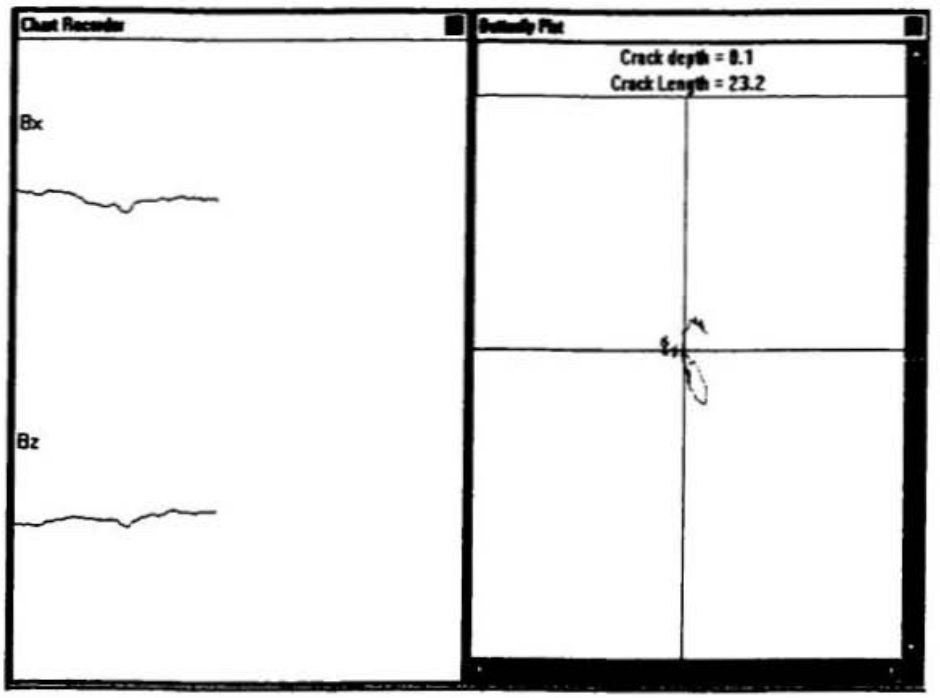

W15T38.wdf – Scanning III

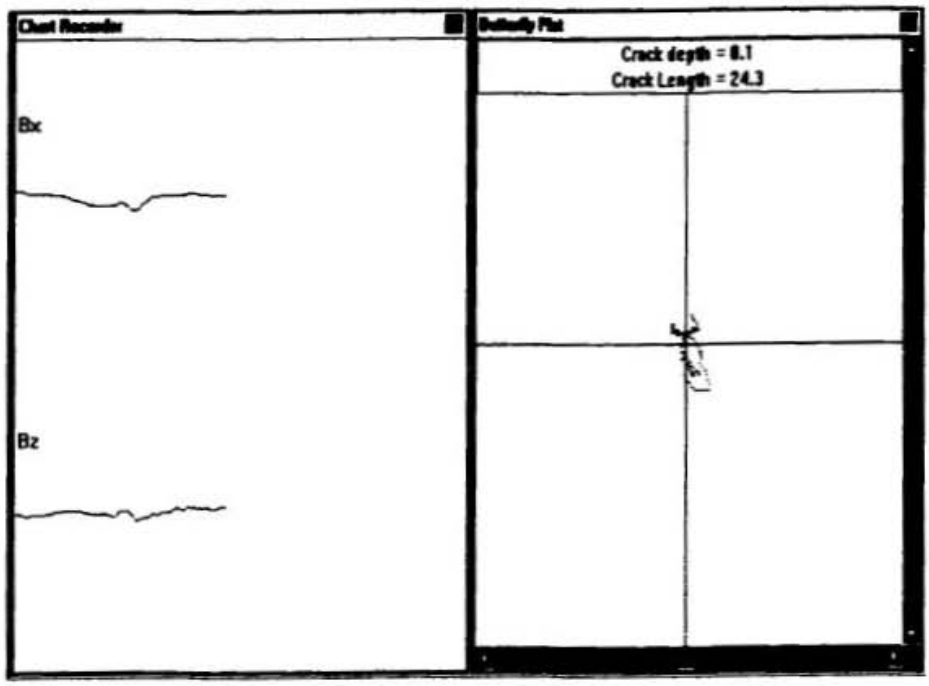

W15T38.wdf – Scanning IV

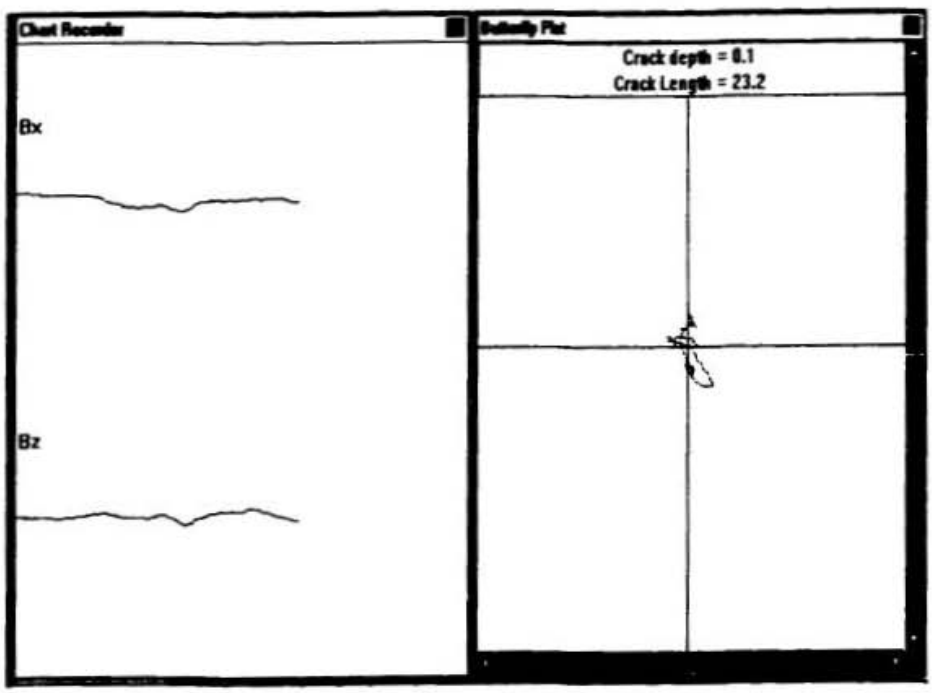

W15T38.wdf – Scanning V

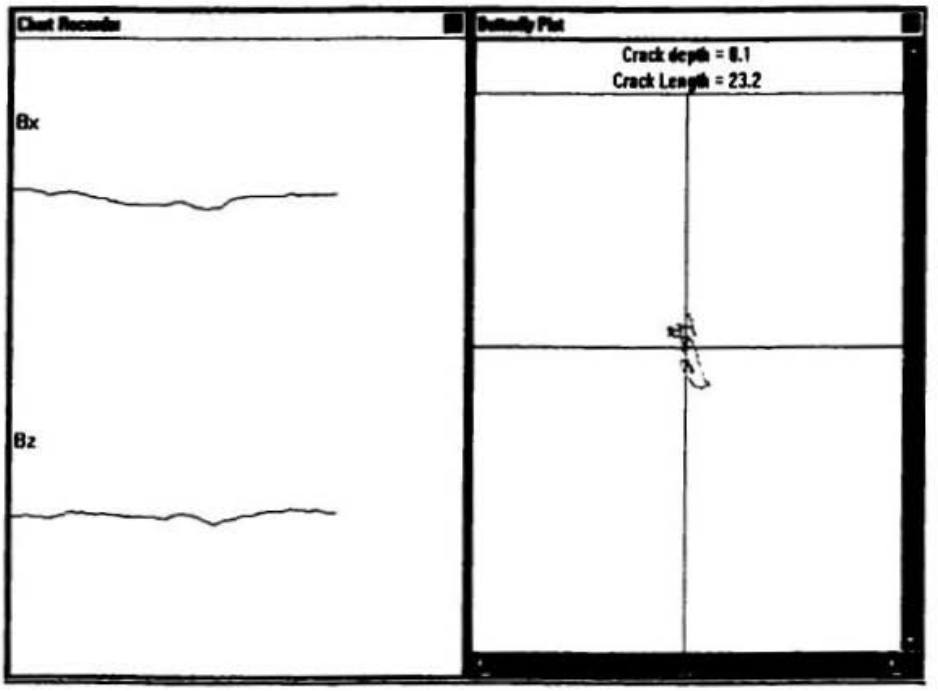

Table C.3. Scanning data from file **W20T38.wdf**

Data from Scanning I			
Pipe wall thickness	: 3.8 mm	Minimum B_x reading	: 1709
Defect depth	: 2.0 mm	Actual length	: 46 mm
Background B_x reading	: 1739	B_z length	: 21 mm
Data from Scanning II			
Pipe wall thickness	: 3.8 mm	Minimum B_x reading	: 1711
Defect depth	: 2.0 mm	Actual length	: 46 mm
Background B_x reading	: 1739	B_z length	: 20 mm
Data from Scanning III			
Pipe wall thickness	: 3.8 mm	Minimum B_x reading	: 1708
Defect depth	: 2.0 mm	Actual length	: 46 mm
Background B_x reading	: 1738	B_z length	: 20 mm
Data from Scanning IV			
Pipe wall thickness	: 3.8 mm	Minimum B_x reading	: 1710
Defect depth	: 2.0 mm	Actual length	: 46 mm
Background B_x reading	: 1739	B_z length	: 21 mm
Data from Scanning V			
Pipe wall thickness	: 3.8 mm	Minimum B_x reading	: 1712
Defect depth	: 2.0 mm	Actual length	: 46 mm
Background B_x reading	: 1741	B_z length	: 21 mm

W20T38.wdf – Scanning I

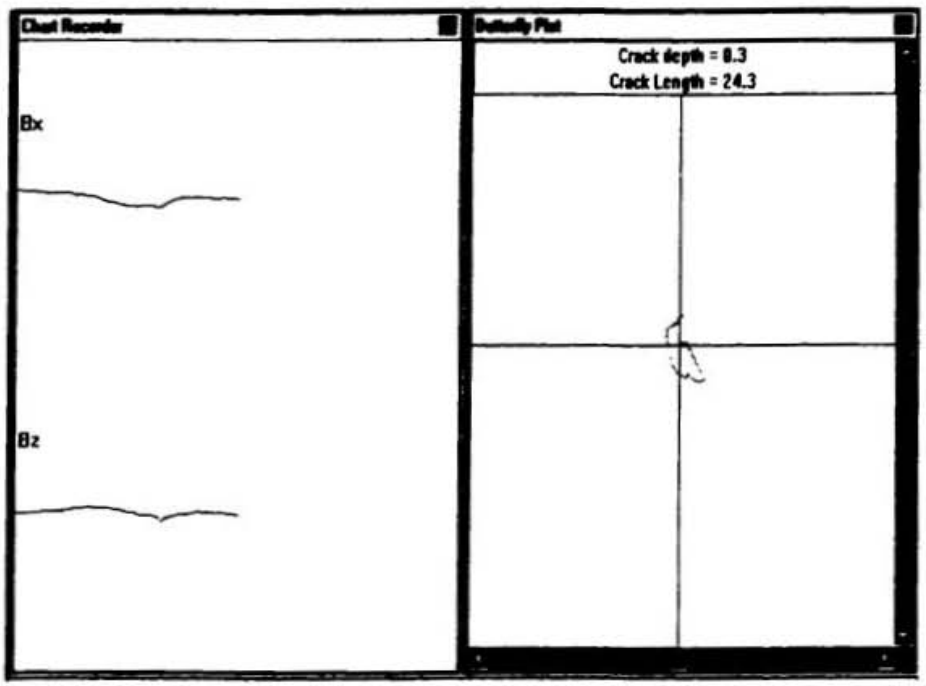

W20T38.wdf – Scanning II

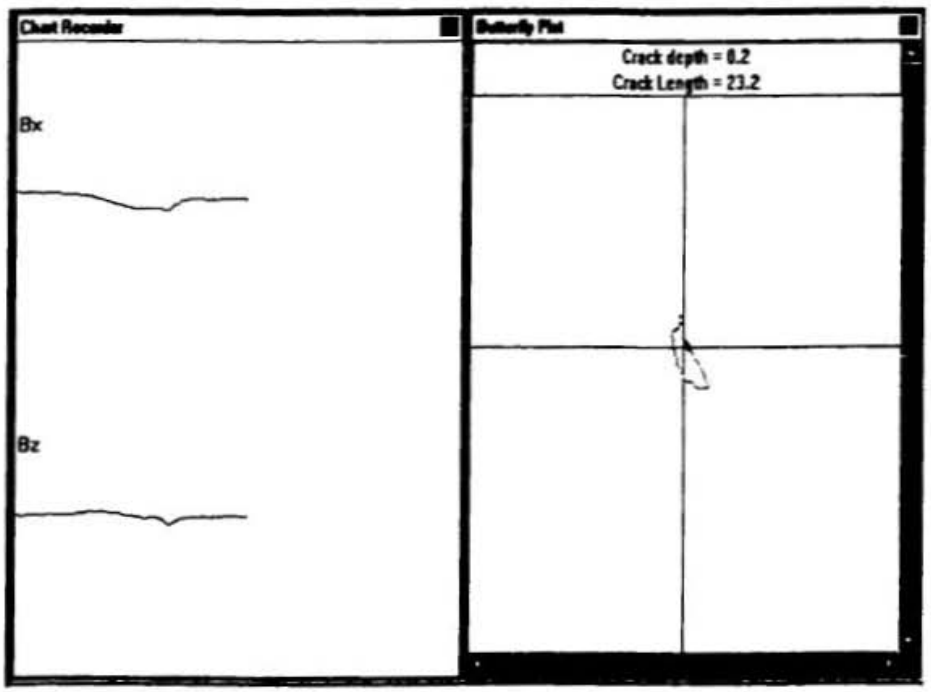

W20T38.wdf – Scanning III

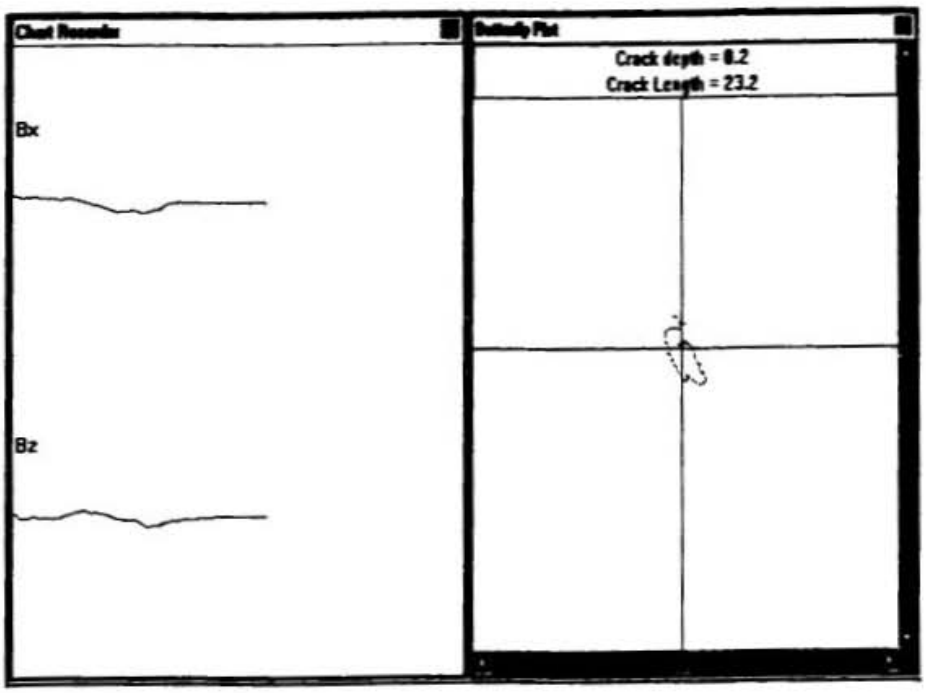

W20T38.wdf – Scanning IV

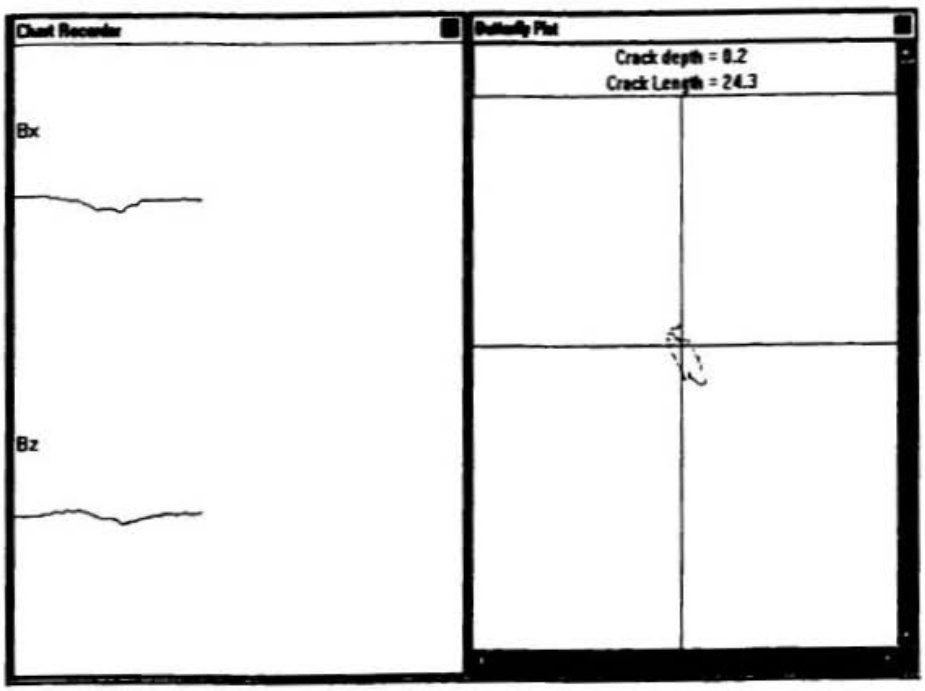

W20T38.wdf – Scanning V

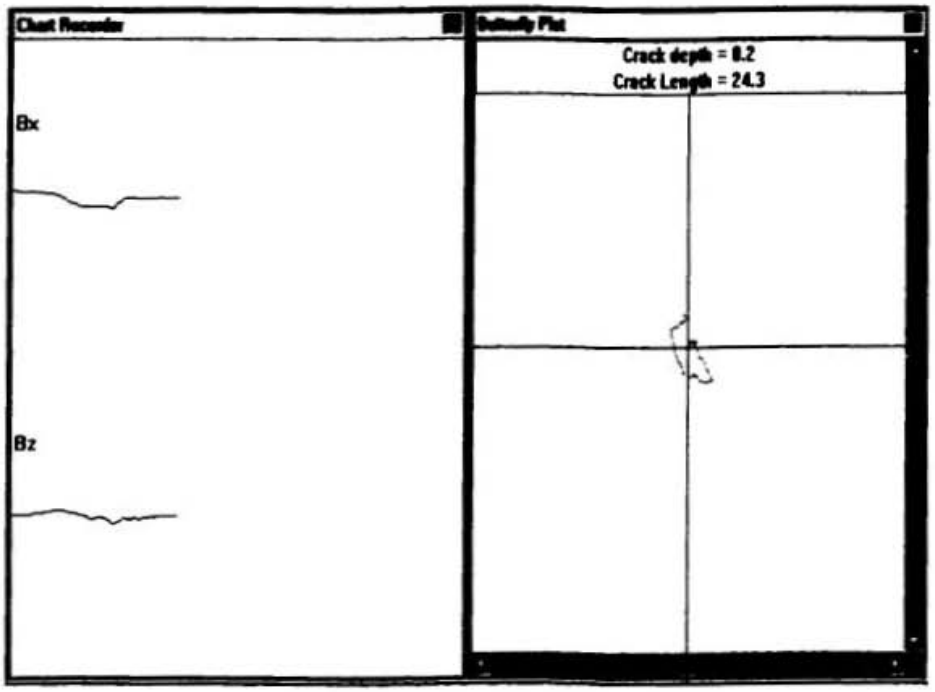

Table C.4. Scanning data from file **W25T38.wdf**

Data from Scanning I			
Pipe wall thickness	: 3.8 mm	Minimum B_x reading	: 1699
Defect depth	: 2.5 mm	Actual length	: 47 mm
Background B_x reading	: 1734	B_z length	: 21 mm
Data from Scanning II			
Pipe wall thickness	: 3.8 mm	Minimum B_x reading	: 1705
Defect depth	: 2.5 mm	Actual length	: 47 mm
Background B_x reading	: 1744	B_z length	: 20 mm
Data from Scanning III			
Pipe wall thickness	: 3.8 mm	Minimum B_x reading	: 1708
Defect depth	: 2.5 mm	Actual length	: 47 mm
Background B_x reading	: 1751	B_z length	: 20 mm
Data from Scanning IV			
Pipe wall thickness	: 3.8 mm	Minimum B_x reading	: 1698
Defect depth	: 2.5 mm	Actual length	: 47 mm
Background B_x reading	: 1731	B_z length	: 22 mm
Data from Scanning V			
Pipe wall thickness	: 3.8 mm	Minimum B_x Reading	: 1699
Defect depth	: 2.5 mm	Actual length	: 47 mm
Background B_x Reading	: 1735	B_z length	: 21 mm

W25T38.wdf – Scanning I

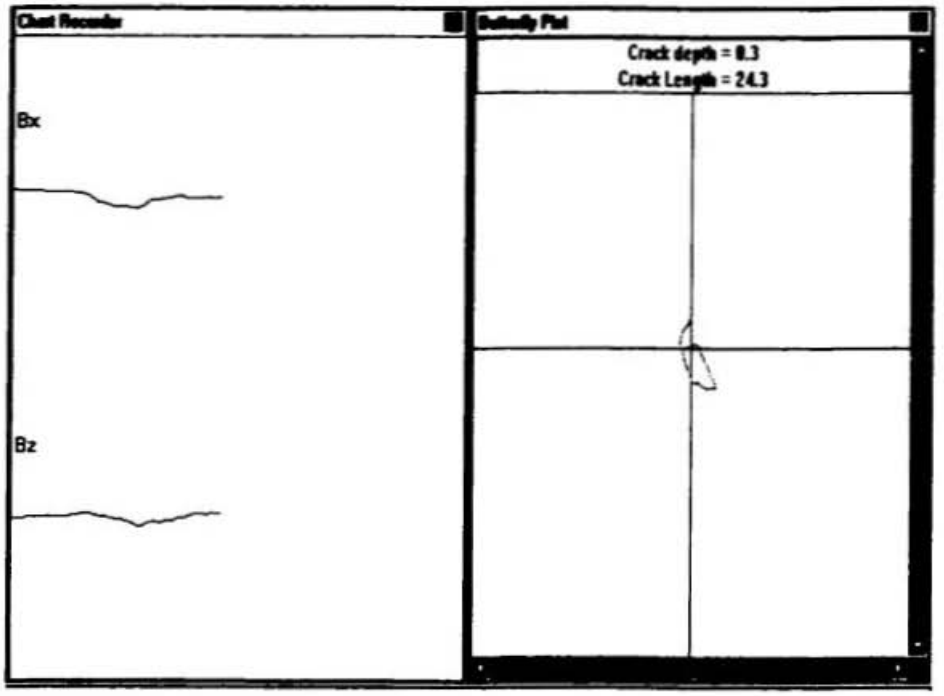

W25T38.wdf – Scanning II

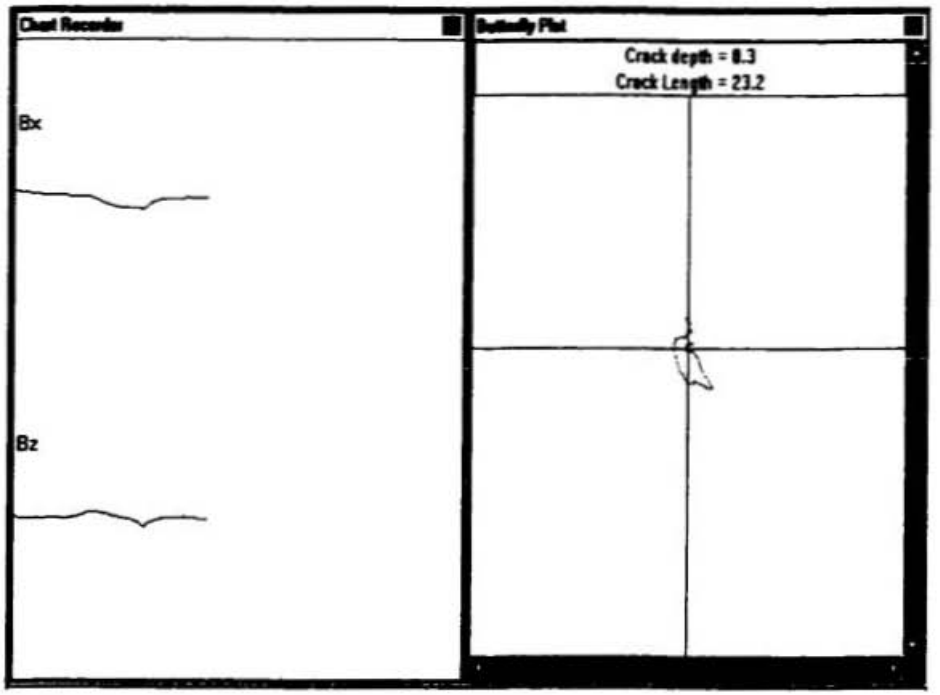

W25T38.wdf – Scanning III

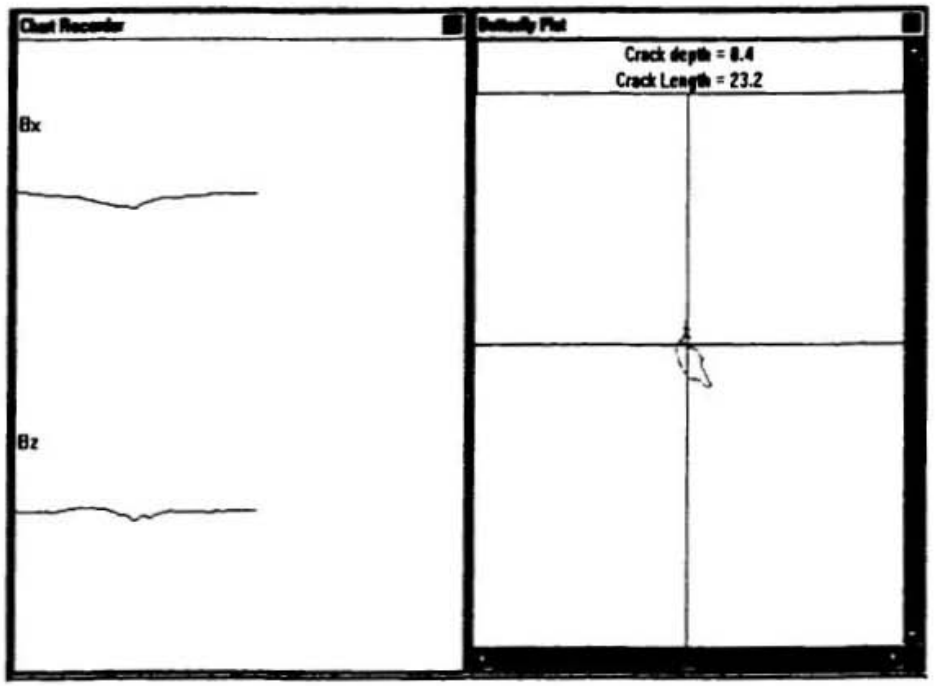

W25T38.wdf – Scanning IV

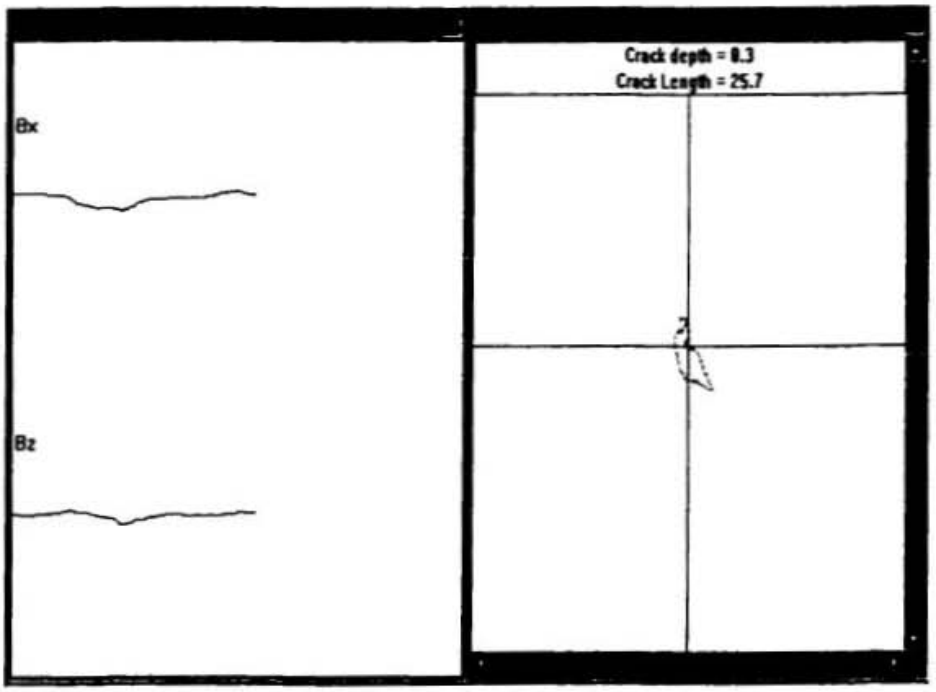

W25T38.wdf – Scanning V

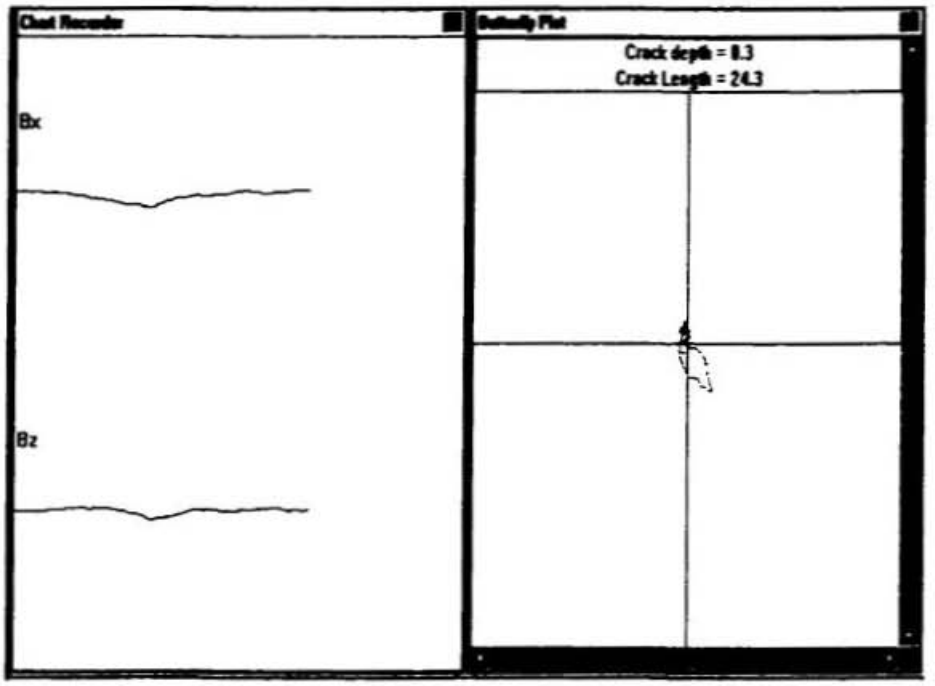

Table C.5. Scanning data from file **W30T38.wdf**

Data from Scanning I			
Pipe wall thickness	: 3.8 mm	Minimum B_x reading	: 1669
Defect depth	: 3.0 mm	Actual length	: 49 mm
Background B_x reading	: 1732	B_z length	: 21 mm
Data from Scanning II			
Pipe wall thickness	: 3.8 mm	Minimum B_x reading	: 1664
Defect depth	: 3.0 mm	Actual length	: 49 mm
Background B_x reading	: 1728	B_z Crack Length	: 21 mm
Data from Scanning III			
Pipe wall thickness	: 3.8 mm	Minimum B_x reading	: 1672
Defect depth	: 3.0 mm	Actual length	: 49 mm
Background B_x reading	: 1732	B_z length	: 21 mm
Data from Scanning IV			
Pipe wall thickness	: 3.8 mm	Minimum B_x reading	: 1668
Defect depth	: 3.0 mm	Actual length	: 49 mm
Background B_x reading	: 1731	B_z length	: 21 mm
Data from Scanning V			
Pipe wall thickness	: 3.8 mm	Minimum B_x reading	: 1677
Defect depth	: 3.0 mm	Actual length	: 49 mm
Background B_x reading	: 1736	B_z length	: 20 mm

W30T38.wdf – Scanning I

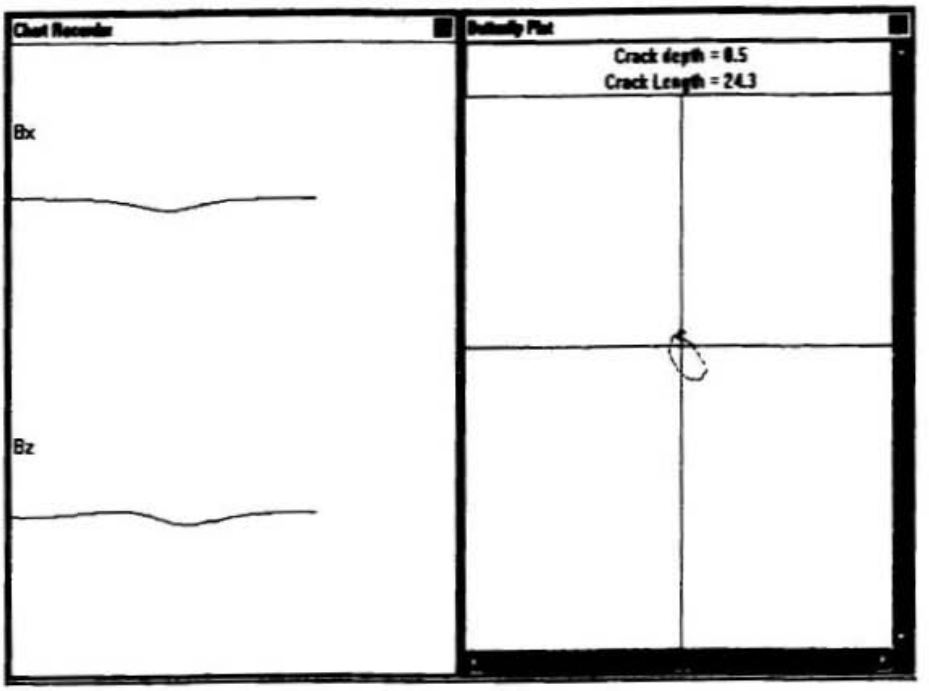

W30T38.wdf – Scanning II

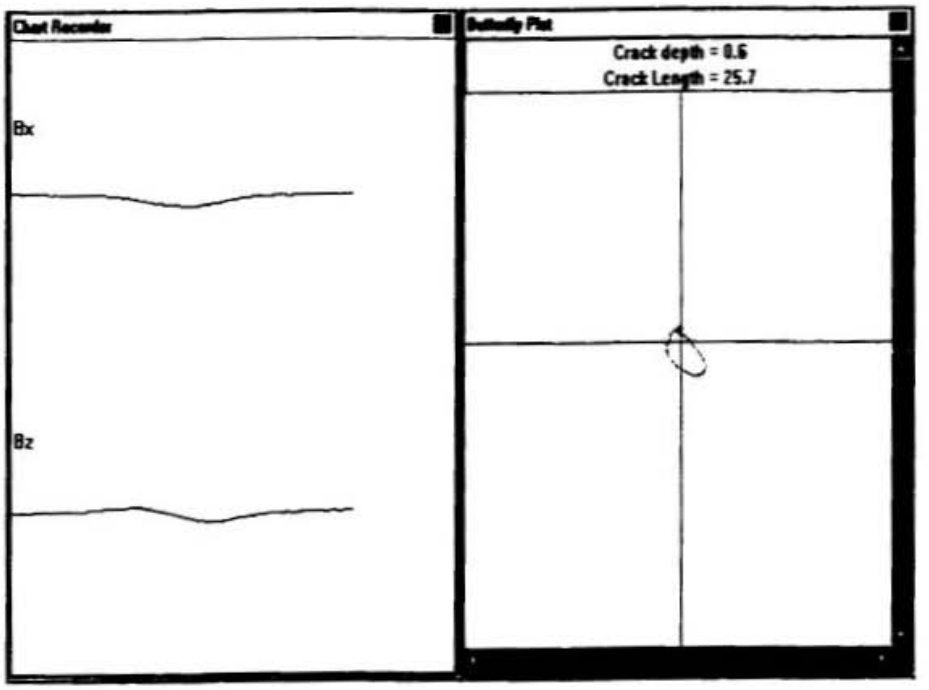

W30T38.wdf – Scanning III

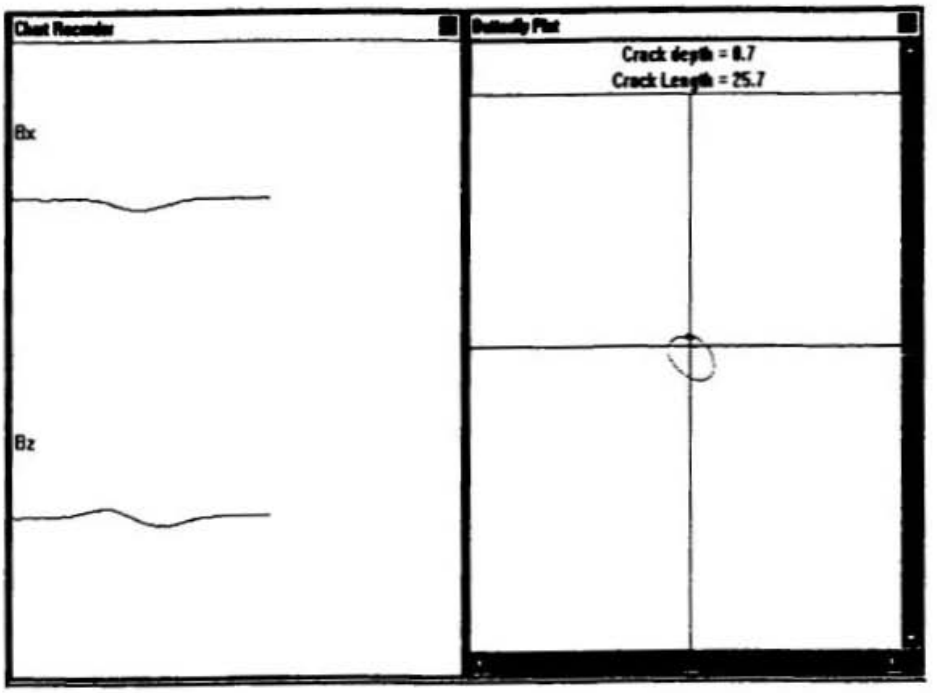

W30T38.wdf – Scanning IV

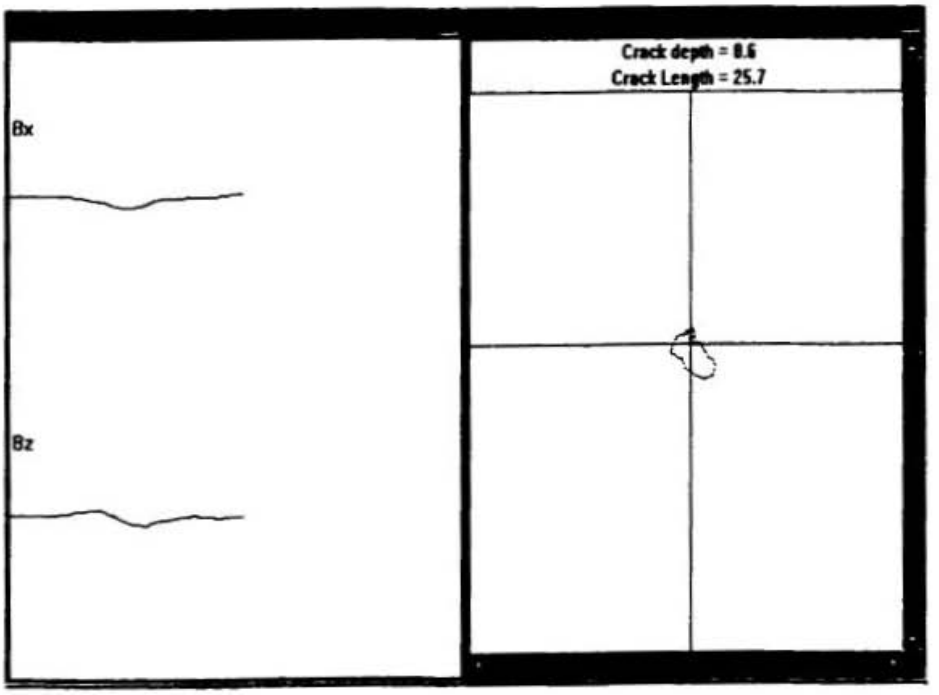

W30T38.wdf – Scanning V

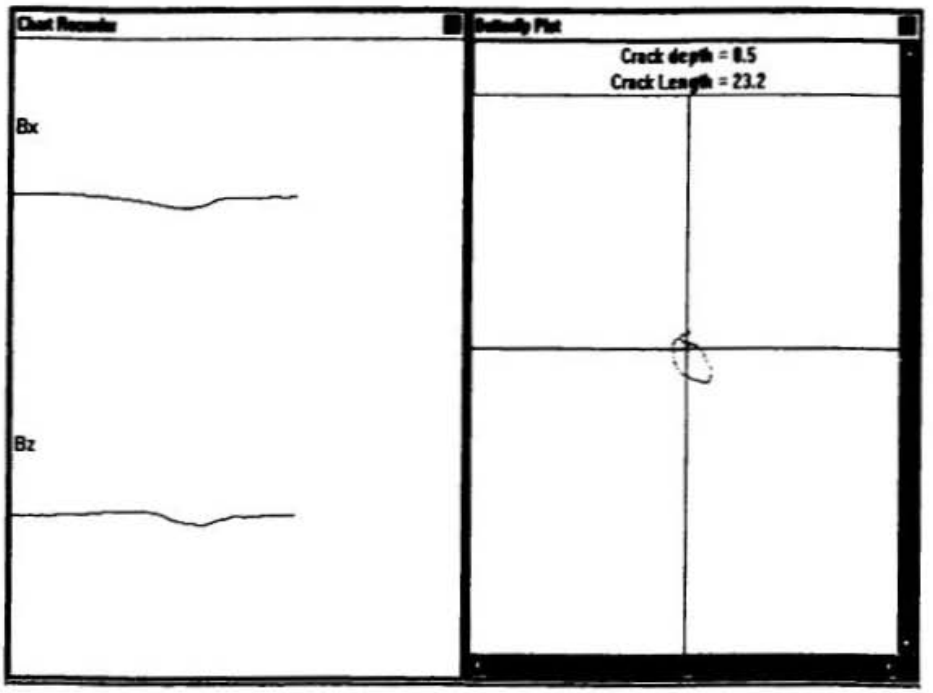

Table C.6. Scanning data from file **W35T38.wdf**

Data from Scanning I			
Pipe wall thickness	: 3.8 mm	Minimum B_x reading	: 1584
Defect depth	: 3.5 mm	Actual length	: 50 mm
Background B_x reading	: 1727	B_z length	: 22 mm
Data from Scanning II			
Pipe wall thickness	: 3.8 mm	Minimum B_x reading	: 1599
Defect depth	: 3.5 mm	Actual length	: 50 mm
Background B_x reading	: 1726	B_z length	: 22 mm
Data from Scanning III			
Pipe wall thickness	: 3.8 mm	Minimum B_x reading	: 1591
Defect depth	: 3.5 mm	Actual length	: 50 mm
Background B_x reading	: 1725	B_z length	: 23 mm
Data from Scanning IV			
Pipe wall thickness	: 3.8 mm	Minimum B_x reading	: 1588
Defect depth	: 3.5 mm	Actual length	: 50 mm
Background B_x reading	: 1727	B_z length	: 20 mm
Data from Scanning V			
Pipe wall thickness	: 3.8 mm	Minimum B_x reading	: 1595
Defect depth	: 3.5 mm	Actual length	: 50 mm
Background B_x reading	: 1724	B_z length	: 22 mm

W35T38.wdf – Scanning I

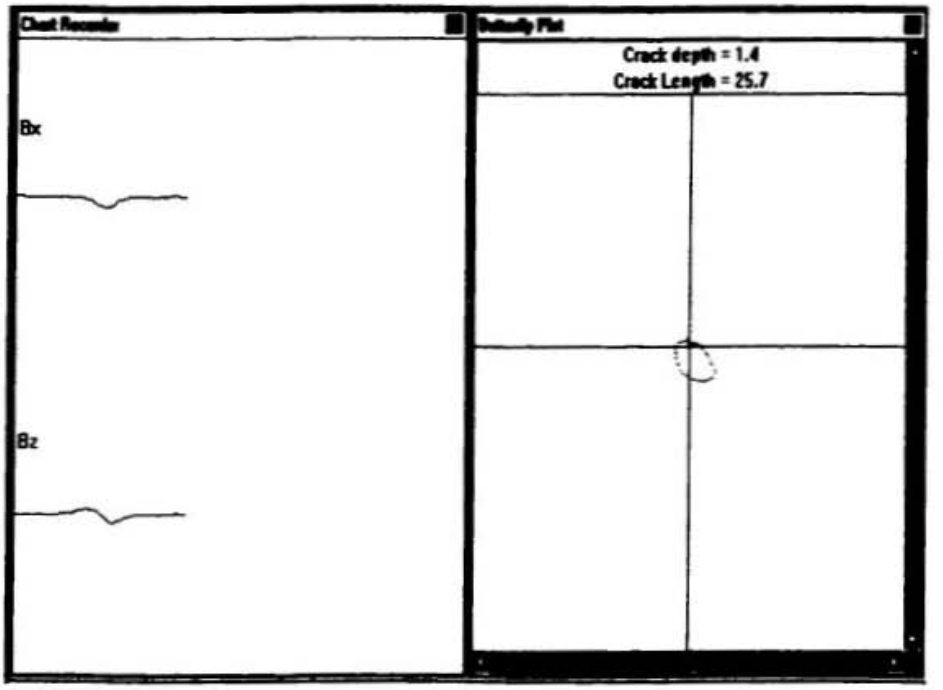

W35T38.wdf – Scanning II

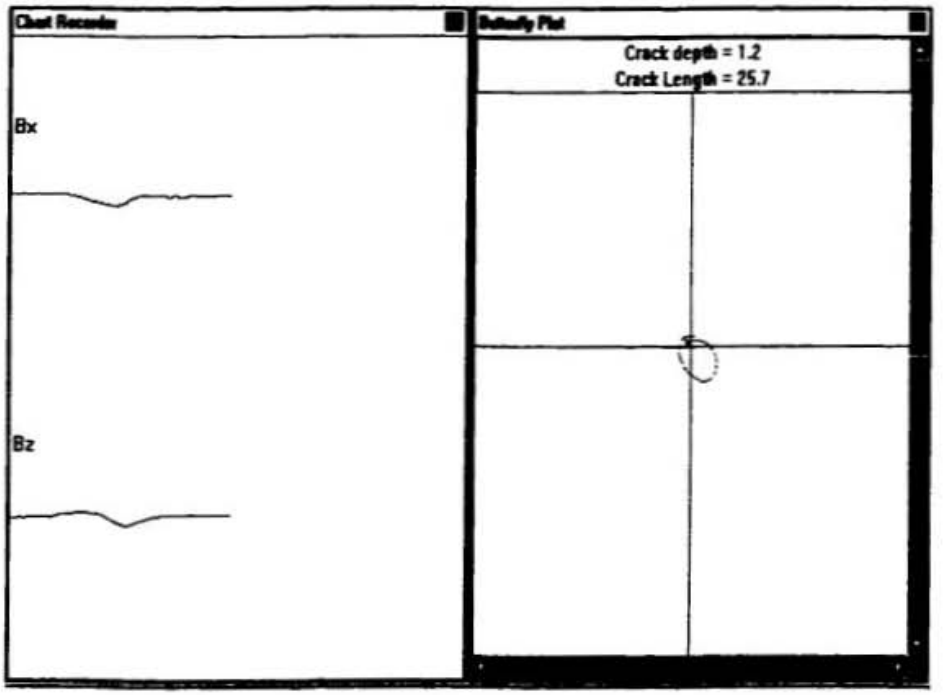

W35T38.wdf – Scanning III

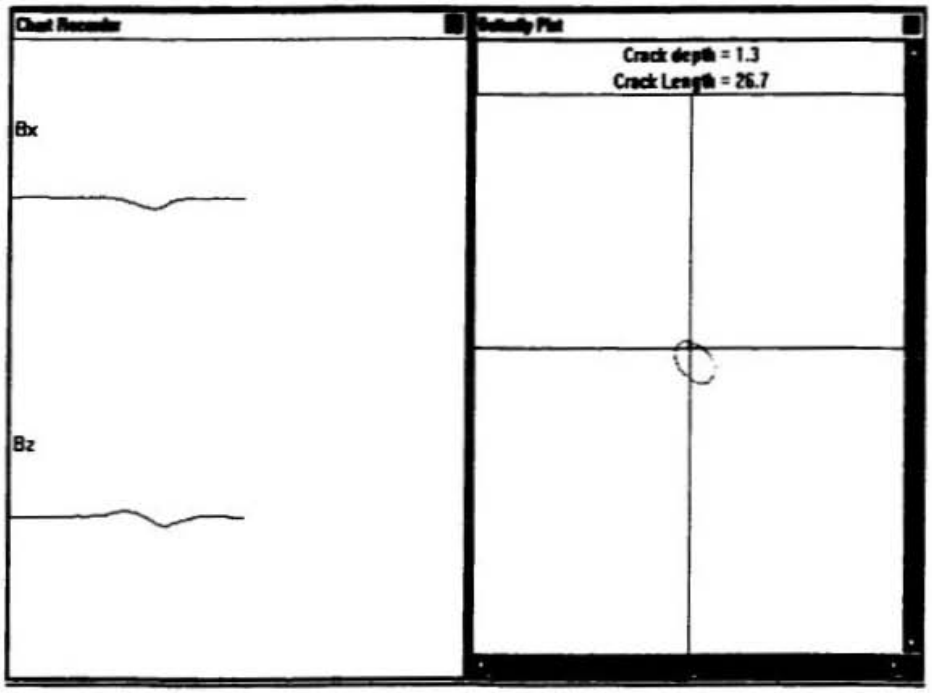

W35T38.wdf – Scanning IV

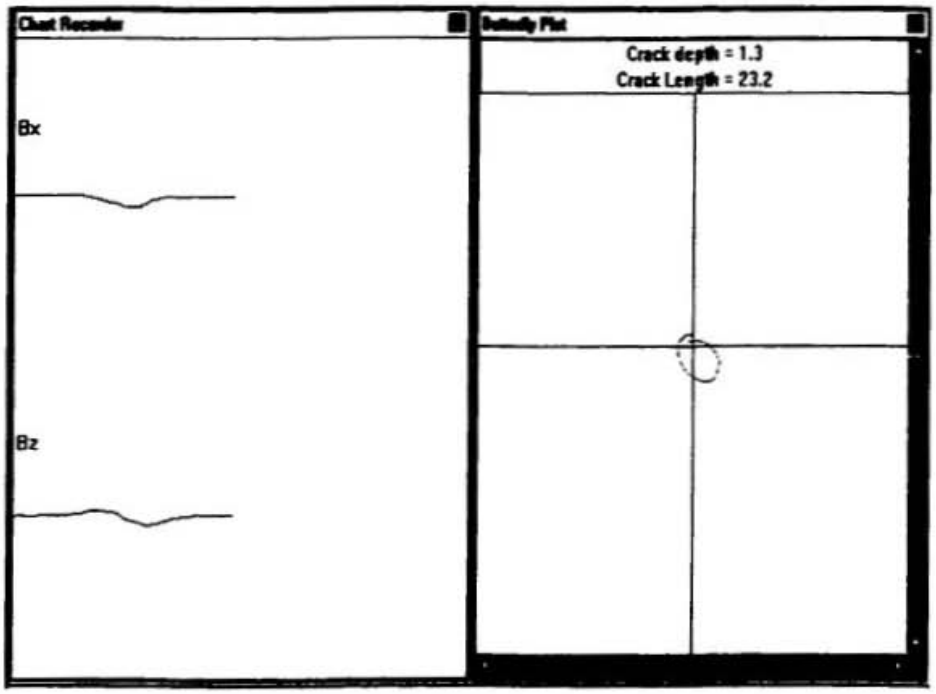

W35T38.wdf – Scanning V

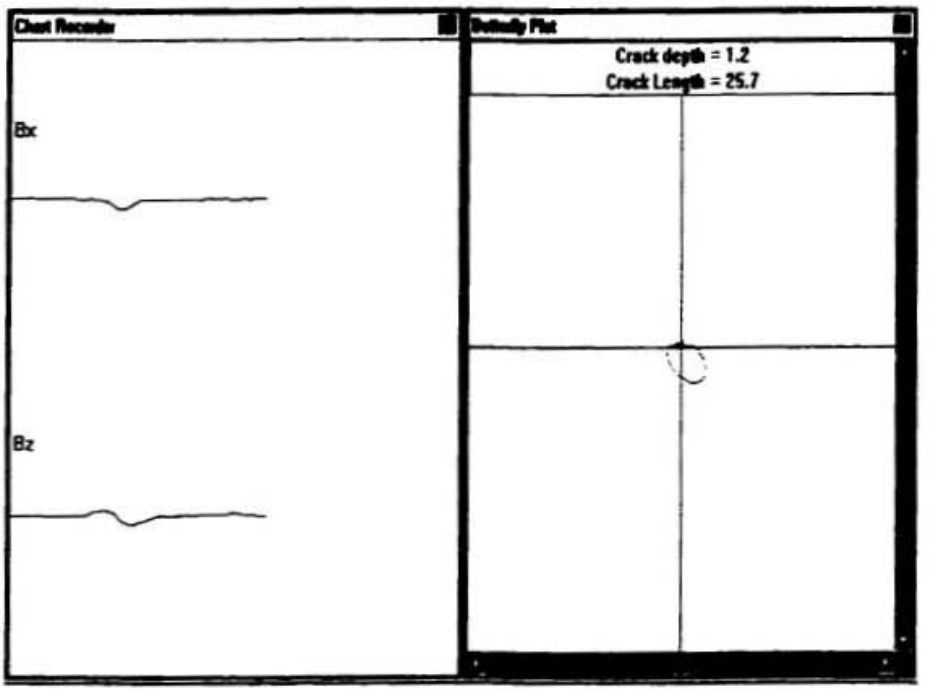

Table C.7. Summary table of scanning data from file **W15T38.wdf**

W15T38.wdf			
Actual Depth	**Signal Ratio**	**Actual Length**	**B_z Length**
1.5	0.009758898	45	20
1.5	0.007449857	45	20
1.5	0.007454128	45	20
1.5	0.010273973	45	21
1.5	0.008571429	45	21
Average	**0.008701657**	**45**	**20.4**

Table C.8. Summary table of scanning data from file **W20T38.wdf**

W20T38.wdf			
Actual Depth	**Signal Ratio**	**Actual Length**	**B_z Length**
2.0	0.017251294	46	21
2.0	0.016101208	46	20
2.0	0.01726122	46	20
2.0	0.016676251	46	21
2.0	0.016657094	46	21
Average	**0.016789413**	**46**	**20.6**

Table C.9. Summary table of scanning data from file **W25T38.wdf**

W25T38.wdf			
Actual Depth	**Signal Ratio**	**Actual Length**	**B_z Length**
2.5	0.020184544	47	21
2.5	0.022362385	47	20
2.5	0.024557396	47	20
2.5	0.019064125	47	22
2.5	0.02074928	47	21
Average	**0.021383546**	**47**	**20.8**

Table C.10. Summary table of scanning data from file **W30T38.wdf**

W30T38.wdf			
Actual Depth	**Signal Ratio**	**Actual Length**	**B_z Length**
3.0	0.036374134	49	21
3.0	0.037037037	49	21
3.0	0.034642032	49	21
3.0	0.036395147	49	21
3.0	0.033986175	49	20
Average	**0.035686905**	**49**	**20.8**

Table C.11. Summary table of scanning data from file **W35T38.wdf**

W35T38.wdf			
Actual Depth	**Signal Ratio**	**Actual Length**	**B_z Length**
3.5	0.082802548	50	22
3.5	0.073580533	50	22
3.5	0.077681159	50	23
3.5	0.080486393	50	20
3.5	0.074825986	50	22
Average	**0.077875324**	**50**	**21.8**

Appendix D

ACFM Scans for the Defects Located in the Inner Surface of the Base Metal of 3.8 mm Pipe Wall Thickness

Table D.1. Scanning data from file **D10T38.wdf**

Data from Scanning I			
Pipe wall thickness	: 3.8 mm	Minimum B_x reading	: 1721
Defect depth	: 1.0 mm	Actual length	: 44 mm
Background B_x reading	: 1738	B_z length	: 18 mm
Data from Scanning II			
Pipe wall thickness	: 3.8 mm	Minimum B_x reading	: 1721
Defect depth	: 1.0 mm	Actual length	: 44 mm
Background B_x reading	: 1738	B_z length	: 21 mm
Data from Scanning III			
Pipe wall thickness	: 3.8 mm	Minimum B_x reading	: 1727
Defect depth	: 1.0 mm	Actual length	: 44 mm
Background B_x reading	: 1740	B_z length	: 18 mm
Data from Scanning IV			
Pipe wall thickness	: 3.8 mm	Minimum B_x reading	: 1724
Defect depth	: 1.0 mm	Actual length	: 44 mm
Background B_x reading	: 1741	B_z length	: 21 mm
Data from Scanning V			
Pipe wall thickness	: 3.8 mm	Minimum B_x reading	: 1725
Defect depth	: 1.0 mm	Actual length	: 44 mm
Background B_x reading	: 1742	B_z length	: 38 mm

D10T38.wdf – Scanning I

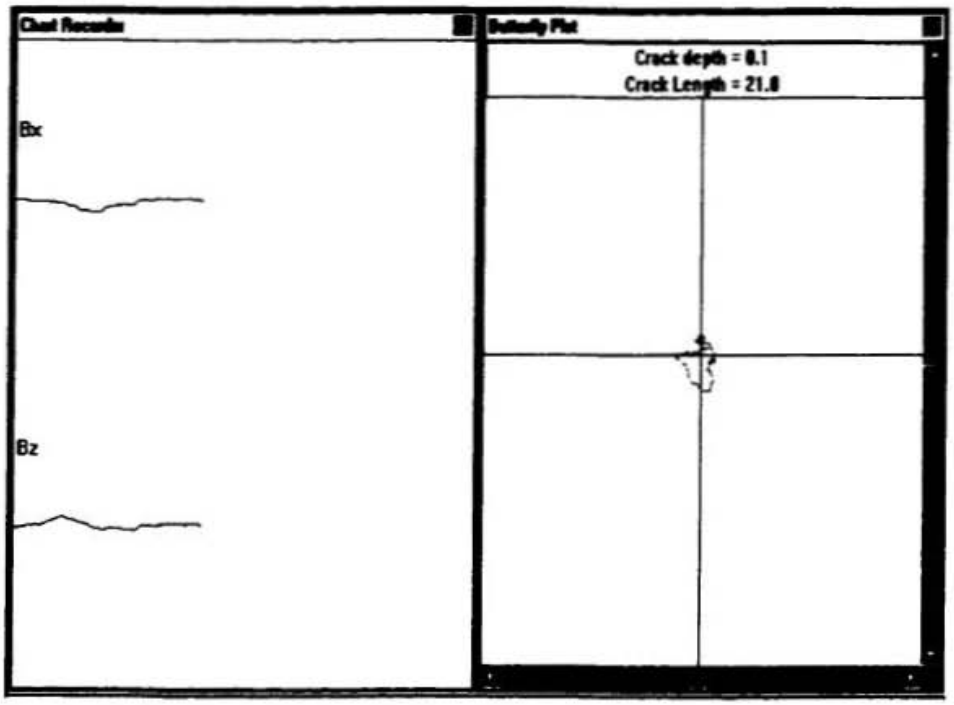

D10T38.wdf – Scanning II

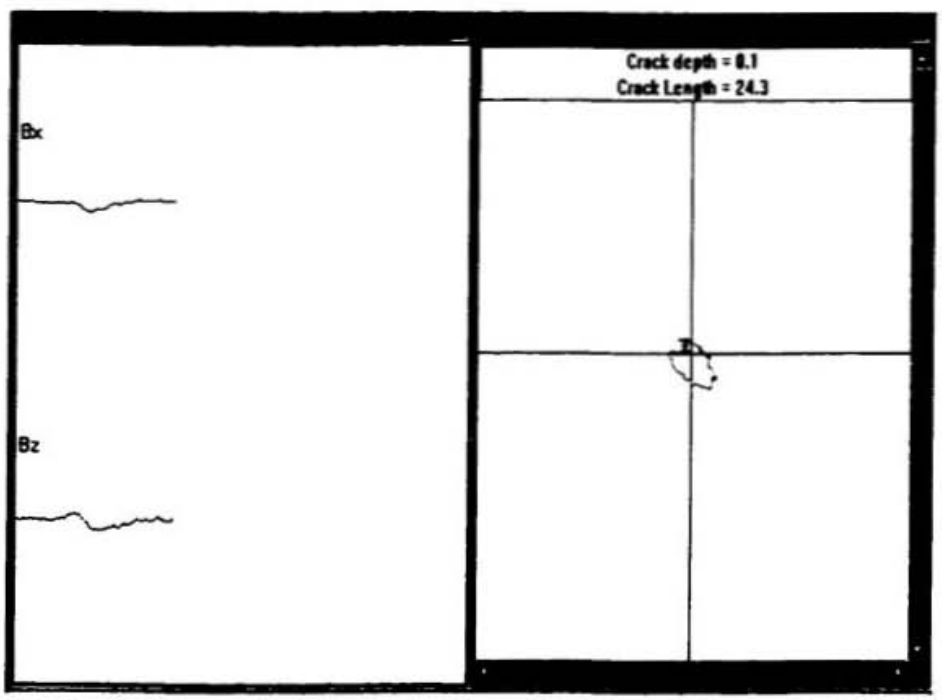

D10T38.wdf – Scanning III

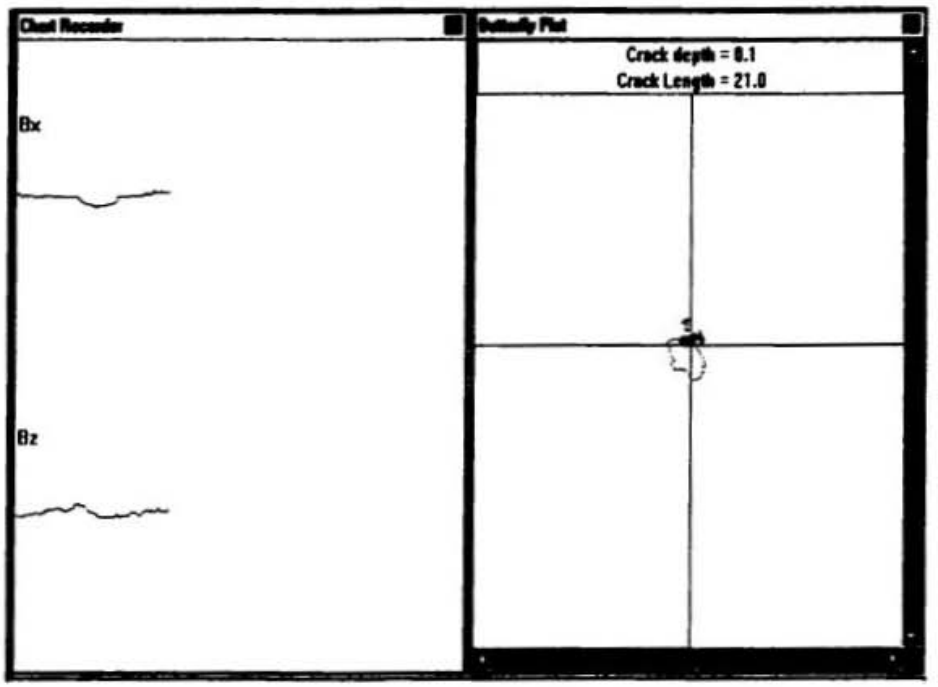

D10T38.wdf – Scanning IV

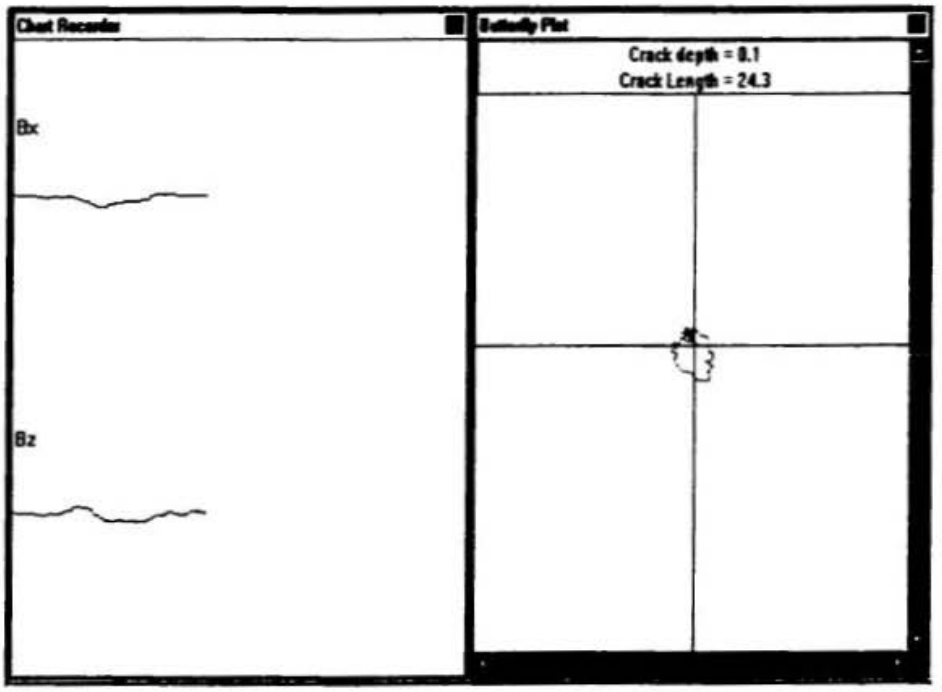

D10T38.wdf – Scanning V

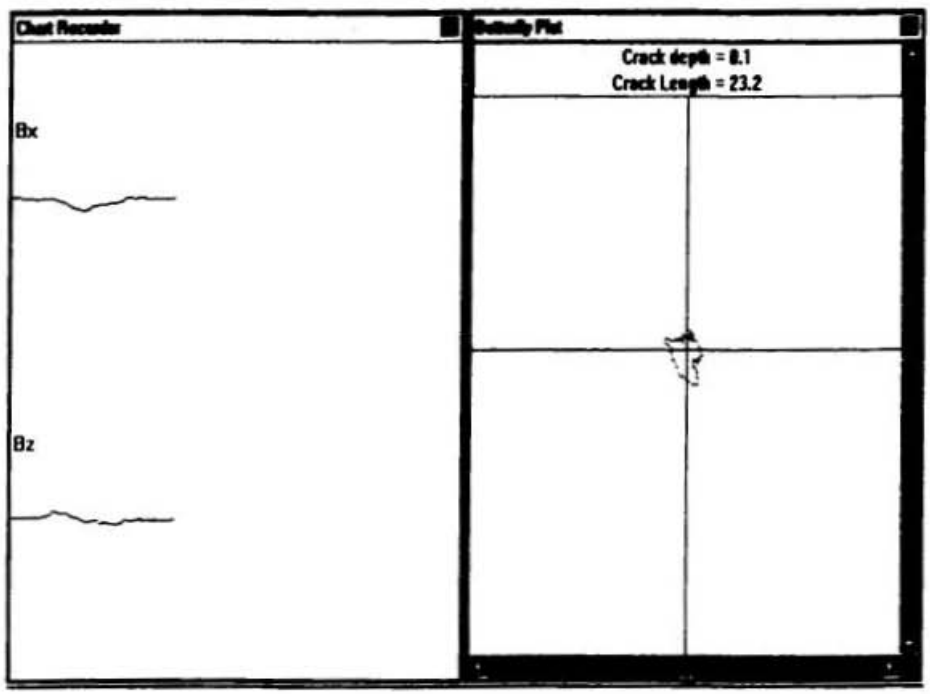

Table D.2. Scanning data from file **D15T38.wdf**

Data from Scanning I			
Pipe wall thickness	: 3.8 mm	Minimum B_x reading	: 1720
Defect depth	: 1.5 mm	Actual length	: 45 mm
Background B_x reading	: 1735	B_z length	: 21 mm
Data from Scanning II			
Pipe wall thickness	: 3.8 mm	Minimum B_x reading	: 1711
Defect depth	: 1.5 mm	Actual length	: 45 mm
Background B_x reading	: 1728	B_z length	: 21 mm
Data from Scanning III			
Pipe wall thickness	: 3.8 mm	Minimum B_x reading	: 1720
Defect depth	: 1.5 mm	Actual length	: 45 mm
Background B_x reading	: 1736	B_z length	: 22 mm
Data from Scanning IV			
Pipe wall thickness	: 3.8 mm	Minimum B_x reading	: 1715
Defect depth	: 1.5 mm	Actual length	: 45 mm
Background B_x reading	: 1733	B_z length	: 20 mm
Data from Scanning V			
Pipe wall thickness	: 3.8 mm	Minimum B_x Reading	: 1735
Defect depth	: 1.5 mm	Actual length	: 45 mm
Background B_x Reading	: 1750	B_z length	: 18 mm

D15T38.wdf – Scanning I

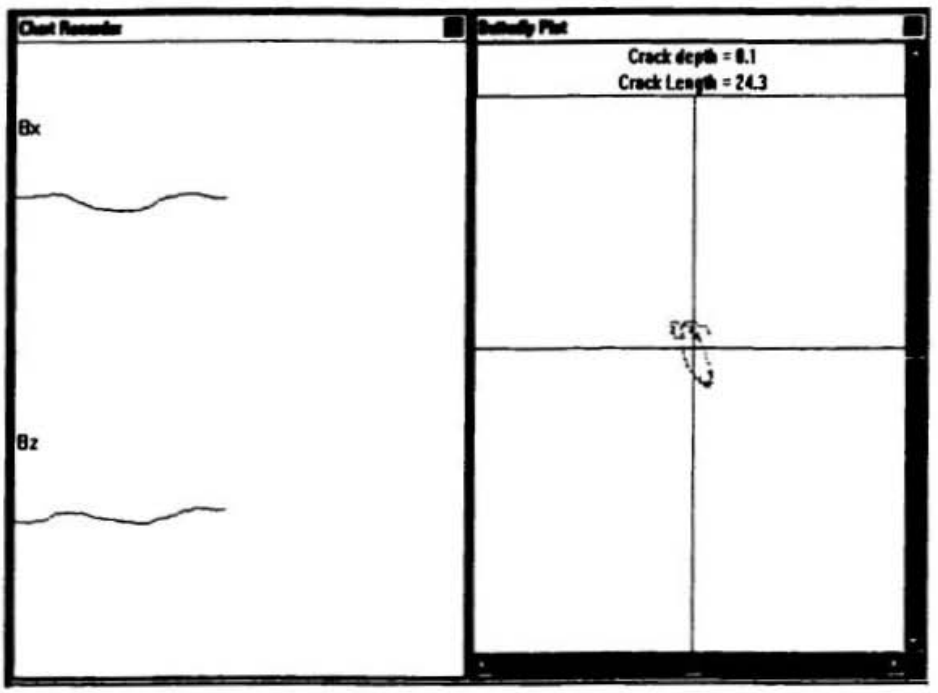

D15T38.wdf – Scanning II

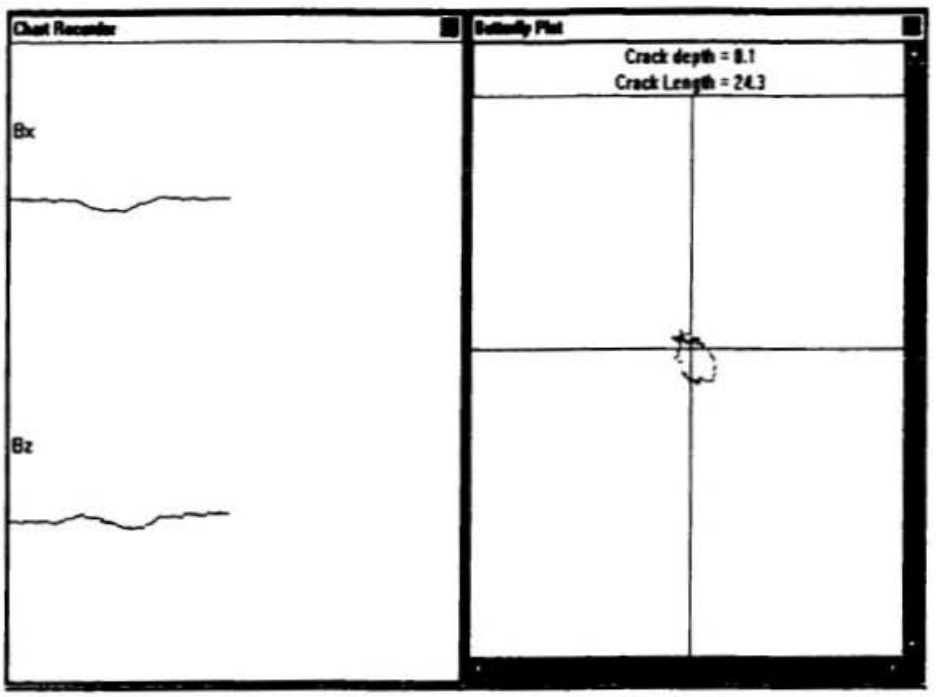

D15T38.wdf – Scanning III

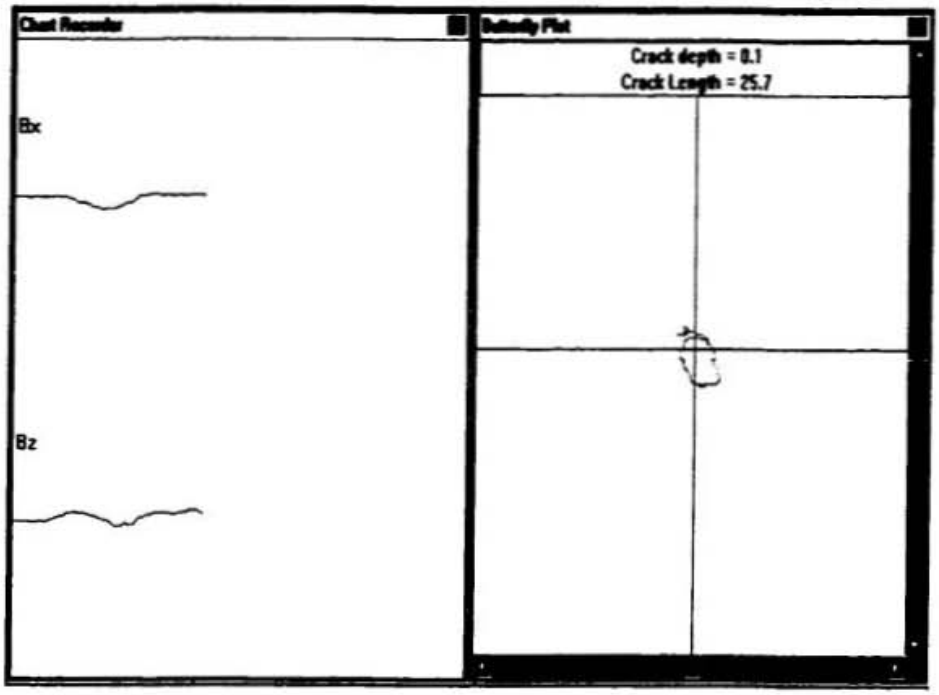

D15T38.wdf – Scanning IV

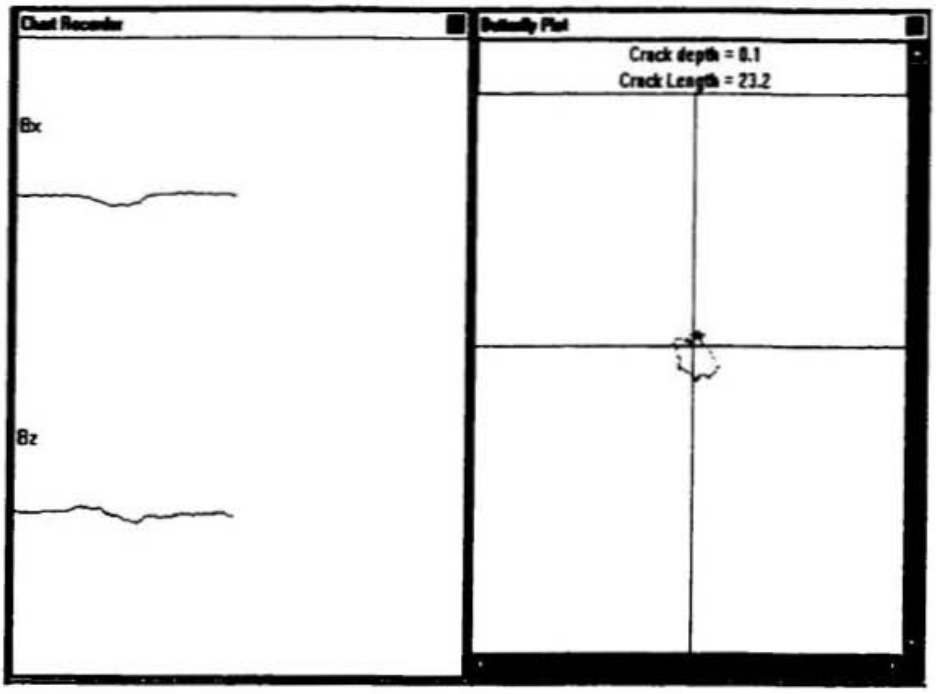

D15T38.wdf – Scanning V

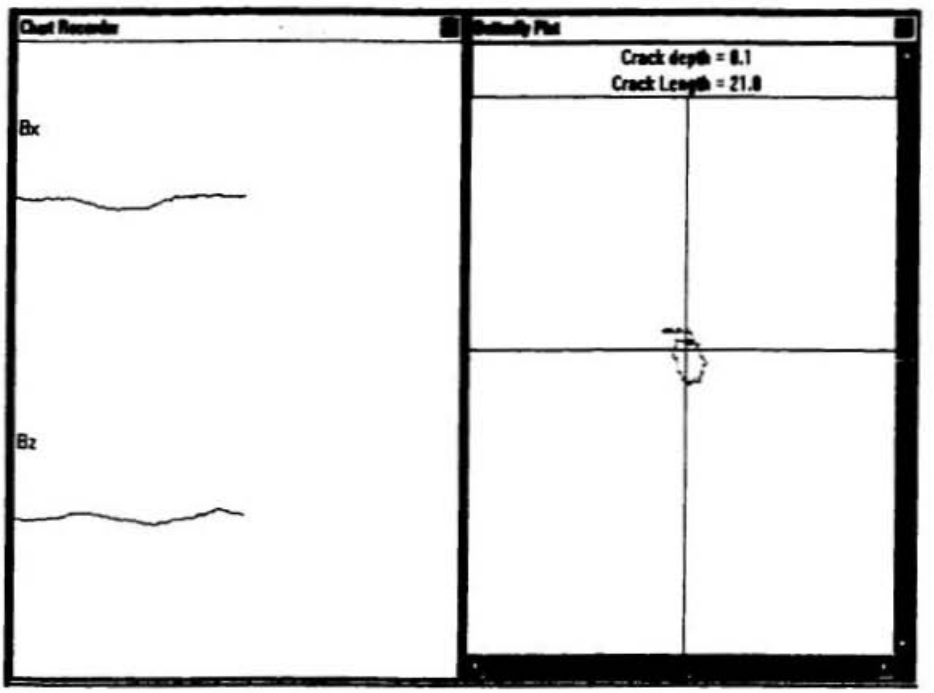

Table D.3. Scanning data from file **D20T38.wdf**

Data from Scanning I			
Pipe wall thickness	: 3.8 mm	Minimum B_x reading	: 1704
Defect depth	: 2.0 mm	Actual length	: 46 mm
Background B_x reading	: 1731	B_z length	: 20 mm
Data from Scanning II			
Pipe wall thickness	: 3.8 mm	Minimum B_x reading	: 1695
Defect depth	: 2.0 mm	Actual length	: 46 mm
Background B_x reading	: 1723	B_z length	: 19 mm
Data from Scanning III			
Pipe wall thickness	: 3.8 mm	Minimum B_x Reading	: 1703
Defect depth	: 2.0 mm	Actual length	: 46 mm
Background B_x Reading	: 1730	B_z length	: 21 mm
Data from Scanning IV			
Pipe wall thickness	: 3.8 mm	Minimum B_x reading	: 1703
Defect depth	: 2.0 mm	Actual length	: 46 mm
Background B_x reading	: 1730	B_z length	: 21 mm
Data from Scanning V			
Pipe wall thickness	: 3.8 mm	Minimum B_x reading	: 1700
Defect depth	: 2.0 mm	Actual length	: 46 mm
Background B_x reading	: 1726	B_z length	: 22 mm

D20T38.wdf – Scanning I

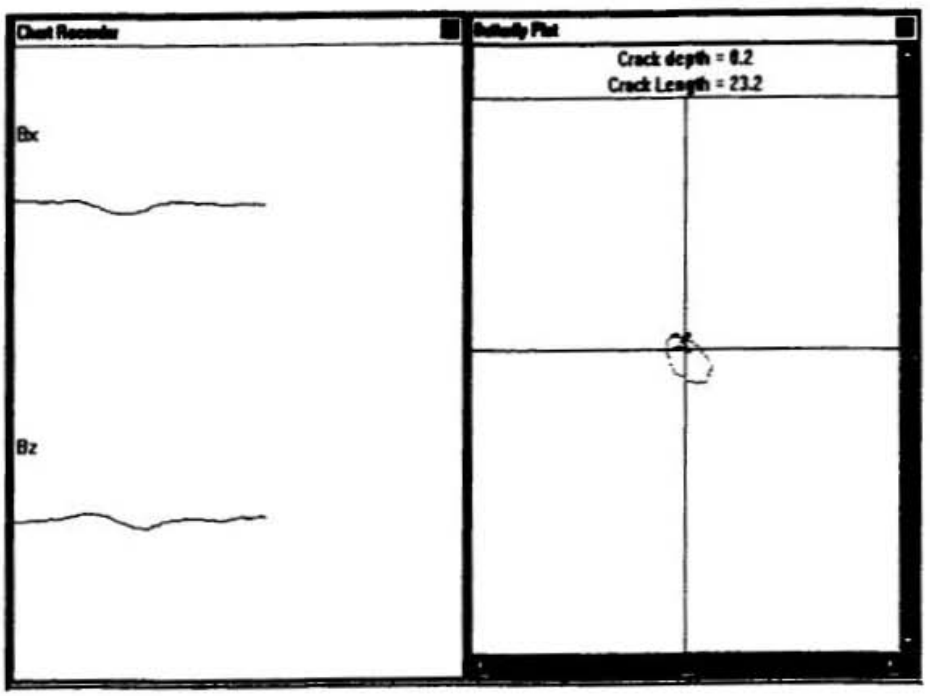

D20T38.wdf – Scanning II

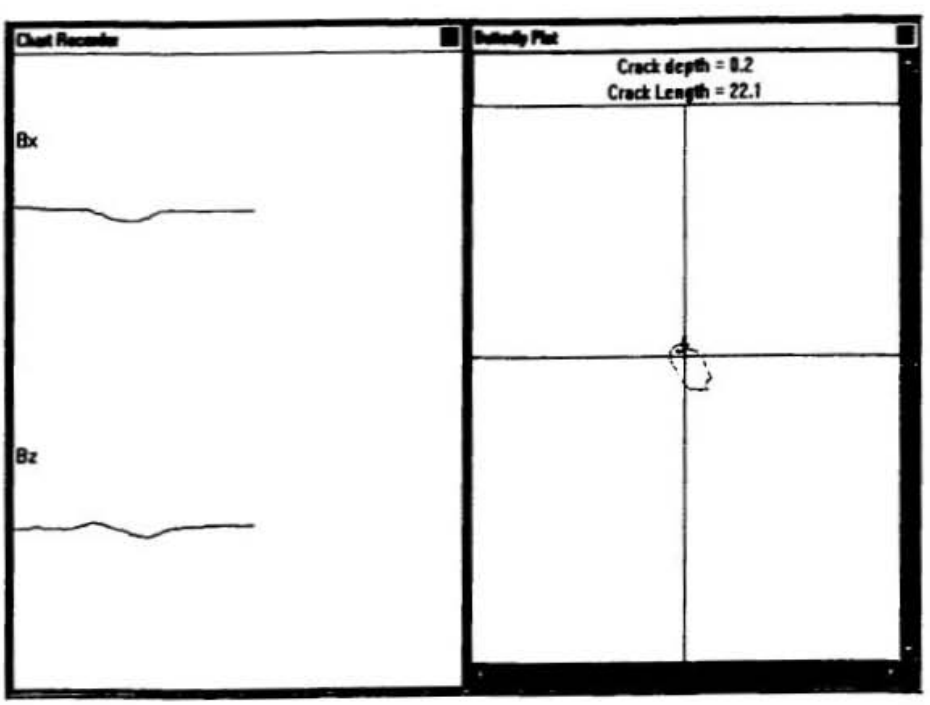

D20T38.wdf – Scanning III

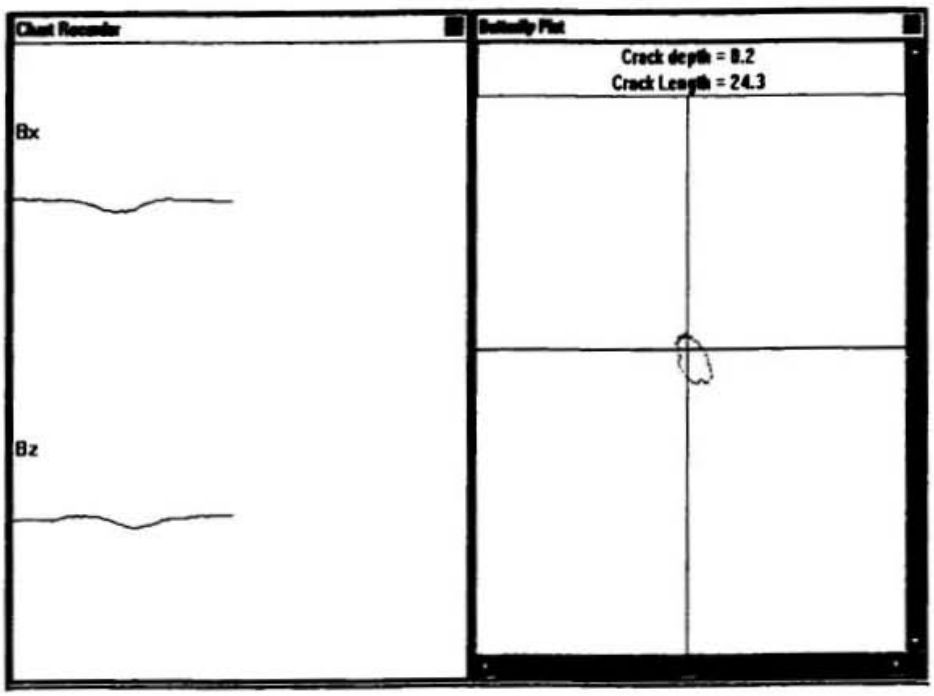

D20T38.wdf – Scanning IV

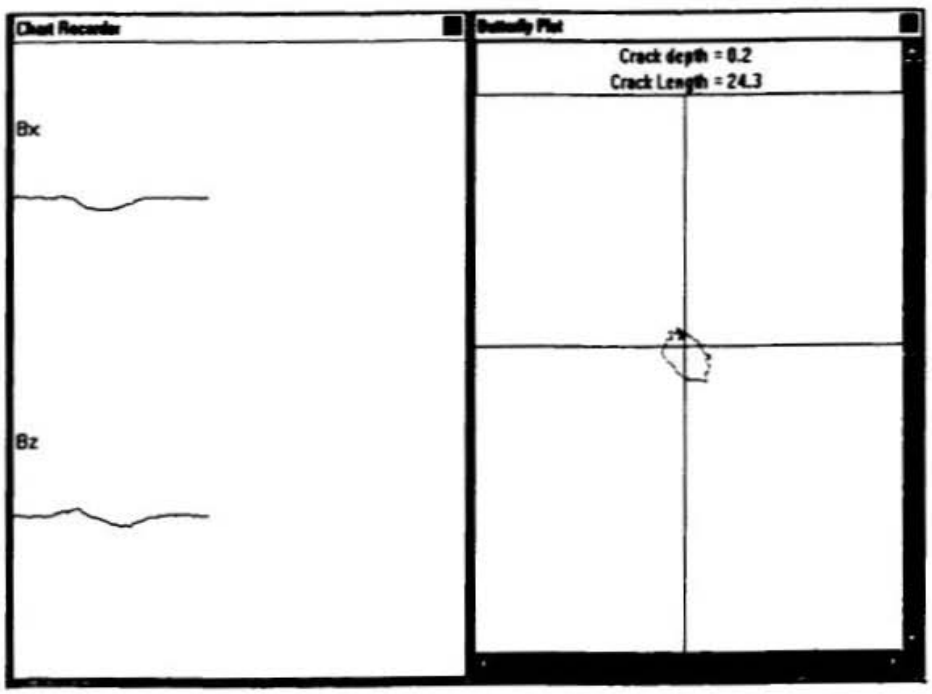

D20T38.wdf – Scanning V

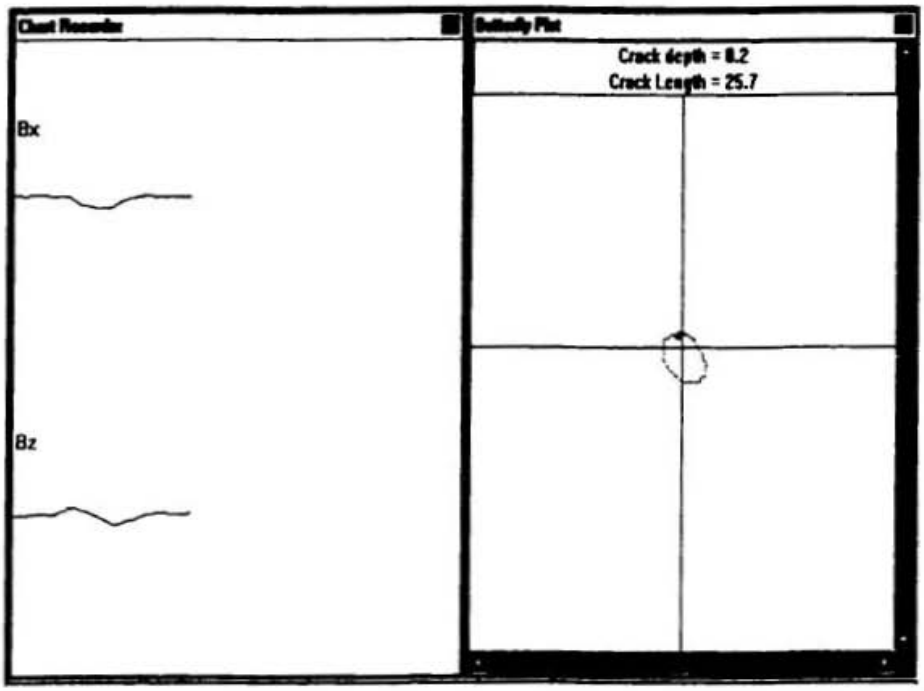

Table D.4. Scanning data from file **D25T38.wdf**

Data from Scanning I			
Pipe wall thickness	: 3.8 mm	Minimum B_x reading	: 1694
Defect depth	: 2.5 mm	Actual length	: 48 mm
Background B_x reading	: 1734	B_z length	: 22 mm
Data from Scanning II			
Pipe wall thickness	: 3.8 mm	Minimum B_x reading	: 1699
Defect depth	: 2.5 mm	Actual length	: 48 mm
Background B_x reading	: 1744	B_z length	: 23 mm
Data from Scanning III			
Pipe wall thickness	: 3.8 mm	Minimum B_x reading	: 1693
Defect depth	: 2.5 mm	Actual length	: 48 mm
Background B_x reading	: 1734	B_z length	: 21 mm
Data from Scanning IV			
Pipe wall thickness	: 3.8 mm	Minimum B_x reading	: 1695
Defect depth	: 2.5 mm	Actual length	: 48 mm
Background B_x reading	: 1737	B_z length	: 21 mm
Data from Scanning V			
Pipe wall thickness	: 3.8 mm	Minimum B_x Reading	: 1692
Defect depth	: 2.5 mm	Actual length	: 48 mm
Background B_x Reading	: 1734	B_z length	: 20 mm

D25T38.wdf Scanning I

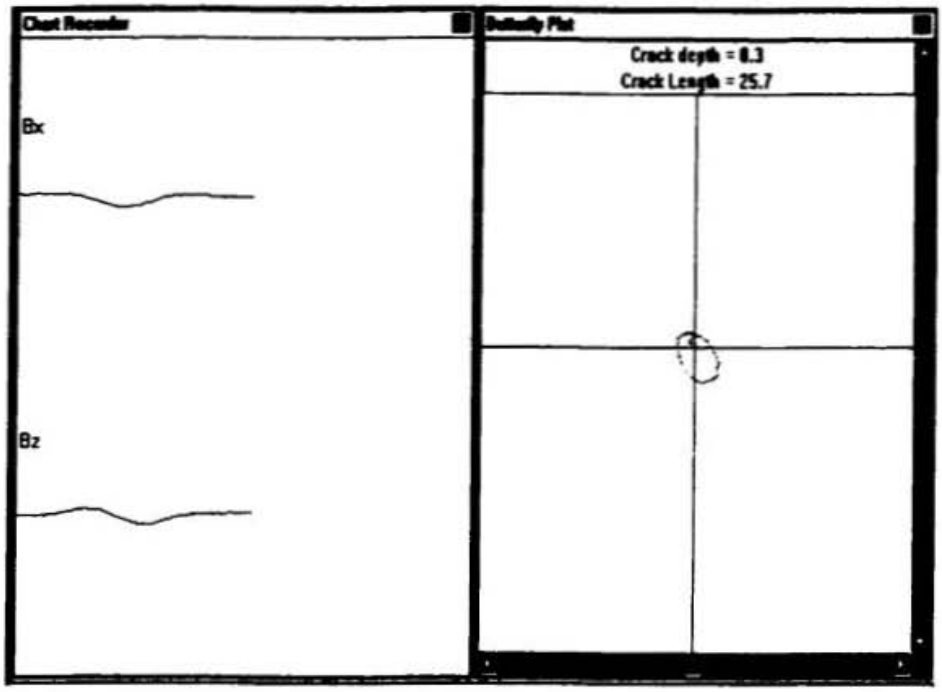

D25T38.wdf Scanning II

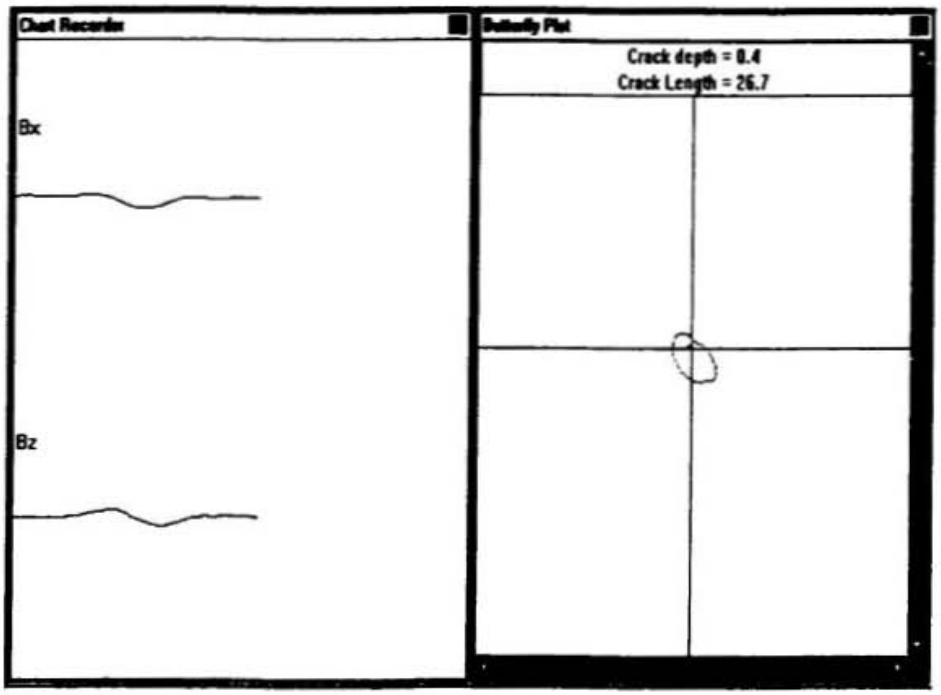

D25T38.wdf Scanning III

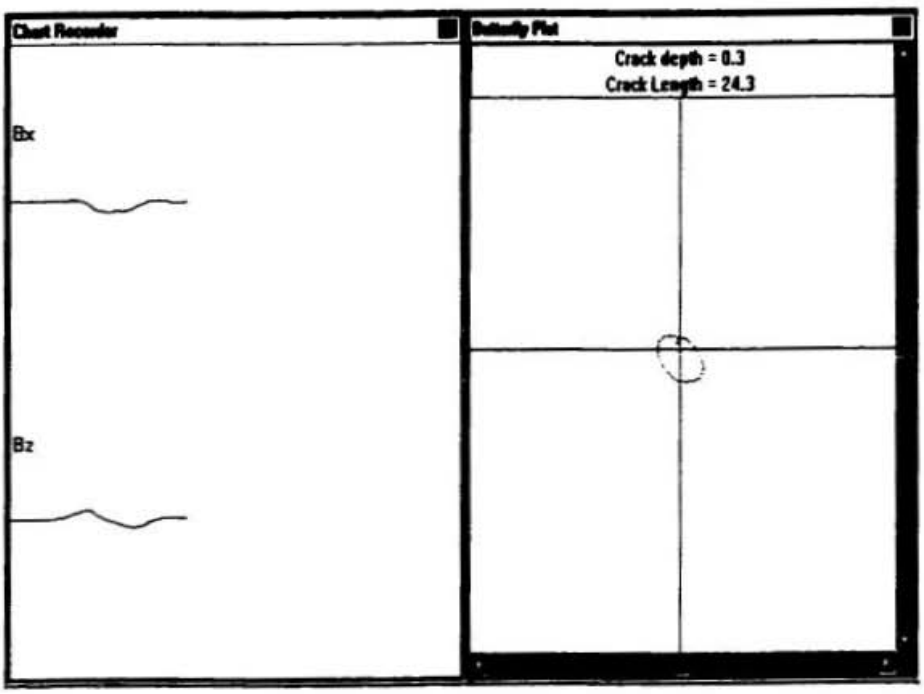

D25T38.wdf Scanning IV

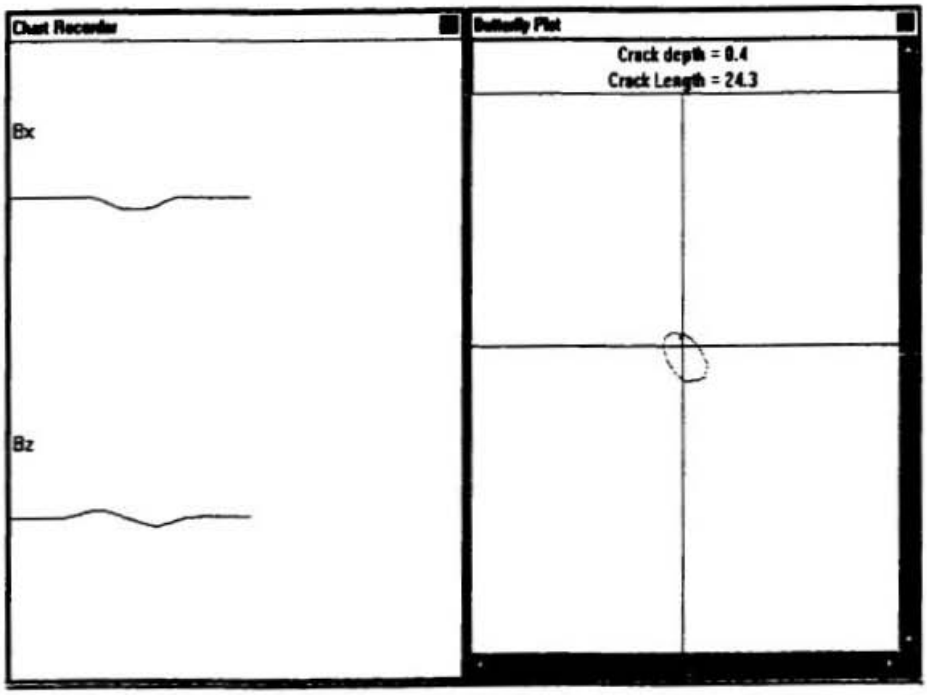

D25T38.wdf Scanning V

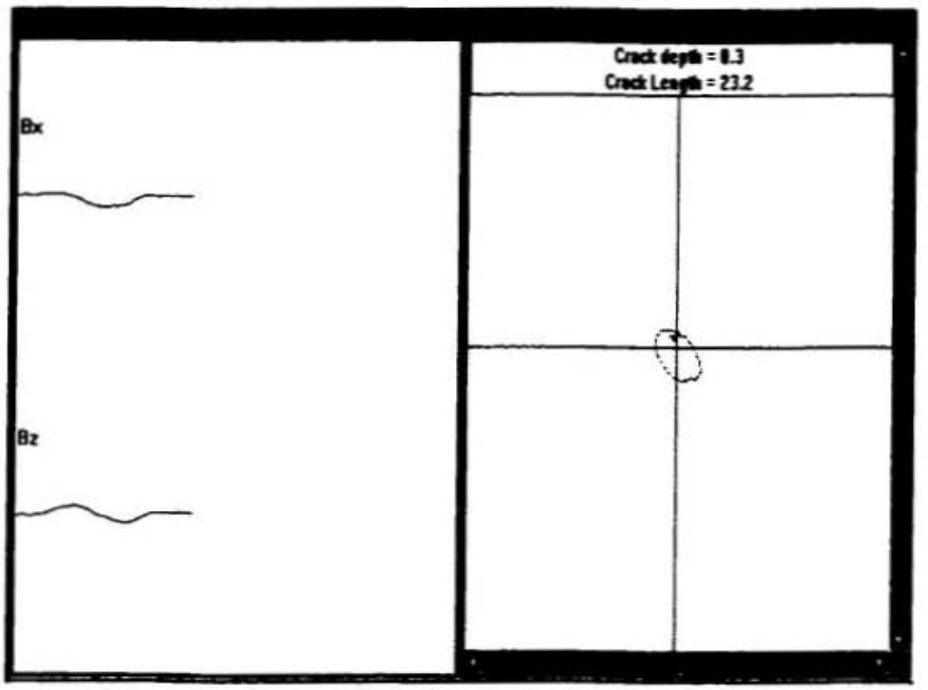

Table D.5. Scanning data from file **D30T38.wdf**

Data from Scanning I			
Pipe wall thickness	: 3.8 mm	Minimum B_x reading	: 1635
Defect depth	: 3.0 mm	Actual length	: 49 mm
Background B_x reading	: 1705	B_z length	: 24 mm
Data from Scanning II			
Pipe wall thickness	: 3.8 mm	Minimum B_x reading	: 1680
Defect depth	: 3.0 mm	Actual length	: 49 mm
Background B_x reading	: 1751	B_z length	: 20 mm
Data from Scanning III			
Pipe wall thickness	: 3.8 mm	Minimum B_x reading	: 1660
Defect depth	: 3.0 mm	Actual length	: 49 mm
Background B_x reading	: 1738	B_z length	: 22 mm
Data from Scanning IV			
Pipe wall thickness	: 3.8 mm	Minimum B_x reading	: 1665
Defect depth	: 3.0 mm	Actual length	: 49 mm
Background B_x reading	: 1733	B_z length	: 22 mm
Data from Scanning V			
Pipe wall thickness	: 3.8 mm	Minimum B_x reading	: 1683
Defect depth	: 3.0 mm	Actual length	: 49 mm
Background B_x reading	: 1758	B_z length	: 21 mm

D30T38.wdf – Scanning I

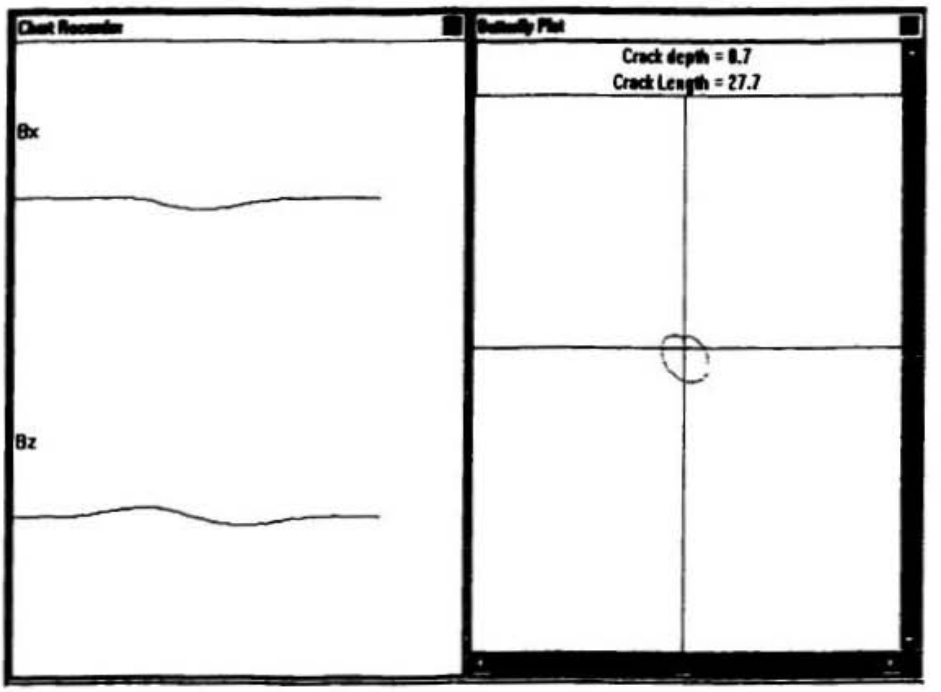

D30T38.wdf – Scanning II

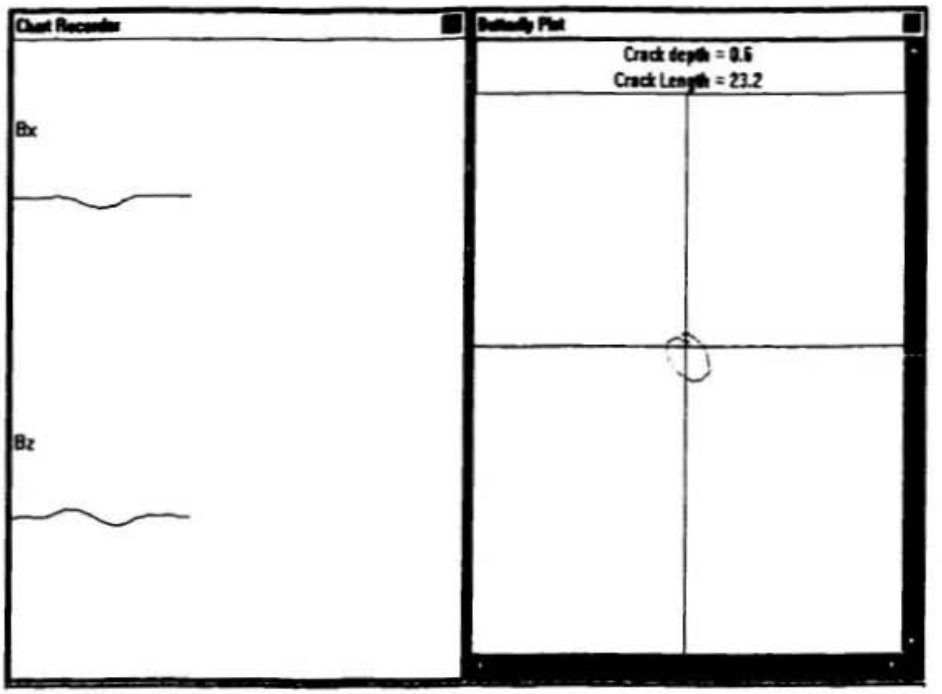

D30T38.wdf – Scanning III

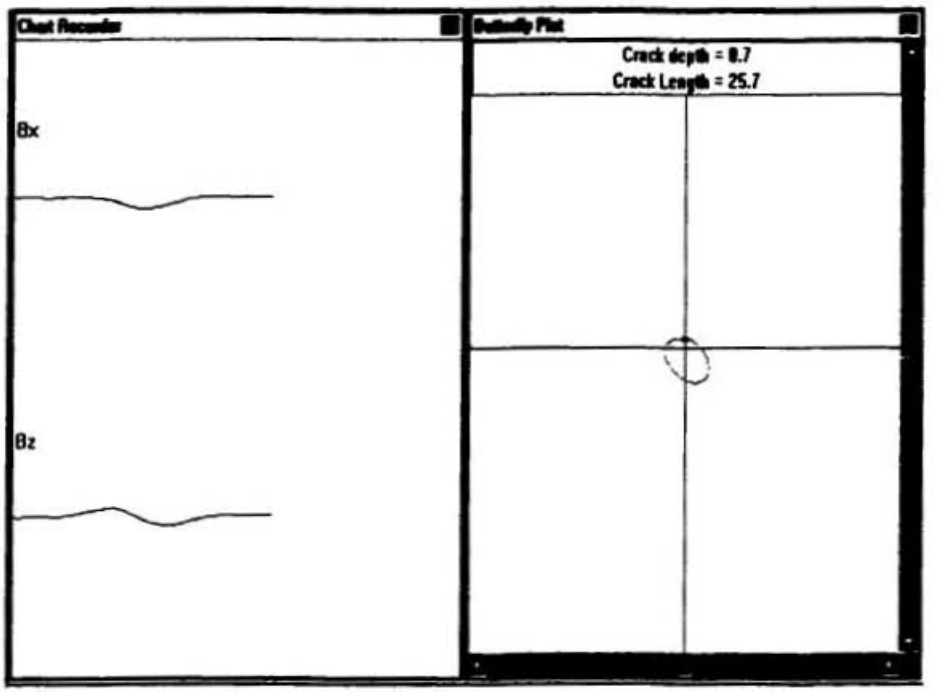

D30T38.wdf – Scanning IV

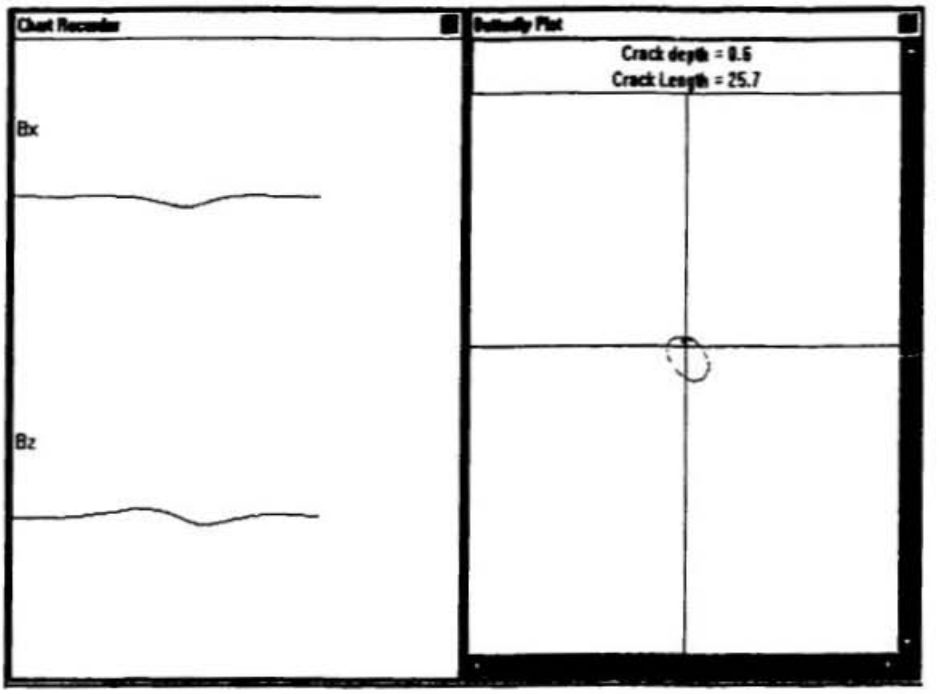

D30T38.wdf – Scanning V

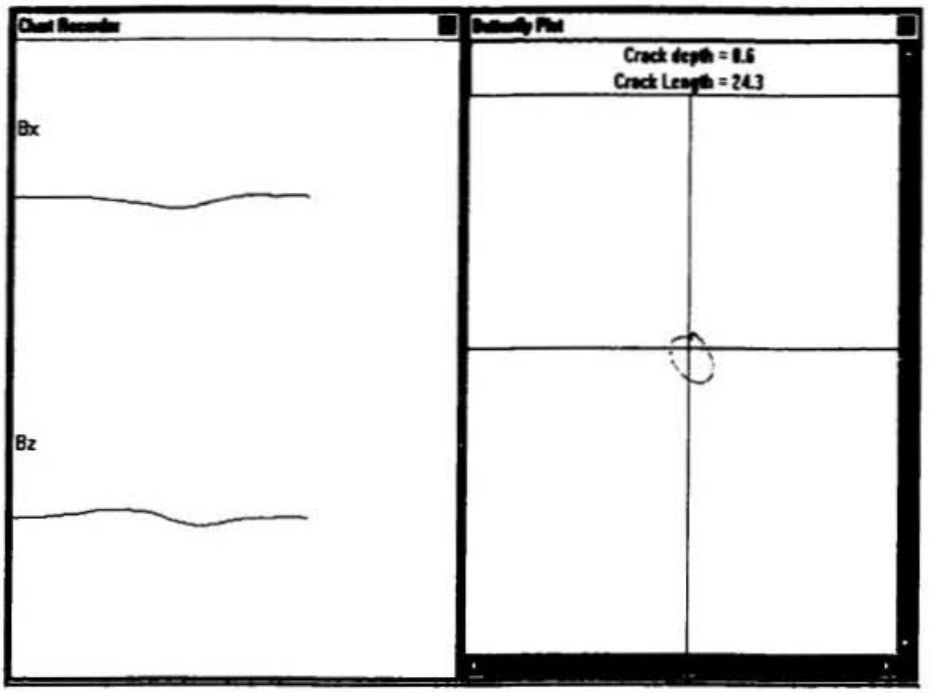

Table D.6. Scanning data from file **D35T38.wdf**

Data from Scanning I			
Pipe wall thickness	: 3.8 mm	Minimum B_x reading	: 1589
Defect depth	: 3.5 mm	Actual length	: 50 mm
Background B_x reading	: 1723	B_z length	: 22 mm
Data from Scanning II			
Pipe wall thickness	: 3.8 mm	Minimum B_x reading	: 1588
Defect depth	: 3.5 mm	Actual length	: 50 mm
Background B_x reading	: 1720	B_z length	: 20 mm
Data from Scanning III			
Pipe wall thickness	: 3.8 mm	Minimum B_x reading	: 1588
Defect depth	: 3.5 mm	Actual length	: 50 mm
Background B_x reading	: 1724	B_z length	: 21 mm
Data from Scanning IV			
Pipe wall thickness	: 3.8 mm	Minimum B_x reading	: 1594
Defect depth	: 3.5 mm	Actual length	: 50 mm
Background B_x reading	: 1734	B_z length	: 22 mm
Data from Scanning V			
Pipe wall thickness	: 3.8 mm	Minimum B_x reading	: 1592
Defect depth	: 3.5 mm	Actual length	: 50 mm
Background B_x reading	: 1726	B_z length	: 22 mm

D35T38.wdf – Scanning I

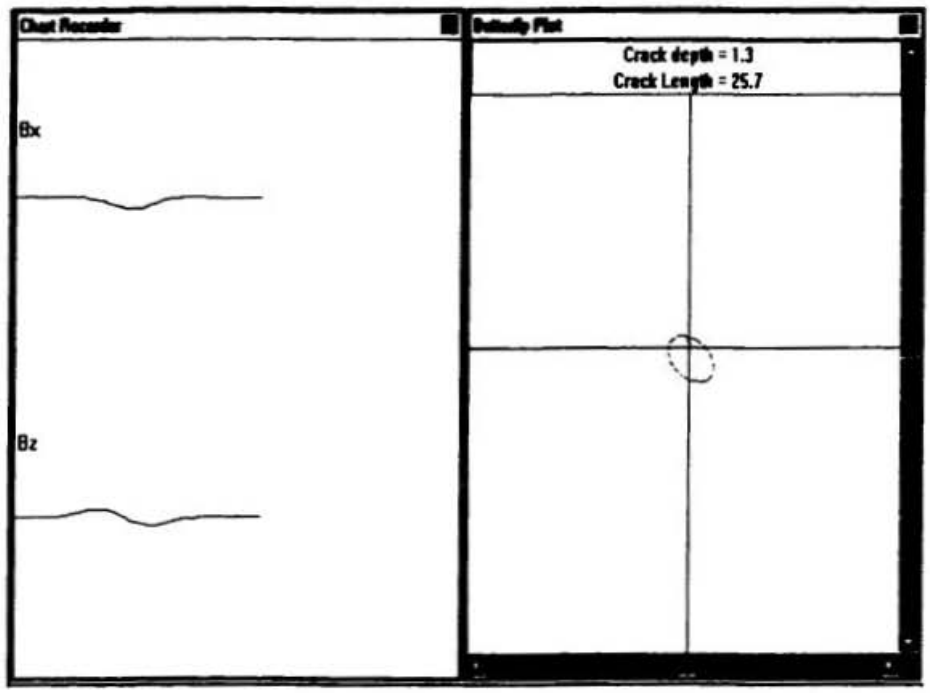

D35T38.wdf – Scanning II

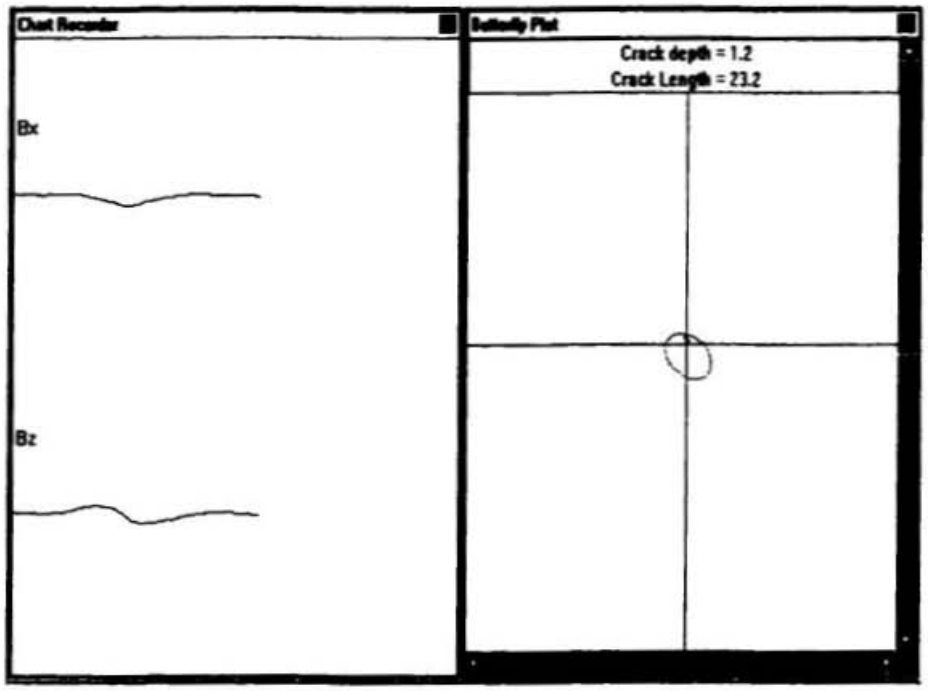

D35T38.wdf – Scanning III

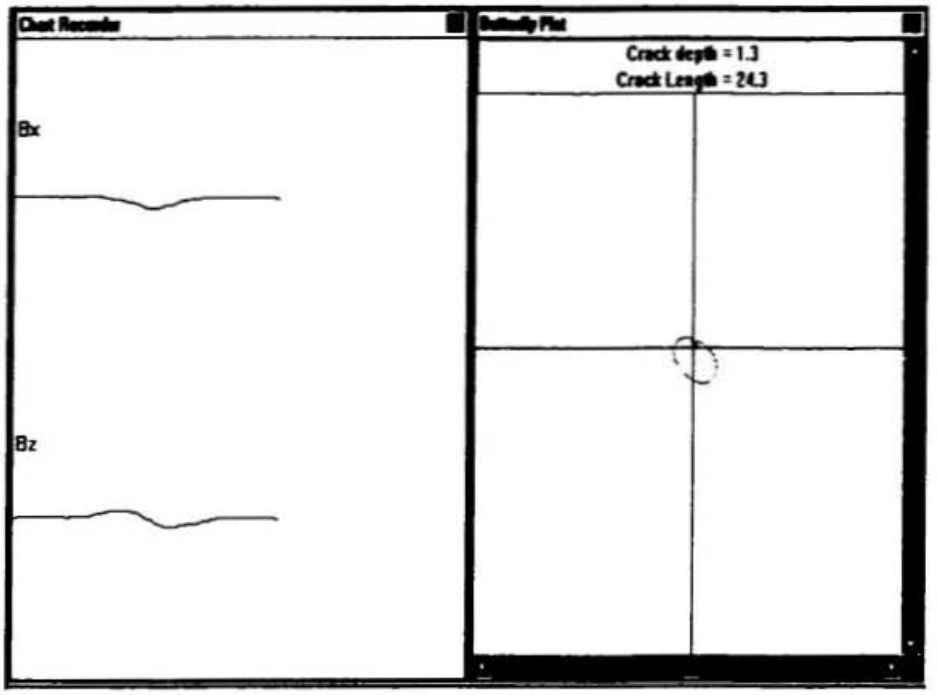

D35T38.wdf – Scanning IV

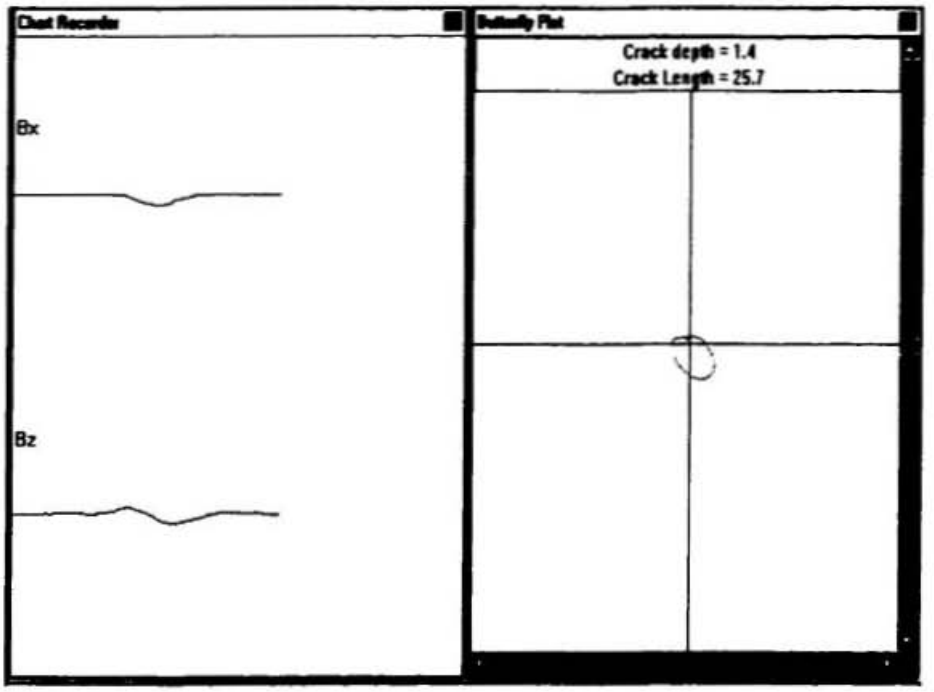

D35T38.wdf – Scanning V

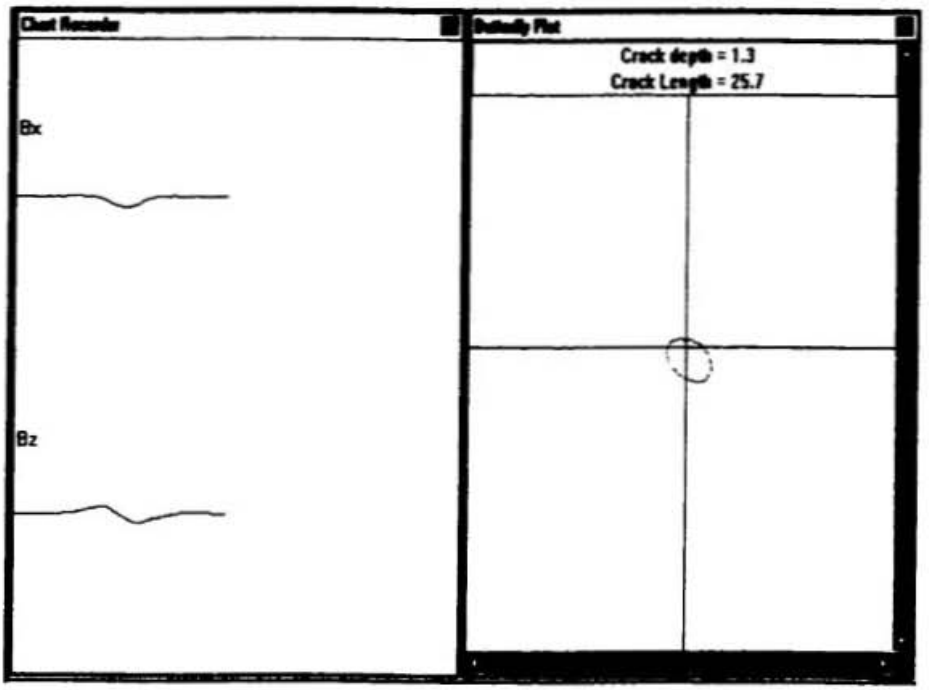

Table D.7. Summary table of scanning data from file **D10T38.wdf**

D10T38.wdf			
Actual Depth	**Signal Ratio**	**Actual Length**	**B_z Length**
1.0	0.009781358	44	18
1.0	0.009781358	44	21
1.0	0.007471264	44	18
1.0	0.009764503	44	21
1.0	0.009758898	44	20
Average	**0.009311476**	**44**	**19.6**

Table D.8. Summary table of scanning data from file **D15T38.wdf**

D15T38.wdf			
Actual Depth	**Signal Ratio**	**Actual Length**	**B_z Length**
1.5	0.008645533	45	21
1.5	0.009837963	45	21
1.5	0.00921659	45	22
1.5	0.010386613	45	20
1.5	0.009158558	45	18
Average	**0.009449051**	**45**	**20.4**

Table D.9. Summary table of scanning data from file **D20T38.wdf**

D20T38.wdf			
Actual Depth	**Signal Ratio**	**Actual Length**	**B_z Length**
2.0	0.01559792	46	20
2.0	0.016250725	46	19
2.0	0.015606936	46	21
2.0	0.015606936	46	21
2.0	0.015063731	46	22
Average	**0.01562525**	**46**	**20.6**

Table D.10. Summary table of scanning data from file **D25T38.wdf**

D25T38.wdf			
Actual Depth	**Signal Ratio**	**Actual Length**	**B_z Length**
2.5	0.023068051	48	22
2.5	0.025802752	48	23
2.5	0.023644752	48	21
2.5	0.02417962	48	21
2.5	0.024221453	48	20
Average	**0.024183326**	**48**	**21.4**

Table D.11. Summary table of scanning data from file **D30T38.wdf**

D30T38.wdf			
Actual Depth	**Signal Ratio**	**Actual Length**	**B_z Length**
3.0	0.041055718	49	24
3.0	0.040548258	49	20
3.0	0.044879171	49	22
3.0	0.039238315	49	22
3.0	0.042662116	49	21
Average	**0.041676716**	**49**	**21.8**

Table D.12. Summary table of scanning data from file **D35T38.wdf**

D35T38.wdf			
Actual Depth	**Signal Ratio**	**Actual Length**	**B_z Length**
3.5	0.077771329	50	22
3.5	0.076744186	50	20
3.5	0.078886311	50	21
3.5	0.080738178	50	22
3.5	0.077636153	50	22
Average	**0.078355231**	**50**	**21.4**